Remote sensing of mixed-phase clouds and their evolution during marine cold air outbreaks in the Arctic

Anna Franziska Weber

München 2025

Remote sensing of mixed-phase clouds and their evolution during marine cold air outbreaks in the Arctic

Anna Franziska Weber

Dissertation
der Fakultät für Physik
der Ludwig-Maximilians-Universität
München

vorgelegt von
Anna Franziska Weber
aus Freising

München, den 28.10.2025

Erstgutachter: Prof. Dr. Bernhard Mayer
Zweitgutachter: Prof. Dr. Markus Rapp
Tag der mündlichen Prüfung: 10.12.2025

Für meine Omas.

Zusammenfassung

Die Arktis erwärmt sich im Zuge des Klimawandels stärker als das globale Mittel. Neben starken Albedoveränderungen durch schmelzendes Meereis spielen Mischphasenwolken und meridionaler Feuchte- und Wärmetransport während Kaltluftausbrüchen eine wichtige Rolle für die arktische Verstärkung. Allerdings sind Mischphasenwolken und insbesondere deren thermodynamisches Phasenverhältnis und Entwicklung während Kaltluftausbrüchen nicht gut in Modellen dargestellt, was zu großen Unsicherheiten in Vorhersagen des zukünftigen Klimas führt. Beobachtungsdaten werden benötigt, um Modelle und Prozessverständnis zu verbessern.

Ziel dieser Arbeit ist es, die makro- und mikrophysikalischen Eigenschaften von arktischen Mischphasenwolken und deren Entwicklung während mariner Kaltluftausbrüche zu charakterisieren. Dazu wurden quasi-lagrangesche, flugzeuggestützte Messungen des hyperspektralen und polarisationssensitiven Kamerasystems specMACS während der HALO–$(\mathcal{AC})^3$-Messkampagne verwendet. Insbesondere wurden die thermodynamische Wolkenphase und Phasenübergänge untersucht. Hierzu wurde eine neue quantitative Methode zur Bestimmung des Phasenverhältnisses basierend auf Polarisationsmessungen entwickelt.

Im Rahmen dieser Arbeit wurden die Polarisationskameras von specMACS erstmals anhand von Labormessungen kalibriert und charakterisiert. Die Kalibrierung ermöglicht die Berechnung von absolut kalibrierten, georeferenzierten Stokes-Vektoren aus den Rohdaten. Eine Sensitivitätsstudie zeigte, dass 3D-Strahlungseffekte aufgrund der 3D-Wolkengeometrie für arktische Mischphasenwolken nicht vernachlässigbar sind. Allerdings sind 3D-Strahlungstransportsimulationen sehr rechenintensiv. Daher wurde eine Parametrisierung der 3D-Wolkengeometrie für polarisierten 3D-Strahlungstransport im sichtbaren Wellenlängenbereich, die „InDEpendent column local halF-sphere ApproXimation“ (IDEFAX), entwickelt. Davon ausgehend wurde ein schneller Vorwärtsoperator, der auf einem neuronalen Netz basiert, konstruiert und für ein simuliertes, realistisches Feld arktischer Mischphasenwolken validiert. Als nächstes wurde die quantitative Methode zur Bestimmung des Phasenverhältnisses entwickelt. Die Grundidee der Methode besteht darin, mithilfe des Vorwärtsoperators simulierte, winkelabhängige Polarisationssignale an Messungen von specMACS zu fitten, um einen quantitativen Eisanteil zu bestimmen. Die Methode wurde anhand synthetischer Daten für idealisierte Wolkenfälle sowie ein realistisches Feld arktischer Mischphasenwolken validiert.

Die Entwicklung der Wolkeneigenschaften wurde zunächst für eine Fallstudie eines starken Kaltluftausbruchs analysiert. Hierfür wurden Messungen mit Rückwärtstrajektorien

kombiniert. Mit zunehmender Aufenthaltszeit über dem Ozean wurden zunehmende Wolkenobergrenzen und horizontale Wolkengrößen, ein nahezu konstanter Bedeckungsgrad und anfänglich zunehmende Tröpfchenradien beobachtet. Zeitgleich mit der Zunahme des Tröpfchenradius wurde ein Phasenübergang von Flüssigwasser- zu Mischphasenwolken detektiert. Eine Analyse der Temperaturabhängigkeit der thermodynamischen Phase der Wolke zeigte, dass Eisbildung durch Gefrieren vorzugsweise bei den kältesten Temperaturen stattfand. Darüber hinaus befand sich in Übereinstimmung mit früheren Untersuchungen eine geometrisch dünne, stärker flüssigwasserdominierte Schicht an der Wolkenobergrenze. Außerdem wurde der Einfluss von Eisprozessen auf die unterkühlten Wolkentröpfchen untersucht. Unter der Annahme eines adiabatischen Wolkenmodells ließen sich die Messungen realistisch beschreiben. Der Einfluss von Kollision und Koaleszenz und Eisprozessen wie Riming, dem Wegener-Bergeron-Findeisen-Prozess oder Eisbildung durch Gefrieren auf die Tröpfchenradien war vernachlässigbar. Die Variabilität der Wolkenentwicklung während aller beobachteten Kaltluftausbrüche war groß. Bei stärkeren Ereignissen wurden größere und schneller ansteigende Wolkenobergrenzen, Wolkengrößen und Tröpfchenradien beobachtet. Zudem erfolgte der Phasenübergang von Flüssigwasser- zu Mischphasenwolken früher und höhere Eisanteile wurden erreicht.

Die in dieser Arbeit entwickelten Methoden und Analysen liefern einzigartige Beobachtungsdaten zu Mischphasenwolken, deren Phasenverhältnis und Entwicklung während mariner Kaltluftausbrüche in der Arktis. Diese Daten können zur Evaluierung von Modellen verwendet werden, um die Darstellung dieser Wolken zu verbessern.

Abstract

The Arctic is warming faster than the global average as a result of climate change. Mixed-phase clouds and meridional transports of heat and moisture during cold air outbreaks play an important role in Arctic amplification, and must be considered alongside the effects of strong albedo changes due to melting sea ice. However, mixed-phase clouds, and in particular, their thermodynamic phase partitioning and evolution during cold air outbreaks are not well represented in models, leading to large uncertainties in future climate projections. Observational data is needed to provide constraints to models and further the process understanding.

This work aims to characterize macro- and microphysical properties of Arctic mixed-phase clouds and their evolution during marine cold air outbreaks using quasi-Lagrangian airborne observations of the hyperspectral and polarized imaging system specMACS during the HALO–$(\mathcal{AC})^3$ measurement campaign. In particular, the cloud thermodynamic phase and phase transitions were investigated. To this end, a new quantitative retrieval of cloud thermodynamic phase partitioning from multi-angle polarimetric imaging was developed.

As part of this work, the polarization-resolving cameras of specMACS were calibrated and characterized for the first time using laboratory calibration measurements. The calibration allows computation of absolute calibrated, georeferenced Stokes vectors from raw data. A sensitivity study showed that 3D radiative effects related to 3D cloud geometry cannot be neglected for low-level Arctic mixed-phase clouds, but 3D radiative transfer simulations are computationally expensive. Therefore, a parameterization of 3D cloud geometry for polarized 3D radiative transfer in the visible wavelength range, the InDEpendent column local halF-sphere ApproXimation (IDEFAX), was developed. Based on this, a neural-network-based fast forward operator was constructed and validated for a simulated realistic field of Arctic mixed-phase clouds. Next, the new quantitative polarized phase retrieval was developed. The basic idea behind this retrieval is to fit simulated multi-angle polarization signals obtained from the forward operator to measurements of specMACS to determine a quantitative ice fraction. The retrieval was validated using synthetic data for idealized cloud cases, as well as a realistic field of Arctic mixed-phase clouds.

The evolution of cloud properties was analyzed for a case study of a strong cold air outbreak by combining measurements with backward trajectories. With increasing time spent over open ocean, cloud top height and horizontal extent increased while cloud fraction remained almost constant. Moreover, an initial increase in droplet radii, coinciding with a transition from the liquid to the mixed-phase regime, was observed. An analysis

of the temperature dependence of the cloud thermodynamic phase indicated that ice formation through freezing occurred preferentially at the coldest temperatures. Moreover, a geometrically thin, more liquid-dominated layer was located at the cloud top, in accordance with previous studies. In addition, the influence of ice processes on supercooled liquid water droplets was investigated. The measurements could be realistically described by assuming an adiabatic cloud model. The influence of collision-coalescence and ice processes, such as riming, the Wegener-Bergeron-Findeisen mechanism, and ice formation through freezing on the droplet radius was negligible. Furthermore, the variability of cloud evolution during all observed cold air outbreaks was large. Larger and faster increasing cloud top heights, cloud sizes, and droplet radii were observed for stronger events. In addition, the transition from the liquid to the mixed-phase regime was earlier and ice fractions were higher during stronger events.

The analyses and methods developed in this work provide unique observational data of mixed-phase clouds, their thermodynamic phase partitioning, and evolution during marine cold air outbreaks in the Arctic which can be used for model evaluation to improve the representation of these clouds.

Publications

First author publications that are part of this thesis:

- Weber, A., Kölling, T., Pörtge, V., Baumgartner, A., Rammeloo, C., Zinner, T., and Mayer, B.: Polarization upgrade of specMACS: calibration and characterization of the 2D RGB polarization-resolving cameras, Atmospheric Measurement Techniques, 17, 1419–1439, doi:10.5194/amt-17-1419-2024, 2024.
- Weber, A., Köcher, G., and Mayer, B.: Parameterization of 3D cloud geometry and a neural-network-based fast forward operator for polarized radiative transfer, Atmospheric Measurement Techniques, 18, 5805–5821, doi:10.5194/amt-18-5805-2025, 2025c.
- Weber, A., Pörtge, V., Emde, C., and Mayer, B.: Retrieval of cloud thermodynamic phase partitioning from multi-angle polarimetric imaging of Arctic mixed-phase clouds, Atmospheric Measurement Techniques, 18, 7581–7601, doi:10.5194/amt-18-7581-2025, 2025d.
- Weber, A., Kirbus, B., Wendisch, M., and Mayer, B.: Quasi-Lagrangian observations of cloud transitions during the initial phase of marine cold air outbreaks in the Arctic – Part 1: Temporal and spatial evolution, EGUsphere, 2025, 1–25, doi:10.5194/egusphere-2025-5831, 2025b.
- Weber, A., Hoffmann, F., and Mayer, B.: Quasi-Lagrangian observations of cloud transitions during the initial phase of marine cold air outbreaks in the Arctic – Part 2: Vertical cloud structure, EGUsphere, 2025, 1–26, doi:10.5194/egusphere-2025-5832, 2025a.

The content of Weber et al. (2024), Weber et al. (2025c), and Weber et al. (2025d) can be found in Sect. 3.1, Sect. 3.3, and Sect. 3.4, respectively. Weber et al. (2025b) and Weber et al. (2025a) include the results of Sect. 4.2 and 4.3. In addition, the introduction in Sect. 1 contains some minor parts of Weber et al. (2025d) and Weber et al. (2025b). The content of the publications has been slightly modified to align conventions, avoid repetition, and enhance clarity. Further publications I actively contributed to as a co-author are:

- Pörtge, V., Kölling, T., Weber, A., Volkmer, L., Emde, C., Zinner, T., Forster, L., and Mayer, B.: High-spatial-resolution retrieval of cloud droplet size distribution from polarized observations of the cloudbow, Atmospheric Measurement Techniques, 16, 645–667, doi:10.5194/amt-16-645-2023, 2023.
- Wendisch, M., Crewell, S., Ehrlich, A., Herber, A., Kirbus, B., Lüpkes, C., Mech, M., Abel, S. J., Akansu, E. F., Ament, F., Aubry, C., Becker, S., Borrmann, S.,

Bozem, H., Brückner, M., Clemen, H.-C., Dahlke, S., Dekoutsidis, G., Delanoë, J., De La Torre Castro, E., Dorff, H., Dupuy, R., Eppers, O., Ewald, F., George, G., Gorodetskaya, I. V., Grawe, S., Groß, S., Hartmann, J., Henning, S., Hirsch, L., Jäkel, E., Joppe, P., Jourdan, O., Jurányi, Z., Karalis, M., Kellermann, M., Klingebiel, M., Lonardi, M., Lucke, J., Luebke, A. E., Maahn, M., Maherndl, N., Maturilli, M., Mayer, B., Mayer, J., Mertes, S., Michaelis, J., Michalkov, M., Mioche, G., Moser, M., Müller, H., Neggers, R., Ori, D., Paul, D., Paulus, F. M., Pilz, C., Pithan, F., Pöhlker, M., Pörtge, V., Ringel, M., Risse, N., Roberts, G. C., Rosenburg, S., Röttenbacher, J., Rückert, J., Schäfer, M., Schaefer, J., Schemann, V., Schirmacher, I., Schmidt, J., Schmidt, S., Schneider, J., Schnitt, S., Schwarz, A., Siebert, H., Sodemann, H., Sperzel, T., Spreen, G., Stevens, B., Stratmann, F., Svensson, G., Tatzelt, C., Tuch, T., Vihma, T., Voigt, C., Volkmer, L., Walbröl, A., Weber, A., Wehner, B., Wetzel, B., Wirth, M., and Zinner, T.: Overview: quasi-Lagrangian observations of Arctic air mass transformations – introduction and initial results of the HALO–$(\mathcal{AC})^3$ aircraft campaign, Atmospheric Chemistry and Physics, 24, 8865–8892, doi:10.5194/acp-24-8865-2024, 2024.

- Ehrlich, A., Crewell, S., Herber, A., Klingebiel, M., Lüpkes, C., Mech, M., Becker, S., Borrmann, S., Bozem, H., Buschmann, M., Clemen, H.-C., De La Torre Castro, E., Dorff, H., Dupuy, R., Eppers, O., Ewald, F., George, G., Giez, A., Grawe, S., Gourbeyre, C., Hartmann, J., Jäkel, E., Joppe, P., Jourdan, O., Jurányi, Z., Kirbus, B., Lucke, J., Luebke, A. E., Maahn, M., Maherndl, N., Mallaun, C., Mayer, J., Mertes, S., Mioche, G., Moser, M., Müller, H., Pörtge, V., Risse, N., Roberts, G., Rosenburg, S., Röttenbacher, J., Schäfer, M., Schaefer, J., Schäfler, A., Schirmacher, I., Schneider, J., Schnitt, S., Stratmann, F., Tatzelt, C., Voigt, C., Walbröl, A., Weber, A., Wetzel, B., Wirth, M., and Wendisch, M.: A comprehensive in situ and remote sensing data set collected during the HALO–$(\mathcal{AC})^3$ aircraft campaign, Earth System Science Data, 17, 1295–1328, doi:10.5194/essd-17-1295-2025, 2025.
- Jurkat-Witschas, T., Voigt, C., Groß, S., Kaufmann, S., Sauer, D., la Torre Castro, E. D., Krämer, M., Schäfler, A., Afchine, A., Attinger, R., Garcia, I. B., Beer, C. G., Bugliaro, L., Clemen, H.-C., Dekoutsidis, G., Ehrlich, A., Grawe, S., Hahn, V., Hendricks, J., Järvinen, E., Klimach, T., Krüger, K., Krüger, O., Lucke, J., Luebke, A. E., Marsing, A., Mayer, B., Mayer, J., Mertes, S., Milenko, R.-Z., Moser, M., Müller, H., Nenakhov, V., Pöhlker, M., Pöschl, U., Pörtge, V., Rautenhaus, M., Righi, M., Röttenbacher, J., Schaefer, J., Schnaiter, M., Schneider, J., Schumann, U., Spelten, N., Stratmann, F., Tomsche, L., Wagner, S., Wang, Z., Weber, A., Wendisch, M., Wernli, H., Wetzel, B., Wirth, M., Zahn, A., Ziereis, H., and Zöger, M.: CIRRUS-HL: Picturing High- and Midlatitude Summer Cirrus and Contrail Cirrus above Europe with Airborne Measurements aboard the Research Aircraft HALO, Bulletin of the American Meteorological Society, 106, E2300 – E2327, doi:10.1175/BAMS-D-23-0270.1, 2025.
- Forster, L., Weber, A., and Mayer, B.: CrystalTrace: a Monte Carlo raytracing algorithm for radiative transfer in cirrus clouds with oriented ice crystals, Atmospheric Measurement Techniques, 18, 7853–7863, doi:10.5194/amt-18-7853-2025, 2025.

Contents

Chapter 1

Introduction

Parts of this section have already been published in Weber et al. (2025d) and Weber et al. (2025b).

1.1 Arctic amplification, clouds, and cold air outbreaks

The Arctic is rapidly changing and is warming two to four times faster than the global average as a result of climate change (Jeffries et al., 2013; Overland et al., 2019; Rantanen et al., 2022). Sea ice extent and thickness are decreasing faster than predicted by models (Stroeve et al., 2012; Screen, 2021), snow cover is changing, and permafrost is thawing increasingly (Beer et al., 2020). The higher climate sensitivity of the Arctic compared to the rest of the globe is known as Arctic amplification (Serreze and Francis, 2006; Serreze and Barry, 2011). The Arctic exhibits some unique characteristics. In particular, large solar zenith angles, the occurrence of polar night and day, frequent and persistent low-level mixed-phase clouds, high and heterogeneous surface albedo due to variations of snow cover, sea ice, and open ocean, and frequent near-surface temperature and moisture inversions distinguish the Arctic from lower latitudes (Wendisch et al., 2017, 2023).

Arctic amplification is a direct response to climate forcing and can be explained by local and remote processes and feedbacks and their complex interactions (Previdi et al., 2021; Wendisch et al., 2023). Local processes include effects of sea ice and surface albedo changes, the Planck and lapse rate feedback, the water vapor feedback, and the cloud feedback. The feedbacks related to temperature and sea ice, namely the Planck feedback, the lapse rate feedback, and the surface albedo feedback, are especially important (Pithan and Mauritsen, 2014; Previdi et al., 2021). In addition, changes in the meridional transport of heat and moisture by the atmosphere and ocean from lower latitudes to the Arctic are an important remote process (Wendisch et al., 2023; Previdi et al., 2021). Furthermore, the Arctic climate is influenced by changing aerosol concentrations due to, for example, increased industrial activity or biogenic emissions in a warmer, more ice-free Arctic and varying transport of

aerosols from lower latitudes into the Arctic (Schmale et al., 2018; Maahn et al., 2021). However, the quantitative contributions of the different processes and feedbacks as well as their interactions are still not completely understood (Wendisch et al., 2019, 2023).

Arctic amplification influences not only the Arctic itself but also affects the mid-latitudes. Melting land ice leads to global sea level rise, and permafrost thawing contributes to increasing greenhouse gas concentrations (Previdi et al., 2021). In addition, changes in atmospheric circulation and the jet stream due to Arctic amplification can increase the frequency of blocking events and lead to extreme weather in the mid-latitudes (Cohen et al., 2014; Walsh, 2014; Cohen et al., 2020).

Despite the importance of the Arctic for the global climate system, future projections of Arctic climate have high uncertainties (Smith et al., 2019; Cohen et al., 2020; Block et al., 2020). These uncertainties arise particularly due to the representation of clouds in climate models (Pithan et al., 2014; Wendisch et al., 2019; Kretzschmar et al., 2020) and the modeling of air mass transformations during meridional transports (Pithan et al., 2018; Nash et al., 2018; Wendisch et al., 2021). Both clouds and meridional transports in the Arctic will be discussed in more detail in the following.

Mixed-phase clouds play a crucial role in the feedback mechanisms related to Arctic amplification (Tan et al., 2023). Clouds modulate the energy budget through scattering, absorption, and emission of solar and thermal radiation. Low-level clouds in the Arctic generally have a warming effect on the surface except for a short period in mid-summer (Intrieri et al., 2002). Arctic cloud cover is expected to increase as the water vapor concentrations rise and sea ice decreases in a warming climate. However, the magnitude of the Arctic cloud feedback is highly uncertain, and clouds in general still contribute the largest uncertainty to future projections of global climate (Block et al., 2020; IPCC, 2021).

Due to their high frequency and persistence, mixed-phase clouds are particularly important in the Arctic. They are observed in 40 % to 70 % of the time with the highest frequencies in spring and fall (Shupe et al., 2006; Shupe, 2011). Despite the inherent instability of the mixed-phase state, Arctic mixed-phase clouds persist on average for 12 hours and occasionally for several days (Shupe et al., 2006; Morrison et al., 2012). A thin layer of supercooled liquid water is typically located at the cloud top, and ice crystals form from this layer through heterogeneous nucleation and sediment downwards. The ice crystals can grow rapidly at the expense of supercooled liquid water via the Wegener-Bergeron-Findeisen process (Wegener, 1911; Bergeron, 1935; Findeisen, 1938). The partitioning and spatial distribution of cloud thermodynamic phase are important quantities, as cloud thermodynamic phase affects cloud cover and cloud lifetime (Pithan et al., 2014). Moreover, liquid water and ice have different optical and radiative properties. Cloud thermodynamic phase partitioning thus determines the radiative effect of clouds (Choi et al., 2014; Matus and L'Ecuyer, 2017), which also impacts surface processes and sea ice extent (Morrison et al., 2012).

Comparisons between observations and model simulations showed that mixed-phase clouds and their microphysics are not well represented in climate and general circulation models (Morrison et al., 2012; Pithan et al., 2014; Komurcu et al., 2014; Cesana et al., 2015, 2022). In particular, accurate modeling of cloud thermodynamic phase partitioning and the

vertical distribution of cloud liquid water poses a challenge (Inoue et al., 2021; Kretzschmar et al., 2019, 2020). Consequently, there are large uncertainties in the projections of future climate due to the insufficient representation of mixed-phase clouds, especially in the Arctic (Tan and Storelvmo, 2019). Future climate projections with an improved representation of mixed-phase clouds recently showed increased global warming and an underestimation of climate sensitivity by current models (Tan et al., 2016; Hofer et al., 2024).

Furthermore, meridional transports of heat and moisture are relevant to Arctic amplification, linking the mid-latitudes and the Arctic (Wendisch et al., 2021). Such meridional transports can happen through warm air intrusions or cold air outbreaks and include intense air mass transformations (Pithan et al., 2018). Warm air intrusions (WAIs) are localized pulses of warm and moist air from lower latitudes that penetrate the Arctic. They occur throughout the year and lead to the formation of low-level clouds, which warm the surface and favor sea ice melt. In contrast, dry Arctic air masses are advected southwards over warm open ocean during marine cold air outbreaks (MCAOs) (Papritz and Spengler, 2017; Fletcher et al., 2016a). The potential temperature difference between the cold advected air masses and the ocean surface can be up to 30 K and leads to convection and the formation of low-level clouds (Papritz and Spengler, 2017). These typically organize into cloud streets oriented along the mean wind direction and transition into cellular structures further downstream (Brümmer, 1999; Pithan et al., 2018). The clouds formed during MCAOs are typically in a mixed-phase regime. In addition, the large temperature gradients create intense surface fluxes of heat and moisture, which are responsible for 60 % to 80 % of oceanic heat loss during winter in the Nordic Seas, affecting deep water formation and sea ice (Papritz and Spengler, 2017). MCAOs are most frequent in winter, but also occur in spring and autumn (Fletcher et al., 2016a). They are related to severe weather events in the mid-latitudes, including cold extremes and heavy snowfall, as well as to polar lows (Pithan et al., 2018).

Future projections and observations indicate that the frequency and intensity of MCAOs decreases in a warming climate due to the decreasing temperature differences between the source regions in the Arctic and the affected regions at lower latitudes (Landgren et al., 2019; Smith and Sheridan, 2021; Dahlke et al., 2022). Moreover, the spatial patterns of MCAO occurrence will shift northwards due to sea ice retreat. MCAOs are often associated with blocking events. Changes in the atmospheric circulation due to global warming will affect the occurrence of these events and hence also influence MCAOs (Woollings et al., 2018; Cohen et al., 2021).

Large-scale as well as high-resolution models are struggling to accurately represent the air mass transformations during meridional transports into and out of the Arctic (Sato et al., 2016; Pithan et al., 2016; Tomassini et al., 2017; Field et al., 2017; Wendisch et al., 2021). Especially the microphysical evolution of clouds during MCAOs and WAIs is difficult to model (Pithan et al., 2014; McCoy et al., 2015; Tan and Storelvmo, 2019; Field et al., 2014; Abel et al., 2017).

Thus, observations of the evolution of clouds and, in particular, their thermodynamic phase partitioning and phase transitions during MCAOs are crucial for improving the understanding of mixed-phase clouds, air mass transformations, and Arctic amplification,

as well as for providing constraints to models (Pithan et al., 2018).

1.2 Previous work

Various observation methods of cloud thermodynamic phase, based on passive and active remote sensing, as well as in situ measurements, have been developed in the past. In addition, several studies investigated MCAOs and the related thermodynamic structure or clouds. The following section gives a brief overview of the previous work on these topics.

Existing retrievals of cloud thermodynamic phase from passive remote sensing use spectral absorption differences between liquid water and ice in the near-infrared. Based on this, Ehrlich et al. (2008) and Jäkel et al. (2013) defined so-called ice indices to distinguish between the liquid, mixed, and ice phases. Thompson et al. (2016) extended the spectral approach by introducing an improved spectrum fitting method. Ruiz-Donoso et al. (2020) studied the horizontal distribution of the ice index in Arctic mixed-phase clouds and combined it with radar measurements. In addition, Wang et al. (2020) developed a machine learning approach with a random forest for phase classification using Meteosat Second Generation data. Cloud thermodynamic phase was also derived from polarization measurements of POLDER (Goloub et al., 2000) and combined with the spectral retrieval of cloud phase from MODIS to distinguish liquid water, mixed-phase, and ice clouds (Riedi et al., 2010). Finally, Mayer et al. (2024) employed a probabilistic approach using passive satellite measurements to classify clouds into mixed, ice, supercooled liquid, and warm liquid. The cloud thermodynamic phase obtained from passive remote sensing is representative for the uppermost part of the clouds close to the cloud top.

Active remote sensing using lidar and radar measurements, on the other hand, allows for studying the vertical structure of cloud thermodynamic phase by using a synergistic retrieval, as in e.g. Mioche et al. (2015). However, the mentioned retrieval methods based on active and passive remote sensing do not provide quantitative phase information about the partitioning between liquid water and ice, but only a simple phase classification. Moreover, the spectral retrievals are strongly affected by 3D radiative effects, especially at large solar zenith angles, which are typical in polar regions.

In situ observations of mixed-phase clouds and cloud thermodynamic phase were analyzed by, e.g., McFarquhar et al. (2007), Jourdan et al. (2010), Mioche et al. (2017), and Moser et al. (2023). In contrast to retrievals based on remote sensing, in situ measurements provide quantitative information about cloud phase partitioning, but provide information only along the one-dimensional flight track. In addition, accurate phase discrimination in mixed-phase clouds is also challenging for in situ measurements (Korolev et al., 2017). In order to obtain accurate quantitative results, a combination of different in situ probes is necessary. Cloud phase partitioning can be determined either through measurements of the liquid and total water content or through the asymmetry parameter. However, the measurements usually have large uncertainties. For example, Moser et al. (2023) found that the uncertainty for in situ measurements of the cloud water content in mixed-phase clouds ranges from 20 to 50 %.

MCAOs have been extensively studied using reanalysis data, ground-based measurements, airborne in situ and remote sensing measurements, satellite observations, and model data. Most studies used an Eulerian perspective with a locally fixed coordinate system, while some others applied a quasi-Lagrangian approach. In the Lagrangian perspective, the coordinate system follows the observed air mass, which allows for investigating its temporal evolution. However, real Lagrangian observations are challenging (Wendisch et al., 2023). Instead, the evolution of air masses can be studied in a quasi-Lagrangian way by applying backward trajectories (Wendisch et al., 2023).

Several studies focused on the properties of clouds during MCAOs. These include dedicated ground-based and ship-based field campaigns providing Eulerian observations of cloud properties (Uttal et al., 2002; Geerts et al., 2022; Shupe et al., 2022; Lackner et al., 2023; Mages et al., 2023; Xia and McFarquhar, 2024). In addition, the microphysical properties of the different cloud regimes during MCAOs and transitions between them were also studied during several airborne field campaigns using in situ data (Young et al., 2016; Abel et al., 2017; Lloyd et al., 2018; Michaelis et al., 2022) as well as remote sensing observations (Ruiz-Donoso et al., 2020). Besides, model data was also applied to investigate the evolution of clouds in MCAOs (Tornow et al., 2021).

Quasi-Lagrangian analyses of cloud properties during MCAOs combining satellite observations with backward trajectories were carried out by Murray-Watson et al. (2023), Wu and Ovchinnikov (2022), Tornow et al. (2023), Mateling et al. (2023), or Seppala et al. (2025). They investigated the temporal evolution of macro- and microphysical cloud properties, derived, e.g., from MODIS or CloudSat data, and their dependency on, e.g., the MCAO strength or aerosol conditions. However, satellite observations of cloud properties in the Arctic are only possible with polar-orbiting satellites and are strongly affected by small-scale variability, which is not resolved by the too coarse resolution satellite measurements (Ahn et al., 2018; Marchant et al., 2020). The retrieval of cloud thermodynamic phase partitioning and other microphysical properties is especially challenging, and most satellite-based studies are restricted to liquid water clouds. Typical scales of inhomogeneity in Arctic clouds are on the order of a few hundred meters (Schäfer et al., 2017, 2018). These scales can only be resolved by high-spatial resolution airborne measurements.

Airborne quasi-Lagrangian observations of clouds during MCAOs in the Arctic were performed during the HALO–$(\mathcal{AC})^3$ measurement campaign (Wendisch et al., 2024). Even though several airborne research campaigns were conducted in the Arctic during the last decades (Forsberg et al., 2023) and some quasi-Lagrangian airborne measurements were collected outside the Arctic (Boettcher et al., 2021), HALO–$(\mathcal{AC})^3$ was the first quasi-Lagrangian airborne campaign targeting MCAOs and WAIs in the Arctic (Wendisch et al., 2024). Schirmacher et al. (2024) analyzed the evolution of precipitation and other cloud properties in the roll convection regime using radar data in two case studies of a stronger and a weaker MCAO during HALO–$(\mathcal{AC})^3$. However, the evolution of cloud thermodynamic phase and other microphysical cloud properties has not been studied in a quasi-Lagrangian way using high-spatial resolution airborne measurements so far.

1.3 Objectives and outline

This work is based on measurements of the specMACS instrument during the HALO–$(\mathcal{AC})^3$ field campaign. specMACS is a hyperspectral and polarized imaging system operated in a downward-looking perspective on board the German research aircraft HALO. It provides high-spatial resolution information about cloud macro- and microphysical properties. The HALO–$(\mathcal{AC})^3$ campaign, conducted in March and April 2022, aimed to improve the understanding of air mass transformations during meridional transports into and out of the Arctic, such as MCAOs. HALO followed a quasi-Lagrangian flight strategy, allowing for studying the evolution of cloud properties during MCAOs. The main objectives of this work are the

- development of a quantitative retrieval of cloud thermodynamic phase partitioning using multi-angle polarimetric imaging, including retrieval validation and an uncertainty assessment, and the
- characterization of macro- and microphysical properties of low-level Arctic mixed-phase clouds and their evolution during MCAOs with a special focus on cloud thermodynamic phase and phase transitions using quasi-Lagrangian airborne remote sensing observations.

The theoretical background for this work, including an introduction to cloud microphysics, MCAOs, radiative transfer, and the adiabatic cloud model, is presented in Sect. 2. In order to achieve the objectives, several steps are necessary. First, the polarization-resolving camera components of specMACS are characterized and calibrated for the first time to convert raw measurements into absolute calibrated, georeferenced Stokes vectors, which are needed for the new phase retrieval. Calibration measurements were conducted in a laboratory and are evaluated in detail. An instrument description and the calibration methods and results are presented in Sect. 3.1. Second, a fast forward operator for polarized radiative transfer in the visible wavelength range for the new phase partitioning retrieval is introduced in Sect. 3.3. A sensitivity analysis showed that 3D radiative effects related to cloud geometry can not be neglected for low-level Arctic mixed-phase clouds, and information about 3D cloud geometry can be derived from the measurements of specMACS. However, polarized 3D radiative transfer simulations are computationally expensive. Therefore, a parameterization of 3D cloud geometry, the InDEpendent column local halF-sphere ApproXimation (IDEFAX), is presented. This parameterization is then applied to construct a fast forward operator and validated using synthetic data. Next, the new quantitative retrieval of cloud thermodynamic phase partitioning from multi-angle polarimetric imaging is introduced in Sect. 3.4. The retrieval determines a quantitative ice fraction, defined as the fraction of the optical thickness of cloud ice to the total cloud optical thickness, by fitting measured multi-angle polarization signals to simulations obtained with the forward operator. The retrieval is validated using synthetic data, and a detailed uncertainty assessment is performed. Finally, the developed polarimetric phase retrieval and other existing retrievals of cloud properties are applied to measurements of specMACS during HALO–$(\mathcal{AC})^3$ and are

combined with backward trajectories to study macro- and microphysical cloud properties and their evolution during MCAOs in a quasi-Lagrangian way. Simultaneous hyperspectral and polarization measurements with specMACS allow for combining the spectral and polarization-based phase retrieval methods. Both methods complement each other due to their different penetration depths and sensitivities, providing a unique opportunity to investigate cloud thermodynamic phase partitioning and phase transitions. The analyses include a detailed case study in Sect. 4.2 as well as a statistical evaluation of all MCAO research flights of the campaign in Sect. 4.3. In the case study, the initial phase of a strong MCAO is analyzed, including the temporal and spatial evolution of cloud macro- and microphysical properties, the temperature dependence of cloud thermodynamic phase, and its vertical distribution. In addition, it is studied how cloud ice influences cloud liquid water by applying an adiabatic cloud model. In the statistical analysis, the variability of the cloud evolution between different MCAO events and its dependence on the MCAO strength are assessed. A summary and outlook are given in Sect. 5.

Chapter 2

Theoretical background

2.1 Cloud microphysics

In the atmosphere, water can exist in all three phases: as water vapor, liquid water, or solid ice. The phase diagram of water, defining its equilibrium states depending on temperature and partial pressure of water vapor, is shown in Fig. 2.1. At the triple point at 273.15 K and 6.11 hPa partial pressure, all three phases can exist in equilibrium. The solid lines indicate the equilibrium (saturation) vapor pressures e_s for phase transitions between vapor and liquid ($e_\mathrm{s,w}$) or vapor and solid ($e_\mathrm{s,i}$). For transitions between the pure liquid or solid phase and the vapor phase at an infinitely extended, flat interface, the saturation vapor pressure is described by the Clausius-Clapeyron equation (Rogers and Yau, 1989; Lamb and Verlinde, 2011; Lohmann et al., 2016)

$$\frac{de_\mathrm{s,w}}{dT} = \frac{L_\mathrm{v} e_\mathrm{s,w}}{R_\mathrm{v} T^2} \qquad \text{and} \qquad \frac{de_\mathrm{s,i}}{dT} = \frac{L_\mathrm{s} e_\mathrm{s,i}}{R_\mathrm{v} T^2}, \tag{2.1}$$

where L_v is latent heat of evaporation, L_s the latent heat of sublimation, T the temperature, and $R_\mathrm{v} = 461\,\mathrm{J\,kg^{-1}\,K^{-1}}$ the gas constant for water vapor. Due to the temperature dependence of the latent heat, no analytical solution to this equation exists, but there are several approximations (Rogers and Yau, 1989; Murphy and Koop, 2005). Below the melting point of 0 °C, supercooled liquid water can be observed. This is, however, not an equilibrium but a metastable state (denoted by the dashed line in Fig. 2.1).

Clouds in the atmosphere consist either of liquid cloud droplets, ice crystals, or a combination of both. Their formation involves phase transitions of water vapor to liquid water, resulting in the formation of liquid cloud droplets, or phase transitions from water vapor to ice or from liquid water to ice, leading to ice formation. These phase transitions correspond to a crossing of the equilibrium lines in the phase diagram. Their thermodynamic drivers are supersaturation of vapor or supercooling of liquid water, due to cooling of rising air masses or entrainment and mixing.

In the following, the formation and growth of liquid cloud droplets and the formation and growth of ice crystals in mixed-phase clouds, including glaciation, are discussed in

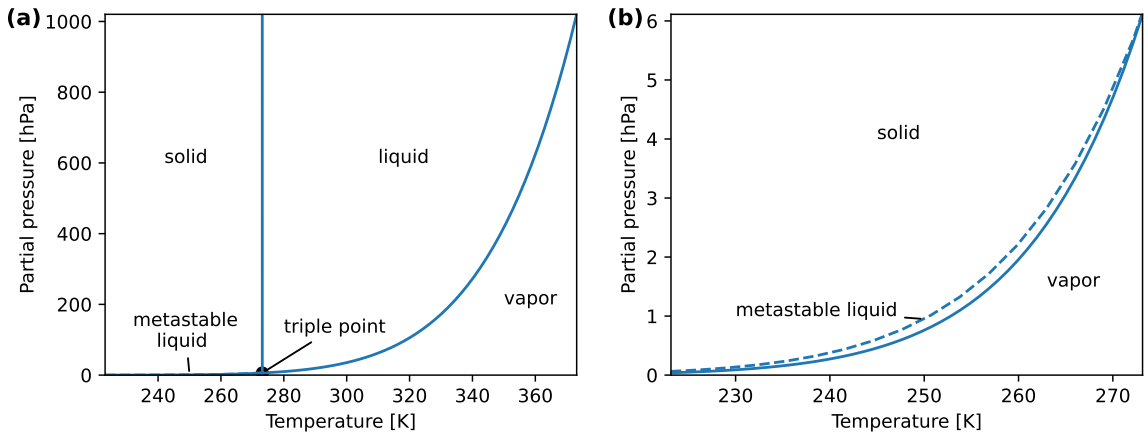

Figure 2.1: Phase diagram of water. Panel **(b)** shows a zoom into the lower left corner of panel **(a)**, left and below the triple point. The dashed line in panel **(b)** indicates the saturation vapor pressure over liquid water, the solid line the saturation vapor pressure over ice for temperatures below 0 °C. The approximations to the Clausius-Clapeyron equation by Murphy and Koop (2005) were used for the vapor pressures over liquid water and ice, and the formula given in Lohmann et al. (2016), chapter 2.4, was applied for the melting curve.

Sect. 2.1.1 and 2.1.2. In addition, the basic characteristics and processes relevant to Arctic mixed-phase clouds, which are the focus of this thesis, are summarized in Sect. 2.1.3.

2.1.1 Liquid clouds

Formation of liquid cloud droplets

The formation of a new phase can, in general, occur through homogeneous or heterogeneous nucleation. Homogeneous nucleation denotes the formation of a new particle from a pure phase, while heterogeneous nucleation involves foreign substances. A phase transition occurs only if the new phase is thermodynamically favored and the parent phase is in a metastable state, such as supersaturated water vapor. However, the phase transition from vapor to liquid reduces the system's entropy and thus involves an energy barrier. A cluster of individual molecules in the liquid phase has to be formed through statistical fluctuations within the vapor phase. The work needed to create this cluster and an interface between the new liquid phase and the parent vapor phase can be described by the change in the system's Gibbs free energy (Lamb and Verlinde, 2011; Lohmann et al., 2016)

$$\Delta G = -\frac{4\pi r^3}{3}\rho_\mathrm{L} R_\mathrm{v} T \ln S + 4\pi r^2 \sigma_\mathrm{LV}, \tag{2.2}$$

where $S = \frac{e}{e_{\mathrm{s,w}}}$ is the so-called saturation ratio, r the radius of the cluster, ρ_L the density of liquid water, and σ_LV the surface tension at the liquid-vapor interface. The change in Gibbs free energy consists of a volume term due to the difference in the chemical potentials of the two phases and a surface term because of the formation of the interface. It depends on the

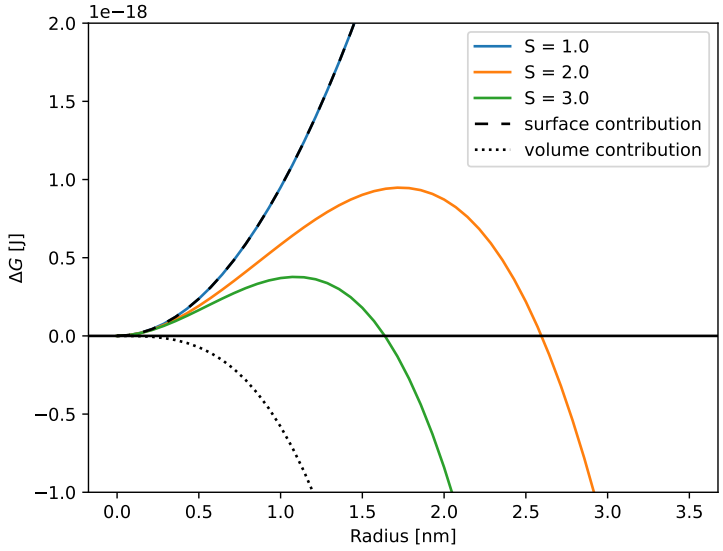

Figure 2.2: Change in Gibbs free energy for condensation as a function of radius for different saturation ratios at a temperature of 273.15 K. The dashed and dotted lines indicate the surface and volume contributions for a saturation ratio of $S = 3$. Similar figures can e.g. be found in Lamb and Verlinde (2011) or Lohmann et al. (2016).

cluster size and the saturation ratio and is plotted for the condensation of water vapor at a temperature of 273.15 K in Fig. 2.2. For $S \leq 1$, the surface term dominates. ΔG increases monotonically with increasing cluster size, and a cluster will thus not grow into a new particle. For larger saturation ratios $S > 1$, the surface term still dominates for small cluster sizes, and ΔG increases with radius until it reaches a maximum where the volume term starts to dominate. The radius at which ΔG has its maximum is called the critical radius. If this radius is reached by a spontaneously formed cluster, the cluster can overcome the energy barrier and will grow further into a cloud droplet. This process is called activation and results in a phase transition from vapor to liquid. The height of the energy barrier and the critical radius decrease with increasing saturation ratio S, and thus the probability for the formation of the new liquid phase increases with increasing supersaturation. However, for homogeneous nucleation in the atmosphere, large supersaturations are needed, which are not observed. There is also a second interpretation of homogeneous nucleation. The saturation vapor pressure over curved surfaces increases with decreasing radius, which inhibits homogeneous nucleation in the atmosphere. This effect is also known as the curvature or Kelvin effect. It follows directly from Eq. 2.2 by computing the critical radius at its maximum and solving for e.

As homogeneous nucleation is not observed in the atmosphere, liquid droplets form via heterogeneous nucleation on pre-existing particles, so-called cloud condensation nuclei (CCNs). CCNs lower the energy barrier through the solute (or Raoult) effect (Lamb and Verlinde, 2011; Lohmann et al., 2016). On the one hand, dissolved ions reduce the equilibrium vapor pressure since ionic bonds are stronger than hydrogen bonds, and fewer

water molecules are present at the surface in a solution, which reduces the rate of exchange of molecules between the two phases at the interface. This reduction of the equilibrium vapor pressure for solutions is proportional to the amount of solute. On the other hand, the droplet formation starts already from a larger radius (the radius of the particle), such that fewer molecules are required in a cluster of the new phase to reach the critical radius. The combination of both effects the Kelvin effect, increasing the saturation vapor pressure over curved surfaces, and the Raoult effect, reducing the saturation vapor pressure for solutions, is called the Köhler curve. It describes the equilibrium vapor pressure of a droplet with a certain radius and including the solute effect relative to the saturation vapor pressure for flat interfaces between two pure phases, which is defined by the Clausius-Clapeyron equation. Most effective CCNs are soluble, rather large, hydrophilic aerosols with typical sizes of around 100 nm. They allow for activation at supersaturations as low as 0.1% (Lamb and Verlinde, 2011). Typical CCN concentrations are on the order of 100 cm^{-3} (Pruppacher and Klett, 1997).

Droplet growth

After formation, cloud droplets initially grow from the vapor phase by adding individual vapor molecules (Lamb and Verlinde, 2011). For this growth mechanism, the vapor pressure must be larger than the equilibrium vapor pressure and the growth is thus driven by supersaturation. Vapor molecules are transported towards the droplet via molecular diffusion. Afterward, surface processes, including the phase transition, lead to vapor removal and latent heat release from the condensation. This creates a vapor and temperature gradient, and the latent heat is transferred away from the droplet. The heat transfer includes energy exchange at the droplet's surface, which is warmed by condensation and heat conduction through the surrounding air away from the droplet. The mass growth rate of a droplet, including all these processes, is described by Maxwell's theory (Rogers and Yau, 1989; Pruppacher and Klett, 1997; Lamb and Verlinde, 2011):

$$\frac{dm}{dt} = 4\pi\rho_{\mathrm{L}} r Z(S-1), \tag{2.3}$$

with

$$Z = (Z_{\mathrm{diff}} + Z_{\mathrm{cond}})^{-1} = \left(\frac{\rho_{\mathrm{L}} R_{\mathrm{v}} T_\infty}{M_{\mathrm{w}} D_{\mathrm{v}} e_{\mathrm{s}}(T_\infty)} + \frac{\rho_{\mathrm{L}} L_{\mathrm{v}}}{M_{\mathrm{w}} k_{\mathrm{T}} T_\infty}\left(\frac{L_{\mathrm{v}}}{R T_\infty} - 1\right)\right)^{-1}. \tag{2.4}$$

Here, k_{T} is the thermal conductivity, D_{v} the diffusivity, and M_{w} the molar mass of water. Generally, the mass growth rate depends on the net supersaturation $S-1$ and the temperature T_∞ of the environment. Z is a diffusivity including vapor transport and heat conduction and determines how fast the droplet grows. It can also be expressed as the sum of two impedances for mass transfer Z_{diff} and heat conduction Z_{cond}, and thus be interpreted as a resistance. Consequently, the linear growth rate for the droplet radius is

$$r\frac{dr}{dt} = Z(S-1). \tag{2.5}$$

Hence, smaller droplets grow faster, which causes a narrow cloud droplet size distribution.

The diffusional growth by condensation is slow and too slow for rain formation in warm clouds (Wallace and Hobbs, 2006). However, the initial growth by condensation is followed by growth from collection through collision and coalescence (e.g. Lamb and Verlinde, 2011). Droplets inside clouds sediment downwards due to gravity, and their fall speeds depend on the droplet mass and thus size. Different fall speeds and turbulence can cause collisions between two cloud droplets. The collision efficiency depends on the size of the collector and the collected drop. For example, very small droplets tend to follow the streamlines around the collector drop and thus have very small collision efficiencies. After a collision, the droplets can either rebound or coalesce. The coalescence efficiency depends on the relative speed of the two colliding particles, their size, and the angle of impact. Cloud droplets grow through a combination of both collisions followed by coalescence, and the total collection efficiency, which defines the growth rate due to collection, is given by the product of the collision and coalescence efficiencies.

2.1.2 Mixed-phase clouds

Mixed-phase clouds are characterized by the coexistence of supercooled liquid cloud droplets and ice crystals. Supercooling is the thermodynamic driver of phase transitions from liquid to solid. However, liquid cloud droplets do not freeze immediately at temperatures below the freezing point due to the energy barrier for the nucleation of the ice phase, similarly to the energy barrier for nucleation of the liquid phase described above. The mixed-phase regime, where both supercooled liquid water and ice crystals are observed in clouds, is between the threshold temperature for homogeneous freezing at about $-40\,°C$ and the melting temperature of ice $0\,°C$ (Korolev et al., 2017). The formation and growth of liquid cloud droplets was already discussed in the previous section. In the following, the formation of ice crystals, their growth, and the glaciation of mixed-phase clouds will be explained.

Formation of ice crystals

Ice crystals in clouds can be classified either as primary or secondary ice. Primary ice refers to the formation of new ice particles without pre-existing ice. Analogously to the formation of liquid cloud droplets, primary ice can be formed through homogeneous or heterogeneous nucleation. The different homogeneous and heterogeneous ice formation mechanisms are displayed in Fig. 2.3. In contrast to liquid cloud droplets, homogeneous nucleation of ice crystals can happen through a direct and an indirect pathway, either directly through deposition from the vapor phase or indirectly via condensation and freezing of a cloud droplet (Lohmann et al., 2016; Lamb and Verlinde, 2011). Both are described by the same equation as the homogeneous nucleation of liquid cloud droplets in Eq. 2.2, replacing the density of liquid water with the density of solid ice and the saturation ratio and surface tension with the respective values for a vapor-ice or liquid-ice interface. Homogeneous nucleation through deposition requires large supersaturations to overcome the energy barrier, similarly to homogeneous nucleation of liquid cloud droplets, and is thus not reached in the

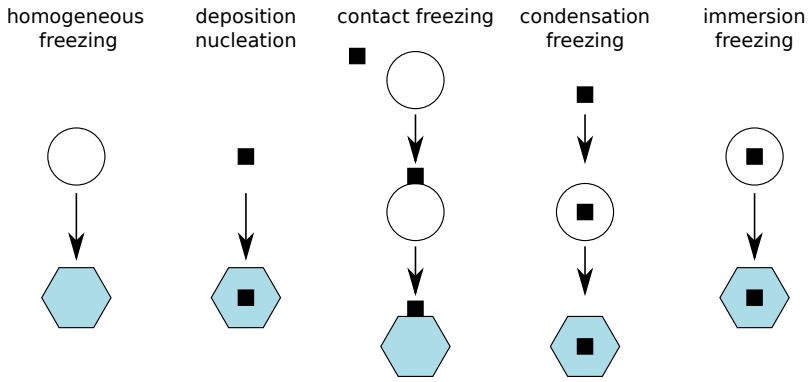

Figure 2.3: Visualization of the different homogeneous and heterogeneous ice formation mechanisms. The black squares indicate ice nuclei (INs), the white circles liquid cloud droplets, and the blue hexagons ice crystals. Similiar figures can be found in e.g. Rogers and Yau (1989), Lamb and Verlinde (2011), or Lohmann et al. (2016).

atmosphere. However, homogeneous freezing of liquid cloud droplets has a smaller energy barrier and is possible under atmospheric conditions. For this, a cluster of the solid phase (a so-called ice embryo) has to form in the parent liquid phase. If the ice embryo reaches a critical size, the droplet freezes. The energy barrier for freezing decreases with increasing supercooling, which is the thermodynamic driver for this phase transition. In addition, the probability for the spontaneous formation of a critical ice embryo increases with increasing droplet size. For example, a droplet with a typical radius of 10 µm can freeze spontaneously at temperatures below −38 °C (Pruppacher and Klett, 1997; Lamb and Verlinde, 2011).

Besides homogeneous nucleation through homogeneous freezing of liquid cloud droplets, ice crystals can also be formed through heterogeneous nucleation in the mixed-phase regime between the threshold temperature for homogeneous freezing of about −40 °C and the melting temperature at 0 °C (Lamb and Verlinde, 2011). During heterogeneous nucleation, ice crystals are formed through deposition or freezing onto the surface of a so-called ice nucleus (IN). By providing a surface, the INs lower the energy barrier for the formation of the ice phase and allow for the formation of ice crystals at much higher temperatures compared to homogeneous freezing. Most effective IN are solid, insoluble crystals with a crystal structure similar to the hexagonal lattice of ice, such that water molecules can align with the crystal surface. The IN AgI is already active at −4 °C. Other IN include mineral dust or biogenic particles. INs become active with increasing supercooling depending on the chemical composition and size of the IN. The concentration of INs in the atmosphere is very small, typically on the order of $1\,\mathrm{L}^{-1}$ (Pruppacher and Klett, 1997), which is much smaller than typical CCN concentrations. Heterogeneous nucleation can happen through different mechanisms as displayed in Fig. 2.3 (Lohmann et al., 2016). Depending on the respective mechanism, supersaturation with respect to liquid water or with respect to ice is necessary for ice formation. Deposition nucleation denotes the direct deposition of water vapor onto an IN and requires high supersaturation with respect to ice. During contact nucleation, an IN diffuses onto the surface of a supercooled liquid cloud droplet, which freezes upon contact. If an IN is coated with some soluble substance that serves as CCN, a solution

can form on its surface and freeze due to supercooling before the CCN becomes activated. This mechanism is called condensation freezing and requires supersaturation with respect to liquid water. Finally, an IN can already be immersed in a droplet before it becomes supercooled. This IN can then serve as a freezing nucleus at lower temperatures, and the droplet freezes through immersion freezing. According to de Boer et al. (2011) and Cui et al. (2006), immersion freezing is the dominant ice formation mechanism in mixed-phase clouds. In addition, there is a contribution from contact freezing (Ansmann et al., 2005).

Secondary ice can be produced only after primary ice crystals already exist. Upon collisions, dendritic ice crystals can break up into a large number of small ice crystals. The collisional breakup enhances the ice crystal number concentration but conserves the total ice mass (Lohmann et al., 2016). Besides, rime-splintering, respectively, the Hallet-Mossop process can produce secondary ice (Lohmann et al., 2016). If supercooled liquid cloud droplets and graupel particles with specific sizes collide, the supercooled droplet freezes upon collision. As the surface of the droplet freezes first, ice splinters can be ejected due to the pressure created within the droplet during freezing. This process is active at temperatures between about $-3\,^{\circ}\mathrm{C}$ to $-8\,^{\circ}\mathrm{C}$ (Lohmann et al., 2016). Other secondary ice production mechanisms include the ice fragmentation during sublimation or thermal shock, droplet fragmentation during freezing, and the activation of IN in transient supersaturation (Korolev and Leisner, 2020). Most secondary ice production mechanisms are not well understood and are currently not able to describe the gap between the observed increased ice particle number concentrations and the IN concentrations (Korolev and Leisner, 2020).

Ice crystal growth

The ice crystals formed via primary homogeneous or heterogeneous nucleation or as secondary ice can grow via diffusion from the vapor phase. The basic principles and description are similar to the diffusional growth of liquid cloud droplets. A detailed description of ice crystal growth can, e.g., be found in Lamb and Verlinde (2011). The main difference between the growth of liquid cloud droplets and ice crystals is the non-spherical shape of the latter. The differences are treated in the mass growth equation by introducing a capacitance and an accommodation coefficient (Lamb and Verlinde, 2011; Lohmann et al., 2016). Due to the molecular structure of water, the crystal lattice of solid water typically has a hexagonal structure. The integration of new vapor molecules into the crystal lattice has multiple stages (Lamb and Verlinde, 2011). First, a vapor molecule gets adsorbed onto the surface, followed by diffusion of the molecule across the surface. It is incorporated into the lattice only if it encounters a step of the lattice where the vapor molecule can bond to the molecules of the crystal. As a consequence, ice crystals grow layer by layer.

The linear growth rates of the ice crystals generally depend on the local supersaturation, defining the amount of available water vapor, and the deposition coefficient, characterizing how efficiently vapor molecules are incorporated into the crystal lattice. Both are non-uniform across the crystal surface, leading to the formation of non-spherical particles (Lamb and Verlinde, 2011). The deposition coefficient depends on the local surface tension, supersaturation, and temperature. Moreover, the surface tension depends on the orientation

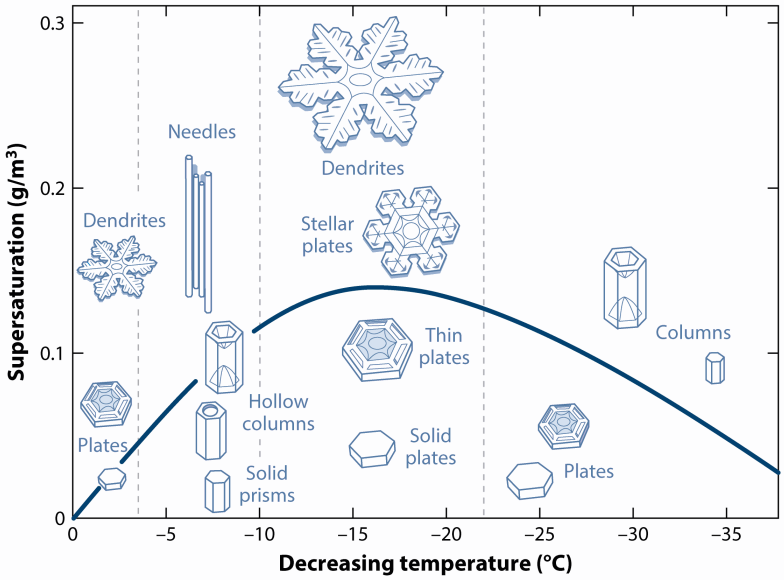

Figure 2.4: Morphology of ice crystals forming at different temperatures and supersaturations. The solid line denotes the supersaturation of liquid water relative to ice. This figure is taken from Fig. 1a from Libbrecht (2017). Used with permission of Annual Reviews, Inc.; permission conveyed through Copyright Clearance Center, Inc.

of the respective crystal face relative to the crystal lattice (Lohmann et al., 2016). Thus, the linear growth rates of the different crystallographic faces differ, resulting also in non-uniform distributions of water vapor and temperature across the crystal surface due to the different rates of vapor uptake and released latent heat. Because of the non-uniform linear growth rates, different ice crystal habits are formed depending on the temperature and supersaturation (Bailey and Hallett, 2009; Takahashi, 2014). Figure 2.4 schematically displays the ice crystal habits which are observed at different temperatures and supersaturations. The so-called primary habits are defined by the aspect ratio of the prism and base faces and depend on temperature. For temperatures between about $-10\,°C$ to $-5\,°C$, the growth rate of the prism faces of the hexagonal crystal is larger than the growth rate of the basal face leading to the formation of columns, whereas the reverse relation creates plates for temperatures between about $-5\,°C$ to $0\,°C$ and $-22\,°C$ to $-10\,°C$ (Pruppacher and Klett, 1997; Libbrecht, 2017). Secondary habits develop out of the primary habits mainly depending on the supersaturation. At high supersaturations, features reaching out furthest into the air with higher supersaturation (such as the crystal corners) grow faster since the surface diffusion is not fast enough anymore to redistribute the vapor molecules across the crystal surface (Pruppacher and Klett, 1997). Hence, more complex structures such as dendrites or needles form at higher supersaturations. However, the reasons for the temperature and supersaturation dependence are still not completely understood (e.g. Lamb and Verlinde, 2011; Libbrecht, 2017).

Besides the diffusional growth from the vapor phase, ice crystals can also grow through collection (also called accretional growth) and create even more complex ice crystal shapes.

In contrast to collision and coalescence for spherical liquid cloud droplets, the fall speeds of ice crystals and the collision and coalescence (sticking) efficiencies depend additionally on the shape of the colliding ice crystal, aggregate, or ice particle (Khain and Pinsky, 2018). The collision of two ice crystals, which stick together after collision, is called aggregation (Lohmann et al., 2016). The sticking efficiency is higher at higher temperatures due to the formation of a quasi-liquid layer on the crystal surface as the temperature approaches the melting point. Aggregation is mainly observed at temperatures larger than $-10\,°C$ close to the melting point. However, the sticking efficiency has a second maximum between $-20\,°C$ to $-10\,°C$, the so-called dendritic growth zone (Mitchell, 1988). This maximum can be explained by collisions of dendrites whose arms get mechanically stuck together. Aggregation reduces the ice crystal number concentration and increases the mean crystal size and mass. Furthermore, riming denotes the collision of a small supercooled liquid cloud droplet with an ice crystal. The droplet freezes upon contact onto the surface of the ice crystal, increasing the density and mass of the crystal. Riming is important for the formation of rain, graupel, and hail. Finally, a small ice crystal colliding with a large liquid drop causes the drop to freeze onto it, which is known as capture nucleation (Lamb and Verlinde, 2011). While the ice particle concentration stays constant, the cloud droplet number concentration is reduced by riming and capture nucleation. In both cases, the sticking efficiency is close to one since the liquid water droplet almost always freezes onto the ice crystal (Lohmann et al., 2016).

Similar to liquid cloud droplets, ice crystals initially grow from the vapor phase. Later on, riming and aggregation lead to precipitation formation (Wallace and Hobbs, 2006). However, the depositional growth of ice crystals is fast compared to the condensational growth of liquid. Supersaturations with respect to ice in clouds are much higher than those with respect to liquid water due to the lower saturation vapor pressure over ice compared to liquid water. This also allows ice crystals to reach precipitating sizes through depositional growth (Lohmann et al., 2016).

Glaciation

Glaciation refers to the conversion of supercooled liquid water into ice (Lamb and Verlinde, 2011). The mass conversion of liquid water to ice happens through the so-called Wegener-Bergeron-Findeisen mechanism (WBF mechanism) (Wegener, 1911; Bergeron, 1935; Findeisen, 1938). For temperatures below $0\,°C$, supercooled liquid water, ice, and water vapor can all coexist. However, the equilibrium vapor pressure with respect to liquid water is larger than the one with respect to ice, as can be seen in Fig. 2.1b. If the vapor pressure is between the saturation vapor pressures above ice (solid line) and liquid water (dashed line), so supersaturated with respect to ice but not supersaturated with respect to liquid water, ice crystals can grow at the expense of supercooled liquid cloud droplets, which is known as the WBF mechanism. In this regime, liquid cloud droplets evaporate, vapor diffuses towards the ice crystals, and the ice crystals grow from the vapor phase. The maximum difference between the saturation vapor pressures with respect to liquid water and ice is at $-12\,°C$. However, the maximum ice crystal growth rates are observed at

slightly lower temperatures due to the latent heat released by the deposition (Lamb and Verlinde, 2011; Khain and Pinsky, 2018).

The WBF mechanism is only active in a distinct regime (Korolev, 2007). Fast ascending air masses experience rapid cooling and supersaturation increases above liquid water saturation. In this case, ice crystals and liquid cloud droplets grow simultaneously. The liquid water competes with the ice for the available water vapor, which limits the growth of ice. Rapidly descending air is warmed, leading to subsaturation and evaporation of both liquid water and ice. For slowly ascending air masses under weak synoptic forcing, supersaturation between liquid water and ice saturation can be reached. Then, the WBF mechanism is active and liquid cloud droplets evaporate while ice crystals grow. The WBF mechanism can rapidly glaciate mixed-phase clouds with glaciation times between a few minutes and hours (Korolev et al., 2017). Due to the different radiative properties of liquid water and ice, it is important for the radiative effect of clouds, and affects precipitation and cloud lifetime. The efficiency of the WBF mechanism depends on the spatial distribution of the liquid water and the ice phase within the cloud. Homogeneously mixed clouds can be glaciated more efficiently due to the on average smaller distances between liquid water and ice compared to clouds with distinct liquid water and ice patches (Lohmann et al., 2016).

A second process relevant for glaciation is ice multiplication (Lamb and Verlinde, 2011). Secondary ice production due to, e.g., fragmentation or rime splintering increases the ice crystal number concentration. This helps to rapidly propagate the ice phase through the cloud and accelerates glaciation.

2.1.3 Characteristics and persistence of Arctic mixed-phase clouds

Mixed-phase clouds are especially important in the Arctic, where they are observed in 40 % to 70 % of the time (Shupe et al., 2006; Shupe, 2011). They occur throughout the year, with the highest frequencies in spring and fall. Furthermore, Arctic mixed-phase clouds exhibit a distinct structure (Morrison et al., 2012; Tan et al., 2023). This structure is visualized together with the most relevant processes for Arctic mixed-phase clouds in Fig. 2.5. Typically, Arctic mixed-phase clouds consist of one or more stratiform cloud layers with a typical geometrical thickness of a few hundred meters to 1.5 km (Shupe et al., 2006). A geometrically thin layer of supercooled liquid water is located at the cloud top. Ice crystals form from this liquid water layer via heterogeneous nucleation and sediment downwards. Typical liquid water paths (LWPs) of these mixed-phase clouds are on the order of $100\,\mathrm{g\,m^{-2}}$ and ice water paths around $10\,\mathrm{g\,m^{-2}}$ (Shupe et al., 2006), which corresponds to a total optical thickness on the order of 10 to 20. Moreover, a capping temperature inversion is found at or above cloud top, frequently also accompanied by a moisture inversion. The strength of the temperature inversion is related to the lower tropospheric stability and influences cloud properties. The moisture inversion is caused either by surface or cloud top radiative cooling or by large-scale transport of moisture (Tan et al., 2023). Arctic mixed-phase clouds are strongly influenced by surface coupling (as will be discussed in detail in the context of cold air outbreaks in Sect. 2.2.2) and the underlying surface type, e.g., sea ice or open ocean. They form if warm, moist air is advected over colder surfaces

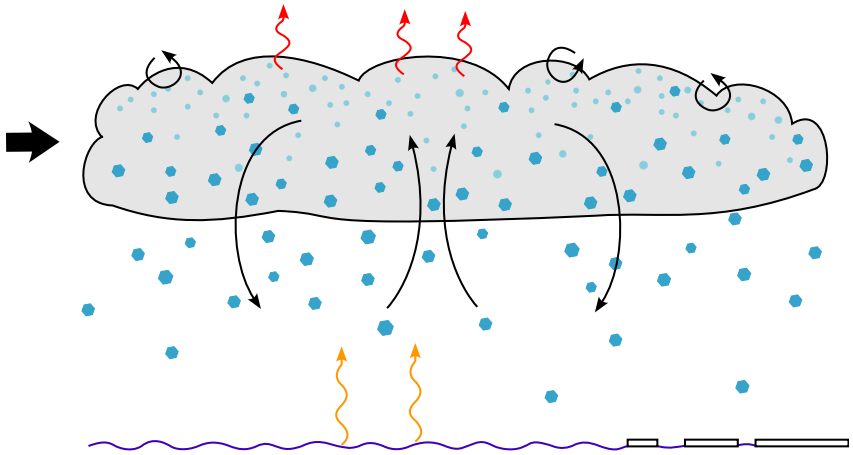

Figure 2.5: Visualization of the characteristics of Arctic mixed-phase clouds, including the supercooled liquid water layer at cloud top (light blue spheres) and precipitating ice (medium blue hexagons), cloud top radiative cooling (red arrows), surface fluxes (orange arrows), updrafts (black arrows), entrainment and mixing (small black arrows), large-scale advection (big black arrow), and different surface types (open ocean and sea ice). The figure is inspired by similar schematics of Arctic mixed-phase clouds in Morrison et al. (2012), Korolev et al. (2017), and Tan et al. (2023).

during warm air intrusions or if cold air masses are advected over warm open ocean during marine cold air outbreaks (Tan et al., 2023; Pithan et al., 2014, 2018). Even though the coexistence of supercooled liquid water and ice in the mixed-phase regime is not a stable state and the WBF mechanism can rapidly lead to glaciation, mixed-phase clouds in the Arctic were observed to persist on average for 12 hours and up to several days (Shupe et al., 2006; Morrison et al., 2012). Possible explanations for this remarkable persistence, as well as local processes and interactions relevant to Arctic mixed-phase clouds are summarized by Morrison et al. (2012) and Tan et al. (2023) and will shortly be described in the following.

The first important process is related to turbulence and updrafts within the clouds. Rising air cools during its ascent in an updraft and becomes initially increasingly supersaturated with respect to ice. If the updraft is strong enough and low enough temperatures are reached, the air masses get supersaturated with respect to liquid water. Then, liquid cloud droplets and ice crystals grow simultaneously, and thus, liquid water is formed in the updraft within the cloud. If, additionally, the vertical velocity of the updraft is high enough such that the resupply of water balances the loss of liquid water through ice formation and precipitation, mixed-phase clouds can persist for long times (Korolev et al., 2017). The updrafts themselves can be created by the supercooled liquid water layer at cloud top: The supercooled liquid water causes radiative cooling at cloud top and thus reduces the static stability. This increases turbulence and creates buoyant updrafts in which liquid water can be formed, and hence represents a self-maintaining feedback.

Secondly, in contrast to lower latitudes, moisture inversions at cloud top frequently occur in the Arctic. These moisture inversions are often related to large-scale advection. Entrainment of moist air from above into the cloud balances the loss of moisture due to sedimenting and precipitating ice crystals and helps to sustain the cloud.

Moreover, surface coupling plays an important role in Arctic mixed-phase clouds. The supercooled liquid water within the cloud causes a longwave radiative warming at the surface. This creates instability and updrafts and enhances surface heat and moisture fluxes. The moisture flux from the surface helps to sustain the cloud, similar to the moisture inversion at cloud top. It resupplies moisture against the loss through precipitation and allows the clouds to persist. However, the surface fluxes are strongly dependent on the surface type.

In addition, there is a liquid-ice feedback mechanism. It was observed that liquid cloud droplets must exist first, before ice crystals start to form within Arctic mixed-phase clouds (Morrison et al., 2012; Lohmann et al., 2016). Enhanced ice formation depletes the liquid water inside the cloud. Due to the negative liquid-ice feedback, this reduces the formation of ice crystals, which helps to sustain the supercooled liquid water.

Finally, aerosols affect mixed-phase clouds (Morrison et al., 2012; Tan et al., 2023). The presence of IN and their concentration are critical for ice formation, ice crystal growth, and glaciation. Higher IN concentrations lead to higher ice crystal number concentrations and faster glaciation, which reduces cloud lifetime. In addition, the CCN concentration affects the cloud droplet number concentration and cloud droplet size. Higher CCN concentrations lead to more but smaller droplets. This directly affects collision and collection processes relevant for precipitation formation and increases cloud lifetime. Furthermore, it enhances the longwave emissivity of the cloud, which increases the surface warming, reduces the stability, and creates updrafts that sustain the cloud as discussed above. Thus, aerosols affect the cloud thermodynamic phase and precipitation, and consequently the cloud radiative effect and cloud lifetime.

2.2 Marine cold air outbreaks

2.2.1 Definition and characteristics

During marine cold air outbreak (MCAO), cold and dry polar air masses are advected off the sea ice edge or continents across warm open ocean (Pithan et al., 2018). The potential temperature difference between the cold advected air masses and the warm ocean surface leads to intense surface fluxes of heat and moisture. Advected air masses are warmed from below and moistened through evaporation at the ocean surface. The so caused destabilization of the atmospheric boundary layer initiates shallow convection and cloud development towards the top of the boundary layer. Moisture and heat are transferred upwards through turbulent mixing, which leads to increasing boundary layer heights and cloud top heights. Hence, the boundary layer deepens with increasing time and distance from MCAO formation, from typically a few hundred meters to 1 km to 2 km geometrical thickness, and the boundary layer is well-mixed or weakly-stable (Brümmer, 1996). Later, the boundary layer can become decoupled from the surface, losing its moisture and aerosol source. An overview of the basic characteristics of MCAOs is displayed in Fig. 2.6, which is from Pithan et al. (2018).

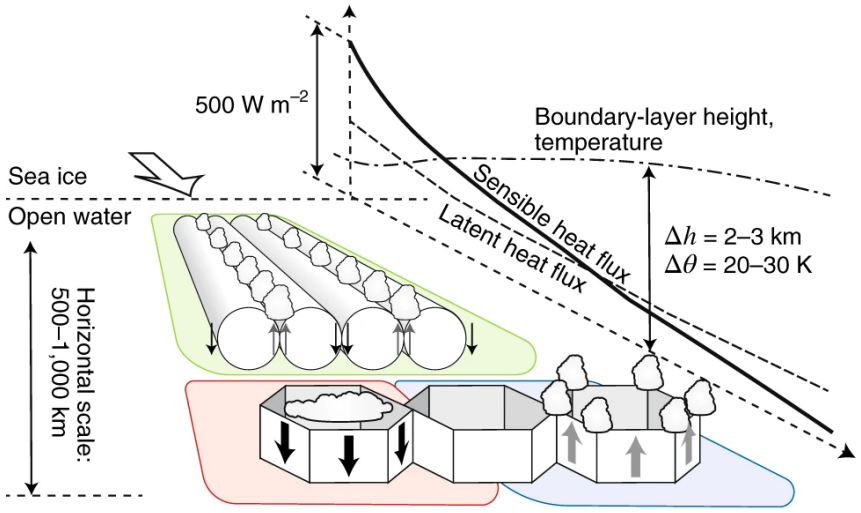

Figure 2.6: Overview of processes and characteristics of MCAOs. The figure is taken from panel (a) of Fig. 2 in Pithan et al. (2018). Reproduced with permission from Springer Nature.

MCAOs in the Northern Hemisphere follow mainly two distinct pathways, either from the Arctic through the North Atlantic towards Europe or via the North Pacific towards Western North America (Fletcher et al., 2016a). The surface temperature gradient across which the cold, dry air mass is advected for the formation of a cold air outbreak can be due to the sea ice edge or the borders of cold continents, sea surface temperature (SST) gradients caused by warm ocean currents such as e.g. the Gulf stream in the North Atlantic, or a combination of both (Fletcher et al., 2016a). MCAOs occur typically downstream of such surface temperature gradients.

Before the formation of a cold air outbreak, air masses are cooled and dried in the interior Arctic with cooling rates of about 1 K day^{-1} (Papritz and Spengler, 2017). At the beginning of a cold air outbreak event, the potential temperature difference between the advected air masses and the warm surface can be as large as 30 K (Papritz and Spengler, 2017). After MCAO formation, the air temperature rapidly increases through diabatic heating with the largest heating rates during the first few hours after MCAO formation amounting to about 5 K day^{-1} to 9 K day^{-1} and up to 15 K day^{-1} for very strong MCAOs. The total surface heat flux consists of sensible and latent heat fluxes. It depends on the differences between the potential air temperature and the potential temperature of the ocean surface, as well as the spatial distribution of the SST along the pathway of the MCAO. While the sensible heat flux increases almost linearly with potential temperature difference, the latent heat flux depends on the SST (Papritz and Spengler, 2017). Surface fluxes of heat and moisture can be up to 500 W m^{-2} (Papritz and Spengler, 2017). They rapidly increase after MCAO formation, the sensible heat flux then slowly decreases with time during a MCAO (see Fig. 2.6). At some point, the latent heat flux dominates over the sensible heat flux.

MCAOs typically last for a few days and have horizontal extents of 500 km to 1000 km (Fletcher et al., 2016a). Zonal and meridional extents are of about equal size, and stronger

cold air outbreaks show larger sizes than weaker ones (Fletcher et al., 2016a). The size and shape of MCAOs are defined by the underlying SST gradient, the size of the synoptic eddy causing the advection, and generally the temporal and spatial scale of the air mass transformation, which depends on the potential temperature difference between the air mass and ocean (Pithan et al., 2018). MCAOs are most frequent in winter but also occur in spring and autumn. While weak events happen throughout the year, strong cold air outbreaks are restricted to the winter months (Fletcher et al., 2016a). Strong MCAOs are mostly found along the sea ice edge and the coast of Greenland. The Fram Strait between Svalbard and Greenland is a hotspot for very strong MCAO events due to the very northern location of the sea ice edge and the comparably warm ocean due to the North Atlantic currents (Papritz and Spengler, 2017). Weaker MCAOs are also observed along SST gradients from the warm North Atlantic ocean currents within the ocean basins. The spatial distribution and intensity of MCAOs exhibit a strong interannual variability, which can be explained by the variability of synoptic weather situations and the related variability of air temperature and partly also sea ice cover (Kolstad et al., 2009).

The intensity of cold air outbreaks can be quantified with the so-called marine cold air outbreak index M_{CAO}, which was introduced by Kolstad and Bracegirdle (2008). It is defined as the difference between the potential skin temperature and the potential temperature at a pressure of 850 hPa (Fletcher et al., 2016a)

$$M_{\mathrm{CAO}} = \theta_{\mathrm{skin}} - \theta_{850\mathrm{hPa}}. \tag{2.6}$$

Other definitions use the sea surface temperature θ_{SST} instead of the skin temperature or potential temperatures at slightly different pressure levels, such as e.g. 800 hPa. MCAO indices larger than 0 K indicate MCAO conditions. MCAO events with indices $0\,\mathrm{K} < M_{\mathrm{CAO}} < 4\,\mathrm{K}$ are commonly classified as weak MCAOs, $4\,\mathrm{K} < M_{\mathrm{CAO}} < 8\,\mathrm{K}$ as moderate, and $M_{\mathrm{CAO}} > 8\,\mathrm{K}$ as strong events (Papritz and Spengler, 2017; Dahlke et al., 2022). Figure 2.7 shows MCAO indices computed from ERA5 data (Hersbach et al., 2023a,b) for the Fram Strait region on 2022-04-27 at 12 UTC in panel (a) and the MODIS satellite image for the same day in panel (b). On this day, a strong MCAO event took place with the largest MCAO indices in the northernmost part of the Fram Strait close to the sea ice edge, and Arctic air masses were advected southwards from the sea ice across open ocean.

MCAOs are typically found in the cold sector of mid-latitude cyclones where cold and dry polar air masses are advected towards the equator over comparably warm open ocean (Kolstad et al., 2009; Fletcher et al., 2016a). The synoptic pattern generally exhibits a pressure dipole with a high pressure anomaly located to the west and a low pressure anomaly to the east of the MCAO (Kolstad et al., 2009). For the Fram Strait, Dahlke et al. (2022) found that the very strong MCAOs observed are associated with a dipole pattern with high pressure over Greenland and low pressure over the eastern Barents Sea. This dipole pattern results in a zonal pressure gradient across the Fram Strait, leading to geostrophic advection of cold air masses along the Fram Strait from the Arctic towards the south. The dipole pattern was generally more pronounced for stronger MCAOs, and the interannual variability of MCAOs in the Fram Strait can partly be explained by the variability of these synoptic patterns.

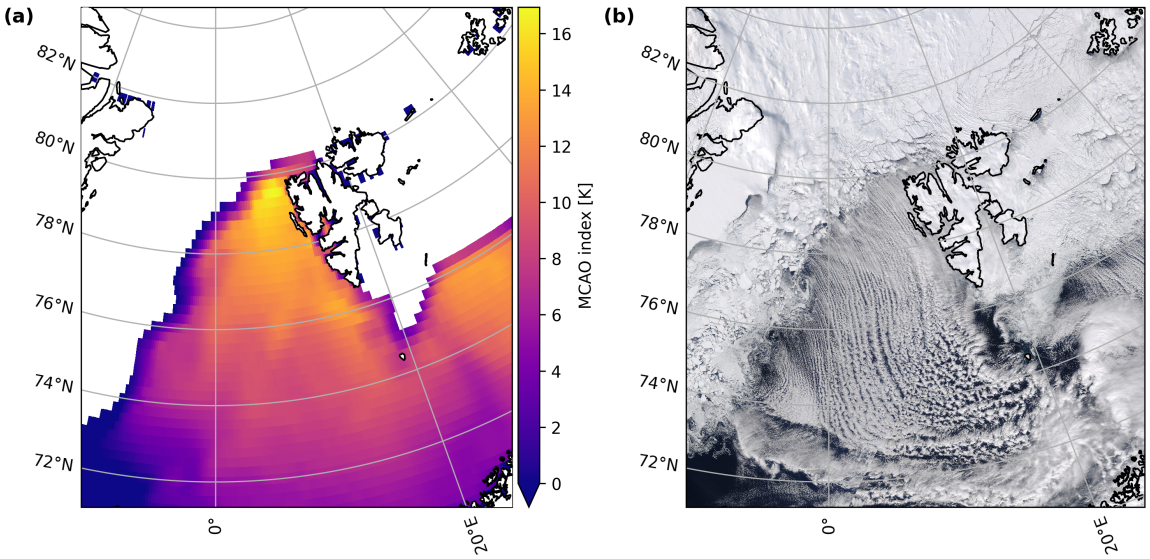

Figure 2.7: MCAO index from ERA5 data (Hersbach et al., 2023a,b) **(a)** and MODIS satellite image downloaded from NASA Worldview (https://worldview.earthdata.nasa.gov/) **(b)** for 2022-04-27. No values of the MCAO index are given above the sea ice.

Marine cold air outbreaks are important since they are related to severe weather such as polar lows, strong winds, heavy snowfall, Arctic fronts, fog or icing, and generally cold extremes, which can have severe impacts on the affected regions (Pithan et al., 2018). In addition, they play a crucial role in the heat exchange between the atmosphere and the ocean due to the large surface latent and sensible heat fluxes. MCAOs are responsible for 60 to 80 % of oceanic heat loss during winter time in the Nordic Seas (Papritz and Spengler, 2017). The overall heat loss is dominated by very few very strong MCAO events with only a small contribution from more frequent weak events. Cooling of the ocean surface due to the turbulent heat fluxes during MCAOs affects the depth of the ocean mixed layer and deep water formation (Papritz and Spengler, 2017). Moreover, sea ice formation is influenced.

2.2.2 Clouds during marine cold air outbreaks

When passing the ice edge, the temperature gradient between the warm surface and advected cold air masses creates intense surface heat and moisture fluxes, which favor the formation of clouds at the top of the shallow boundary layer. During the first few hours after the formation of a MCAO, cloud fraction and LWP rapidly increase (Murray-Watson et al., 2023). Moreover, within the first few hundred kilometers after MCAO formation, roll convection is typically observed. The clouds organize into cloud streets oriented along the wind direction (Brümmer, 1999; Pithan et al., 2018). These comparably thin, line-shaped clouds can also be seen in the MODIS satellite image in Fig. 2.7b in the northern part of the MCAO region stretching southwards from the sea ice edge. The organization into cloud streets and roll convection can be explained by the heterogeneity of the surface temperature

between open ocean and sea ice in the marginal sea ice zone upstream (Gryschka et al., 2014). The scales of the surface heterogeneities determine the wavelength of the roll convection. Typical horizontal wavelengths of the observed rolls are a few kilometers and increase with increasing boundary layer height (Brümmer, 1999). As the boundary layer deepens with time, cloud top height increases and the clouds evolve. The boundary layer is well-mixed with temperature and moisture inversions at its top (Abel et al., 2017). The cloud streets in the initial phase of a cold air outbreak are liquid-dominated with little cloud ice, volume mean diameters of liquid cloud droplets between 10 µm to 25 µm were observed (Abel et al., 2017), and the effective radius of liquid cloud droplets increases with time. As the effective radius reaches sizes where collision and coalescence become important and ice formation increases, precipitation sets in. The cloud droplet number concentration is typically small, with initially about $200\,\mathrm{cm}^{-3}$, since the advected Arctic air masses have only low aerosol concentrations. It further reduces with time due to precipitation and entrainment of subsaturated tropospheric air into the clouds, which also depletes the aerosol concentration (Tornow et al., 2022; Murray-Watson et al., 2023).

After several hours, a transition of cloud morphology from the cloud streets into deeper, more convective, towering, cumuliform cellular structures is observed (Brümmer, 1999; Field et al., 2014). This transition is schematically displayed in Fig. 2.6 and is also visible in the satellite image in Fig. 2.7b further to the south. The cellular clouds are more glaciated, have larger ice mass and ice number concentrations, and larger particle sizes are observed compared to the stratiform cloud streets (Abel et al., 2017). In addition, the liquid water path is more variable and maxima of LWP are located in the convective cores of the clouds. A thin layer of supercooled liquid water is typically located at the cloud top. Importantly, enhanced precipitation is observed in this cloud regime (Abel et al., 2017), leading eventually to slowly decreasing LWP and gradually decreasing cloud fraction (Murray-Watson et al., 2023). Furthermore, the cloud albedo of the cloud streets in the initial phase is higher compared to the open cells at later stages of the MCAO, highlighting the importance of the two different cloud regimes for the cloud radiative effect (McCoy et al., 2017; Tornow et al., 2021).

The observed transition from cloud streets to cells, or from stratocumulus to cumulus clouds, can be related to surface fluxes and boundary layer instability, precipitation, as well as dynamical forcings such as wind shear (Brümmer, 1999; Abel et al., 2017). Stratocumulus to cumulus transitions were studied extensively for the subtropics, e.g., by Sandu and Stevens (2011).

Increasing sea surface temperatures along the pathway of a MCAO lead to increased latent heat fluxes, dominating at some point over the decreasing sensible heat fluxes (see Fig. 2.6). The latent heat release from condensation inside the cloud layer grows and finally exceeds the surface heating (Brümmer, 1999). This causes a decoupling of the boundary layer from the surface and a transition to a more convective, conditionally unstable boundary layer compared to the well-mixed cloud street regime. The buoyancy of the cloud layer rises due to the increased latent heat release, mixing and entrainment of air from the free troposphere into the cloud are enhanced, and the inversion strength at the top of the boundary layer weakens (Sandu and Stevens, 2011). In contrast, the sub-cloud layer remains dry and has

lower buoyancy than the cloud above. Due to this decoupling of cloud layer and surface, the cloud loses its moisture source from the surface while precipitation and cloud top entrainment continue to deplete cloud water, which eventually leads to dissipation and breakup of the clouds. At the same time, water vapor accumulates in the sub-cloud layer, which becomes conditionally unstable compared to the upper cloud layer due to continued surface heating. This favors the formation of new, more convective, cumuliform clouds organized into cellular structures (Sandu and Stevens, 2011).

In addition, precipitation plays an important role in the transition of cloud morphology (Abel et al., 2017). Enhanced precipitation causes a cooling and moistening of the sub-cloud layer through the evaporation of hydrometeors. This aids the formation of cumulus clouds in this layer (Stevens et al., 1998) and induces or reinforces a decoupling of the boundary layer, similarly to above. According to Abel et al. (2017), precipitation can be the dominant factor for boundary layer decoupling in MCAOs over the surface heat fluxes governed by the sea surface temperature. Ice formation and mixed-phase processes such as riming are additionally important as they are strongly linked to precipitation formation (Pithan et al., 2018; Tornow et al., 2021). In addition, aerosol depletion through precipitation influences the cloud transitions (Tornow et al., 2021; Murray-Watson et al., 2023). Lower aerosol concentrations result in lower cloud droplet number concentrations, faster droplet growth, and thus earlier onset of precipitation, which affects the cloud transition and timing of the breakup.

Finally, wind shear and the vertical wind profile influence the organization of clouds into distinct patterns. Brümmer (1999) observed similar average wind speeds but larger wind shear for the roll regime compared to the cell regime. However, wind shear plays only a minor role in the observed transition of cloud morphology during MCAOs (Brümmer, 1999). In general, the temporal development of clouds in MCAOs also depends on the intensity of the MCAO (Murray-Watson et al., 2023; Fletcher et al., 2016b). Stronger MCAOs show higher maximum LWP, cloud fraction, optical thickness, and cloud top height. Moreover, larger amounts of cloud ice were observed in strong MCAOs (Fletcher et al., 2016b).

Compared to average maritime clouds, MCAO clouds have a higher cloud fraction and lower cloud optical thickness (Fletcher et al., 2016b). Due to the comparably low cloud top heights, they have only a small longwave radiative effect at the top of the atmosphere. In addition, their shortwave radiative effect is small since MCAOs predominantly occur in the wintertime. However, MCAO clouds have a stronger longwave warming effect on the surface compared to average maritime clouds, mainly due to their higher cloud fraction. This warming effect is, however, offset by the large surface fluxes during MCAOs.

2.2.3 Modelling challenges and future projections

Weather and climate models struggle to correctly represent clouds and convection in MCAOs (Pithan et al., 2014, 2018). On the one hand, cloud microphysics in mixed-phase clouds is challenging. On the other hand, air mass transformations during MCAOs are determined by a combination of boundary layer turbulence, cloud microphysics, interactions between atmosphere, ocean, and sea ice, as well as by interactions with the large-scale circulation.

The correct representation of the different turbulent heat fluxes involving the surface and the atmosphere and their interactions, as well as the radiative effect of the clouds, is particularly challenging for models (Solomon et al., 2023). In addition, cold air outbreaks and the associated clouds fall into a regime where the convection and boundary layer parameterizations in models can not be treated independently (Tomassini et al., 2017; Field et al., 2017). Models generally underestimate the LWP in MCAO clouds, but they are in general able to simulate the transition from cloud streets to open cells (e.g. Field et al., 2014). Improvements are particularly needed for the simulation of cloud thermodynamic phase partitioning and precipitation efficiency (Pithan et al., 2018).

Future projections of global climate in climate models indicate a reduced frequency and intensity of MCAOs (Landgren et al., 2019; Smith and Sheridan, 2021). The stronger warming of the atmosphere in a warming climate compared to the ocean due to their different heat capacities leads to generally smaller temperature differences between cold air masses and the ocean surface and thus smaller MCAO indices and an increased static stability of the lower atmosphere. In addition, the Arctic warms faster than the mid latitudes, known as Arctic amplification, which further reduces the temperature difference between the source regions of MCAOs and the affected regions (Pithan et al., 2018). The strongest decrease of MCAOs is projected for the winter months December and January in the Nordic Seas, and the MCAO season generally shortens (Landgren et al., 2019). In addition, there is a northward shift of the formation regions of MCAOs due to sea ice retreat. Hence, formerly sea ice-covered regions experience an increase of MCAO activity whereas the overall activity decreases. Observational trends of MCAO formation and intensity from reanalysis data also show a statistically significant decrease of MCAOs in winter, except for March (Dahlke et al., 2022).

Meridional air mass transformations, such as cold air outbreaks, are often associated with blocking events (Pithan et al., 2018). The occurrence of blocking events is influenced by the stratosphere, in particular the polar vortex and sudden stratospheric warmings, as well as by the tropics, and is changing in a warming climate (Francis and Vavrus, 2015; Woollings et al., 2018; Cohen et al., 2021). Thus, changes of the global atmospheric circulation in a warming climate also affect the occurrence, intensity, and pathways of MCAOs. Furthermore, variations of the SSTs due to a changed ocean circulation influence MCAOs (Papritz and Spengler, 2017). On the other hand, MCAOs themselves control oceanic heat loss, which feeds back to the ocean circulation due to their importance for deep water formation. Moreover, changes in aerosol concentrations in the Arctic, e.g., due to increased industrial activity, increased sea spray, or biogenic emissions in a warmer, more ice-free Arctic, affect the development and transition of clouds during MCAOs (Schmale et al., 2018; Maahn et al., 2021; Murray-Watson et al., 2023).

2.3 Electromagnetic radiation and radiative transfer

2.3.1 Radiative quantities

Electromagnetic radiation consists of electromagnetic waves transporting energy (Griffiths, 2013). Electromagnetic waves are solutions to Maxwell's equations and are composed of coupled electric and magnetic field components $\boldsymbol{E}$ and $\boldsymbol{B}$. A frequently used description of these fields is monochromatic plane waves (Griffiths, 2013; Petty, 2006):

$$\boldsymbol{E} = \boldsymbol{E_0} \exp(i\boldsymbol{kr} - iwt) \tag{2.7}$$

$$\boldsymbol{B} = \boldsymbol{B_0} \exp(i\boldsymbol{kr} - iwt), \tag{2.8}$$

with complex amplitudes $\boldsymbol{E_0}$ and $\boldsymbol{B_0}$. This simple form of solution is very convenient since any electromagnetic wave can be expressed as a superposition of monochromatic plane waves (Griffiths, 2013). The physical quantities are given by the real parts of $\boldsymbol{E}$ and $\boldsymbol{B}$. A monochromatic plane wave as described in Eq. 2.7 propagates in the direction of the wave vector $\boldsymbol{k}$. The wave vector is related to the wavelength λ via $\|\boldsymbol{k}\| = k = \frac{2\pi}{\lambda}$. Monochromatic radiation generally consists of a single wavelength, whereas broadband radiation is a superposition of many monochromatic waves with different wavelengths. The wavelength is an important quantity since the interaction of electromagnetic radiation with matter, such as absorption, is strongly dependent on it (Petty, 2006). Electromagnetic radiation can cover a very large range of wavelengths. The radiation emitted by the sun, for example, covers wavelengths between approximately 0.1 µm and 4 µm. The wavelength range between 390 nm to 780 nm is referred to as the visible spectrum, while near infrared radiation includes wavelengths between 780 nm to about 3 µm, and thermal radiation covers wavelengths between about 4 µm and 100 µm (Hecht, 2018). Electromagnetic waves propagate through vacuum at the speed of light, c. For propagation through linear homogeneous media, the speed is reduced by the inverse of the refractive index n of the medium (Griffiths, 2013): $v = \frac{c}{n}$. The propagation speed is also related to the wave's wavelength and frequency f via $v = \lambda f$. Moreover, electromagnetic waves are transverse waves as follows directly from Maxwell's equations for vacuum or linear homogeneous media (Griffiths, 2013). The electric and magnetic field components, $\boldsymbol{E}$ and $\boldsymbol{B}$, are mutually perpendicular and orthogonal to the direction of propagation. Hence, the electromagnetic field oscillates in a plane that is normal to the direction of propagation. The so-called polarization defines the exact orientation of the oscillations of the electric field and will be further discussed in the following section. In addition, the absolute value of the amplitude of the magnetic field is linearly proportional to the amplitude of the electric field through $E_0 = \frac{c}{n} B_0$, and the electric and magnetic fields are in phase.

As mentioned before, electromagnetic radiation transports energy. The magnitude and direction of the energy flux density is described by the Poynting vector (Griffiths, 2013)

$$\boldsymbol{P} = \frac{1}{\mu}(\boldsymbol{E} \times \boldsymbol{B}), \tag{2.9}$$

where μ is the magnetic permeability of the medium. The Poynting vector is typically abbreviated with $\boldsymbol{S}$, but denoted here with $\boldsymbol{P}$ to avoid confusion with the later introduced

Stokes vector. The time mean of the absolute value of the Poynting vector is known as irradiance F (often also called E). It describes the mean radiative energy passing per unit time through a unit area perpendicular to the direction of propagation and is thus directly related to the mean power, respectively radiant flux Φ (Petty, 2006):

$$F = \langle P \rangle_T = \frac{1}{2} \epsilon v E_0^2 = \frac{d\Phi}{dA}. \tag{2.10}$$

Here, the square brackets denote a temporal mean and ϵ is the electric permittivity of the medium. The irradiance is proportional to the squared amplitude of the electric field and depends on the distance to the radiation source. It is given in units of $\mathrm{W\,m^{-2}}$. For some applications, the energy flux in a given direction within a small solid angle is of interest. The radiance or intensity I (commonly also denoted as L) provides this information and can be obtained from the irradiance by differentiation (Petty, 2006):

$$I = \frac{dF}{\cos\theta d\Omega} = \frac{d\Phi}{dA \cos\theta d\Omega}. \tag{2.11}$$

It describes the mean power per unit projected area and per solid angle in the direction defined by Ω and has a unit of $\mathrm{W\,m^{-2}\,sr^{-1}}$. For all of the introduced quantities, also spectral forms such as the spectral radiance exist, which describes the radiance per unit wavelength and typically has units of $\mathrm{W\,m^{-2}\,nm^{-1}\,sr^{-1}}$.

In summary, the propagation direction, wavelength (spectrum), polarization state, and intensity completely characterize electromagnetic radiation and define its interaction with matter through absorption, emission, scattering, or reflection (Zinth and Zinth, 2013; Bohren and Huffman, 2004).

2.3.2 Polarization

Since this work is based on polarization measurements and the interaction of radiation with matter depends on its polarization state, the polarization of electromagnetic waves will be discussed in more detail in this section. As mentioned before, electromagnetic waves are transverse waves implying that the electric and magnetic fields oscillate in a plane perpendicular to the direction of propagation. By definition, polarization describes the direction of oscillation of the electric field component within this plane (Petty, 2006). An electric field with a preferred direction of oscillation is called polarized, whereas an unpolarized electric field oscillates randomly (Bohren and Huffman, 2004). Depending on the orientation of the oscillations defined by the complex amplitude of the electric field, $\boldsymbol{E_0}$, different polarization states are distinguished (Zdunkowski et al., 2007; Zinth and Zinth, 2013). Linearly polarized electric fields oscillate along a straight line with a fixed orientation perpendicular to the direction of propagation. In contrast, electric fields have a left-handed or right-handed circular polarization if their electric field vectors describe a circle over time. The most general polarization state is called elliptical polarization, which is a combination of both linear and circular polarization. Electromagnetic radiation is a superposition of many monochromatic plane waves, and in general, is partially polarized.

It is fully polarized if all individual electromagnetic waves have the same polarization, and unpolarized if the individual waves are completely uncorrelated (Hansen and Travis, 1974; Bohren and Huffman, 2004).

To obtain a quantitative description of the polarization of an electromagnetic wave, the electric field is decomposed into two orthogonal components parallel and perpendicular to a plane of reference (Bohren and Huffman, 2004):

$$\boldsymbol{E} = (E_{\parallel}\hat{\boldsymbol{e}}_{\parallel} + E_{\perp}\hat{\boldsymbol{e}}_{\perp})\exp(i\boldsymbol{kr} - iwt). \tag{2.12}$$

The unit vectors $\hat{\boldsymbol{e}}_{\parallel}$ and $\hat{\boldsymbol{e}}_{\perp}$ are orthogonal to the direction of propagation and oriented parallel and perpendicular, respectively, to the plane of reference (van de Hulst, 1981). Depending on the application, this plane of reference is typically chosen to be either the principal plane or the scattering plane. The scattering plane contains the directions of the incident and scattered radiation. For reflection on a plane surface, the principal plane is defined by the surface normal and the direction of the incident radiation. For atmospheric applications, the principal plane is usually defined as the plane created by the zenith and the direction of the incident solar radiation. A detailed description of the different reference planes can be found in Eshelman and Shaw (2019).

Based on this, the so-called Stokes vector can be defined. It was introduced by Stokes (1851) and Chandrasekhar (1960) and provides a quantitative description of polarization (Bohren and Huffman, 2004; Hansen and Travis, 1974):

$$\boldsymbol{S} = \begin{pmatrix} I \\ Q \\ U \\ V \end{pmatrix} = \begin{pmatrix} \langle E_{\parallel}E_{\parallel}^{*} + E_{\perp}E_{\perp}^{*}\rangle \\ \langle E_{\parallel}E_{\parallel}^{*} - E_{\perp}E_{\perp}^{*}\rangle \\ \langle E_{\parallel}E_{\perp}^{*} + E_{\perp}E_{\parallel}^{*}\rangle \\ i\langle E_{\parallel}E_{\perp}^{*} - E_{\perp}E_{\parallel}^{*}\rangle \end{pmatrix} = \begin{pmatrix} I_0 + I_{90} \\ I_0 - I_{90} \\ I_{45} - I_{135} \\ I_{\text{right-handed}} - I_{\text{left-handed}} \end{pmatrix}. \tag{2.13}$$

Here, the square brackets denote a time average and the asterisks the complex conjugate of the corresponding quantity. The different components of $\boldsymbol{S}$ are called Stokes parameters. I is the total intensity, Q and U describe linear polarization, and V represents circular polarization. In the atmosphere, however, circular polarization can be neglected (Emde et al., 2015; Hansen and Travis, 1974). The Stokes vector has the dimension of radiance and can be measured using polarizers through the relations given on the right-hand side of Eq. 2.13 (Hansen and Travis, 1974). It is defined relative to a reference plane as discussed above. In the scattering plane, U vanishes for single scattering due to symmetries, and Q contains the entire polarization information. For unpolarized light, $Q = U = V = 0$. Another useful quantity is the degree of linear polarization (DOLP), which is defined as $DOLP = \sqrt{Q^2 + U^2}$ and is independent of the choice of the reference plane (Bohren and Huffman, 2004).

Reflection, transmission, or scattering of electromagnetic radiation changes its polarization. The change of the Stokes vector through such an interaction can be computed using a 4×4 transformation matrix called the Mueller matrix $\mathbf{M}$ (Bass et al., 1995):

$$\boldsymbol{S'} = \mathbf{M}\boldsymbol{S}. \tag{2.14}$$

One example for a Mueller matrix is the rotation matrix $\mathbf{M_{rot}}$, which rotates the Stokes vector by an angle σ from one reference coordinate system to another one (Mishchenko et al., 2002):

$$\mathbf{M_{rot}}(\sigma) = \begin{pmatrix} 1 & 0 & 0 & 0 \\ 0 & \cos 2\sigma & -\sin 2\sigma & 0 \\ 0 & \sin 2\sigma & \cos 2\sigma & 0 \\ 0 & 0 & 0 & 1 \end{pmatrix}. \tag{2.15}$$

2.3.3 Radiative transfer

Electromagnetic radiation passing through the atmosphere interacts with various atmospheric constituents. Molecules, aerosols, or clouds can all absorb, emit, or scatter electromagnetic radiation (Petty, 2006). The transfer of electromagnetic radiation through the atmosphere, including the mentioned interaction processes, is described by the radiative transfer equation (RTE). It was first formulated by Chandrasekhar (1960) and its differential form including polarization reads (Hovenier and Van Der Mee, 1983; Zdunkowski et al., 2007):

$$\frac{d\boldsymbol{S}(\Omega)}{k_{\text{ext}} \cdot ds} = -\boldsymbol{S}(\Omega) + (1-\omega_0)\boldsymbol{B}_{\text{Planck}}(T) + \frac{\omega_0}{4\pi}\int_{4\pi} \mathbf{Z}(\Omega,\Omega')\boldsymbol{S}(\Omega')d\Omega'. \tag{2.16}$$

The first term of Eq. 2.16 describes the extinction of radiation and is also known as the Beer-Bouguer-Lambert extinction law. The extinction coefficient k_{ext} is the sum of the absorption coefficient and the scattering coefficient: $k_{\text{ext}} = k_{\text{abs}} + k_{\text{sca}}$. In addition, Ω is the solid angle defining the direction of interest, $\boldsymbol{S}$ is the Stokes vector introduced in the previous section, and ds is a small distance along the path given by Ω.

The second term of the RTE quantifies the emission of radiation. The emission can be calculated using the (unpolarized) Planck function $\boldsymbol{B}_{\text{Planck}}(T) = (B_{\text{Planck}}(T), 0, 0, 0)^T$, which describes the radiance emiited by a blackbody and depends on temperature. The single scattering albedo ω_0 specifies the fraction of the total extinction that is due to scattering:

$$\omega_0 = \frac{k_{\text{sca}}}{k_{\text{ext}}}. \tag{2.17}$$

Hence, $(1-\omega_0)$ is the contribution of absorption, which, according to Kirchhoff's law, equals the emission.

Finally, the last term on the right-hand side of Eq. 2.16 is related to the scattering of radiation. Here, the matrix $\mathbf{Z}$ is defined as (Hovenier and Van Der Mee, 1983)

$$\mathbf{Z}(\Omega,\Omega') = \mathbf{M_{rot}}(\sigma_2)\mathbf{P}(\Omega,\Omega')\mathbf{M_{rot}}(\sigma_1), \tag{2.18}$$

where $\mathbf{P}(\Omega,\Omega')$ is the so-called scattering phase matrix and $\mathbf{M_{rot}}$ the Mueller rotation matrix. The first component of the phase matrix, P_{11}, is known as the phase function and describes the probability density for scattering of radiation from a direction Ω' into the direction Ω. P_{12} is the polarized phase function and is related to the Stokes vector component Q. The scattering of radiation crucially depends on the wavelength and the size

of the particle by which it is scattered. Depending on the size parameter $x = \frac{2\pi r}{\lambda}$ with the particle radius r, different scattering regimes are distinguished.

The scattering by small particles compared to the wavelength, with $x \ll 1$, such as the scattering of solar radiation by molecules in the atmosphere, is known as Rayleigh scattering. The scattering coefficients in the Rayleigh regime are proportional to $\frac{1}{\lambda^4}$ (Petty, 2006). Hence, shorter wavelengths are scattered much more strongly compared to longer wavelengths. Figure 2.8 displays the phase function and the polarized phase function for Rayleigh scattering as a function of scattering angle, which is the angle between the direction of the incident and scattered radiation. The complete phase matrix for Rayleigh scattering has six non-zero entries and can, for example, be found in Hansen and Travis (1974). Rayleigh scattering creates polarization depending on the scattering angle. Unpolarized incident radiation remains unpolarized for scattering into the forward and backward directions, but becomes fully polarized at a scattering angle of 90° (Petty, 2006).

In contrast, scattering of radiation by particles that are large compared to the wavelength ($x \gg 1$) can be described by geometrical optics. In this limit, the ray-tracing method can be applied, and individual light rays are traced through particles such as large raindrops or large ice crystals. The reflection and refraction of the light rays at the particle are described by Fresnel's equations and Snell's law (Hansen and Travis, 1974). However, the geometric optics approximation does not include diffraction.

Finally, Mie theory (Mie, 1908) provides a solution to Maxwell's equations for scattering on spherical particles for all size parameters, including the range where $x \approx 1$ and neither the Rayleigh scattering nor the geometrical optics approximations can be applied. The solution in the Mie approximation is given by an infinite series including Mie coefficients that depend on the complex refractive index of the spherical particle and the size parameter (Hansen and Travis, 1974; Petty, 2006). The number of terms after which the infinite series can be truncated is approximately equal to the size parameter. A complete derivation can be found in, e.g. Bohren and Huffman (2004). Mie theory is, for example, applied to describe the scattering of solar radiation by liquid cloud droplets. In the limits of very small and very large size parameters, Mie theory converges to the Rayleigh and geometric optics approximations. Figure 2.8 shows the phase functions for Mie scattering by spherical cloud droplets with a typical effective radius of 10 µm. The phase function has a strong forward scattering peak. In addition, the local maximum (minimum) of the (polarized) phase function at around 140° scattering angle is known as the cloudbow.

For non-spherical particles, Mie theory cannot be applied and other methods to compute phase matrices have to be applied (Liou and Yang, 2016). They usually assume randomly oriented particles. In this case, the number of non-zero elements in the phase matrix is reduced due to symmetries. A parameterization of the scattering phase matrix for ice crystals with different shapes is, for example, provided by Yang et al. (2013). The green curves in Fig. 2.8 show the phase function and polarized phase function for an aggregate of 8 columns with an effective radius of 50 µm. The phase function has a strong forward peak and a local maximum corresponding to the 22° halo is visible at the respective scattering angle.

The RTE in Eq. 2.16 is an integro-differential equation, which cannot be solved analytically

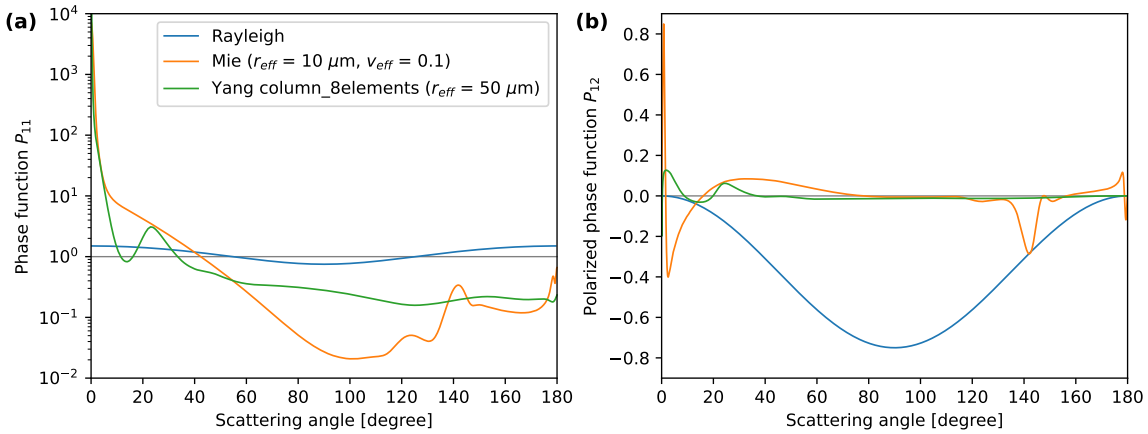

Figure 2.8: Scattering phase functions **(a)** and polarized phase functions **(b)** for Rayleigh scattering, Mie scattering, and ice crystal scattering for the aggregate of 8 columns with moderate surface roughness as defined by Yang et al. (2013) for a wavelength of 550 nm. The effective radius and variance were 10 µm and 0.1, respectively, for the Mie phase functions and the effective radius was 50 µm for the parameterization by Yang et al. (2013).

(Petty, 2006; Zdunkowski et al., 2007). Thus, approximations and numerical solutions have to be applied. In the thermal wavelength range, the scattering component can be neglected and the RTE reduces to the so-called Schwarzschild equation, which can be solved analytically. For the computation of radiances in the solar spectral range, different approximations exist. In the plane-parallel approximation, the optical properties are assumed to be homogeneous in the horizontal direction, and the only remaining spatial coordinate is the vertical direction. This approximation is well suited whenever the horizontal variation of the radiative properties is small compared to the vertical variation (Zdunkowski et al., 2007). Based on the plane-parallel approximation, the successive orders of scattering, discrete ordinate method, or adding-doubling methods provide quasi-exact solutions to the RTE (Petty, 2006; Zdunkowski et al., 2007). These are also known as one-dimensional radiative transfer solvers.

For atmospheric components such as three-dimensional clouds or a heterogeneous surface, the horizontal variability, however, has to be accounted for. A simple approximation to three-dimensional radiative transfer that still allows for applying the mentioned one-dimensional solvers, is the independent column approximation (ICA) with plane-parallel clouds (Gabriel and Evans, 1996). In this approximation, every vertical column of a three-dimensional cloud field is treated independently and approximated by a plane-parallel cloud. The traditional independent column approximation has been extended, for example, to different tilted independent column approximations to improve the representation of three-dimensional radiative effects (Wissmeier et al., 2013).

Full three-dimensional radiative transfer simulations including polarization can be obtained with the Monte Carlo method (Marchuk et al., 1980; Marshak and Davis, 2005; Mayer, 2009). In this method, individual photons are traced through the atmosphere where they get scattered, absorbed, or reflected until they reach the detector. This allows for the

computation of physically correct solutions to the radiative transfer equation for complex problems including the variation of optical properties in all three dimensions. Due to its statistical nature, the Monte Carlo method requires a large number of photons to produce noise-free results, making it relatively expensive in terms of computational cost.

2.3.4 Radiative properties of clouds

The radiative properties of clouds are determined by their thermodynamic phase – and, in the case of ice crystals, also by the crystal shape – as well as by the cloud droplet and ice crystal size distribution, and the geometrical thickness of the cloud layer, as these properties together define the key variables of the RTE: the extinction coefficient (or optical thickness), the single scattering albedo, and the phase matrix. Hence, all of these parameters will be briefly discussed below.

Generally, clouds can consist of liquid cloud droplets, ice crystals, or a mixture of both. The thermodynamic phase of a cloud affects its radiative effect in various ways. Liquid water and ice have different complex refractive indices and thus different absorption and scattering coefficients. These differences between liquid water and ice in the near-infrared are, for example, exploited by spectral retrievals of the cloud thermodynamic phase (Ehrlich et al., 2008). In addition, liquid water droplets are spherical, whereas ice crystals have hexagonal or more complex shapes. Thus, liquid water droplets and ice crystals also have different scattering phase matrices.

Besides the thermodynamic phase, the cloud droplet and ice crystal size distributions are important quantities. As mentioned before, the particle size relative to the wavelength of the radiation determines the scattering regime and hence the scattering properties. The liquid cloud droplets and ice crystals inside a cloud generally have all different sizes. The cloud droplet size distribution $n(r)$ quantifies the number of cloud droplets with a certain radius r. A modified gamma distribution is typically assumed for the shape of the distribution (Hansen, 1971). In the case of non-spherical ice crystals, the crystal size is generally described by the maximum dimension D instead of the radius, and the ice crystal size distribution is accordingly written as $n(D)$ (Liou and Yang, 2016). Integrating the cloud droplet size distribution over all droplet radii yields the cloud droplet number concentration (Grosvenor et al., 2018)

$$N_{\mathrm{d}} = \int_0^\infty n(r)dr, \tag{2.19}$$

which is the total number of droplets per unit volume and usually given in units of cm^{-3}. Analogously, an ice crystal number concentration can be obtained by integrating the ice crystal size distribution. The modified gamma distribution assumed for the size distribution is defined by two parameters related to the mean radius of the distribution and the distribution width. Typically, the effective radius introduced by Hansen (1971) is used to define a representative size instead of a volume mean radius, as it is more strongly linked

to the radiative properties of the cloud:

$$r_{\text{eff}} = \frac{\int_0^\infty \pi r^3 n(r) dr}{\int_0^\infty \pi r^2 n(r) dr}. \tag{2.20}$$

For ice crystals, different definitions of the effective diameter exist (McFarquhar and Heymsfield, 1998). In this work, the following definition of the effective diameter $D_{\text{eff}} = 2r_{\text{eff}}$ is used (Liou and Yang, 2016):

$$D_{\text{eff}} = \frac{3}{2} \frac{\int V(D) n(D) dD}{\int A(D) n(D) dD}. \tag{2.21}$$

Here, V is the volume and A the projected area of an ice crystal. The liquid water content (LWC) is the mass of liquid water per unit volume and, for spherical particles, can be computed using (Grosvenor et al., 2018)

$$\text{LWC} = \frac{4\pi\rho_{\text{w}}}{3} \int_0^\infty r^3 n(r) dr, \tag{2.22}$$

where ρ_{w} is the density of liquid water. Similarly, the ice water content (IWC), the mass of ice per unit volume, can be calculated as follows (Heymsfield et al., 2013; Liou and Yang, 2016):

$$\text{IWC} = \int m(D) n(D) dD = \rho_{\text{i}} \int V(D) n(D) dD. \tag{2.23}$$

Often, the mass of an ice crystal with a given maximum dimension $m(D)$ is computed using mass size relationships (Heymsfield et al., 2013). LWC and IWC are typically given in $\mathrm{g\,m^{-3}}$. Moreover, the extinction coefficient for spherical cloud droplets can be expressed as (Petty, 2006)

$$k_{\text{ext}} = \pi \int_0^\infty Q_{\text{ext}}(r) r^2 n(r) dr. \tag{2.24}$$

The extinction efficiency $Q_{\text{ext}}(r)$ can, for example, be calculated using Mie theory and converges to $Q_{\text{ext}} \approx 2$ in the geometrical optics limit. Vertical integration of the extinction coefficient finally leads to the definition of the optical thickness of a cloud:

$$\tau_{\text{ext}} = \int_{z_{\text{base}}}^{z_{\text{top}}} k_{\text{ext}}(z) dz, \tag{2.25}$$

where z_{base} and z_{top} are the cloud base and cloud top height, respectively. Depending on the application and the sensitivity of the instruments, cloud base height and cloud top height can be defined differently. In this work, the cloud top height is computed from measurements of the specMACS instrument using a stereographic retrieval (Kölling et al., 2019), and the obtained cloud top height corresponds to the altitude of $\tau \approx 1$ below cloud top (Volkmer et al., 2024). The cloud base height cannot be directly retrieved using a passive imaging system and is thus inferred from a combination of dropsonde measurements and the stereographic retrieval results. By combining the above equations, direct relationships between microphysical quantities such as water content and effective radius, and optical properties like the extinction coefficient or optical thickness can be obtained.

2.4 Adiabatic cloud model

A rising air parcel cools as it expands. Its temperature follows the dry adiabatic temperature gradient $\Gamma_\mathrm{d} = g/c_\mathrm{p}$. When supersaturation is reached, condensation sets in. The temperature gradient is then described by the moist adiabatic lapse rate Γ_m, which is smaller than Γ_d due to the latent heat release during condensation. A derivation can for example be found in Rogers and Yau (1989) or Curry and Webster (1999). The adiabatic cloud model describes the evolution of such a rising air parcel. The adiabatic liquid water content of the parcel can be calculated with (Brenguier et al., 2000)

$$\mathrm{LWC}_\mathrm{ad} = C_\mathrm{w} h, \tag{2.26}$$

where $h = z - z_\mathrm{base}$ is the height above cloud base. The condensation rate C_w can be computed from the air temperature T and pressure p of the parcel (Grosvenor et al., 2018):

$$C_\mathrm{w} = \rho_\mathrm{a} \frac{c_\mathrm{p}}{L_\mathrm{v}} \left(\Gamma_\mathrm{d} - \Gamma_\mathrm{m}(T, p)\right). \tag{2.27}$$

Here, ρ_a is the air density of the parcel, L_v the latent heat of evaporation, and c_p the specific heat of dry air at constant pressure. The actual liquid water content of the air parcel is smaller than the adiabatic liquid water content due to entrainment of dry ambient air into the cloud. The adiabatic cloud model assumes a constant cloud droplet number concentration with height and that the actual liquid water content is related to the adiabatic liquid water content through (Brenguier et al., 2000; Grosvenor et al., 2018)

$$\mathrm{LWC} = f_\mathrm{ad} \mathrm{LWC}_\mathrm{ad}, \tag{2.28}$$

where f_ad is the adiabaticity, which accounts for the effects of entrainment. The adiabaticity is either assumed constant or parameterized through entrainment models (de Rooy et al., 2013).

Another parameter to introduce is k, which relates the volume mean radius r_v to the effective radius (Martin et al., 1994):

$$k = \frac{r_\mathrm{v}^3}{r_\mathrm{eff}^3}. \tag{2.29}$$

k has a typical value of $k = 0.8$ for maritime clouds (Martin et al., 1994; Pawlowska and Brenguier, 2000).

The above equations can be combined to obtain a relation for the effective radius as a function of height using the adiabatic cloud model:

$$r_\mathrm{eff} = \left(\frac{3}{4\pi\rho_\mathrm{w}}\right)^{1/3} (f_\mathrm{ad} C_\mathrm{w})^{1/3} (k N_\mathrm{d})^{-1/3} h^{1/3}. \tag{2.30}$$

A derivation of this formula is given in Appendix A. Further relations, for example, for the cloud droplet number concentration as a function of effective radius and cloud optical thickness can be obtained from the adiabatic cloud model (Grosvenor et al., 2018).

Chapter 3

Methods

3.1 The specMACS instrument

This section was already published in Weber et al. (2024), except for parts of the discussion in Sect. 3.1.5.

This work is based on observations of the specMACS instrument (Ewald et al., 2016). It originally consisted of two hyperspectral cameras in the visible and near-infrared wavelength range and was first operated on the ground, later in a sideward-looking, and finally in a downward-looking perspective on board the German research aircraft HALO. Before the EUREC^{4}A field campaign (Stevens et al., 2021) in 2019, the spectrometers were complemented by two 2D RGB polarization-resolving cameras with a large field of view and high angular and spatial resolution. With that, specMACS became a hyperspectral and polarized airborne imaging system. Hyperspectral and polarization-resolving cameras are operated on the same platform, allowing for combined and improved retrievals of cloud properties. A detailed instrument description is given in Sect. 3.1.1.

As part of this work, the polarization-resolving cameras of specMACS were completely characterized and calibrated for the first time, and the calibration of one of the spectrometers was repeated. In general, any digital imaging sensor has imperfections and non-uniformities due to manufacturing and sensor electronics, which have to be assessed and characterized by calibration. In addition, an absolute calibration is necessary for certain retrievals, such as the polarimetric phase retrieval developed in this work. The polarization-resolving cameras can be classified as division-of-focal-plane polarimeters. There are a variety of different calibration techniques for division-of-focal-plane polarimeters, which have been reviewed by Giménez et al. (2019, 2020). Lane et al. (2022), for example, calibrated the monochrome version of the polarization-resolving cameras from the same manufacturer as the cameras of specMACS. However, they did not provide an absolute calibration. Rodriguez et al. (2022) calibrated a camera with the same sensor, but the assumptions they made are not applicable to the specific instrument setup of specMACS, since the specMACS setup includes not only lenses but also a window in front of the cameras.

The characterization and calibration of the polarization-resolving cameras presented below consist of a geometric calibration as well as a radiometric calibration. The radiometric calibration includes a dark signal and noise characterization, a linearity analysis, vignetting correction, polarization calibration, spectral calibration, and absolute radiometric calibration. With that, georeferenced, absolute calibrated Stokes vectors, which are rotated into the scattering plane, can be computed from raw measurements. Here, the scattering plane is the plane containing the direction of the incoming solar radiation and the viewing direction for every pixel. The calibration measurements were completed at the Calibration Home Base (CHB) (DLR Remote Sensing Technology Institute, 2016) and the calibration methods and results are presented in the sections 3.1.2 and 3.1.3. Finally, the calibration results were applied to measurement data of the sunglint, which is formed by the reflection of sunlight on water surfaces. The sunglint is a known target, so the calibration results could be validated by comparing the calibrated measurements with radiative transfer simulations of the sunglint in Sect. 3.1.4. Finally, the results are discussed in Sect. 3.1.5.

3.1.1 Instrument description

The spectrometer of the Munich Aerosol Cloud Scanner (specMACS) is a hyperspectral and polarized imaging system developed and operated by the Meteorological Institute of the Ludwig-Maximilians-Universität München (Ewald et al., 2016). It is mainly used for the remote sensing of cloud macro- and microphysical properties.

Originally, specMACS consisted of two hyperspectral cameras, so-called VNIR and SWIR, which are sensitive to the wavelength range from 400 to 1000 and from 1000 to 2500 nm, respectively. Both cameras were characterized and calibrated by Ewald et al. (2016) for the first time in 2014. The VNIR and SWIR are line-spectrometers with a field of fiew of 32.7° and 35.5° in across-track direction, respectively, and measure with 30 Hz. They have a spatial resolution of about 10 m at typical flight altitudes, and 800 and 256 spectral channels with a typical spectral bandwidth of 2.5 nm to 4 nm and 7.5 nm to 12 nm, respectively. Together with the calibration of the polarization-resolving cameras in 2021, the calibration of the VNIR camera was repeated and showed no changes beyond the measurement uncertainties. The calibration measurements of the SWIR camera could not be repeated in 2021, since the camera had to be sent to the manufacturer for repair.

In the past, specMACS was operated in a ground-based setup before it was integrated into the German High Altitude and LOng range (HALO) research aircraft (Krautstrunk and Giez, 2012), first looking through the aircraft side window. Since 2016, specMACS has operated from a nadir-looking perspective in the rear of the fuselage of the HALO research aircraft. For that, the cameras were mounted into a pressurized housing with temperature stabilization and humidity control, and a 2 cm thick quartz glass window (Heraeus Herasil 102) in front of the cameras.

In 2019 for theEUREC^4A field campaign (Stevens et al., 2021), the hyperspectral cameras were complemented by two 2D RGB polarization-resolving cameras, so-called polLL and polLR (polarization camera looking to the lower left (LL) and lower right (LR) relative to the flight direction, previously called polA and polB in Pörtge et al., 2023). Both cameras

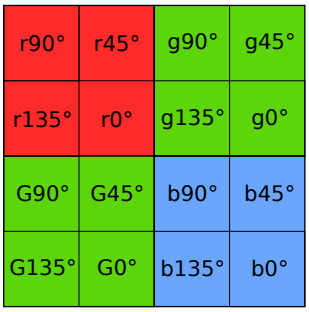

Figure 3.1: Pixel layout of a super-pixel with the color and polarization filter array.

are LUCID Vision Phoenix 5.0 MP Polarization Model cameras (LUCID Vision Labs Inc., 2023) with Sony's IMX250MYR sensor (Sony Semiconductor Solutions Corporation, 2023). They measure in a synchronized manner with an acquisition frequency of 8 Hz and have an auto-exposure control system similar to the one described in Ewald et al. (2016). The sensor of a single camera has 2448×2048 px. It comprises a combination of a color filter array and a polarizer filter array and can be classified as a division-of-focal-plane polarimeter. The color filter array consists of a Bayer pattern of red, green, and blue color channels, and the polarizer filter array consists of four different on-chip directional polarizers with 0, 45, 90, and 135° polarization directions. A block of 4×4 px forms a super-pixel, whose pixel layout is visualized in Fig. 3.1. A super-pixel can be subdivided into blocks of 2×2 px for each color with the four different polarizers on each pixel. The on-chip directional polarizers are placed below the on-chip microlenses to reduce the distance between the polarizers and the photodiodes. With this specific sensor layout, simultaneous measurements of 0, 45, 90, and 135° polarization directions are possible and Stokes vectors can be calculated. The Stokes vector, introduced in Sect. 2.3.2, provides a full characterization of electromagnetic radiation and a quantitative description of polarization. It can be computed from the measurements with (e.g., Hansen and Travis, 1974)

$$\boldsymbol{S} = \begin{pmatrix} I \\ Q \\ U \\ V \end{pmatrix} = \begin{pmatrix} \left(I_0 + I_{45} + I_{90} + I_{135}\right)/2 \\ I_0 - I_{90} \\ I_{45} - I_{135} \\ I_{\text{right-handed}} - I_{\text{left-handed}} \end{pmatrix} . \tag{3.1}$$

The polarization-resolving cameras can measure the I, Q, and U component of the Stokes vector. I is the total intensity, and Q and U specify linear polarization. V describes circular polarization and is negligible in the atmosphere (e.g., Hansen and Travis, 1974; Emde et al., 2015). The disadvantage of the filter array is that the measurements suffer from sparsity and instantaneous-field-of-view errors. These errors can however be reduced by applying interpolation strategies (Ratliff et al., 2009; Tyo et al., 2009; Gao and Gruev, 2011).

Each of the cameras is combined with a Cinegon 1.8/4.8 lens by Schneider-Kreuznach. The aperture is optimized for the operation on board the HALO research aircraft and set to a fixed value of 5.6. The two polarization-resolving cameras are installed with partially overlapping fields of view as shown in Fig. 3.2. This allows for a large overall field of view

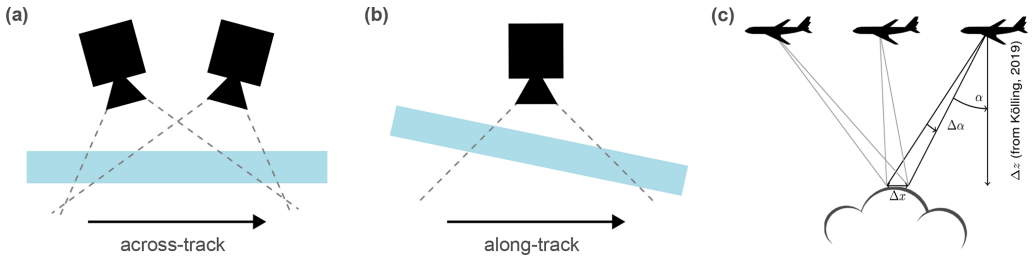

Figure 3.2: (a, b) Installation geometry of the two polarization-resolving cameras. The window in front of the cameras is shown in light blue, the dashed lines indicate the field of view of the cameras. **(c)** Observation geometry (panel from Fig. 3 in Pörtge et al., 2023; citation in the panel refers to Kölling et al., 2019).

Lenses	Cinegon 1.8/4.8 by Schneider-Kreuznach
Focal length	4.8 mm
Aperture	1.8–8 (set to 5.6)
Along-track field of view	91°
Across-track field of view	78°
Cameras	Phoenix 5.0 MP Polarization Model
Sensor	Sony IMX250MYR CMOS
Shutter type	Global
Sensor resolution	5.0 MP
Sensor pixels	2448×2048
Pixel size	$3.45\mu\text{m} \times 3.45\mu\text{m}$
Maximum frame rate	22 Hz
Bit depth	12 bit (scaled to 16 bit)
Dynamic range maximum	65 535 DN
Combined field of view	$91° \times 117°$

Table 3.1: Specifications of the polarization-resolving cameras.

without the distortions of a fish-eye camera. A single camera has a field of view of 91° in the along-track direction and 78° in the across-track direction, and the maximum combined field of view is about 91° along-track and 117° across-track. The window in front of the cameras is tilted by 12° in the flight direction relative to the base plate of the instrument (see Fig. 3.2). A detailed description of the camera geometry is given in the following section. The specifications of the polarization-resolving cameras are summarized in Table 3.1. Example measurements of the polarization-resolving cameras are shown in Pörtge et al. (2023) and in the following sections of this work, for example in Fig. 3.16.

Applications of the data of the two polarization-resolving cameras so far have been the stereographic retrieval of 3D cloud geometry (Kölling et al., 2019, who do not use

polarization information) and the retrieval of cloud droplet size distribution from polarized observations of the cloudbow (Pörtge et al., 2023). While flying above a scene, certain (cloud) targets are sampled from different viewing angles (see Fig. 3.2c, figure from Pörtge et al., 2023). This allows for the stereographic reconstruction of the target locations in three-dimensional space from which the 3D cloud geometry is derived. But it also provides multi-angle polarimetric information which can be used for retrievals like the derivation of cloud droplet size distribution by Pörtge et al. (2023).

3.1.2 Geometric calibration

Both applications of the polarization-resolving cameras need an accurate geometric calibration for the correct localization of the targets. The geometric calibration consists of two steps. First, the camera model has to be defined and camera intrinsics and distortion coefficients have to be determined. Second, the exact location and orientation of the cameras in a fixed 3D world coordinate system have to be found in order to obtain georeferenced data.

The camera model describes the transformation from world coordinates to pixel coordinates. It relates every pixel to its viewing direction, including distortions, e.g., due to lenses along the optical path. The parameters of the camera model include camera intrinsic parameters, distortion coefficients, and extrinsic parameters and can for example be computed with the chessboard calibration method (Zhang, 2000; Heikkila and Silven, 1997). Multiple views of known targets like the corners of a chessboard can be used to fit the camera model and solve for the model parameters. Chessboard corners are the intersections of straight lines that are easily detectable and allow the model to be fitted up to subpixel accuracy.

The geometric camera calibration was performed using the OpenCV library (Bradski, 2000) similarly to Kölling et al. (2019). But OpenCV's rational camera model was applied instead of the thin prism model. In total, 249 images of a chessboard with 9×6 corners with a 65 mm × 65 mm square size on an aluminum composite panel were used for the polLL camera and 212 images of the same chessboard for the polLR camera. Figure 3.3 shows an example image of the chessboard measured by the polLR camera. The images were taken such that the chessboard corners were distributed over the entire field of view. All measurements were done with the cameras assembled inside the housing with the window in front of them as during aircraft operation. Due to the large field of view of the cameras and the consequential large incident angles on the window and its thickness of 2 cm, the window introduces a shift of the viewing directions. This shift results in an additional angle- and distance-dependent distortion of the detected chessboard corners. It cannot easily be included in the camera model, since it does not change the direction itself. In order to reduce the impact of the shift, the chessboard images were taken with the chessboard at a few meters distance from the instrument – as far away as possible to minimize the impact of the window but close enough to detect all corners correctly. The mean root mean square reprojection error of the best-fit camera model of the polLL and polLR camera amounted to 0.18 and 0.20 px, respectively. The field of view of a single camera

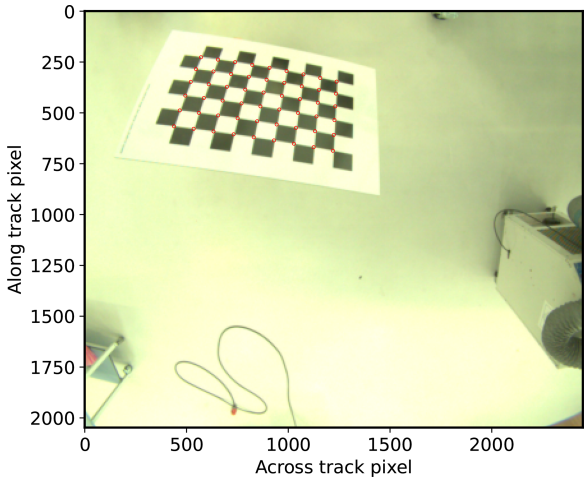

Figure 3.3: Chessboard image taken by the polLR camera. The red circles indicate the detected chessboard corners.

amounted to $91° \times 78°$ (along-track × across-track) and the maximum combined field of view to $91° \times 117°$, corresponding to a maximum combined swath of about 20 km × 33 km at a typical flight altitude of 10 km. In addition, the mean angular resolution is 0.04° in the along-track and across-track directions or about 10 m at a typical flight altitude of 10 km and a target at ground height. With the acquisition frequency of 8 Hz, the polarization-resolving cameras provide data with high angular resolution for angular sampling at a typical flight speed of 200 $\mathrm{m\,s^{-1}}$, which corresponds to an angular resolution of up to 0.14° for a target at 10 km distance.

In the second step, the camera position and orientation for georeferencing had to be determined. Precise information about aircraft position (latitude, longitude, and altitude of the aircraft) and attitude (roll, pitch, and yaw angles) is available from the Basic HALO Measurement and Sensor System (BAHAMAS). BAHAMAS includes an inertial measurement unit, which is GPS-referenced with data from a global navigation satellite system (Giez et al., 2021). The data are acquired with a rate of 100 Hz. After post-processing, the accuracy of the BAHAMAS data is 0.05 m for position data, 0.003° for roll and pitch angles, and 0.007 ° for true heading (Giez et al., 2021). However, the BAHAMAS sensor is located at the front part of the aircraft, while the specMACS instrument is integrated in the boiler room in the rear part. Because of that, the accuracy of the BAHAMAS attitude data for the specMACS instrument is expected to be reduced because of bending and stretching of the aircraft fuselage during a flight. The orientation and position of the polarization-resolving cameras relative to the aircraft were determined with the method described by Kölling (2020). An initial guess of the camera position and orientation is provided from the design documents. The rotation angles were then optimized by projecting specMACS measurements onto satellite images and matching features such as coastlines, lakes, or big roads. This was done once for every measurement campaign, since the instrument could be slightly misaligned after each integration into the aircraft. The orientation angles were optimized up to differences of 0.05°, which corresponds to a shift of 8.7 m at the ground for

a flight altitude of 10 km.

3.1.3 Radiometric characterization

Besides the geometric calibration, the cameras were also characterized radiometrically. The output of each pixel is given as a digital number (DN). In order to convert this digital number into an absolute radiometric signal, the sensor needs to be calibrated. This calibration includes the investigation of inter-pixel variations due to imperfections of the sensor material as well as other influences from the sensor electronics and optical components. In general, the sensor signal S can be expressed as

$$S = S_0 + S_\mathrm{d} + \mathcal{N}, \tag{3.2}$$

with the radiometric signal S_0, the dark signal of the sensor S_d, and the sensor noise $\mathcal{N}$ (Ewald et al., 2016). The different components of the sensor signal will be characterized in the following sections. The calibration measurements were performed at the Calibration Home Base (CHB; DLR Remote Sensing Technology Institute, 2016; Gege et al., 2009) of the Remote Sensing Technology Institute of the German Aerospace Center (DLR) in Oberpfaffenhofen in November 2021. All measurements were taken with the cameras mounted inside the housing as during aircraft operation. For radiometric measurements, the large integrating sphere (LIS) of the CHB was used, which is suited for the calibration of instruments with a large field of view. The LIS has a diameter of 1.65 m and an exit port of up to 55 cm, and its intensity can be changed using different combinations of its 18 different lamps. Only pixels illuminated by the lower hemisphere of the LIS were included in the analysis of the radiometric calibration data because the coating of the lower hemisphere was newer than the coating of the upper hemisphere, and due to the large field of view of the cameras, the edge between both hemispheres was visible in the calibration data. If not stated otherwise, all properties are given pixel-wise. Angle brackets denote a temporal average, and spatial averages are indicated by an overbar.

Dark signal

The dark signal S_d is a pixel-dependent offset signal that the sensor measures when no light penetrates the camera. It can directly be measured from an averaged dark frame, $\langle S \rangle = \langle S_0 + S_\mathrm{d} + \mathcal{N} \rangle$, since $S_0 = 0$ if no light enters the camera and $\langle \mathcal{N} \rangle \to 0$. The dark signal can be split into two components and is generally dependent on exposure time t_exp and temperature T:

$$S_\mathrm{d}(T) = i_\mathrm{dc}(T) t_\mathrm{exp} + S_\mathrm{read}. \tag{3.3}$$

The dark current i_dc is caused by thermally generated electrons whose generation rate increases with increasing temperature. The read-out offset S_read originates from the A/D converters within the sensor. In contrast to the hyperspectral cameras, the polarization-resolving cameras do not have external shutters, which means that no dark signal can be characterized during measurement periods. Because of that, the dark signal for any measurement during field campaigns is estimated from the laboratory characterization.

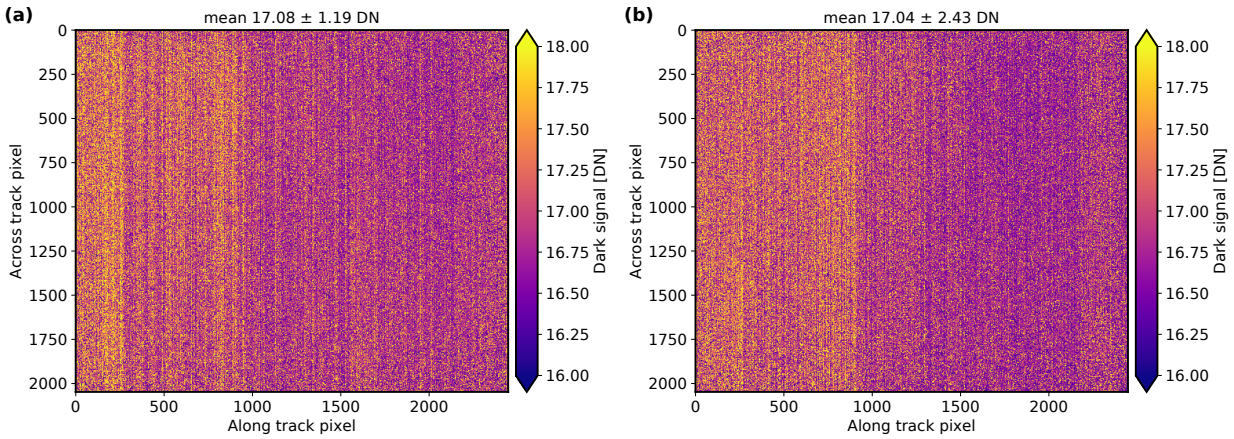

Figure 3.4: Spatial distribution of the dark signal averaged over 100 dark measurements with 50 frames each at an exposure time of 5 ms and constant temperature for the polLL camera **(a)** and polLR camera **(b)**.

For the analysis of the spatial structure of the dark signal, in total 5000 dark frames were averaged. The measurements were taken with an exposure time of 5 ms and at constant temperature. Results of this analysis are shown in Fig. 3.4. Mean and standard deviations of the dark signal across the sensor pixels of the polLL and polLR camera amounted to 17.08 ± 1.19 and 17.04 ± 2.43 DN, respectively. These dark-signal levels correspond to 0.026 % of the digital-number range, which has a dynamic range maximum of 65 535 DN. For typical signal levels of 30 000 DN, the dark signal accounts for 0.057 % of the total signal.

In addition, the temperature dependence of the dark signal was investigated (see Fig. 3.5). During two measurement series, the temperature varied from about 35 to 38 and 34 to 37 °C. The temperature was measured by the data logger of the instrument inside the housing and is used as a proxy for the temperature of the sensors. From the analysis, dark-signal drifts of 0.016 and 0.012 DN K^{-1} were found for the polLL and polLR camera, respectively. Temperature variations during a research flight are usually greatest during takeoff and amount to up to 10 K until the aircraft reaches its cruising level and the temperature is stabilized at 25 °C for the remainder of the flight. Thus, the total dark-signal drift due to temperature variations during a research flight is 0.16 and 0.12 DN for polLL and polLR.

Lastly, the dependence of the dark signal on exposure time was analyzed. Dark-signal measurements were performed by averaging over 50 frames for exposure times between 0.05 and 100 ms at constant temperature. Figure 3.6 shows slightly increasing dark-signal levels with exposure time. The total dark-signal drift due to varying exposure time is 0.23 and 0.22 DN for the polLL and polLR camera. Typical exposure times during aircraft operation are below 10 ms.

In summary, the dark-signal level of both cameras is very small with only minor spatial variations and variations with exposure time and negligible temperature dependence. Thus, constant values of 17.08 and 17.04 DN are used for all channels of the polLL and polLR camera, respectively, for the dark-signal correction. The total standard deviation of the

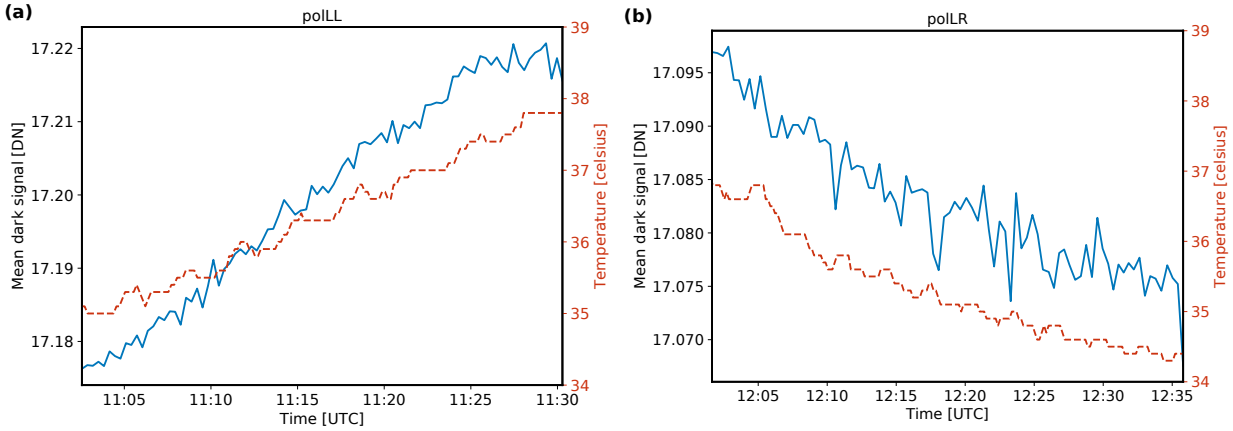

Figure 3.5: Temperature dependence of the dark signal averaged over 50 frames for each temperature at an exposure time of 5 ms for the polLL camera **(a)** and polLR camera **(b)**. The dashed red curves indicate the temperature variations; the solid blue curves show the mean dark signal.

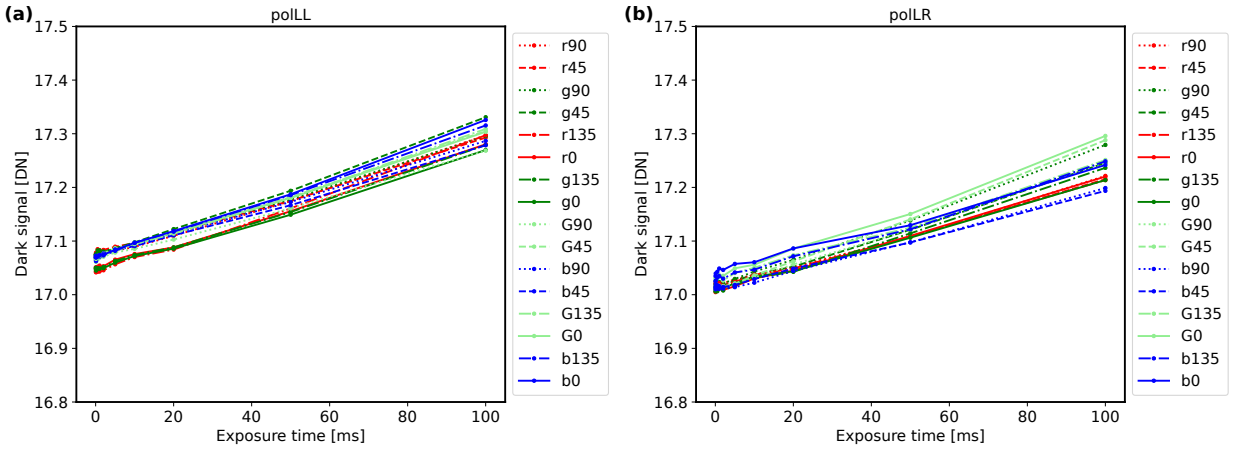

Figure 3.6: Exposure time dependence of the dark signal averaged over 50 frames at constant temperature for the polLL camera **(a)** and polLR camera **(b)**. The different lines show the different color and polarization channels.

dark signal including spatial variations, temperature variations, and variations with exposure time is 1.22 and 2.44 DN for polLL and polLR. For typical signal levels of 30 000 DN, the total dark-signal drift corresponds to 0.004 % and 0.008 % of the signal.

Linearity

Furthermore, the linearity of the sensors was investigated following Forster et al. (2020). According to Ewald et al. (2016), the radiometric signal measured by a perfectly linear sensor with absolute radiometric response R should depend linearly on input radiance L and exposure time t_{exp}:

$$\widetilde{S_0} = RLt_{\mathrm{exp}} = s_{\mathrm{n}}t_{\mathrm{exp}}, \tag{3.4}$$

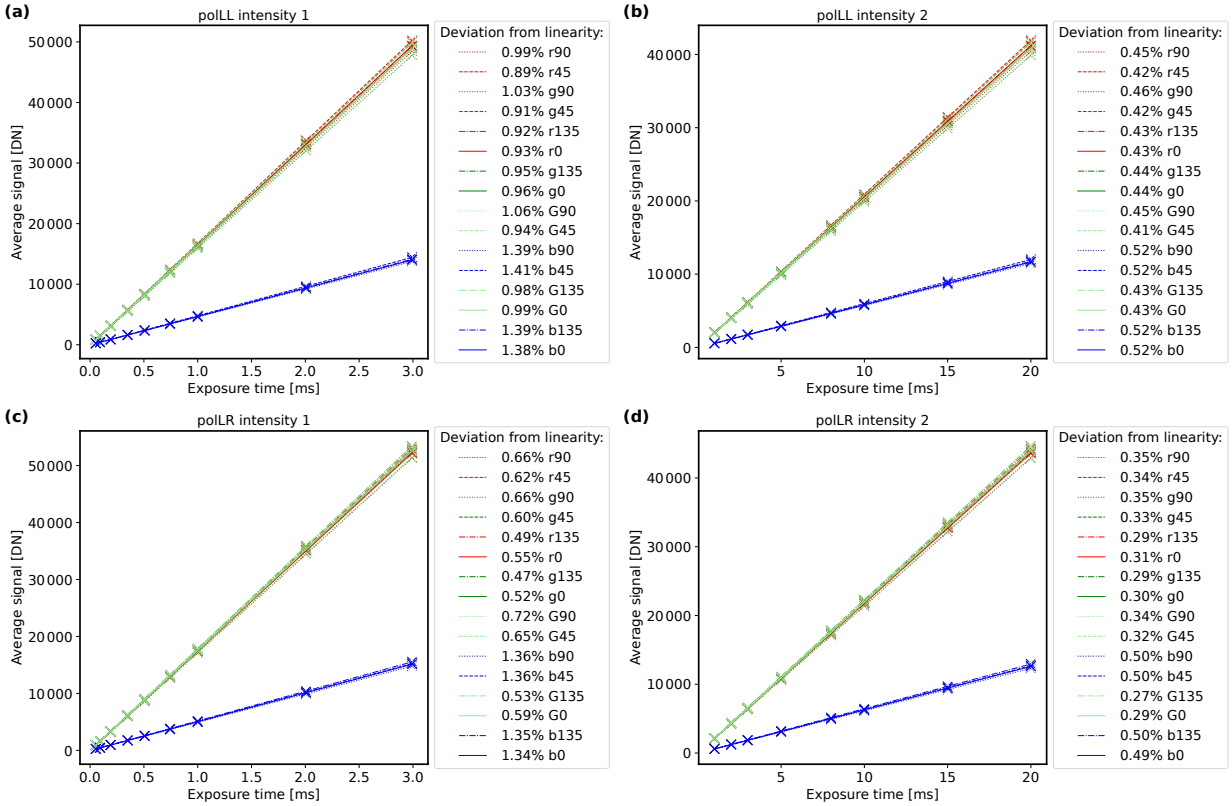

Figure 3.7: Linearity of the mean radiometric signal S_0 with exposure time for the different channels of the polLL camera **(a, b)** and the polLR camera **(c, d)** for two different intensities of the large integrating sphere. The dots indicate the observed signal; the lines are a linear fit assuming a perfectly linear sensor. The deviation of the observed signal of each channel from the linear model is given in the legends.

with the normalized signal or photocurrent $s_\mathrm{n} = RL$. A deviation between the observed signal S_0 and the signal expected from a perfectly linear sensor $\widetilde{S_0}$ is known as photoresponse non-linearity. To examine the linearity of the polarization-resolving cameras, measurements with different exposure times were taken above the large integrating sphere assuming that the exposure time is linear. 1000 frames were measured with an acquisition rate of 8 Hz for each exposure time and averaged. The output of the LIS has a standard deviation $\sigma = 0.02\,\%$ over a time period of 330 s and can thus be considered temporarily stable for the duration of the measurements (Baumgartner, 2013). The linearity of the signal with exposure time was analyzed for two different output intensities of the LIS in order to cover a large range of exposure times. The second intensity was about 12 % of the first intensity. Figure 3.7 shows the average radiometric signal $\langle S_0 \rangle$ as a function of exposure time for all different channels of the polLL and polLR camera for both intensities. The mean deviation of the observed signal from the perfectly linear signal of an ideal sensor was determined from a linear fit to the data. Its values are given for every channel in the figure and are generally larger for the measurements at smaller exposure times and higher LIS intensity (panels a and c). The mean deviations across all pixels of a certain color are 0.68 %, 0.70 %,

and 0.96 % for the red, green, and blue color channel of the polLL camera and 0.45 %, 0.45 %, and 0.93 % for the polLR camera.

Noise

Noise in general consists of signal noise (photon shot noise) and dark noise. Dark noise is, analogously to the dark signal, composed of dark current noise due to statistical fluctuations of thermally generated electrons and read noise from the electronic read-out process. Photon shot noise originates from the temporally random distribution of photons arriving at the detector. The number of photons measured during a certain time interval can be described by a Poisson distribution. The standard deviation of a Poisson distribution with expectation value N is proportional to $\sqrt{N}$. Thus, the photon shot noise is directly proportional to the square root of the number N of photoelectrons and the conversion gain k, and the total noise $\sigma_{\mathcal{N}}$ can be written as

$$\sigma_{\mathcal{N}} = \sqrt{\sigma_{\text{shot}}^2 + \sigma_{\text{r}}^2} = \sqrt{k^2 N + \sigma_{\text{r}}^2}\,, \tag{3.5}$$

where σ_{shot} is the photon shot noise and σ_{r} the read noise (Janesick, 2007). For a linear sensor, the measured signal is directly proportional to the number of photons N. To analyze the noise characteristics of the polarization-resolving cameras, the pixel-wise standard deviation was computed across 1000 frames, which were taken above the LIS for different exposure times and two different output intensities of the LIS in order to cover a large enough signal range. Then, two-dimensional histograms of variance and noise as a function of averaged, dark-signal-corrected signal were calculated and the Poisson model was fitted to them. This was done separately for every color and polarization channel. Figure 3.8 displays the results for the r90 channel of the polLL and polLR camera. For a typical signal level of 30 000 DN, the noise is around 400 DN or 1.3 %. All other channels show similar results. The noise characteristics of both cameras are well captured by the Poisson model. Panels (a) and (c) show the expected linear relationship between the variance and the signal, while the noise scales with the square root of the signal in panels (b) and (d). Deviations from the Poisson model would be an indication of sensor non-linearities or non-Poisson noise.

Spectral response

The polarization-resolving cameras have a color filter array with red, green, and blue color channels. Measurements of the spectral response functions were performed using the Oriel MS257 monochromator of the CHB in the monochromator setup. The wavelength uncertainty in the monochromator is ±0.1 nm in the relevant wavelength range with a spectral bandwidth smaller than 0.54 nm and a relative radiometric uncertainty between 0.6 % and 0.9 % (Baumgartner, 2019, 2022). Measurements were performed for wavelengths between 370 and 750 nm in steps of 5 nm at an exposure time of 5 ms for both cameras. At every wavelength 50 frames were taken and averaged. Since the monochromator illuminates only a few pixels (about 8×8), measurements were performed at seven different positions in

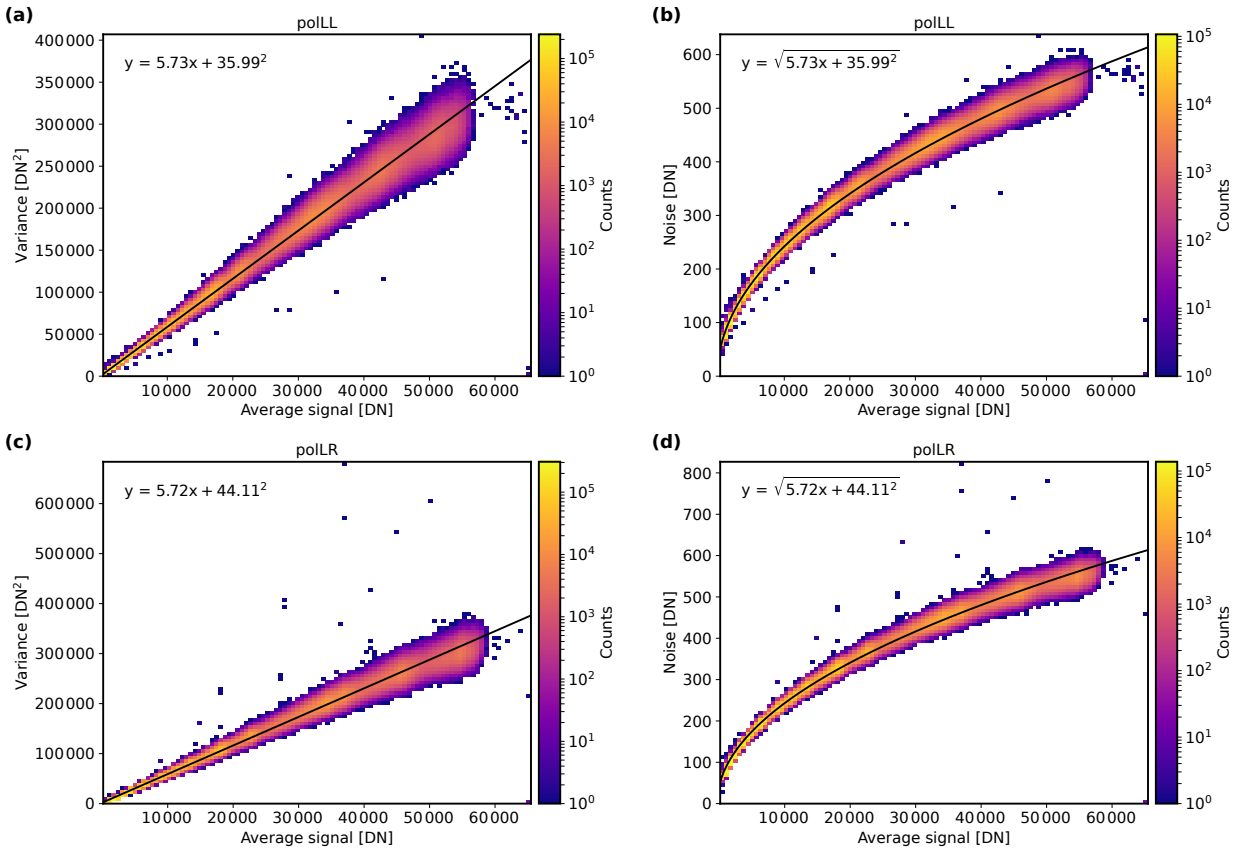

Figure 3.8: Noise characteristics of the r90 channel of the polLL camera **(a, b)** and the polLR camera **(c, d)**. Panels **(a)** and **(c)** show two-dimensional histograms of the variance as a function of average dark-signal-corrected signal and panels **(b)** and **(d)** the noise. The solid black lines denote the least-squares fit of the Poisson model given by the equation in the respective panel.

the across-track direction and three different positions in the along-track direction in order to cover a certain number of pixels distributed across the sensor. Dark measurements were substracted from the data, the data was corrected for the monochromator intensity, and the spectral response functions were normalized to 1. Figure 3.9 shows the resulting mean spectral response functions across all measured pixels for every channel of the polLL and polLR camera. The uncertainties include the standard deviation across the different pixels and the monochromator uncertainties. In general, there are only very small differences between the spectral response functions for the different polarization directions of each color. Center wavelengths and full width at half maximum (FWHM) were determined from a Gaussian fit for the red, green1, green2, and blue color channels. Values of 621 nm (FWHM = 66 nm), 548 nm (118 nm), 545 nm (117 nm), and 468 nm (87 nm) were obtained for the center wavelengths of the polLL camera and 621 nm (67 nm), 548 nm (119 nm), 545 nm (117 nm), and 468 nm (87 nm) for polLR.

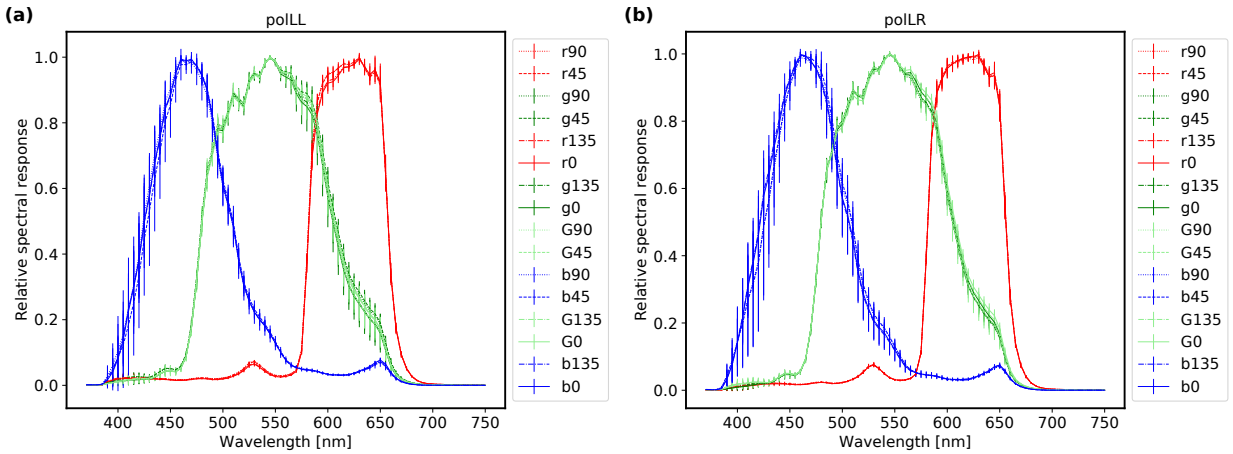

Figure 3.9: Relative spectral response function with uncertainty for the different color and polarization channels of the polLL camera **(a)** and polLR camera **(b)**.

Polarization calibration

In addition to general digital imaging errors, polarimeters have additional inaccuracies due to imperfections of the polarizers. Transmission, diattenuation, and orientation of the single on-chip directional polarizers can vary across the sensor due to misalignments and non-uniformities from manufacturing. These variations have to be compensated for by polarization calibration in order to correctly reconstruct the polarization signal from the measurements. There are a variety of different calibration techniques such as single-pixel calibration (Powell and Gruev, 2013), super-pixel calibration (Powell and Gruev, 2013; Lane et al., 2022), and more complex calibration techniques based on super-pixel calibration (e.g., Chen et al., 2015; Zhang et al., 2016). Giménez et al. (2019, 2020) reviewed different calibration methods for division-of-focal-plane polarimeters. They found that the super-pixel calibration method performs well and that more complex calibration methods do not improve the calibration results significantly. Hence, the super-pixel calibration method was applied. In general, the transformation of an incident Stokes vector $\boldsymbol{S} = (I, Q, U)^T$ into the measured intensities $\boldsymbol{I} = (I_0, I_{45}, I_{90}, I_{135})^T$ can be described by

$$\boldsymbol{I} = \mathbf{A}\boldsymbol{S} + \boldsymbol{d}\,, \tag{3.6}$$

where $\boldsymbol{d} = (d_0, d_{45}, d_{90}, d_{135})^T$ is the dark signal, which was already characterized in Sect. 3.1.3, and $\mathbf{A}$ is the so-called transfer matrix. The aim of the polarization calibration is to determine the transfer matrix $\mathbf{A}$. This was done following two approaches. First, a theoretical polarization camera model was introduced for the transfer matrices for the entire sensor. Second, laboratory calibration measurements were used to compute transfer matrices and validate the model.

Since the super-pixel method combines pixels with all four different polarizers in a 2×2 px neighborhood, it suffers from instantaneous-field-of-view errors. However, these errors can be reduced by interpolation (Ratliff et al., 2009; Tyo et al., 2009; Gao and Gruev, 2011). Thus, the measurements were interpolated using a bilinear interpolation method in order to

obtain measurements of all four polarization directions and all colors at every pixel before the super-pixel calibration was applied to every pixel. To avoid artifacts from extrapolation, the outermost super-pixel was excluded. The bilinear interpolation allows for very fast data analysis. It performs well in scenes without sharp edges, which are typically encountered in the application to the remote sensing of clouds. In the future, improved interpolation methods adapted to the combination of color and polarization filter arrays like the methods by Mihoubi et al. (2018) or Morimatsu et al. (2020) could be applied.

Theoretical polarization camera model

First, the theoretical polarization camera model is presented. The transfer matrix of an ideal sensor follows from Eq. 3.1:

$$\mathbf{A_{ideal}} = \frac{1}{2}\begin{pmatrix} 1 & 1 & 0 \\ 1 & 0 & 1 \\ 1 & -1 & 0 \\ 1 & 0 & -1 \end{pmatrix} . \tag{3.7}$$

Manufacturing imperfections lead to a deviation of the pixel transfer matrices from the ideal matrix and to variations between the pixels. Lane et al. (2022) calibrated the monochromatic version of the polarization-resolving cameras from the same manufacturer. They focused on the central pixels of the sensor and found that the transfer matrices are consistent across this sensor region and a single matrix can be applied to all pixels. In addition, the deviation between the measured matrices and the ideal matrix was small for the central pixel region with small incident angles which they considered.

The polarization-resolving cameras of specMACS are integrated into a housing with a window. This window can change the polarization state of the light passing through it and therefore must be considered in the polarization calibration. Its impact on the polarization can be described by the Mueller matrix of a linear diattenuator $\mathbf{M_{window}}$, which is given in Bass et al. (2010). The matrix depends on the incident angles on the window as well as the refractive index of the window and is computed for every pixel and every color. The refractive index for every color is obtained by integrating the wavelength-dependent refractive index of the window with the spectral response functions of the cameras. Moreover, the incident angles can be calculated using the geometric calibration. Figure 3.10 shows the 1,1 and 1,2 components of $\mathbf{M_{window}}$ for the red channel of both cameras. The 1,1 component describes the total transmission through the window, which is slightly reduced towards the corners with increasing incident angles on the window. $M_{\mathrm{window},\,1,2}$ specifies the impact of the window on the polarization.

In total, the transfer matrix is calculated with

$$\mathbf{A} = \mathbf{A_{ideal}}\mathbf{M_{window}} . \tag{3.8}$$

This transfer matrix does not include the lenses in front of the cameras. Since the lenses are in reality a combination of lenses whose exact design is not known to us, it was not possible

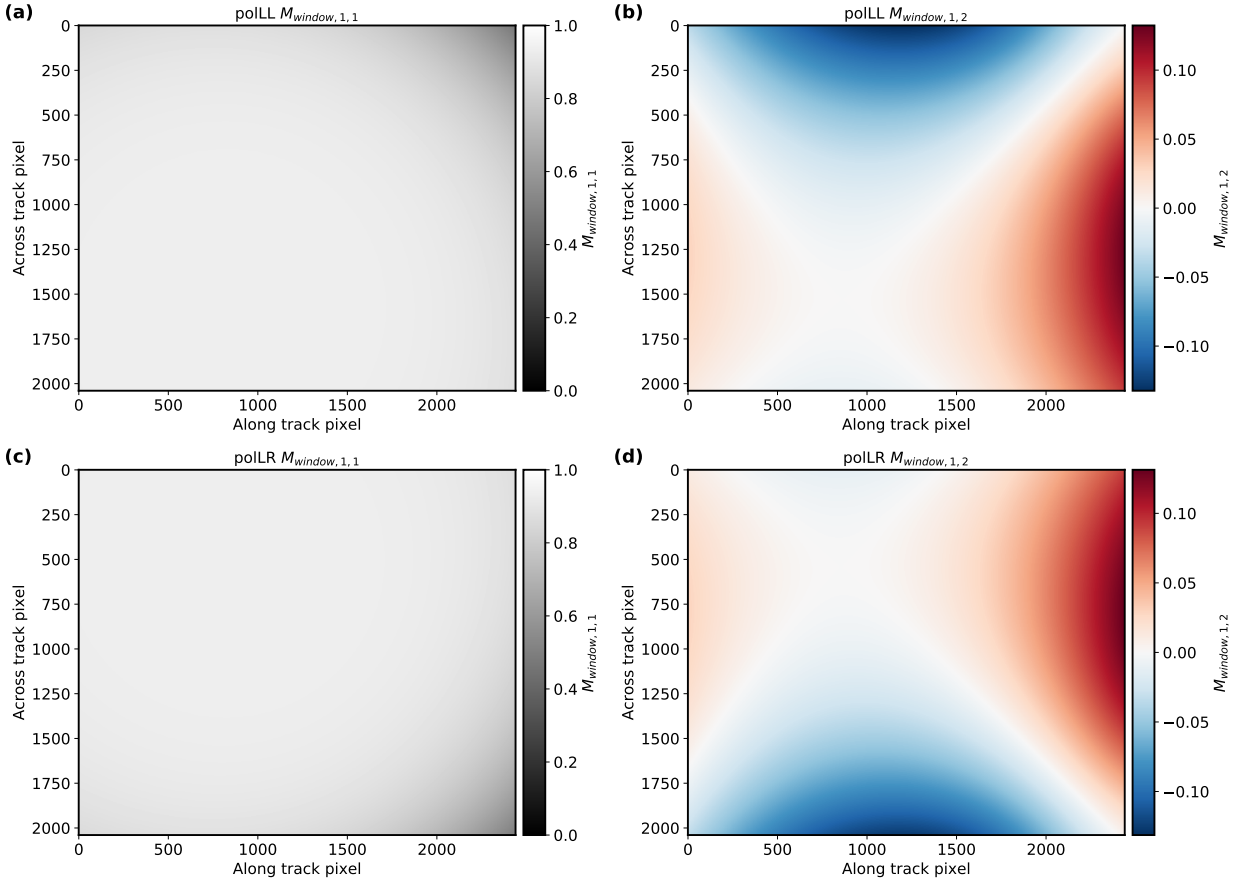

Figure 3.10: The 1,1 and 1,2 components of the Mueller matrix describing the window for the red channel of the polLL and polLR camera.

to include a theoretical Mueller matrix for the lenses as well. According to Lane et al. (2022), the choice of the camera lens has only little influence on the transfer matrices for the central pixel region of the camera where the incident angles of the rays are small. Thus, it is assumed that the theoretical model of the transfer matrices is a good approximation. However, lenses can introduce polarization aberrations, especially for larger incident angles towards the corner regions (Chipman et al., 2018). This effect is not included in the theoretical polarization calibration model. Because of that, the theoretical model was validated with a laboratory polarization calibration.

Laboratory polarization calibration

For the laboratory polarization calibration, calibration measurements were performed with the polarizer setup of the CHB. A linear polarizer (Moxtek UBB01A) was mounted at a motorized rotation stage between specMACS and the large integrating sphere. This rotatable polarizer has a contrast ratio larger than 1000 for incident angles up to $\pm 20°$. With respect to the measurement precision of the polarization cameras, the calibration

light source was thus considered as perfectly linearly polarized. The polarizer was rotated from −180 to 180° in steps of 15° and 50 frames were taken per angle and averaged. Due to the large field of view of the polarization-resolving cameras and the limited size of the polarizer, only a small part of the sensor was illuminated by the LIS with the polarizer. In order to cover at least large parts of the field of view, the entire instrument was tilted and measurements were taken for 32 different tilt angles in along-track and across-track direction and in nadir direction. Consequently, polarization measurements were achieved for 28.8 % of the pixels of the polLL camera and 29.6 % of the pixels of the polLR camera. Because of the size and the large weight of the specMACS instrument including the complete aircraft housing and environment control, tilting the instrument is very difficult, and it was not possible to obtain measurements for the entire field of view. The intensity of the sphere was monitored and stayed constant during the measurements.

The polarization calibration measurements were evaluated using the super-pixel calibration method. Since the output of the LIS after passing the polarizer was not known, normalized quantities were used similarly to Lane et al. (2022):

$$\boldsymbol{I}_\mathrm{n} - \boldsymbol{d}_\mathrm{n} = \mathbf{A}\boldsymbol{S}_\mathrm{n}, \tag{3.9}$$

with the normalized intensities $\boldsymbol{I}_\mathrm{n} = \frac{2}{I_0+I_{45}+I_{90}+I_{135}}\boldsymbol{I}$, the normalized dark signal $\boldsymbol{d}_\mathrm{n} = \frac{2}{I_0+I_{45}+I_{90}+I_{135}}\boldsymbol{d}$, and the normalized incoming Stokes vector

$$\boldsymbol{S}_\mathrm{n} = \begin{pmatrix} 1 \\ \cos 2\phi \\ \sin 2\phi \end{pmatrix}. \tag{3.10}$$

Here, ϕ is the polarization angle of the rotatable linear polarizer. With that, $\mathbf{A}$ could be fitted from the measured dark signal $\boldsymbol{d}_\mathrm{n}$ and intensities $\boldsymbol{I}_\mathrm{n}$ for every pixel using Eq. 3.9.

The Stokes vector and the transfer matrix are always defined relative to a reference plane. In connection with the polarization calibration, three different reference systems are distinguished. The laboratory reference system is defined by the plane containing the 0° axis of the linear polarizer between the large integrating sphere and the instrument and the normal of this polarizer. Moreover, the reference plane for the camera reference system for each camera is given by the x–z plane of the camera coordinate system with the x axis parallel to the 0° direction of the polarizers on the sensor and the z axis normal to the focal plane array of the camera. Finally, the Stokes vectors can be rotated from the camera reference system into the scattering plane. The scattering plane is the plane containing the vector of the incoming solar radiation and the viewing direction of each pixel. Sketches visualizing the different reference systems can for example be found in Eshelman and Shaw (2019). The transformation from the camera coordinate system to the scattering plane is known from the geometric calibration and varies between different observation geometries with different vectors of the incoming solar radiation. Thus, with the laboratory polarization calibration, transfer matrices in the camera reference system should be computed.

For that, the polarizer angles ϕ for the incoming Stokes vectors $\boldsymbol{S}_\mathrm{n}$ are defined relative to the 0° axis of the linear polarizer between the large integrating sphere and the instrument and the transfer matrices are first computed in the laboratory reference frame with the normalized super-pixel method described above. Therefore, the laboratory measurements for different tilt angles were comined into one laboratory reference system and Eq. 3.9 was solved in a least-squares sense similarly to Rodriguez et al. (2022) for the transfer matrices using the measured intensities and dark signal as well as the incoming Stokes vectors computed from the polarizer angles ϕ. Only illuminated pixels with viewing directions within ±20° perpendicular to the polarizer, where the polarizer can be considered perfect, were included. In addition, pixels with dirt or reflections on the window were excluded. With the resulting transfer matrices, Stokes vectors in the laboratory reference frame can be computed from measured intensities.

In a second step, the obtained transfer matrices were transformed from the laboratory reference system into the camera reference system. The direct determination of the rotation from the laboratory to the camera reference frame through the identification of the polarizer orientation visible in the measurements was not possible due to the angle-dependent shift introduced by the window, which is relevant at small distances. However, for single scattering, the U component of the Stokes vector is zero in the scattering plane due to symmetries. This fact was used to find the rotation from the laboratory to the camera reference frame using measurements taken during the EUREC^{4}A campaign (Stevens et al., 2021) by minimizing U along the scattering plane. Contributions from multiple scattering can in principle cause deviations of U from zero. To minimize the influence of multiple scattering, measurements from EUREC^{4}A without clouds and with a minimum amount of aerosol were chosen. The computed transfer matrices were applied to measurement data from the EUREC^{4}A campaign to compute Stokes vectors in the laboratory reference frame. Then, the obtained Stokes vectors were rotated with a single rotation matrix first from the laboratory into the camera reference system and next for every pixel from the camera reference system into the scattering plane. Since the transformation from the camera reference system to the scattering plane is known, it was possible to optimize for the rotation from the laboratory to the camera reference system by minimizing the absolute value of U along the scattering plane. With that, transfer matrices in the camera reference system were obtained for every measured pixel by applying this rotation matrix to the transfer matrices in the laboratory reference system obtained during the first step.

The mean and standard deviation of $\mathbf{A}$ across all measured sensor pixels for the red channel of the polLL and polLR camera are

$$\mathbf{A}_\mathrm{polLL,red} = \frac{1}{2}\begin{pmatrix} 0.988 & 0.972 & 0.012 \\ 1.010 & -0.021 & 0.986 \\ 0.991 & -0.976 & -0.014 \\ 1.006 & 0.025 & -0.984 \end{pmatrix} \pm \begin{pmatrix} 0.012 & 0.008 & 0.058 \\ 0.005 & 0.059 & 0.007 \\ 0.012 & 0.005 & 0.057 \\ 0.006 & 0.060 & 0.007 \end{pmatrix} \tag{3.11}$$

and

$$\mathbf{A}_{\mathrm{polLR,red}} = \frac{1}{2}\begin{pmatrix} 0.989 & 0.972 & -0.019 \\ 1.007 & 0.019 & 0.993 \\ 0.991 & -0.978 & 0.016 \\ 1.010 & -0.012 & -0.991 \end{pmatrix} \pm \begin{pmatrix} 0.010 & 0.008 & 0.057 \\ 0.005 & 0.060 & 0.007 \\ 0.010 & 0.005 & 0.059 \\ 0.005 & 0.059 & 0.007 \end{pmatrix}. \tag{3.12}$$

Other channels gave similar results. These transfer matrices include the impact of the entire optical system on the polarization including the window and the lenses. Since normalized intensities were used, they do not contain variations in absolute transmission across the sensor and absolute radiometric pixel response non-uniformity, which can be calibrated separately with a flat-field calibration. The deviation of the computed transfer matrices from the ideal matrix is small, as is the standard deviation of the transfer matrices across the sensor pixels. This indicates that the assumption of the ideal transfer matrix in the theoretical polarization model does not introduce large calibration errors.

A first quality check of the super-pixel polarization calibration is the reconstruction error, which is the relative deviation of the reconstructed Stokes vectors $\boldsymbol{S}_{\mathrm{n,r}} = \mathbf{A}^{-1}\left(\boldsymbol{I}_{\mathrm{n}} - \boldsymbol{d}_{\mathrm{n}}\right)$ using the measured intensities and the computed inverse transfer matrix from the incoming Stokes vectors $\boldsymbol{S}_{\mathrm{n}}$. The mean reconstruction error across all pixels was negligible for the I component of the Stokes vector for both cameras. For the Q component it amounted to $(-0.37 \pm 0.60)\,\%$ for the red channel of the polLL camera, $(-0.25 \pm 0.42)\,\%$ for the red channel of the polLR camera, and values on the same order of magnitude for the other color channels of both cameras. In addition, the relative calibration error introduced by Lane et al. (2022) was computed for the red, green, and blue color channels of the polLL and polLR cameras. The error is defined as

$$\mathrm{Err} = \frac{2}{\sqrt{3}}\|\mathbf{A} - \mathbf{A}_{\mathbf{ideal}}\|_{\mathrm{F}}, \tag{3.13}$$

where $\|\ \|_{\mathrm{F}}$ is the Frobenius norm. It gives the upper limit of the error which is made when a polarization-resolving camera is used uncalibrated by applying the ideal transfer matrix and if the light is totally linearly polarized. For partially polarized light, the error is smaller (Lane et al., 2022). The relative calibration error of the mean transfer matrix for the red, green, and blue color channel amounts to 3.5 %, 3.5 %, and 4.6 % for the polLL camera and 3.1 %, 3.1 %, and 4.0 % for the polLR camera. These small errors indicate that the cameras are close to ideal cameras concerning polarization and that the error introduced by using the ideal transfer matrix instead of the transfer matrices obtained from the laboratory polarization calibration is small. The polarization calibration error when using the theoretical polarization camera model introduced in the previous section is expected to be even smaller, since the model additionally includes the window. Moreover, polarization measurements of clouds are usually only partially polarized, leading to a reduced relative polarization calibration error. Hence, the polarization calibration results from the theoretical model covering the entire field of view will be used in the following.

Vignetting correction

Vignetting describes the intensity fall-off from pixels in the center towards pixels at the edges of the sensor. On the one hand, the brightness of off-axis image points is naturally reduced due to the geometry of the optical system. On the other hand, optical vignetting is caused by optical components like lenses. Off-axis incident light is blocked by physical components like the aperture and the edge of a lens, leading to an intensity decrease for rays with larger angles towards the sensor edges (Gross, 2011; Bass et al., 2010). Vignetting can be corrected for by applying a flat-field model F, which approximates the vignetting functions. The flat-field-corrected signal can be computed from the radiometric signal with

$$S_{\mathrm{F}} = S_0/F. \tag{3.14}$$

Here, the parabolic vignetting model by Kordecki et al. (2016), defined as

$$F = a_x x^2 + b_x x + a_y y^2 + b_y y + c, \tag{3.15}$$

was used since it showed a better agreement with the observed vignetting compared to typical radial models for F. x and y are the pixel coordinates. All other parameters have to be determined from measurements of a uniformly illuminated scene. For that, flat-field measurements were performed using the LIS. Stokes vectors were computed from the dark-signal-corrected intensities with the transfer matrices from the polarization calibration and the normalized I component of the Stokes vector was used to fit the flat-field model for every color channel separately. Again, only the lower hemisphere of the LIS was included in the analysis, and pixels with reflections and dirt on the window were excluded. Figures 3.11 and 3.12 display the results of the red channel for the polLL and polLR camera, respectively. All other channels showed a similar behavior. The mean deviation between the model and the measurements for the red, green, and blue channel is $(0.0 \pm 1.2)\,\%$, $(0.0 \pm 1.3)\,\%$, and $(0.0 \pm 1.4)\,\%$ for polLL and $(0.0 \pm 1.3)\,\%$, $(-0.1 \pm 1.3)\,\%$, and $(0.0 \pm 1.3)\,\%$ for polLR. Due to the large field of view of the instrument compared to the size of the LIS and the large size and weight of the instrument, it was not possible to perform flat-field measurements covering the entire field of view of the cameras with the calibration setup at the CHB. Because of that, the model was chosen for the vignetting correction in order to obtain a vignetting correction for the entire field of view despite some non-negligible residuals between the vignetting model and the flat-field measurements. The residuals include inhomogeneities of the LIS as well as deviations of the photoresponse non-uniformity of the cameras from the vignetting model. For future calibrations, flat-field measurements covering the entire field of view could be taken and directly be used for a more accurate flat-field correction which, for example, also includes pixel-to-pixel variations. In addition, possible inhomogeneities of the LIS could be accounted for by taking several measurements while rotating the tilted instrument above the LIS.

Absolute radiometric response

Finally, the dark-signal-corrected, exposure-time-normalized, and flat-field-corrected Stokes vectors have to be converted into absolute radiances. In general, the absolute radiance L in

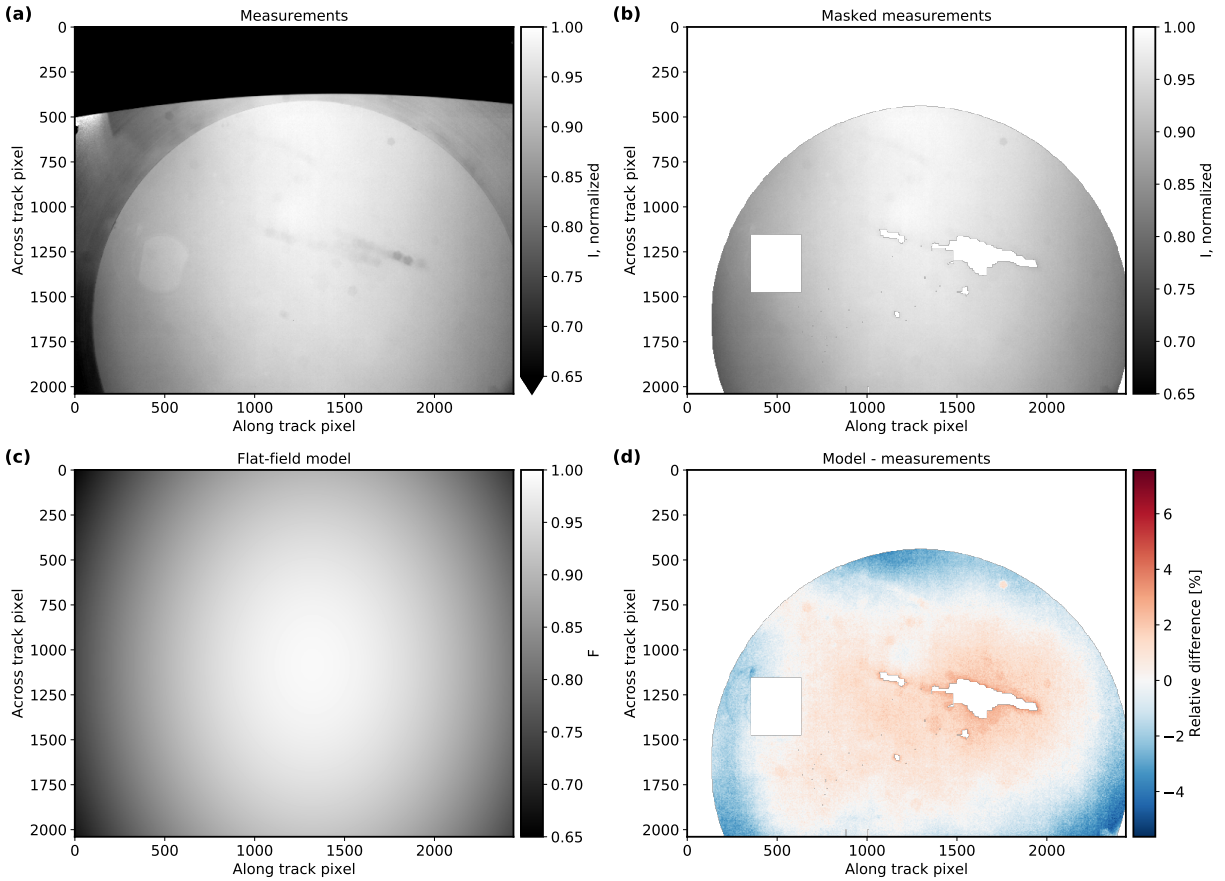

Figure 3.11: Flat-field model results for the red channel of the polLL camera. **(a)** Mean normalized, dark-signal-corrected total intensity. **(b)** Part of measurement in panel **(a)** used in the vignetting correction (removed LIS upper hemisphere, reflections, and dirt-affected areas). **(c)** Vignetting model fitted to the measurements. **(d)** Relative difference between vignetting model and measurements.

$\mathrm{mW\,m^{-2}\,nm^{-1}\,sr^{-1}}$ is computed from the normalized signal s_n in $\mathrm{DN\,s^{-1}}$ with the absolute radiometric response R (Ewald et al., 2016):

$$L = R^{-1} \cdot s_\mathrm{n}. \tag{3.16}$$

Here, the normalized signal is given by the exposure-time-normalized and vignetting-corrected Stokes vector

$$\boldsymbol{s}_\mathrm{n} = \boldsymbol{S}_0 / \left(F t_\mathrm{exp}\right), \tag{3.17}$$

with $\boldsymbol{S}_0 = \mathbf{A}^{-1}(\boldsymbol{I} - \boldsymbol{d})$. In order to determine the absolute radiometric response, measurements of the LIS were used again. 1000 frames were averaged and the exposure-time-normalized, vignetting-corrected Stokes vectors were computed. The measured output spectrum of the LIS was integrated with the spectral response functions to obtain radiance values L for every color channel. Then, the absolute radiometric response R was computed

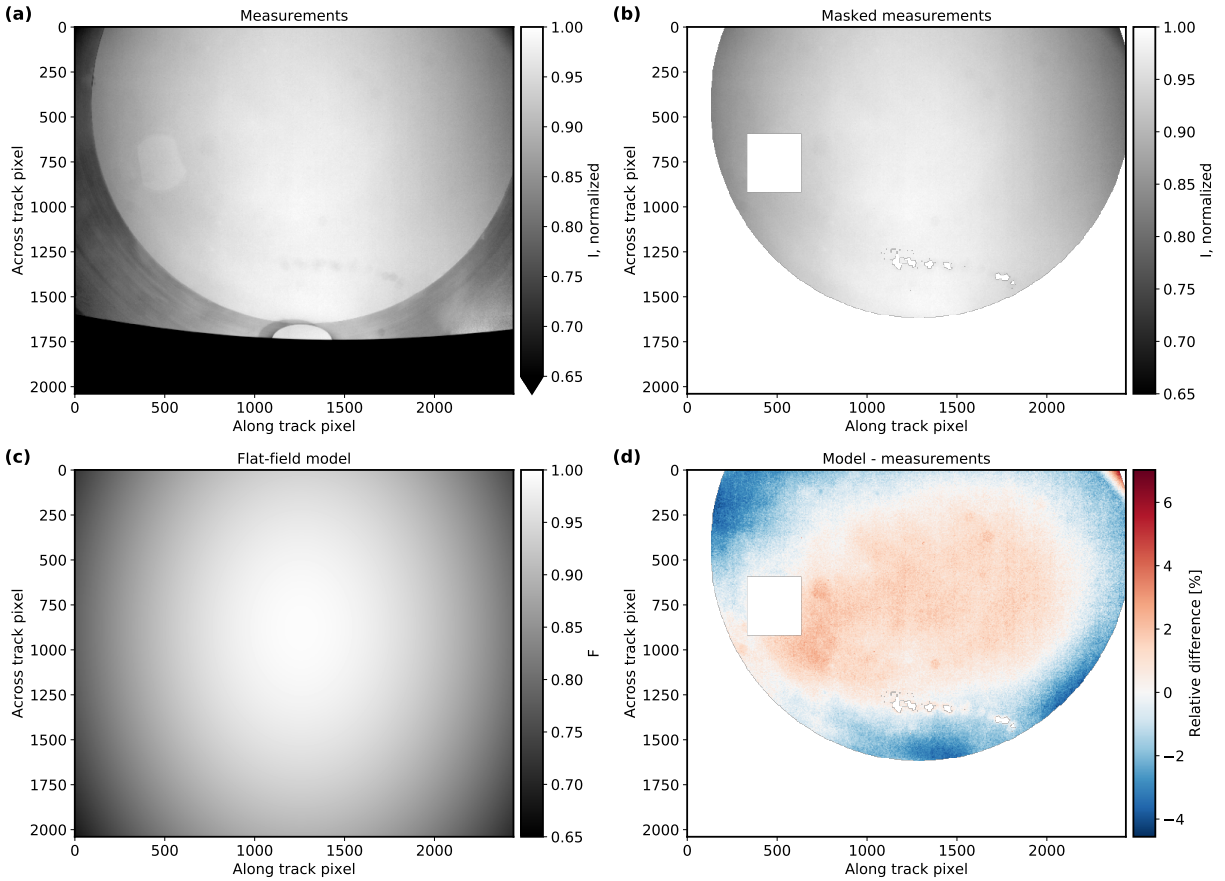

Figure 3.12: Flat-field model results for the red channel of the polLR camera. **(a)** Mean normalized, dark-signal-corrected total intensity. **(b)** Part of measurement in panel **(a)** used in the vignetting correction (removed LIS upper hemisphere, reflections, and dirt-affected areas). **(c)** Vignetting model fitted to the measurements. **(d)** Relative difference between vignetting model and measurements.

using only the I component of the normalized Stokes vectors $s_{\mathrm{n},0}$:

$$R = \frac{s_{\mathrm{n},0}}{L}. \tag{3.18}$$

Assuming that the photoresponse non-uniformity had already been accounted for by applying the vignetting correction, a single absolute radiometric response was computed for all pixels of a color channel by taking the mean across all pixels of the channel. Table 3.2 summarizes the resulting values of and uncertainties in the absolute radiometric response R for the red, green, and blue color channels of the polLL and polLR camera. The relative uncertainties in the absolute radiometric response are 1.6 %, 2.2 %, and 3.0 % for the red, green, and blue channels of the polLL camera and 1.6 %, 1.9 %, and 3.3 % for the polLR camera. These uncertainties include the standard deviation of R across all pixels, the uncertainty in the output of the LIS (Rammeloo and Baumgartner, 2023) as well as the spatial non-uniformity of the LIS, and the uncertainty in the spectral response functions. The photoresponse non-uniformity remaining after the vignetting correction is contained in the standard deviation

	Red	Green	Blue
polLL	$44\,120 \pm 706$	$60\,823 \pm 1367$	$31\,607 \pm 950$
polLR	$46\,549 \pm 766$	$65\,471 \pm 1247$	$34\,559 \pm 1137$

Table 3.2: Absolute radiometric response R for the different color channels of the polLL and polLR camera in $\mathrm{DN\,s^{-1}\,(mW\,m^{-2}\,nm^{-1}\,sr^{-1})^{-1}}$ with uncertainties.

of R across all pixels. The systematic difference between the absolute radiometric response of the two cameras could come from the manual aperture setting.

In summary, absolute calibrated Stokes vectors in the camera reference system can be calculated from the interpolated measured intensities via

$$\boldsymbol{S} = \mathbf{A^{-1}}(\boldsymbol{I} - \boldsymbol{d})/(RFt_{\mathrm{exp}})\,. \tag{3.19}$$

For further application of the measured polarization data to retrievals like the retrieval by Pörtge et al. (2023), the Stokes vector of each pixel is rotated into its scattering plane with the Mueller rotation matrix $\mathbf{M_{rot}}$ (e.g., Mishchenko et al., 2002):

$$\boldsymbol{S} = \mathbf{M_{rot}}\mathbf{A^{-1}}\,(\boldsymbol{I} - \boldsymbol{d})\,/\,(RFt_{\mathrm{exp}})\ . \tag{3.20}$$

Total radiometric uncertainty

The estimation of the total radiometric uncertainty was achieved similarly to Ewald et al. (2016) by applying Gaussian error propagation. The uncertainty in the radiometric signal S_0 (here $\boldsymbol{I}_0 = \boldsymbol{I} - \boldsymbol{d}$) is given by the uncertainties in the dark signal σ_{d} and the instantaneous noise of the signal $\sigma_{\mathcal{N}}$:

$$\sigma_{\boldsymbol{I}_0} = \sqrt{\sigma_{\mathrm{d}}(t_{\mathrm{exp}}, T)^2 + \sigma_{\mathcal{N}}^2}. \tag{3.21}$$

The uncertainty in the dark signal consists of the dark-signal drift due to the temperature and exposure time dependence and the standard deviation of the dark signal across all sensor pixels as discussed in Sect. 3.1.3. The noise is a function of the signal and given in Sect. 3.1.3. Next, the uncertainty in the normalized and vignetting-corrected Stokes vectors can be computed. It consists of the uncertainty in the radiometric signal $\sigma_{\boldsymbol{I}_0}$, the uncertainty due to the sensor non-linearity discussed in Sect. 3.1.3, the uncertainty in the polarization calibration in Sect. 3.1.3, and the uncertainty in the vignetting correction in Sect. 3.1.3. The uncertainty in the polarization calibration is composed of the uncertainty in the transfer matrices σ_{A} and a rotation uncertainty in the Stokes vectors σ_{rot} due to the uncertainty in the geometric calibration when rotating the Stokes vectors into the scattering plane.

$$\frac{\sigma_{\boldsymbol{s}_{\mathrm{n}}}}{\boldsymbol{s}_{\mathrm{n}}} = \sqrt{\left(\frac{\sigma_{\boldsymbol{I}_0}}{\boldsymbol{I}_0}\right)^2 + \left(\frac{\sigma_{\mathrm{nonlin}}}{\boldsymbol{s}_{\mathrm{n}}}\right)^2 + \left(\frac{\sigma_{\mathrm{A}}}{\boldsymbol{s}_{\mathrm{n}}}\right)^2 + \left(\frac{\sigma_{\mathrm{rot}}}{\boldsymbol{s}_{\mathrm{n}}}\right)^2 + \left(\frac{\sigma_{\mathrm{F}}}{F}\right)^2} \tag{3.22}$$

The upper limit of the uncertainty in the transfer matrices was estimated with the deviation of the laboratory transfer matrices from the ideal transfer matrix using the error defined

by Lane et al. (2022). This is a very conservative estimate of the upper limit, the impact of the window in the transfer matrices was included and the applied transfer matrices are thus more accurate than the ideal transfer matrix alone. Additionally, typical observations of clouds are only partially polarized, leading to a smaller relative polarization calibration error. The rotation error is zero for the I component of the Stokes vector, since the total intensity is invariant under rotations, but it is non-zero for Q. Finally, the total radiometric uncertainty is given by the combination of the uncertainty in the normalized Stokes vectors and the absolute radiometric response:

$$\frac{\sigma_{\boldsymbol{S}}}{\boldsymbol{S}} = \sqrt{\left(\frac{\sigma_{\boldsymbol{s}_\mathrm{n}}}{\boldsymbol{s}_\mathrm{n}}\right)^2 + \left(\frac{\sigma_\mathrm{R}}{R}\right)^2}. \tag{3.23}$$

The uncertainty estimation was done for every color channel. Typical values of the total radiometric uncertainty for the I and Q components of the Stokes vector are given in Table 3.3. The largest contribution to the total radiometric uncertainty is due to the polarization calibration. In general, total radiometric uncertainty is larger towards the corner regions and smaller in the center of the image. Due to the larger incident angles, the impact of the lenses as well as the window on polarization increases towards the corners, leading to an increased uncertainty in the polarization calibration compared to the center region.

Another important quantity for polarization applications is the DOLP which can be computed from the Stokes vector with $\mathrm{DOLP} = \sqrt{Q^2 + U^2}/I$. Its relative uncertainty was computed via Gaussian error propagation from the uncertainties above. For Stokes vectors rotated into the scattering plane, the U component of the Stokes vector is much smaller than Q. Thus, neglecting the U component, the relative uncertainty in the DOLP can be calculated with $\sigma_\mathrm{DOLP}/\mathrm{DOLP} = \sqrt{(\sigma_I/I)^2 + (\sigma_Q/Q)^2}$. Since the degree of linear polarization is invariant under rotations and independent of the absolute radiometric response, its uncertainty was computed from the relative radiometric uncertainties in I and Q in Eq. 3.22, neglecting the uncertainty in the absolute radiometric calibration and the rotation error. It amounts to 5.4 %, 5.4 %, and 6.9 % for the red, green, and blue channels of polLL and 4.8 %, 4.9 %, and 6.2 % for polLR for the same typical signal level and DOLP as in Table 3.3. The uncertainties in the DOLP are large compared to other polarimetric instruments like RSP, AirHARP, or AirMSPI (Knobelspiesse et al., 2019; Diner et al., 2013). However, the uncertainties in the transfer matrices are a very conservative estimate, as discussed above. A substantial part of this error might actually be due to the difficult calibration procedure, and therefore the instrument error might be over-estimated, but there are no means to decide if this is the case. In addition, Lane et al. (2022), who calibrated the monochromatic version of the same sensor, found maximum measurement errors of 3 % to 8 % for the DOLP even though they focused on the central pixel region where the errors are expected to be smaller. In general, the uncertainties could be reduced by a more accurate laboratory calibration with a setup that allows for taking polarization and flat-field calibration measurements for the entire field of view of the cameras.

			Red	Green	Blue
polLL	Relative radiometric uncertainty $\frac{\sigma_{s_\mathrm{n}}}{s_\mathrm{n}}$	I	3.8 %	3.8 %	4.9 %
		Q	3.8 %	3.9 %	4.9 %
	Absolute radiometric uncertainty $\frac{\sigma_S}{S}$	I	4.1 %	4.4 %	5.7 %
		Q	4.1 %	4.5 %	5.8 %
polLR	Relative radiometric uncertainty $\frac{\sigma_{s_\mathrm{n}}}{s_\mathrm{n}}$	I	3.4 %	3.4 %	4.4 %
		Q	3.5 %	3.5 %	4.4 %
	Absolute radiometric uncertainty $\frac{\sigma_S}{S}$	I	3.8 %	3.9 %	5.5 %
		Q	3.8 %	4.0 %	5.5 %

Table 3.3: Relative radiometric uncertainty $\frac{\sigma_{s_\mathrm{n}}}{s_\mathrm{n}}$ and absolute radiometric uncertainty $\frac{\sigma_S}{S}$ of the red, green, and blue color channels of the polLL and polLR cameras for a typical signal level of 30 000 DN and a typical value of the DOLP of 0.5 as in the cloudbow region.

3.1.4 Calibration validation

Finally, the calibration was applied to measurement data to compute georeferenced, absolute calibrated Stokes vectors rotated into the scattering plane. Moreover, the results are compared to simulations in order to validate the calibration. The sunglint originates from specular reflection of sunlight on the rough ocean surface. Observations of the sunglint are very well suited for a validation of the calibration with simulations, since it is a known target. Sunglint observations have for example been used for the in-flight calibration of POLDER (Toubbe et al., 1999). Figure 3.13a–d show an example sunglint observation of the polLR camera measured on 22 January 2020 at 16:20 UTC west of Barbados above the tropical Atlantic Ocean during the EUREC^{4}A field campaign. The sunglint is visible as a maximum in the total intensity in panel (a) and minimum in Q in panel (c) around the specular direction. The U component in panel (d) is much smaller than Q, as is expected for Stokes vectors rotated into the scattering plane.

Polarized simulations of this specific observation were performed with libRadtran (Mayer and Kylling, 2005; Emde et al., 2016) and the Monte Carlo solver MYSTIC (Mayer, 2009; Emde et al., 2010). For the ocean surface, the bidirectional reflectance distribution function (BRDF) by Cox and Munk (1954a,b) was used, which was extended to polarization by considering the polarization-dependent Fresnel reflectivities. The sunglint shape and maximum intensity depend on wind speed and wind direction. The wind speed affects the width of the sunglint and can be fitted to measurements. For that, several simulations were performed for different wind speeds and the best-fit wind speed was determined by a least-squares fit to the observation data along the scattering plane. Wind direction was taken from data of the METEOR ship, which was measuring close to the location of the HALO aircraft at the time of the observation. Since the measurement was taken above the tropical Atlantic Ocean, the tropical maritime aerosol mixture from the OPAC library (Hess et al., 1998) was assumed and aerosol mass concentrations for the mixture were

derived from data of the WALES lidar (Wirth et al., 2009), which was also measuring on board HALO using the method by Gutleben (2020). An example observation with only small amounts of aerosol was chosen to reduce the uncertainty due to uncertainties in the retrieval and measurements of aerosol mass concentrations. In order to obtain simulations for the different color channels, a spectrum was simulated and integrated with the spectral response functions derived during the laboratory calibration. To exclude situations with cirrus clouds above the HALO aircraft during the observation, the BACARDI cloud flag (Ehrlich et al., 2021) was used. An undetected cirrus cloud between the sun and the aircraft would lead to a reduced sunglint intensity and discrepancies between observations and simulations.

Simulation results for the observation in Fig. 3.13a–d are shown in Fig. 3.13e–h. In general, the simulation and observation agree well. Both simulated and observed Stokes vectors are rotated into the scattering plane for comparison. The Q component is much larger than the U component, as is expected from symmetries. Differences between the observation and the simulation and their mean and standard deviation across all pixels can be seen in Fig. 3.13i–l. The mean absolute difference between the observation and simulation is smaller than $0.7\,\mathrm{mW\,m^{-2}\,nm^{-1}\,sr^{-1}}$ for all Stokes vector components. Mean relative differences in the I and Q components are $-1.1\,\%$ and $3.0\,\%$, respectively. Thus, the observation and simulation agree within the expected uncertainties. The small-scale structures which are visible in the sunglint observations are due to the orientation of single waves on the ocean surface, which, of course, is not represented in the simulation. The I component of the measured Stokes vectors is smaller than the simulations around the sunglint maximum, and the Q component in the same region is larger in the measurements compared to the simulations while the differences between simulated and observed I and Q components are small outside the sunglint; see Fig. 3.13i and k. This can be explained by the uncertainty in the wind speed and wind direction for the ocean BRDF in the simulations, since they affect the sunglint maximum intensity. An error in the absolute radiometric calibration would lead to differences across the entire field of view also outside the sunglint. The degree of linear polarization shows in general only small differences of 0.02 ± 0.03 with the largest values towards the corners. Since the degree of linear polarization is independent of the absolute calibration, the deviations between measurements and simulations are due to the uncertainty in the polarization calibration or a deviation of the assumed atmospheric constituents in the simulation from the observed ones which affect the polarization in the simulations. The differences could for example be explained by a small polarization impact of the lens in front of the camera or of the on-chip microlenses, which are not included in the theoretical polarization calibration. A more accurate laboratory calibration of the entire field of view including the corners would be necessary to quantify their impact. Due to the size and weight of the instrument, it was not possible to take calibration measurements for the corner regions with the setup at the CHB. In addition, deviations of the assumed aerosol properties from the measured ones could have an impact. The larger deviations of U from zero in the observations compared to the simulations can also be explained by the uncertainty in the polarization calibration and the aerosol properties with the polarization calibration being the dominant factor. In addition, uncertainties in the geometric calibration

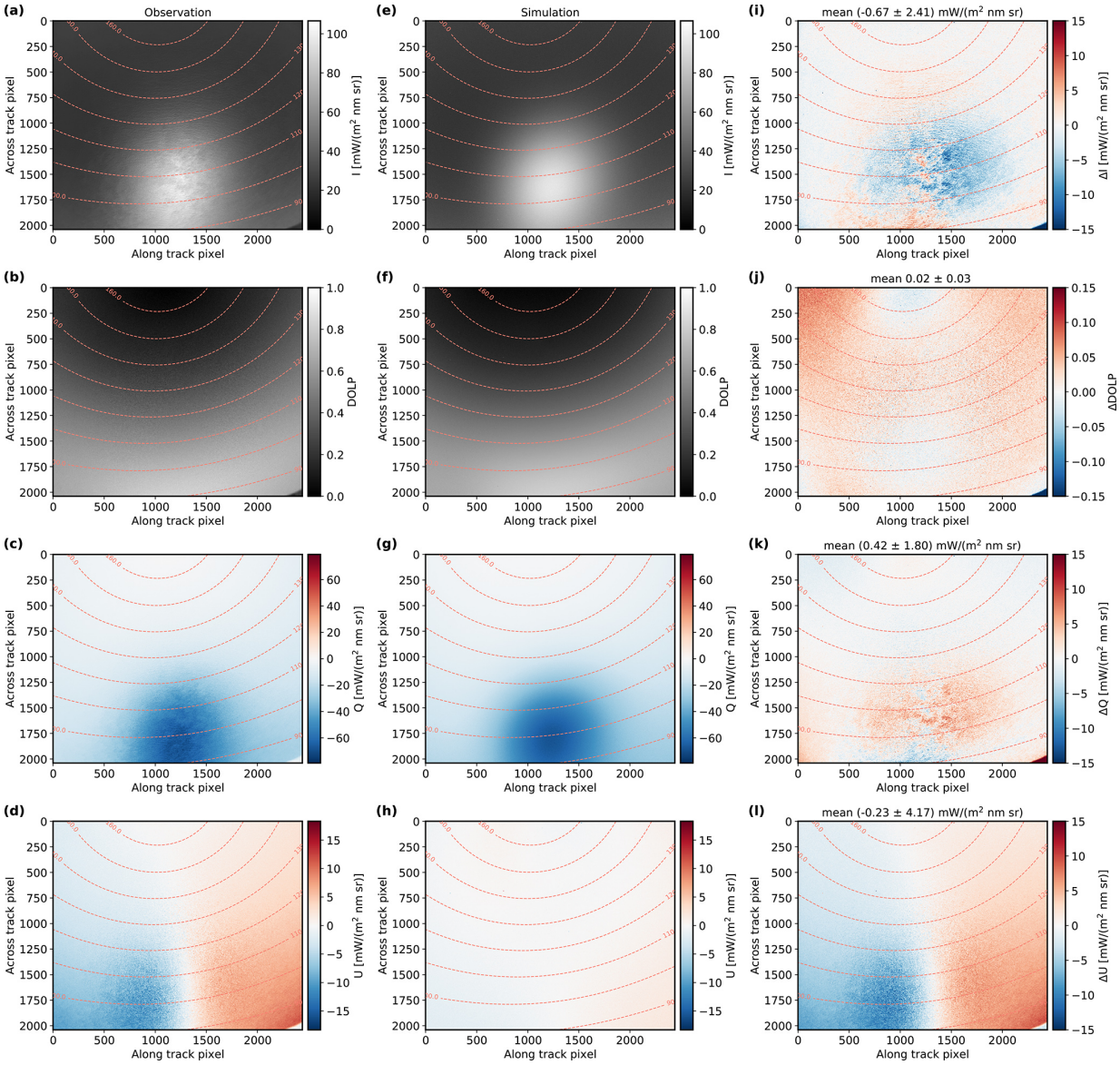

Figure 3.13: **(a–d)** Example sunglint observation of the green channel of the polLR camera on 22 January 2020 at 16:20 UTC. **(e–h)** Sunglint simulation corresponding to the observation in panels **(a)**–**(d)**. **(i–l)** Absolute difference in the sunglint observation and simulation in panels **(a)**–**(d)** and **(e)**–**(h)**. Mean and standard deviation of the absolute differences are given in the respective titles. **(a, e, i)** Total intensity. **(b, f, j)** Degree of linear polarization, **(c, g, k)** Q component of the Stokes vector. **(d, h, l)** U component of the Stokes vector. The dashed lines indicate scattering angles.

lead to uncertainties in the rotation into the scattering plane, which could cause deviations from zero. However in summary, the observation and simulation agree within the expected uncertainties. For more accurate results, a laboratory polarization calibration for the entire field of view is necessary to include the polarization impact of all optical components. Moreover, the spatial field of the dark signal could be used instead of a single value for the dark-signal correction to further reduce the calibration uncertainties for retrievals of,

e.g., aerosol or land properties with very small signal levels. In addition to the validation of the laboratory calibration, the sunglint observations and simulations could also be used for an in-flight calibration, which is very useful to continuously monitor the stability of the cameras between laboratory calibrations.

3.1.5 Discussion

In 2019, before the EUREC^{4}A field campaign, the hyperspectral cameras of specMACS were complemented by two 2D RGB polarization-resolving cameras. The two polarization-resolving cameras have a large combined field of view of about $91° \times 117°$ (along-track $\times$ across-track) and high angular and spatial resolution. In this work, a complete calibration and characterization of the polarization-resolving cameras was performed and the calibration of the VNIR spectrometer from Ewald et al. (2016) was repeated. To this end, calibration measurements at the Calibration Home Base. Concerning the VNIR camera, no significant differences between the calibration from 2016 and the new calibration were found.

With the calibration of the polarization-resolving cameras, georeferenced, absolute calibrated Stokes vectors rotated into the scattering plane can be obtained from the raw data. The geometric calibration of the polarization-resolving cameras included a chessboard calibration for the determination of the camera model as well as a method for georeferencing. In addition, a radiometric calibration of the two cameras was completed. The dark signal was characterized to account for 0.057 % of the signal for typical signal levels with a small spatial variability across the sensor pixels, exposure time dependency, and temperature dependency of in total 0.004 % and 0.008 %. Moreover, the noise characteristics were captured well by the Poisson model and the non-linearity of the sensor was found to be below 1 %. Furthermore, the spectral response for every channel was computed from the calibration measurements and a polarization calibration was performed. For the polarization calibration, a theoretical camera model was used, which was validated with a laboratory calibration. Flat-field measurements were made and evaluated to obtain a vignetting correction. Finally, an absolute radiometric calibration of the cameras was carried out and the total radiometric uncertainty was calculated, which ranges between 3.8 % and 5.8 % for the different channels of the two cameras for typical signal levels. The uncertainty is dominated by the uncertainty in the polarization calibration and increases from the center of the sensor towards the corners.

Afterward, the calibration was applied to measurement data from the EUREC^{4}A campaign and validated with simulations. For that, observations of the sunglint, which is a well-characterized target, were used and the observations were compared to polarized radiative transfer simulations of the same measurement scene. This method could also be used for an in-flight calibration of the polarization-resolving cameras to continuously monitor the stability of the sensor in between laboratory calibrations. Agreement between observations and simulations within the characterized accuracy was found and thus the calibration was validated.

Nevertheless, there are some possible improvements that could be realized in the future. These include an improved polarization calibration of the polarization-resolving cameras

of specMACS. Especially in the corners of the sensor, the calibration uncertainties are high, and calibration artifacts can be observed in some polarization measurements. Due to technical reasons and the large size and weight of the specMACS instrument, it was not possible to perform polarization calibration measurements for the entire field of view of the sensor at the CHB, and a theoretical polarization calibration model had to be applied for this purpose. In the future, polarization calibration measurements should be taken at a calibration facility that allows for the entire field of view of the sensor to be characterized. A second issue is related to the georeferencing of the specMACS measurements. For this, accurate information about the location and, in particular, the orientation of the instrument and hence the aircraft are needed. This data is provided by BAHAMAS. However, the BAHAMAS sensors are located in the front of the aircraft, while specMACS is integrated in the boiler room in the rear part. Stretching and bending of the aircraft during a flight leads to increased uncertainties of the aircraft attitude measurements and thus the georeferencing for specMACS. These uncertainties could be reduced by installing an additional inertial measurement unit, such as BAHAMAS, in the rear part of the aircraft. Moreover, if parts of the specMACS instrument have to be replaced in the future, the addition of a polarization channel at longer wavelengths should be considered. These wavelengths are less affected by Rayleigh scattering, allowing for improved retrieval results.

3.2 The HALO–$(\mathcal{AC})^3$ measurement campaign

The data used in this work was measured during the airborne HALO–$(\mathcal{AC})^3$ campaign (Wendisch et al., 2024; Ehrlich et al., 2025), which took place in March and April 2022 in Kiruna and Svalbard. The focus of the campaign was to study air mass transformations during meridional transports of air masses into and out of the Arctic, such as cold air outbreaks and warm air intrusions. The aim was to collect a comprehensive observational dataset that can be used to constrain models and improve the representation of processes relevant to the Arctic in numerical models.

For this, the HALO aircraft (Krautstrunk and Giez, 2012), based in Kiruna, operated together with the Polar 5 (P5) and Polar 6 (P6) aircraft (Wesche et al., 2016), based in Longyearbyen at Svalbard. HALO was equipped with its remote sensing setup (Stevens et al., 2019) including radar and lidar measurements, a thermal imager, the hyperspectral and polarized imaging system specMACS, and dropsondes. In addition, the P6 aircraft conducted in situ measurements in strong coordination with the P5 aircraft, which also contained remote sensing instrumentation. Moreover, there were several research flights with coordination of all three aircraft. Data from the different instruments of all aircraft are published on PANGAEA (Ehrlich et al., 2025).

Overall, the campaign followed a quasi-Lagrangian sampling strategy. Trajectory calculations were employed for the flight planning to follow and sample the same air masses multiple times. Measurements were performed above open ocean and above sea ice to contrast the different surface conditions. The measurement flights covered mostly the Greenland and Norwegian Seas, the Fram Strait, and went up to the central Arctic. Figure 3.14 shows an

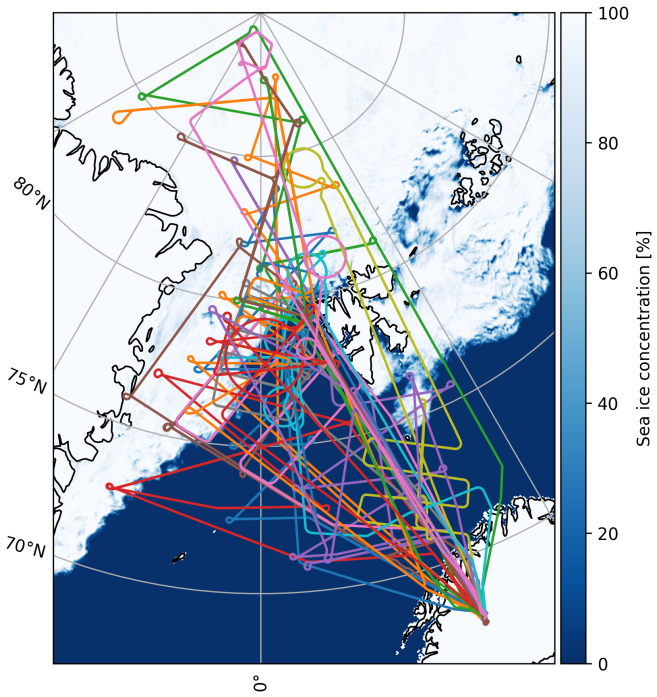

Figure 3.14: Overview of all flight tracks of the HALO aircraft during the HALO–$(\mathcal{AC})^3$ measurement campaign. The contours indicate the sea ice concentration from the combined AMSR2-MODIS dataset (Ludwig et al., 2020) on 2022-04-01 in the middle of the campaign.

overview of all flight tracks of the HALO aircraft.

3.3 Forward operator for polarized 3D radiative transfer

This section was already published in Weber et al. (2025c).

In general, clouds have a complex three-dimensional geometry, and cloud properties vary vertically and horizontally. This complex 3D structure leads to different 3D radiative effects due to horizontal transfer of radiation. The finite extent of clouds allows, for example, for the escape of radiation through the cloud sides on the one hand and side illumination effects on the cloud side oriented towards the incoming solar radiation on the other hand. In addition, variations of cloud top inclination relative to the sun lead to different projected areas and thus radiation enhancements or reductions, including shadowing effects. Three-dimensional radiative effects can influence radiation on a local level as well as affect larger areas. They can lead to both roughening and smoothing of the brightness field (e.g., Marshak et al., 1995; Várnai and Marshak, 2003). The causes and impacts of those different 3D effects were studied quantitatively, for example, by Várnai and Marshak (2003). 3D radiative effects

may also include effects due to spatial variations of microphysical properties of clouds, like the cloud droplet or ice crystal size. The work presented in the following, however, focuses on 3D radiative effects due to cloud geometry.

Realistic three-dimensional radiative transfer simulations are very expensive, so 1D plane-parallel clouds in the independent column approximation (ICA) are assumed for most operational retrievals of cloud properties and also with model data. In the ICA, every pixel is treated independently and represented by a plane-parallel cloud. However, Di Girolamo et al. (2010) found that the plane-parallel assumption was consistent with only 24 % of the observed reflectances from satellite instruments for solar zenith angles smaller than 60° and with even less for larger solar zenith angles. Due to this assumption and the neglect of 3D radiative effects, there are significant biases in typical bispectral retrievals (Nakajima and King, 1990) of optical thickness (e.g., Várnai and Marshak, 2002) and effective radius (Marshak and Davis, 2005; Vant-Hull et al., 2007).

Polarization is, in general, less influenced by three-dimensional radiative effects because it is dominated by single scattering. However, 3D radiative effects can still have a non-negligible effect on polarization measurements. Cornet et al. (2010), for example, studied the influence of 3D cloud geometry on polarized reflectances for cirrus clouds and found non-negligible biases also for the polarization signal for high spatial resolutions of 80 m as well as for low resolutions of 10 km.

There are different approaches to correcting retrieval results or simulated radiances for three-dimensional radiative transfer effects. Alexandrov et al. (2024) developed a correction based on the aspect ratio of the observed cloud to correct for retrieval errors due to 3D effects in the cloud optical thickness values retrieved from MODIS measurements. Scheck et al. (2018) introduced a cloud top inclination correction for simulated radiances of optically thick clouds. Meyer et al. (2022) used a machine learning approach to correct 1D radiative transfer simulation results for numerical weather prediction models for three-dimensional radiative effects. They were able to correct 70 % to 80 % of the three-dimensional radiative effects missed by one-dimensional radiative transfer simulations. For the thermal wavelength range, Schäfer et al. (2016) and Fielding et al. (2020) showed that the sub-grid-scale three-dimensional cloud geometry and the resulting three-dimensional radiative effects in numerical weather prediction and climate models can be parameterized through the cloud edge length. However, we are not aware of any similar approximation of 3D cloud geometry for the computation of radiances in the visible wavelength range.

In the following, a new parameterization of 3D cloud geometry for polarized 3D radiative transfer in the visible wavelength range is presented and applied to obtain a fast forward operator. The InDEpendent column local halF-sphere ApproXimation (IDEFAX) is based on the ICA. However, it uses a new simplified cloud model instead of the plane-parallel approximation. The 3D cloud geometry of an individual column is approximated by a field of half-spherical clouds that are defined by two local surface orientation angles and the cloud fraction, as visualized in Fig. 3.17. A spherical cloud shape as an approximation to real clouds was already proposed by Davis (2002). The addition of only three parameters in the IDEFAX compared to the plane-parallel ICA makes it simple to implement and simple enough to tabulate simulated radiances. The forward operator for polarized 3D

radiative transfer provides the Stokes vector components I, Q, and U and accounts for 3D cloud geometry using the new IDEFAX. Instead of a look-up table, artificial neural networks were trained as a forward operator for both the IDEFAX and the plane-parallel ICA. To validate the IDEFAX and the neural network forward operator, a realistic cloud field consisting of low-level Arctic mixed-phase clouds was simulated using the Weather research and Forecasting (WRF) model (Skamarock et al., 2019). Real three-dimensional polarized radiative transfer simulations of the cloud field performed with the Monte Carlo 3D radiative transfer solver MYSTIC (Mayer, 2009) were then compared to simulated radiances from the IDEFAX and the plane-parallel ICA, and the respective neural network forward operator.

The forward operator was constructed for retrievals of the polarization-resolving cameras of specMACS, such as the new phase retrieval developed in this work. However, it is, in principle, also applicable to other measurements or model data. Cloud 3D geometry can be derived from the specMACS measurements using the stereographic reconstruction method by Kölling (2020), which uses contrasts in total intensity measurements. Especially for measurements with large solar zenith angles, as during the HALO–$(\mathcal{AC})^3$ measurement campaign (Wendisch et al., 2024) in the Arctic, three-dimensional radiative effects become very important and retrievals need to consider the effects of 3D cloud geometry.

In the following, the cloud simulations conducted with the WRF model are explained in Sect. 3.3.1 followed by an overview of the radiative transfer model MYSTIC in Sect. 3.3.2. Next, the developed simplified cloud model for the IDEFAX is described in Sect. 3.3.3 and the neural network forward operator setup, training, and results are given in Sect. 3.3.4. The IDEFAX and the neural network forward operator are validated using 3D radiative transfer simulations for the cloud field simulated with the WRF model in Sect. 3.3.5 and the results are discussed in Sect. 3.3.6.

3.3.1 WRF simulations

A realistic cloud field was simulated to test different approximations of 3D cloud geometry for polarized radiative transfer and to validate them against full 3D radiative transfer simulations. The simulations were performed with the Weather research and Forecasting (WRF) model version 4.6 (Skamarock et al., 2019) using four two-way nested domains with a nesting ratio of 5:1. For this study, only data from the innermost domain are used. The inner domain extends from 4.74°E to 7.24°E and from 79.22°N to 79.67°N (25 km×25 km) with a horizontal grid spacing of 100 m and 200 vertical levels. The simulation covers the time period from 00:00 UTC to 15:00 UTC on 2022-04-01. Initial and boundary conditions were provided by ERA5 reanalysis data (European Centre for Medium-Range Weather Forecasts, 2019) at 0.25° grid spacing. Important simulation physics options include the two-moment bulk microphysics scheme by Morrison et al. (2009), the unified Noah Land Surface Model (LSM; Tewari et al., 2004), the Mellor-Yamada-Nakanishi Level 2.5 planetary boundary layer (PBL) scheme (MYNN2; Nakanishi and Niino, 2006, 2009; Olson et al., 2019), and the rapid radiative transfer model for general circulation models as the radiation scheme (RRTMG; Iacono et al., 2008).

Next, the output of the WRF model was converted to input for the radiative transfer model, where clouds are defined by their liquid or ice water content and respective effective radius. LWC and IWC are directly included in the WRF model output. All liquid hydrometeors were interpreted as liquid water clouds and all frozen hydrometeors as ice clouds for the radiative transfer simulations. The liquid water cloud effective radii $r_{\text{eff,wc}}$ and ice cloud effective radii $r_{\text{eff,ic}}$ needed for radiative transfer were computed from the liquid water content and ice water content and the respective number concentrations from the model output following the equations by Martin et al. (1994). Different methods for computing ice effective radii from the model output were tested and showed similar results. From the IWC, LWC, and liquid and ice effective radii fields, liquid and ice optical thickness fields were computed. In the end, the effective radii were set to typical values of 10 μm for liquid water and 50 μm for ice clouds throughout the cloud field, and LWC and IWC scaled accordingly, keeping the optical thickness conserved. By assuming constant effective radii, additional effects due to variations of the effective radius were excluded. Generally, however, the variation of radiances due to varying effective radii is small in the visible wavelength range.

Figure 3.15 displays the part of the obtained cloud field on 2022-04-01 at 03:00 UTC that is visible in the radiative transfer simulations in Sect. 3.3.2 and 3.3.5. The upper row shows horizontal fields of liquid water (a) and ice optical thickness (b), and the bottom row shows vertical cross sections of the cloud field along the southernmost edge at a latitude of 79.22° north for the LWC (c) and IWC (d). On the simulated day on 2022-04-01, there was a marine cold air outbreak in the Fram Strait. During a cold air outbreak, cold and dry polar air masses are transported southwards. When they pass the marginal sea ice zone and reach open ocean, convection sets in and clouds are formed. They usually first organize into cloud streets and later on develop more cellular structures (Fletcher et al., 2016a; Papritz and Spengler, 2017). This is also visible in the simulated cloud field in panels (a) and (b), where the optical thickness shows cloud streets oriented roughly in the north-south direction. The clouds have cloud top heights smaller than 1000 m, and liquid water is located more towards the top of the clouds, whereas the ice is concentrated in the lower part, as can be seen in panels (c) and (d).

3.3.2 Radiative transfer model

The radiative transfer simulations were performed with the radiative transfer model libRadtran (Mayer and Kylling, 2005; Emde et al., 2016) using the Monte Carlo solver MYSTIC (Mayer, 2009), which allows for full 3D radiative transfer simulations including polarization (Emde et al., 2010). In Monte Carlo radiative transfer simulations, photons are traced through the atmosphere, where they can be scattered by clouds, aerosols, and molecules, reflected by the Earth's surface, or absorbed, until they reach the detector. The chosen viewing geometry is a typical viewing geometry of the polarization-resolving cameras of the specMACS instrument during the HALO–$(\mathcal{AC})^3$ campaign and corresponds to the measurements on 2022-04-01 at 10:18 UTC. The part of the cloud field that is covered by the instrument field of view for the chosen viewing geometry is indicated by the black

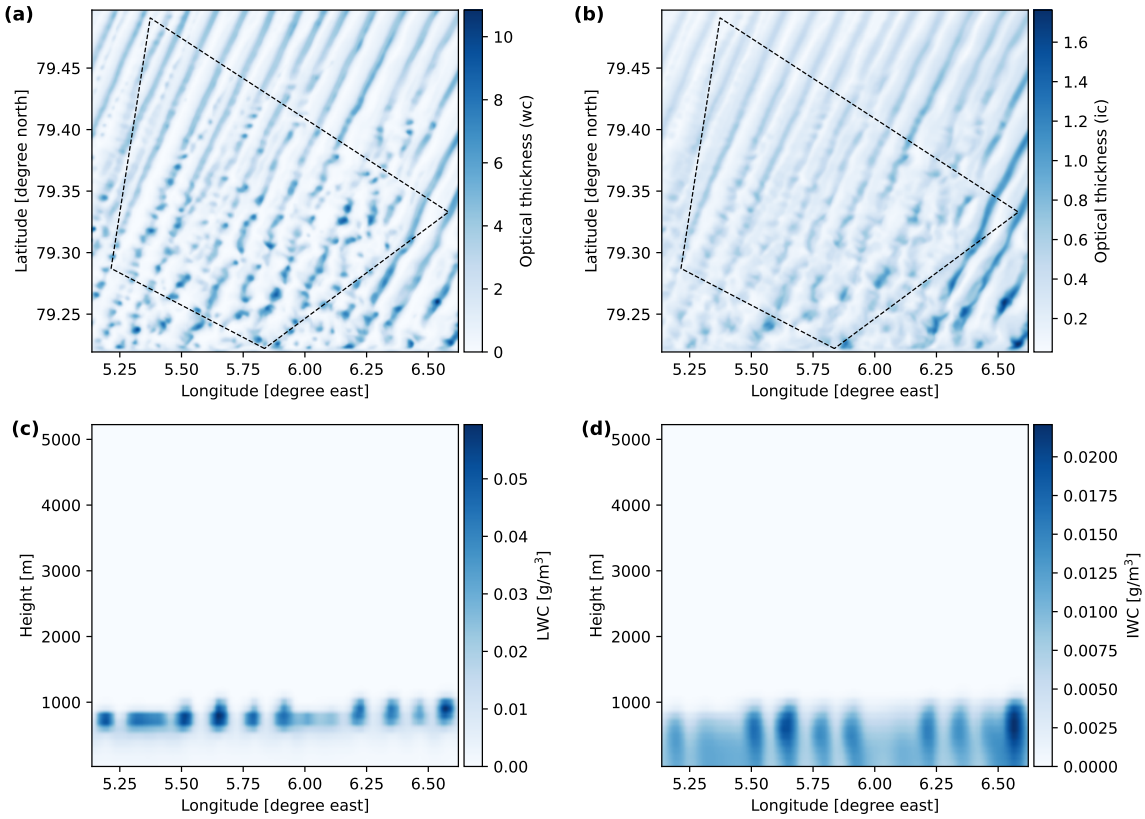

Figure 3.15: WRF cloud field. **(a, b)** Optical thickness for liquid water and ice clouds, respectively. **(c, d)** Vertical cross sections of LWC and IWC along latitude 79.22° north. The dashed lines indicate the part of the cloud field that is covered by the field of view of the instrument and visible in the radiative transfer simulations in Sect. 3.3.2 and 3.3.5.

dashed lines in Fig. 3.15. Radiative transfer simulations for the specMACS instrument were already used by Volkmer et al. (2024), but their work included only liquid water clouds. The solar zenith angle for the radiative transfer simulations was 75.6°. Concerning cloud optical properties, phase functions according to Mie theory (Mie, 1908) were used for liquid water clouds, and the ice optical properties by Yang et al. (2013) for the aggregate consisting of eight columns with moderate crystal roughness were used for ice clouds. This habit was chosen as a compromise between pristine plates and columns and more complex aggregates. The simulations were done for a US standard atmosphere and using the ocean BRDF by Cox and Munk (1954a,b) with a wind speed of $10\,\mathrm{ms}^{-1}$ and 0° wind direction, which means wind coming from the north. The obtained Stokes vectors for all simulations were rotated into the scattering plane and converted to reflectivity via

$$R_I = \frac{\pi I}{F_0 \cos(\mathrm{sza})} \qquad \text{and} \qquad R_Q = \frac{\pi Q}{F_0 \cos(\mathrm{sza})}, \tag{3.24}$$

where I and Q are the first and second Stokes vector components describing total intensity and linear polarization, sza is the solar zenith angle, and F_0 is the extraterrestrial solar

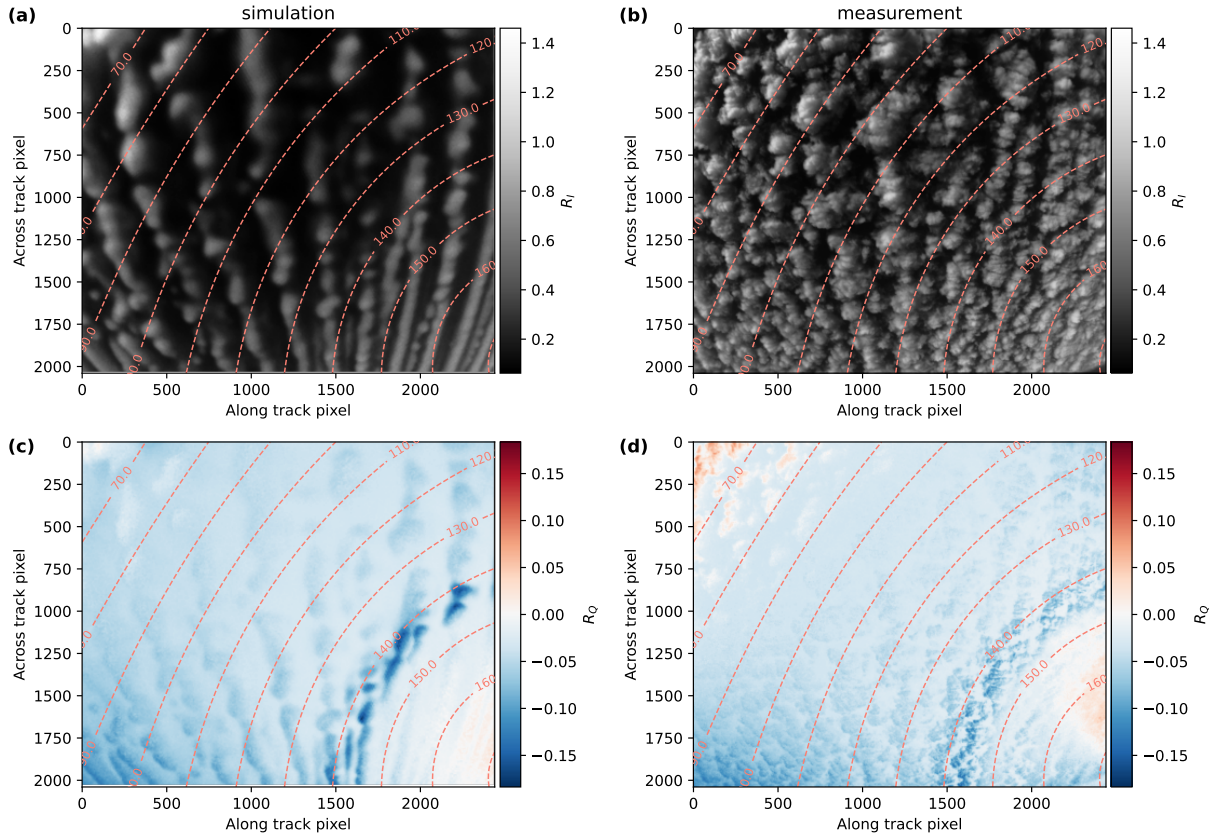

Figure 3.16: Full 3D radiative transfer simulation using the WRF cloud field **(a, c)** and specMACS measurement on 2022-04-01 10:18 UTC **(b, d)** for the green color channel. Panels **(a, b)** show the reflectivity R_I, whereas panels **(c, d)** show the reflectivity for the Q component of the Stokes vector, R_Q. The dashed lines indicate the scattering angles.

irradiance.

Figure 3.16 shows 3D radiative transfer simulations for the green color channel of specMACS and the WRF cloud field as described above in panels (a) and (c) and the corresponding real measurement in panels (b) and (d). The radiative transfer simulations have the same spatial resolution of about 10 m as the measurements. The upper row displays the total reflectance R_I, and the bottom row shows the polarized reflectance R_Q. In the polarization signal, the cloudbow is visible as a minimum in R_Q in the lower-right corner. It is formed by single scattering by liquid droplets. The simulation in general looks smoother than the measurement, which is due to the lower spatial resolution of the WRF cloud simulations (100 m) compared to the high-resolution measurements (10 m). The overall structure of the simulated clouds as well as the absolute values of the simulated R_I and R_Q are realistic compared to the measurements. The bipolar structures in the polarization signal of the measurements in the upper-left and lower-right corners in panel (d) are calibration artifacts due to the more uncertain polarization calibration in the corners of the sensor.

3.3.3 Simplified cloud model

With the WRF simulations and the radiative transfer model, it was possible to test different simplified cloud models to approximate 3D cloud geometry for polarized radiative transfer (see Fig. 3.17). Realistic three-dimensional clouds have a complex cloud surface geometry, as visualized in Fig. 3.17a. The basic idea was to find a simplified description of the 3D clouds that covers most of their 3D characteristics but is simple enough to be defined by a small number of parameters, such that radiances, respectively Stokes vectors, for the approximation could be tabulated.

In the case of the plane-parallel approximation (Fig. 3.17c), a cloud is completely defined by its cloud top height (cth), cloud base height, optical thickness τ, and effective radius (r_{eff}). To further reduce the number of parameters, the geometrical thickness d of the cloud, and thus the cloud base height, was parameterized through the optical thickness of the cloud using the adiabatic cloud model introduced in Sect. 2.4 (e.g., Grosvenor et al., 2018):

$$d = \sqrt{\frac{4}{3}\frac{\rho_{\text{w}} r_{\text{eff}}}{f_{\text{ad}} C_{\text{w}}}\tau}. \tag{3.25}$$

Here, ρ_{w} is the density of liquid water. The adiabaticity is set to a typical value of $f_{\text{ad}} = 0.3$ (Ishizaka et al., 1995; Merk et al., 2016) and the condensation rate to $C_{\text{w}} = 2.5 \times 10^{-6}\,\text{kg}/(\text{m}^3\text{m})$ (Min et al., 2012). A derivation of the formula based on the adiabatic cloud model can be found in Appendix B. For the computation of the geometrical thickness from the optical thickness, the constant effective radius of the simulated cloud field (see Sect. 3.3.1) is applied. Hence, optically thick clouds are also geometrically thicker, and a one-dimensional cloud can be described only by its cloud top height, optical thickness, and effective radius. Although the geometrical thickness of a cloud affects the Rayleigh scattering within a cloud, the sensitivity of simulated Stokes vectors to the cloud geometrical thickness is comparably small, which allows for the described approximation of the cloud geometrical thickness through the cloud optical thickness.

In the next step, different cloud geometries were tested as approximations to the real three-dimensional clouds. This included box clouds to account for the finite cloud size, tilted clouds to approximate the effect of cloud top inclination, and half-spherical clouds that include both finite cloud size and cloud top inclination. In all cases, the tested approximations of 3D cloud geometry are combined with the ICA and thus applied independently to every pixel. This means that, for example, in the case of one-dimensional clouds, an independent simulation is performed for every pixel, with a plane-parallel cloud located at the cloud top height and having the optical thickness and effective radius of that pixel. An explanation for how these parameters can be obtained for every pixel from measurement or model data is given in detail in Sect. 3.3.5. In this work, the simulated pixel size was about 10 m because this is the spatial resolution of the measurements of specMACS. For other applications, the pixel size could be chosen differently. A comparison of simulated Stokes vectors obtained with the different approximations against full 3D radiative transfer simulations of the realistic cloud field from the WRF model showed that neither the finite cloud size (represented by the box clouds) nor the surface orientation (represented by the

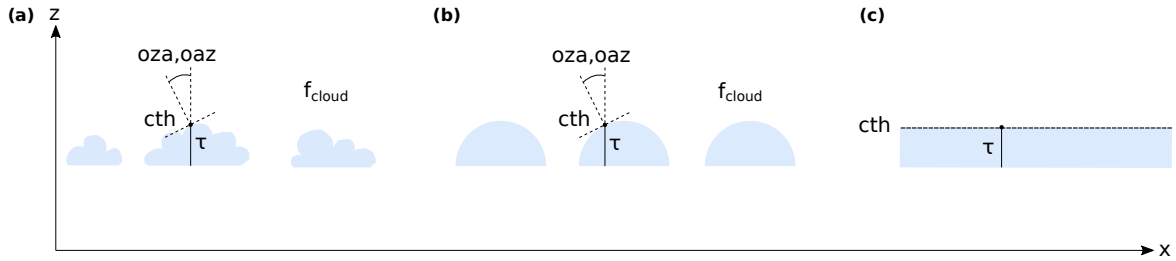

Figure 3.17: Definition of different cloud geometries and parameterizations. **(a)** Full three-dimensional clouds. **(b)** Half-spherical clouds. **(c)** One-dimensional clouds.

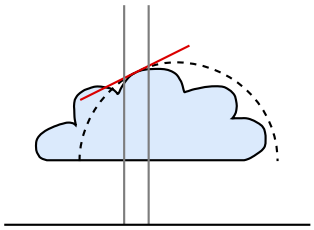

Figure 3.18: Basic geometry of the IDEFAX. The gray lines indicate a single column of a complex cloud. This column is approximated by the dashed half-spherical cloud, which has the same surface orientation and cloud top height as the real cloud in the considered column.

tilted clouds) alone is sufficient to capture the basic 3D radiative effects.

The cloud model that showed the best agreement with the full 3D cloud field was a field of half-spherical clouds, as shown in Fig. 3.17b. We call this new approximation the InDEpendent column local halF-sphere ApproXimation (IDEFAX). The half-spherical clouds are, in addition to cloud top height, optical thickness, and effective radius, described by a surface orientation zenith (oza) and azimuth (oaz) angle and the cloud fraction (f_{cloud}). Their geometrical size is defined through the optical thickness as above. Here, the surface orientation zenith angle is the angle between the local surface normal of the cloud surface at a given point on the cloud surface and the vertical. The surface orientation azimuth angle is the angle between the principal plane, which contains the sun vector and the vertical, and the plane formed by the surface normal and the vertical (see also Fig. 3.17). Surface orientation angles can directly be derived from the cloud geometry of model or measurement data, e.g., by fitting a plane through the 3D points describing the cloud surface in neighboring pixels as in Scheck et al. (2018) or, in the case of application to specMACS data, from the stereographic retrieval of cloud 3D geometry by Kölling (2020). In the ICA, individual pixels are treated independently, and thus the real 3D cloud for every pixel is approximated by an independent field of half-spherical clouds. For that, a specific target point on a half-sphere is defined by the surface orientation azimuth and zenith angles of the considered pixel, and the half-sphere is placed such that the target point is located at the given cloud top height, see Fig 3.18. This half-sphere is part of a field of half-spheres with a given cloud fraction. The cloud fraction is the ratio of the number of cloudy pixels to the total number of pixels, and thus, it contains non-local information. It can be computed from measurement or model data by applying a cloud mask. Hence, a cloud field consisting

of half-spherical clouds as described above is constructed such that the number of cloudy pixels within the cloud field corresponds to the given cloud fraction. The cloud fraction has an upper limit that is less than unity because half-spheres cannot completely fill the model domain. An isolated half-spherical cloud not embedded in a cloud field showed less agreement with full 3D radiative transfer simulations than the field of half-spherical clouds defined through the cloud fraction. Clouds in MYSTIC are defined on a regular grid. For the half-spherical clouds, the step size of the grid boxes building up a cloud was chosen such that the optical thickness per step was less than 0.5 to avoid artifacts from the steps, but also to minimize the required amount of memory. This internal step size is independent of the simulated pixel size.

In the case of mixed-phase clouds, the clouds are defined by their total optical thickness and the ice fraction, which is here defined as the ratio of the ice optical thickness to the total optical thickness. They are simulated as clouds with homogeneously mixed liquid water and ice in the parameterization.

3.3.4 Neural network forward operator

Although only three extra parameters are required for the approximation of 3D cloud geometry through half-spherical clouds with the IDEFAX, a look-up table that includes radiative transfer simulation results for all necessary parameters would be prohibitively large because 11 parameters (see Table 3.4) are already needed for simple one-dimensional clouds. The computation and interpolation within the look-up table would be expensive, and the memory requirements would be high. Therefore, the look-up table was replaced with a simple feed-forward neural network. Artificial neural networks allow for very fast inference with little storage space needed. In addition, neural networks are, by definition, differentiable (if differentiable activation functions are used), which allows for the direct computation of gradients. This can be advantageous if the neural network is applied in retrievals that use optimization. Separate neural networks were trained for one-dimensional clouds in the classical ICA and the half-spherical clouds of the IDEFAX.

Training data were computed using MYSTIC by randomly sampling all input parameters within their boundaries. The WRF simulations are independent of the generation of training data and the neural network training and were used only to validate the IDEFAX and the neural network forward operators in Sect. 3.3.5. Table 3.4 summarizes all input parameters that were used for the training of the neural networks. They include geometrical information like the solar zenith angle, viewing zenith and azimuth angles, sensor height, and cloud top height, as well as information about cloud microphysical properties such as the total optical thickness, ice fraction, and effective radius and variance of a cloud. The cloud microphysical properties for measurement data are, in most cases, unknown and derived by retrievals. Finally, the forward operators include the ocean surface with the ocean BRDF by Cox and Munk (1954a,b) as the lower boundary defined by wind speed and wind direction. Compared to the other parameters, the exact values of the wind speed and wind direction describing the ocean surface are less relevant for radiative transfer simulations of clouds. For the IDEFAX, the cloud surface orientation zenith and azimuth angles and

Parameter	Abbreviation	Minimum	Maximum
Solar zenith angle	sza	0°	80°
Viewing zenith angle	vza	0°	70°
Viewing azimuth angle	vaz	0°	180°
Sensor height	zout	8000 m	15000 m
Cloud top height	cth	500 m	13000 m
Total optical thickness	τ	0	8
Ice fraction	f_{ice}	0	1
Liquid cloud effective radius	$r_{\text{eff,wc}}$	1 μm	40 μm
Liquid cloud effective variance	$v_{\text{eff,wc}}$	0.01	0.32
Surface wind speed	u10	1 m/s	15 m/s
Surface wind direction	uphi	0°	360°
Cloud surface orientation zenith angle	oza	0°	60°
Cloud surface orientation azimuth angle	oaz	-180°	180°
Cloud fraction	f_{cloud}	0	1

Table 3.4: Input parameters, their abbreviations, and their ranges. The last three parameters are for half-spherical clouds in the IDEFAX only.

the cloud fraction are additional parameters. The azimuthal angles are defined relative to the principal plane. All simulations were performed for a US standard atmosphere, and the cloud base height was parameterized through the optical thickness as discussed in Sect. 3.3.3. Moreover, the ice cloud effective radius was assumed to be 50 μm and the aggregate of eight columns with moderate surface roughness by Yang et al. (2013) was used as the ice crystal habit. Depending on the application, ice crystal effective radius and habit could be added as additional parameters in the future. The ranges for all input parameters were chosen so that they cover the typical ranges measured by an aircraft instrument. Due to the focus on polarization, optical thickness values were sampled only up to an optical thickness of 8. The polarization signal saturates latest at an optical thickness of around 5, such that the full range is already covered for the chosen optical thickness boundaries. For other applications, the boundaries of the input parameters could be adjusted. All input parameters were normalized within their boundaries for the neural network training.

The output quantities of the neural networks are the Stokes vector components I, Q, and U, converted to reflectivity. In the following, the results of the neural network setup and training for the green color channel (which has a center wavelength close to 550 nm) of one polarization-resolving camera of the specMACS instrument are shown. The results for the other visible color channels of the specMACS instrument are similar and thus potentially also the results for visible wavelength channels of other instruments. The radiative transfer simulations for the training data were done for a spectrum covering the wavelength range from 380 nm to 690 nm in 10 nm steps with a standard deviation of the simulation results of 4 % per wavelength and then integrated to the green wavelength channel by applying

the spectral response function of the polarization-resolving cameras. In total, 20 million random samples were computed for the one-dimensional clouds with 11 input parameters and 40 million random samples for the more complex IDEFAX with 14 input parameters. These were obtained by performing individual radiative transfer simulations for randomly chosen sets of values for the input parameters listed in Table 3.4. Two million samples of the simulated training data were used for testing.

Next, both neural networks were trained and hyperparameters tuned until a good setup was found. Training and tuning included testing different network sizes with different numbers of hidden layers and numbers of total parameters, batch sizes, learning rates, activation functions, and parameter transformations (similar to Scheck (2021) and Baur et al. (2023)). In the following, the results for the best models will be shown. For both the one-dimensional and the IDEFAX models, a weighted mean squared error was used as loss function. Q and U were given 10 times the weight of I to account for the different orders of magnitudes of I, Q, and U. In addition, the loss was multiplied by a factor of 1000 to avoid vanishing gradient problems. In general, the dependence of the cloudbow on the effective radius and variance was difficult for the neural networks to learn because the cloudbow is a strongly nonlinear feature. The addition of the scattering angle as an input parameter improved the performance, and smaller loss values were obtained. The scattering angle was computed from the solar and viewing geometry. In addition, the optical thickness was transformed logarithmically, and a square root transformation was applied to the output Stokes vectors, as in Scheck (2021). Moreover, a sine-cosine transformation was applied to the wind direction and surface orientation azimuth angles to avoid the jump from 360° to 0°. This means that the viewing azimuth angle was described by cos(vaz) and sin(vaz).

After hyper-parameter tuning for the one-dimensional clouds, a neural network with eight hidden layers and 64 nodes per layer, corresponding to 30000 parameters in total, gave the best results. More parameters resulted in overfitting, whereas fewer parameters were not able to capture all the details of the Stokes vector fields. Neural networks with fewer or more hidden layers showed worse results compared to the neural network with eight hidden layers. Moreover, the exponential linear unit (elu) activation function and a linear output activation function were used in the best model setup. Other activation functions like the cheap soft unit (csu) or the hyperbolic tangent (tanh) gave worse results. Finally, a batch size of 1024 and the Adam optimizer with a learning rate of 1.0×10^{-4} were applied in the network training of the best model. It was trained for 2000 epochs using an early stopping routine to get the most accurate results. Error statistics for the best model for one-dimensional clouds, including the bias, root mean square error (RMSE), and mean absolute error (MAE), for I, Q, and U, are summarized in Table 3.5. The statistics were computed from the test data. The obtained biases are 2 to 3 orders of magnitude smaller than typical signal levels. In addition, the errors are significantly lower than the measurement uncertainties of typical polarization-resolving instruments, which are on the order of a few percent (e.g., Weber et al., 2024, see Sect. 3.1.3).

The neural network using half-spherical clouds with the IDEFAX was trained similarly to the network for plane-parallel clouds. The best results were found for a neural network with six hidden layers and 97 nodes per layer, resulting in a total number of parameters

Neural network	Parameter	Bias	RMSE	MAE
1D clouds	I	2.7×10^{-4}	5.0×10^{-3}	3.5×10^{-3}
	Q	-7.9×10^{-6}	1.4×10^{-3}	7.6×10^{-4}
	U	1.1×10^{-4}	9.7×10^{-4}	6.3×10^{-4}
Half-spherical clouds	I	-4.8×10^{-4}	2.8×10^{-2}	1.2×10^{-2}
	Q	8.7×10^{-5}	9.2×10^{-3}	1.7×10^{-3}
	U	8.1×10^{-5}	1.3×10^{-3}	6.9×10^{-4}

Table 3.5: Error statistics for the best neural networks for one-dimensional clouds and half-spherical clouds in the IDEFAX for I, Q, and U computed using the test data.

of about 50000. As for the 1D clouds, the elu activation function and a linear output activation were used, and the model was trained for 2000 epochs using early stopping. In addition, a batch size of 1024 and a learning rate of 1.0×10^{-4} for the Adam optimizer showed the most accurate results. The obtained prediction errors of the neural network for the half-spherical clouds in the IDEFAX computed from the test data are also summarized in Table 3.5. The errors, especially for I, are larger compared to the neural network for 1D clouds. However, they are still smaller than typical measurement uncertainties. This is because the half-spherical cloud geometry introduces more non-linearities, particularly for the intensity, and is thus much more difficult for a neural network to learn.

For fast emulation, the fornado module by Scheck (2021) was used, which is optimized for predictions of small neural networks. In addition, it allows the computation of adjoints based on the Tapenade tool for automatic differentiation (Hascoet and Pascual, 2013), which can be used for optimization routines in retrievals. The full 3D simulations of the images displayed in Fig. 3.20 took on the order of several days on an Intel® Xeon(R) W-2245 CPU @ 3.90GHz processor. The plane-parallel ICA simulations with MYSTIC needed about a day, and the IDEFAX simulations with MYSTIC on the order of a few days. In contrast, the predictions with the neural networks in Fig. 3.22 took only on the order of seconds, with slightly larger computation times for the IDEFAX than for the plane-parallel ICA. Thus, a total speed up of the computation time by a factor of about 10^5 can be achieved by using the neural network forward operators instead of performing polarized Monte Carlo radiative transfer simulations.

3.3.5 Validation of the IDEFAX and the neural network forward operator

Both the IDEFAX and the neural network forward operators were validated against full 3D radiative transfer simulations with MYSTIC for the realistic cloud field obtained from the WRF simulations. The radiative transfer simulations were performed for a wavelength of 550 nm, which is close to the center wavelength of the green color channel of the specMACS polarization-resolving cameras that the neural networks were trained for and used the

settings described in Sect. 3.3.2. The radiances obtained from the 3D radiative transfer model were then compared to radiances for the same cloud field computed with the IDEFAX and the plane-parallel ICA. In addition, the comparison was repeated with the neural network forward operators for the IDEFAX and plane-parallel clouds for the green color channel of specMACS, also to validate the forward operators.

The input parameters defining the cloud geometry and microphysics for the different simulations (see Table 3.4) were determined as follows. The first step in any ICA application is the assignment of a cloud model column to every pixel of a simulated radiance field respectively the geolocalization of the measured signal. The assignment is straightforward for nadir viewing directions, but not at all trivial for slant viewing directions. For model data, the column corresponding to a certain pixel can be defined as the column where the first scatter event of a photon propagating backward from the sensor into its viewing direction takes place. This approach is, for example, applied in the TICA DIR approximation by Gabriel and Evans (1996) and Wissmeier et al. (2013). Hence, 1000 photons were traced for every pixel, and the column was selected based on the mean location of the first scatterings. In the case of measurements, geolocalization is possible from the known sensor position and viewing directions and information about the cloud top height, which can be derived from the measurement data, for example, through stereographic methods. Volkmer et al. (2024) showed that the cloud top heights computed from the mean locations of the first scatter events correspond well to cloud top heights obtained with a stereographic retrieval. Thus, the chosen method for the column assignment through the locations of the first scattering is reasonable and consistent between model and measurement data.

Afterward, the input parameters for every simulated pixel could be determined. The height of the mean locations of the first scatter events from the column assignment was used as the cloud top height for every pixel. This height corresponds approximately to the height where the optical thickness reaches 1, as it was used for the cloud top height in model data in Scheck et al. (2018) and as it is obtained from measurements. As the clouds in the introduced approximations are defined such that their cloud top height is the height where the cloud water first exceeds zero, the height definition through an optical thickness of 1 or the location of the first scatter event is not entirely consistent with that, and the approximated clouds are shifted vertically relative to the real clouds. However, the deviation between the cloud top heights is small and affects only the amount of Rayleigh scattering above and within the cloud. Thus, it has only a negligible influence on the simulated radiances. In the future, this could nevertheless be accounted for, if necessary.

Once the cloud top height is known, the cloud surface orientation can be computed. It can be determined by fitting a plane through the three-dimensional points defining the cloud top height for neighboring columns as in (Scheck et al., 2018). Surface orientation angles can then be calculated from the normals of the fitted planes. Alternatively, a triangular mesh describing the three-dimensional surface of the cloud can be obtained through Poisson surface reconstruction as in Kölling (2020). The surface orientation zenith and azimuth angles are, in this case, derived from the triangular cloud surface mesh by computing the closest point on the surface mesh for the three-dimensional location of every pixel and using the respective surface normal. Here, the latter method was chosen, as it is operationally

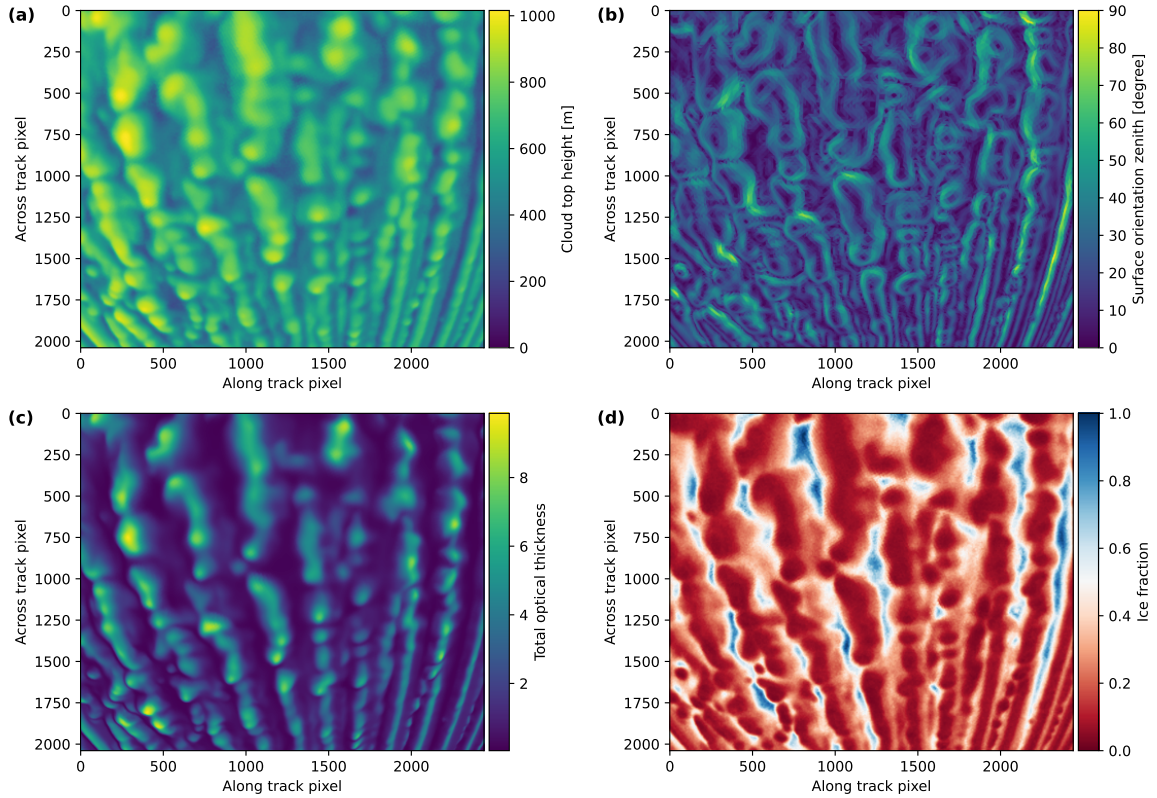

Figure 3.19: Cloud geometry and microphysics for the parameterization. **(a)** Cloud top height. **(b)** Cloud surface orientation zenith angle. **(c)** Total optical thickness. **(d)** Ice fraction.

applied to the specMACS measurements. Fig. 3.19a and 3.19b show the resulting cloud top height and surface orientation zenith angles. Cloud top heights are around 800 to 1000 m. The surface orientation zenith angle is close to 0 in the center of the clouds and increases towards the edges.

Furthermore, the cloud fraction can be computed from a cloud mask as the ratio of the number of cloudy pixels to the total number of pixels. Cloudy pixels can be defined either as pixels where the optical thickness of the corresponding column in the model data exceeds a certain threshold value or by a cloud mask from measurement data based on the brightness of the pixels. Here, the brightness-based cloud mask for the specMACS instrument introduced in Pörtge et al. (2023) was applied to the simulated radiances. However, the results were very similar compared to the model-based cloud mask. For the shown case, a single cloud fraction was computed from the cloud mask for the entire measurement range because the simulated cloud field is comparably homogeneous. For other cases with a more inhomogeneous distribution of clouds, only a subsection of the measurements surrounding the considered pixel should be used to compute the local cloud fraction for every simulated pixel. The cloud fraction defines the distance between the half-spherical cloud representing the cloud at the considered pixel and the surrounding half-spheres of the cloud field of the IDEFAX. Thus, the cloud fraction should represent

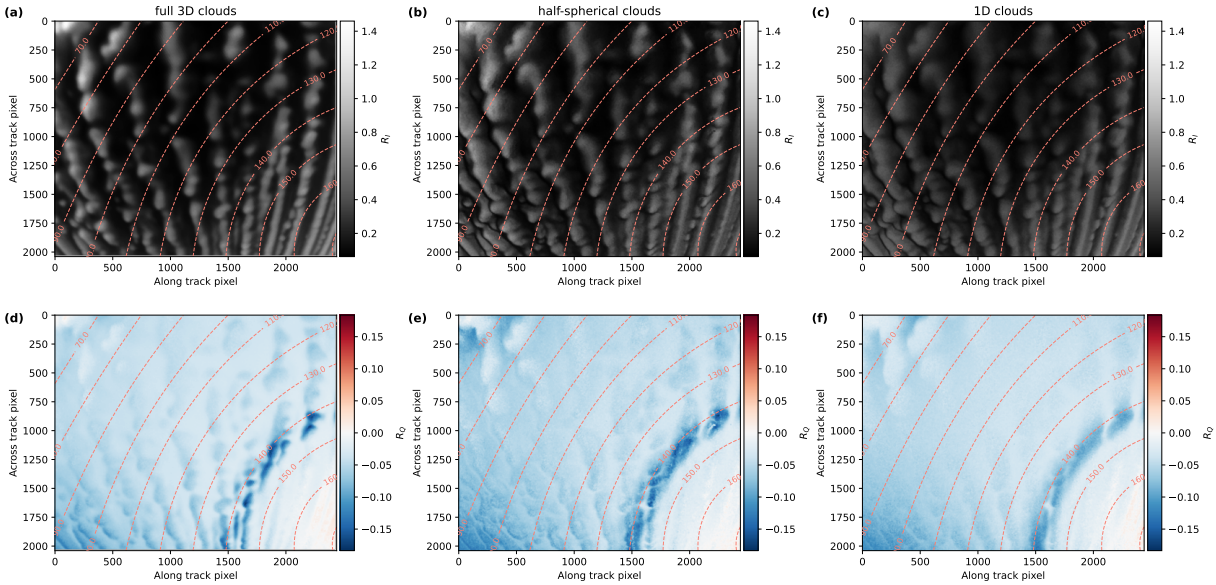

Figure 3.20: Simulation results for realistic three-dimensional clouds **(a, d)**, the IDEFAX **(b, e)** and the plane-parallel ICA **(c, f)**. Panels **(a, b, c)** show the reflectivity R_I, and panels **(d, e, f)** show R_Q. The dashed lines indicate the scattering angles.

this average distance.

Concerning the cloud microphysics for the radiative transfer simulations, the total vertical optical thickness of the respective column in the model data was used as optical thickness, as is common in the ICA. To determine the ice fraction, the scatter type of the first scatter event was saved for every pixel in addition to the location of the first scatter events for the column assignment. The ice fraction was computed as the ratio of the number of scatterings on ice to the total number of scatterings. Similar results are obtained by simply taking the mean ice fraction of the grid boxes where the first scatter events take place for every pixel. Because the polarization signal is dominated by single scattering, this definition of the ice fraction through the first scattering was chosen. To exclude biases and uncertainties due to this definition, the analysis was repeated for pure liquid clouds as described below. Fig. 3.19c and 3.19cd display the total optical thickness and the ice fraction for every pixel. The simulated clouds have total optical thicknesses of around 6 to 10. The ice fraction is smallest in the centers of the clouds due to the liquid at cloud top and increases for lower cloud top heights towards the edges of the clouds. All other parameters (such as, e.g., the effective radii) were kept as described in Sect. 3.3.2 for the three-dimensional simulation.

Figure 3.20 shows the radiative transfer simulation results for the realistic three-dimensional clouds (left column), the IDEFAX (middle column), and the one-dimensional approximation (right column) for the total reflectivity (upper row) and polarized reflectivity (lower row). Visually, the results for the IDEFAX are much closer to the full three-dimensional simulation than the simulation using the one-dimensional ICA. The simulations based on the IDEFAX show lower values in the areas facing away from the sun as well as enhancements in the parts of the clouds that are oriented towards the sun, which is coming from the upper left. This

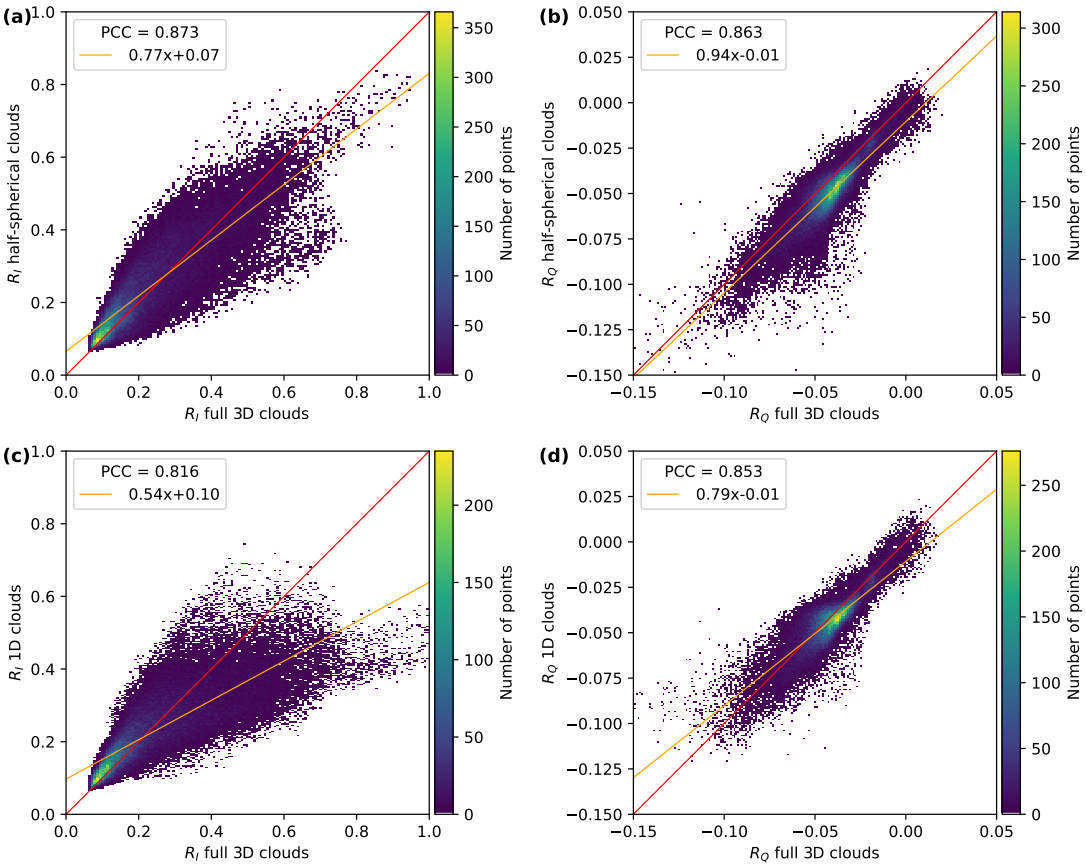

Figure 3.21: Scatter plots of the simulations with half-spherical clouds in the IDEFAX and one-dimensional clouds in the ICA against the full three-dimensional simulation for R_I **(a, c)** and R_Q **(b, d)**. Panels **(a)** and **(b)** show the comparison for half-spherical clouds, and panels **(c)** and **(d)** for one-dimensional clouds. The red curve represents the identity, and the orange curve shows a linear fit to the data. The fit parameters and the Pearson correlation coefficients (PCC, corresponding to the R value) are given in the legends.

cannot be covered by one-dimensional clouds. In addition, the polarization signal is closer to the full 3D simulations for the IDEFAX with a more pronounced cloudbow and a less smooth signal than in the one-dimensional approximation. The IDEFAX is also quantitatively closer to the three-dimensional simulation compared to the one-dimensional results. Fig. 3.21 shows scatter plots of the simulations using the IDEFAX and the plane-parallel ICA against the full 3D simulations for I and Q, as well as linear fits. The linear fits are closer to the identity for the IDEFAX and the correlation coefficients are higher than those of the 1D simulation. The improvement in the agreement from the one-dimensional approximation to the IDEFAX is larger for I than for Q. This can be expected because the polarization signal is dominated by single scattering and therefore less affected by three-dimensional radiative effects than the intensity. The difference in the correlation coefficients between the plane-parallel ICA and the IDEFAX is relatively small. The reason for this is that clear-sky pixels without clouds or with very small optical thickness values were included

in the analysis. These pixels are represented by the large number of pixels with small reflectivity in Fig. 3.21. The difference between the plane-parallel ICA, the IDEFAX, and the full 3D radiative transfer simulations for these pixels is small, leading to increased correlation coefficients. If only cloudy pixels are considered, correlation coefficients of 0.52 and 0.70 are obtained for R_I and 0.89 and 0.90 for R_Q for the plane-parallel ICA and the IDEFAX, respectively. The increase in the correlation coefficients for R_I for cloudy pixels is significant. Overall, the addition of three parameters (cloud surface orientation zenith and azimuth angles and cloud fraction) for simulations with half-spherical clouds, in addition to cloud top height and optical thickness as for 1D clouds, shows significant improvement towards full three-dimensional clouds and is simple.

The same analysis as discussed above was repeated for a cloud field consisting of pure liquid clouds to exclude potential uncertainties from the computation of the ice fraction for mixed-phase clouds. For that, the clouds of the WRF cloud field were converted to entirely liquid clouds, conserving the total optical thickness for every grid cell and the cloud geometry. The analysis for pure liquid water clouds showed very similar results (not shown) compared to the mixed-phase clouds, which further validates the introduced parameterization of 3D cloud geometry.

In addition to the IDEFAX method itself, the neural network forward operators were validated against full 3D radiative transfer simulations with MYSTIC in a similar way. Figure 3.22 shows radiative transfer simulations for the green wavelength channel of specMACS for the WRF cloud field using the plane-parallel ICA or the IDEFAX, similar to Fig. 3.20 but obtained with the neural networks. The simulations with the neural networks look very similar to the Monte Carlo radiative transfer simulations. In addition, Figure 3.23 shows the corresponding scatter plots as in Fig. 3.21 for the neural network forward operators. The results of the neural network forward operators are very similar to the results from the radiative transfer simulations above, indicating that the training was accurate and the prediction errors of the neural networks are small. Small deviations between the Monte Carlo simulations and the neural networks are expected due to the random noise present in the Monte Carlo simulations.

3.3.6 Discussion

Three-dimensional radiative effects are important but often neglected due to computational reasons. In this work, a fast forward operator for polarized 3D radiative transfer in the visible wavelength range was introduced. For this, a new approximation of three-dimensional cloud geometry for polarized radiative transfer in the visible wavelength range, the InDEpendent column local halF-sphere ApproXimation (IDEFAX), was developed. Different cloud geometry approximations were tested on their ability to reproduce 3D radiative effects. Three-dimensional radiative effects were best reproduced by an independent column approximation, where each simulated pixel is represented by a field of half-spherical clouds defined by the surface orientation zenith and azimuth angles and the cloud fraction. The approximation of 3D cloud geometry with the IDEFAX has only three additional parameters defining the cloud geometry compared to the plane-parallel ICA. It is simple

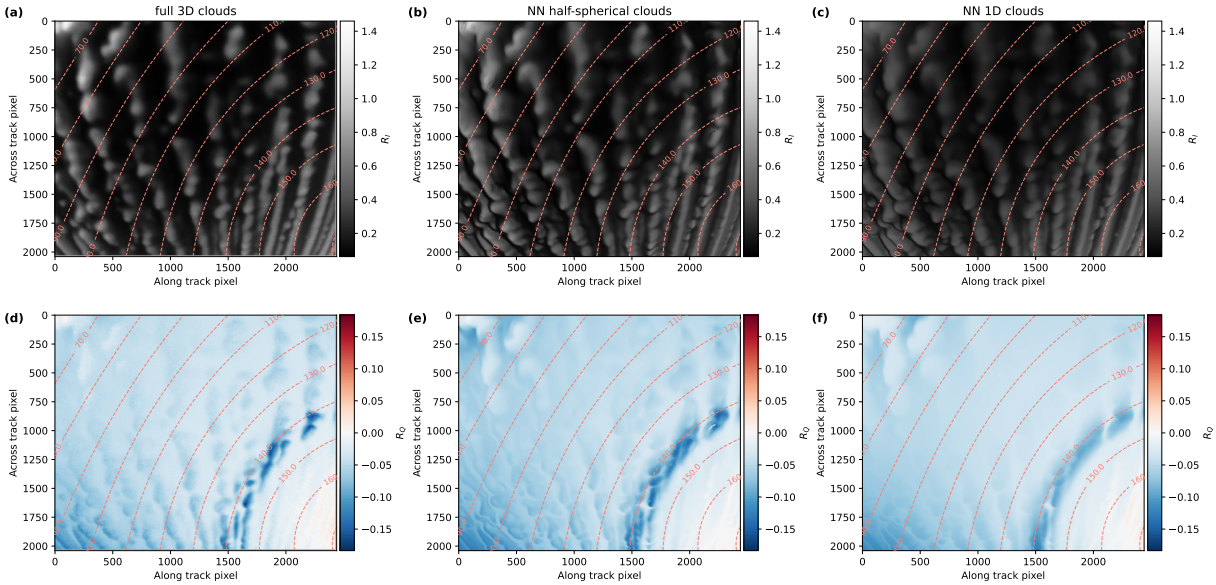

Figure 3.22: Simulation results of I and Q for the green color channel of specMACS with the neural network trained for 1D clouds in panels **(c, f)** and for half-spherical clouds with the IDEFAX in panels **(b,e)**. The simulations correspond to the radiative transfer simulations in Fig. 3.20 and use the same input parameters for every pixel. The dashed lines indicate the scattering angles.

enough to allow for tabulation of simulated radiances such that 3D cloud geometry can directly be accounted for in retrievals. In addition to the cloud fraction of the considered cloud field, only local information is needed for every column. The implementation of the IDEFAX is thus as simple as for the plane-parallel ICA.

A forward operator based on a simple look-up table would have been computationally expensive due to the large number of parameters defining cloud and viewing geometry. Thus, the look-up table was replaced with artificial neural networks for both the IDEFAX and the plane-parallel ICA. The neural network forward operators allow for very fast inference of the first three Stokes vector components I, Q, and U with only small memory requirements and can directly be used for retrievals. They are constructed to be used for (multi-angle polarimetric) retrievals with the polarization-resolving cameras of the specMACS instrument but could, however, also be adapted for other polarimetric measurements. The prediction errors of the trained neural networks are small compared to typical measurement uncertainties of polarimetric instruments.

The IDEFAX and the neural network forward operators were validated against 3D radiative transfer simulations with MYSTIC for a realistic field of low-level Arctic mixed-phase clouds simulated with the WRF model. There was a significant improvement towards full 3D simulations with the introduced IDEFAX compared to plane-parallel clouds in the classical ICA, which are usually assumed for retrievals. Due to the implementation with neural networks, the computation time of radiances with the IDEFAX is comparable to the plane-parallel ICA and about 5 orders of magnitude faster than 3D radiative transfer simulations with MYSTIC for the shown example.

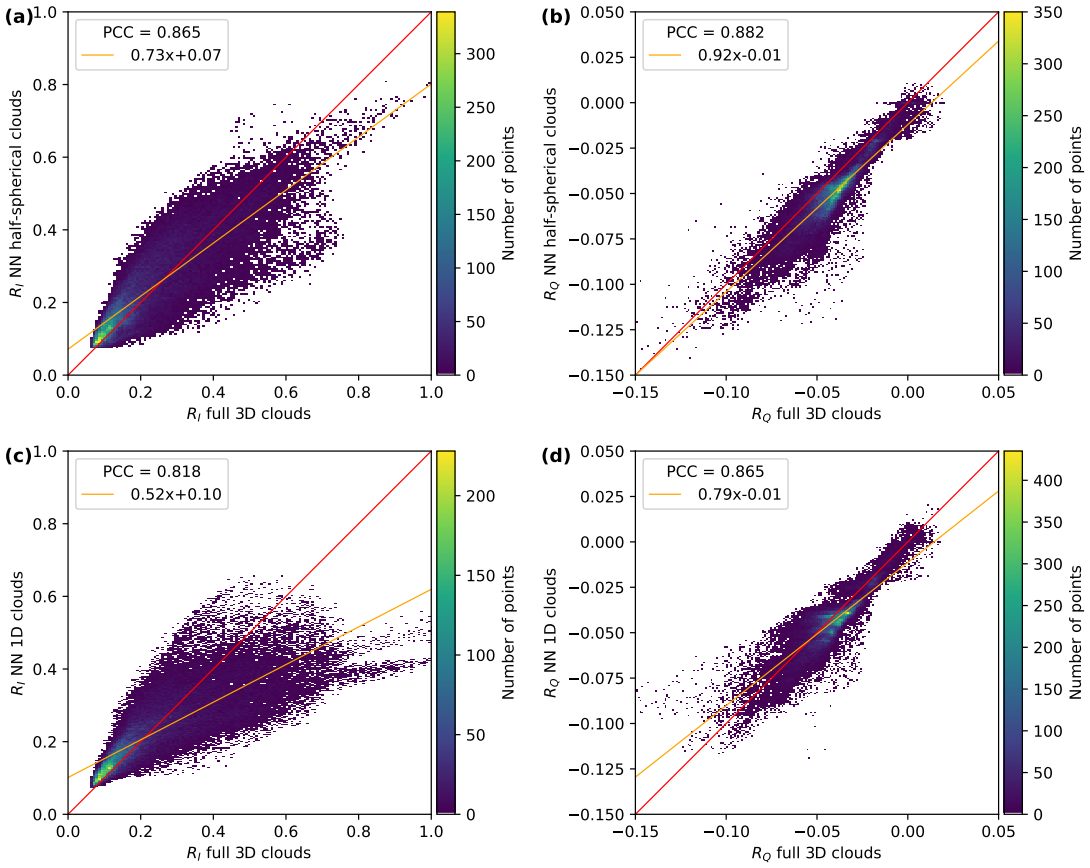

Figure 3.23: Scatter plots of the simulations with the neural networks for half-spherical clouds with the IDEFAX and one-dimensional clouds against the full three-dimensional simulation for R_I **(a, c)** and R_Q **(b, d)**. Panels **(a)** and **(b)** show the comparison for half-spherical clouds, panels **(c)** and **(d)** show the comparison for one-dimensional clouds. The red curve represents the identity, and the orange curve shows a linear fit to the data. The fit parameters and the Pearson correlation coefficients (PCC, corresponding to the R value) are given in the legends.

The introduced IDEFAX and forward operators are, in principle, also applicable to other multi-angle polarimetric measurements such as measurements by the Research Scanning Polarimeter (Cairns et al., 1999), AirHARP (Martins et al., 2018), SPEX airborne (Smit et al., 2019), AirMSPI (Diner et al., 2013), or POLDER (Deschamps et al., 1994). Potential further applications might include the field of data assimilation. For example, the fast forward operators used for the assimilation of satellite images (Scheck, 2021; Baur et al., 2023) so far include only the cloud top inclination correction by Scheck et al. (2018) for thick clouds and could be improved by applying the IDEFAX for optically thinner clouds. The number of input parameters of the neural networks could be extended, more dimensions could be included, or the parameter ranges could be adjusted for other polarimetric measurements, for new retrievals, or model applications.

A potential improvement of the neural network training (especially if more parameters are included) could be the application of Fourier feature mapping to improve the learning of

high-frequency features and reduce the spectral bias (Tancik et al., 2020). This could help to further reduce biases and errors, especially for non-linear features such as the cloudbow and the non-linear dependence of the radiances on viewing and orientation geometry angles, which are difficult to learn.

For the approximation itself and the validation, some assumptions were made. The effective radii were set to constant values for the radiative transfer simulations with the WRF cloud field. Thus, the effect of spatial variations in the effective radii was excluded here, as the focus was on 3D cloud geometry. In the visible wavelength range, variations of the effective radius affect mostly the cloudbow, which is highly sensitive to the cloud droplet size distribution. The cloudbow, however, is caused by single scattering and thus not strongly influenced by 3D radiative effects.

Moreover, the IDEFAX and the ICA with plane-parallel clouds assume homogeneously mixed clouds, whereas the clouds obtained from the WRF simulations have a layered structure, with liquid at cloud top and ice below, as observed in typical Arctic mixed-phase clouds. To investigate the impact of this assumption, the validation in Sect. 3.3.5 was repeated for pure liquid clouds (not shown). The mixed-phase clouds were converted to liquid clouds by keeping the total optical thickness and thus the 3D cloud geometry conserved. The analysis with pure liquid clouds showed similar results. Thus, the additional uncertainty caused by the assumption of homogeneously mixed clouds and the definition of the ice fraction is small for the cloud case shown. The ice fraction here can be interpreted as an effective ice fraction of a homogeneously mixed cloud that has the same radiative effect as a layered cloud.

Finally, there could be an influence of the horizontal resolution with which the cloud surface orientation angles for the half-spherical clouds of the IDEFAX are computed. The triangular surface mesh used for the computation of the surface orientation angles in this study was constructed with a spatial resolution of 100 m. The simulated clouds were comparably smooth, but measurements of real clouds are generally more structured, and the resolution used for the description of the cloud surface is more important. To quantitatively investigate which spatial scales of cloud geometry variations dominate the 3D radiative effects, cloud simulations with higher horizontal resolution would be necessary. In addition, different instrument resolutions could also be studied in the future.

The introduced IDEFAX works well for the shown case of low-level Arctic mixed-phase clouds. In principle, the IDEFAX should be applicable to other cumuliform clouds whose 3D geometry resembles a half-spherical shape. On the other hand, the best agreement with the plane-parallel assumption was found for stratiform clouds (Di Girolamo et al., 2010). Thus, depending on the morphology of the observed cloud, either a plane-parallel assumption in the classical ICA for very flat stratiform clouds or the IDEFAX for cumuliform clouds will be more appropriate. However, the quantification of the transition region between the two cases remains challenging. Further validation studies are needed to test the IDEFAX for other cloud cases and investigate how generalizable it is.

3.4 Polarized retrieval of cloud thermodynamic phase partitioning

The content of this section was already published in Weber et al. (2025d), except for the additional uncertainty assessment in Sect. 3.4.5 and parts of the discussion in Sect. 3.4.6.

As part of this work, a new quantitative retrieval method of cloud thermodynamic phase partitioning using multi-angle polarimetric imaging was developed. Liquid water and ice have different shapes and different optical properties, resulting in different polarization signals. Using the polarization signal is therefore a possibility to estimate the cloud thermodynamic phase, which is representative for the cloud top. The basic idea of the retrieval is to fit simulated multi-angle signals of the second Stokes vector component Q (describing linear polarization) along the scattering plane to measured multi-angle signals of Q to determine the ice fraction, which is here defined as the ratio of the ice optical thickness to the total optical thickness. For the optimization, the neural network forward operator for polarized 3D radiative transfer introduced in Sect. 3.3 is used, assuming either plane-parallel clouds or using the InDEpendent column local halF-sphere ApproXimation (IDEFAX), where the 3D cloud geometry is accounted for. The retrieval of cloud thermodynamic phase partitioning is explained in the following Sect. 3.4.1. Next, the vertical signal location of the retrieved ice fraction is characterized in Sect. 3.4.2. Moreover, the retrieval was validated using synthetic measurements computed with the Monte Carlo radiative transfer solver MYSTIC (Mayer, 2009; Emde et al., 2010) operated in libRadtran (Mayer and Kylling, 2005; Emde et al., 2016) for idealized cloud cases and for realistic low-level Arctic mixed-phase clouds, which were simulated with the Weather research and Forecasting (WRF) model (Skamarock et al., 2019). The results are summarized in Sect. 3.4.3. Afterward, the retrieval was applied to measurements of the 2D RGB polarization-resolving cameras of the specMACS instrument (Ewald et al., 2016; Weber et al., 2024) taken during the HALO–$(\mathcal{AC})^3$ campaign (Wendisch et al., 2024; Ehrlich et al., 2025) in Sect. 3.4.4. Finally, an additional uncertainty assessment was carried out whose results are described in Sect. 3.4.5, followed by a discussion in Sect. 3.4.6.

3.4.1 Retrieval description

As discussed by Goloub et al. (2000), the polarization signal is sensitive to cloud thermodynamic phase since liquid water and ice have different optical properties. While liquid cloud droplets are spherical, ice crystals have irregular shapes with varying complexities and thus different (polarized) scattering phase functions. Figure 3.24 shows radiative transfer simulations of the Stokes vector components I (a) and Q (b) along the scattering plane for a homogeneously mixed plane-parallel cloud with a total optical thickness of 5 and varying ice fractions. The ice fraction f_{ice} is here defined as the fraction of the ice optical thickness

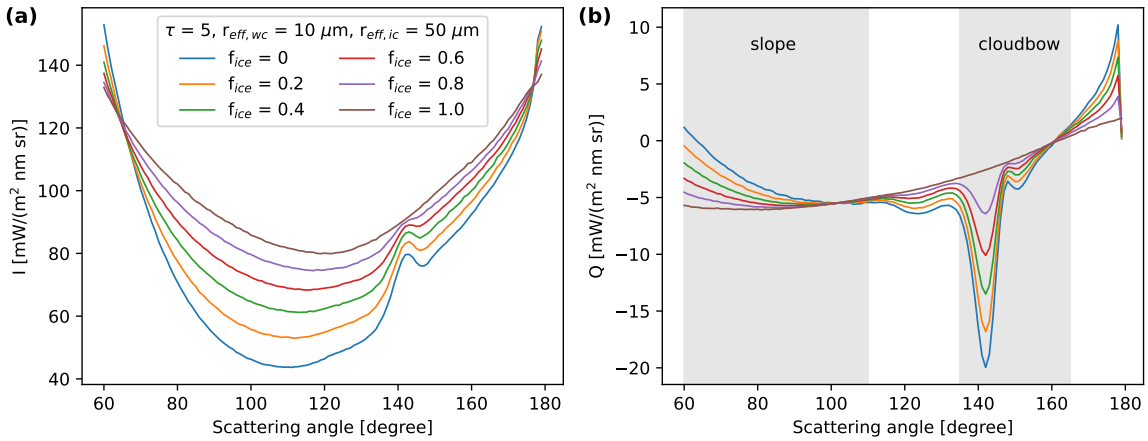

Figure 3.24: Simulation of I **(a)** and Q **(b)** along the scattering plane for a homogeneously mixed plane-parallel cloud with a total optical thickness 5 and varying ice fractions. The simulations were performed for 550 nm wavelength, a solar zenith angle of 70°, and using the ice optical properties by Yang et al. (2013) as implemented by Emde et al. (2016) for moderately rough 8-column aggregates. Effective radii for liquid and ice clouds were 10 μm and 50 μm, respectively.

to the total optical thickness

$$f_{\text{ice}} = \frac{\tau_{\text{ice}}}{\tau_{\text{liquid}} + \tau_{\text{ice}}}. \tag{3.26}$$

The simulations were performed using the library for radiative transfer libRadtran (Mayer and Kylling, 2005; Emde et al., 2016) and the Monte Carlo solver MYSTIC (Mayer, 2009; Emde et al., 2010; Buras and Mayer, 2011). Focusing on the polarization signal Q in Fig. 3.24b, there are three angular ranges that are sensitive to cloud thermodynamic phase partitioning. In the cloudbow range from 135° to 165° scattering angle, the amplitude of the minimum at around 140° scattering angle decreases with increasing ice fraction until no minimum is visible anymore. This minimum is the so-called cloudbow, which is formed by scattering on (spherical) liquid cloud droplets. Observation of the cloudbow indicates the presence of liquid water and absence of the cloudbow a pure ice cloud. The cloudbow is also strongly sensitive to the cloud droplet size distribution and the effective radius and variance of the cloud droplet size distribution can be derived from cloudbow measurements using the cloudbow retrieval by Pörtge et al. (2023). Similarly, the glory close to 180° backscatter direction is caused by scattering on liquid cloud droplets and is not visible for pure ice clouds. The glory angular range is, however, outside the field of view of the specMACS instrument for large solar zenith angles as in the Arctic and covers only a small angular range. Therefore, the glory signal is not used for the retrieval. Finally, the slope of the polarization curve changes depending on the partitioning between liquid water and ice in the angular range between 60° and 110°, which we therefore call slope range. Increasing ice fractions lead to a less negative slope.

The basic idea of the retrieval is to fit simulated multi-angle signals of Q as in Fig. 3.24b to measured signals, similarly to the cloudbow retrieval of cloud droplet size distribution. Depending on the viewing and solar geometry, this fit is done for the cloudbow range

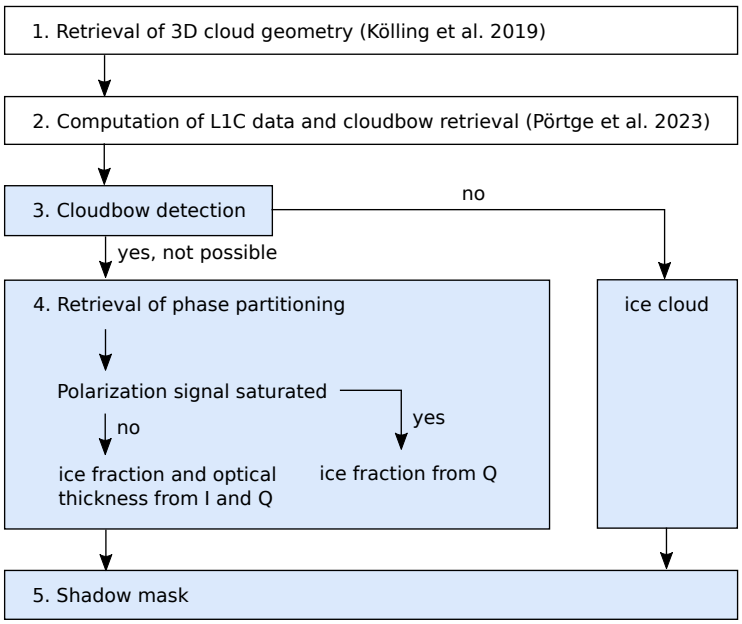

Figure 3.25: Overview of the different retrieval steps.

or the slope range. An overview of the different retrieval steps is given in Fig. 3.25 and the individual retrieval steps are explained in more detail in the following sections. First, the stereographic retrieval of 3D cloud geometry by Kölling et al. (2019) is applied to the measurements. The obtained information is then used to identify cloud targets and geolocate them to compute so-called L1C data, which is aggregated signals of observations at different scattering angles for the individual targets (Pörtge et al., 2023). In case the cloudbow range is covered, the cloudbow retrieval by Pörtge et al. (2023) is applied to determine the effective radius and variance of liquid cloud droplets. After these preparatory steps, the actual phase partitioning retrieval starts. At the beginning, a simple cloudbow detection is performed. If the cloudbow is geometrically possible but not visible, the cloud consists of pure ice and the ice fraction equals to 1. If a cloudbow is detected, the cloud is either a liquid water or a mixed-phase cloud and the phase partitioning is retrieved in step 4. Here, cases where the polarization signal is saturated and not saturated are distinguished. In the former case, the ice fraction is directly derived from a fit of Q. In the latter case, the polarization signal is also dependent on the optical thickness and a combination of I and Q is used to derive both ice fraction and optical thickness. For the optimization, the neural network forward operator for polarized 3D radiative transfer by Weber et al. (2025c) introduced in Sect. 3.3 is used, assuming either one-dimensional clouds, as it is done in most retrievals, or the IDEFAX accounting for 3D cloud geometry. In the IDEFAX, the 3D cloud geometry is approximated through an independent column approximation, where each column is represented by an independent field of half-spherical clouds. The field of half-spherical clouds is defined by the local surface orientation zenith and azimuth angles and the cloud fraction. The application of the IDEFAX is possible since information about 3D cloud geometry is available from the stereographic retrieval. Finally, a geometric

shadow mask is applied to the results since the cloudbow retrieval and the retrieval of cloud thermodynamic phase partitioning are not accurate in shadow regions. All steps 1 to 5 are described in more detail in the following Sect. 3.4.1 to 3.4.1.

Retrieval of 3D cloud geometry

The first step of the retrieval is the stereographic reconstruction of 3D cloud geometry applying the method by Kölling et al. (2019). The stereographic retrieval detects features with high contrast in measurements of the unpolarized intensity. While flying above a scene, the same features are viewed from different perspectives, which allows for triangulation and the derivation of the location of the features in 3D space. For this, features are identified and matched in successive images such that, in the end, a point cloud describing the cloud surface in 3D space is obtained. A mesh of triangular surfaces describing the cloud surface can then be constructed from the point cloud through Poisson surface reconstruction as described in Kölling (2020). This triangular surface mesh is used for the geometric shadow mask in Sect. 3.4.1 and to compute cloud surface orientation angles for every identified cloud target for the parameterization of 3D cloud geometry in the IDEFAX forward operator. For each observed target on a cloud, the closest point on the surface mesh and the corresponding surface normal of the mesh are computed. The orientation zenith and azimuth angles are then derived from the surface normal, the local zenith, and the vector pointing towards the sun.

Computation of L1C data and cloudbow retrieval

In the second step, L1C data is computed from the measurements with the method by Pörtge et al. (2023), which was extended from the cloudbow range to cover the complete scattering angle range. Here, L1C data means aggregated signals of different target points on the cloud for all observed viewing angles. For this, clouds are detected with a cloud mask and cloud targets are identified. Geolocalization of the targets is then possible using the cloud top heights from the stereographic retrieval of cloud geometry and the known viewing geometry. Finally, signals of the individual cloud targets for different viewing angles are aggregated from successive images. The multi-angle signals are processed to an angular resolution of 0.3° inside the cloudbow range in order to resolve the large gradients in the cloudbow range and 1° otherwise.

In addition, the cloudbow retrieval of effective radius and variance of the cloud droplet size distribution (Pörtge et al., 2023) is performed if the cloudbow range is covered. The cloudbow fit uses the scattering angle range from 135° to 165° and is applied if at least the minimum cloudbow range from 136.9° to 160° (Shang et al., 2015) is observed. For the computation of L1C data, the temporal resolution of the measurements was reduced to 4 Hz, which is sufficient for the given angular resolution and reduces computation time.

Cloudbow detection

The first part of the actual thermodynamic phase retrieval is the cloudbow detection, whose aim is to provide a pre-selection of the data. The basic idea of the cloudbow detection is to check whether a minimum is present in the polarization signal in the cloudbow range (see Fig. 3.26b). The cloudbow is formed by scattering on spherical liquid water droplets and is thus an indication of cloud thermodynamic phase. If the observation of the cloudbow is geometrically possible and the cloudbow is visible, one can conclude that the cloud is either a liquid water or a mixed-phase cloud. Otherwise, it is a pure ice cloud and the ice fraction $f_{\text{ice}} = 1$. In case the geometry does not allow for observing the cloudbow, no prior information about the thermodynamic phase of the cloud is available and the retrieval of cloud phase partitioning is continued with the next step. Here, the cloudbow was considered to be geometrically possible if at least 135° to 140° scattering angle were observed, such that at least a large part of the minimum is covered. To decide whether a cloudbow is detected, the minimum of Q between 135° and 165° or the maximum observed scattering angle is computed. Then, the maximum between 135° and the scattering angle of the minimum is determined. If the difference between the maximum and minimum is larger than the average standard deviation of the measured signal, the observation is classified as cloudbow.

In order to quantify the accuracy of the cloudbow detection method, 2000 measured signals were labeled manually and the confusion matrix was computed from the manual labels and the classification from the cloudbow detection described above. To reduce the error of the derived ice fractions, the number of signals with cloudbow that are falsely classified as no cloudbow should be minimized, since this would lead to an overestimation of the ice fraction. This is the reason for the comparable generous choice of one standard deviation difference for detecting a cloudbow. If too many signals without cloudbow are falsely classified as cloudbow, the computation time of the retrieval increases, but the accuracy of the retrieved ice fraction is not affected. From the 1688 signals with cloudbow in the dataset, 4 % were falsely classified as no cloudbow, whereas 23.4 % of the signals without cloudbow were detected as cloudbow. During the manual labeling, it was sometimes difficult to decide whether a cloudbow was still visible or not. To reduce personal biases, the manual labeling was done by different people.

Retrieval of cloud phase partitioning

The core of the phase retrieval is the retrieval of cloud phase partitioning in step 4. The basic idea is to fit radiative transfer simulations to measured multi-angle signals of I and Q as in Fig. 3.24. Depending on the viewing geometry, this fit is done either for the cloudbow range for scattering angles between 135° and 165° or for the slope range between 60° and 110° scattering angle. The minimum angular range that must be observed for the cloudbow range is from 136.9° to 160° such that the cloudbow retrieval can be applied. For the slope range, scattering angles between at least 80° and 110° scattering angle must be measured since the derived ice fractions become very uncertain for smaller angular ranges as the

sensitivity decreases (see Fig. 3.24) and smaller scattering angles are not always observed due to the viewing geometry of the instrument.

A simple look-up table containing the radiative transfer simulations is not possible due to the large number of (known) parameters the measurements are sensitive to. These include the viewing and solar geometry (solar zenith angle, viewing zenith and azimuth angle, sensor height) which are known from the aircraft data, cloud top height and cloud surface orientation zenith and azimuth angles obtained from the stereographic retrieval, effective radius and variance of the cloud droplet size distribution from the cloudbow retrieval, and the cloud fraction needed for the IDEFAX which is computed using the cloud mask by Pörtge et al. (2023). Unknown parameters are the total optical thickness and the ice fraction. Hence, the neural network forward operator for polarized 3D radiative transfer by Weber et al. (2025c) and introduced in Sect. 3.3 was used for the fit. The neural networks predict I and Q converted to reflectivity for the different color channels of the polarization-resolving cameras of specMACS under the assumption of plane-parallel clouds or using the IDEFAX with half-spherical clouds. It was shown by Weber et al. (2025c) and in Sect. 3.3 that the complex 3D cloud geometry of low-level Arctic mixed-phase clouds can effectively be approximated through a half-spherical cloud that is defined by a surface orientation zenith and azimuth angle and embedded in a cloud field with a specified cloud fraction. Depending on the observed cloud type, generally either the application of the plane-parallel assumption or the IDEFAX will be more appropriate. Moreover, the neural networks assume an ice effective radius of $50\,\mu$m, the habit of the 8-column aggregates with moderate roughness from Yang et al. (2013), and the ocean reflection function by Cox and Munk (1954a,b) combined with the Fresnel reflection matrix to include polarization. The default wind speed if no other information is available is $10\,\mathrm{ms}^{-1}$. The wind speed determines the shape of the sunglint and, therefore, might influence the measurements. However, due to the large solar zenith angles in the Arctic, the sunglint is outside the field of view of the instrument. Mixed-phase clouds are assumed to be homogeneously mixed in the forward operator. Thus, the retrieved ice fraction has to be interpreted as an effective ice fraction under the assumption of a homogeneously mixed cloud. The influence of this assumption and the vertical attribution of the retrieved ice fraction will be further discussed in Sect. 3.4.2 and 3.4.3.

I and Q, of course, also depend on the optical thickness. Figure 3.26 shows simulation results for a homogeneously mixed cloud with a constant ice fraction of 0.5 for varying optical thickness values. In contrast to I, which still grows for an optical thickness of 10, Q saturates quickly with increasing optical thickness. If the polarization signal is saturated, it is independent of the optical thickness and the ice fraction can directly be derived from Q. Otherwise, I and Q have to be combined to simultaneously derive the optical thickness and ice fraction. The uncertainties of the derived ice fraction in this case are larger as I is more strongly affected by 3D radiative effects than Q and both have different penetration depths, as will be discussed in Sect. 3.4.2 and 3.4.3. To decide whether the signal is saturated or not, measurements of the total intensity I are compared to simulations with a worst-case assumption of $f_{\mathrm{ice}} = 1$, since ice clouds are brighter than liquid clouds (see Fig. 3.24a). The measured polarization signal is considered saturated if the measurement of I of the

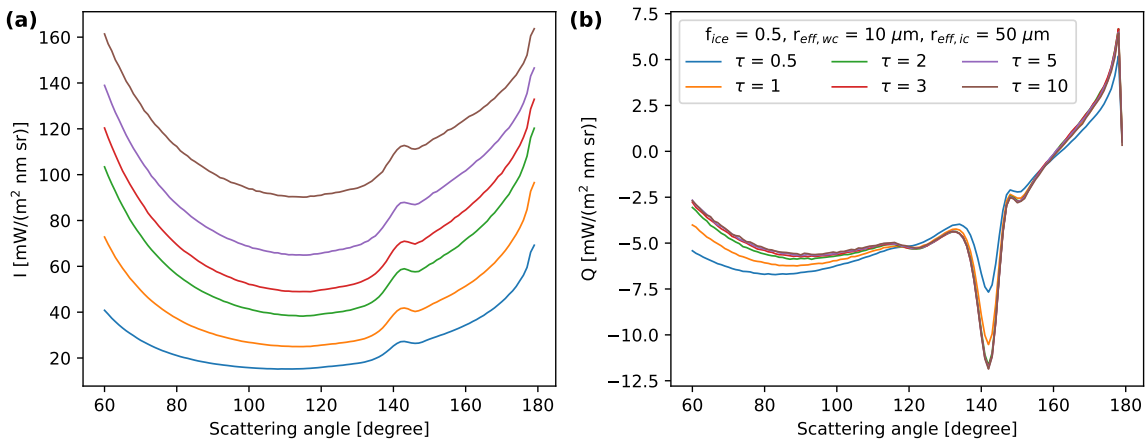

Figure 3.26: Simulation of I **(a)** and Q **(b)** along the scattering plane for a homogeneously mixed plane-parallel cloud with an ice fraction of 0.5 and varying total optical thickness. The simulations were performed for 550 nm wavelength, a solar zenith angle of 70°, and using the ice optical properties by Yang et al. (2013) as implemented by Emde et al. (2016) for the habit column_8elements with moderate roughness. Effective radii for liquid and ice clouds were 10 μm and 50 μm, respectively.

closest to nadir direction is larger than the calculated I for an optical thickness threshold value of 5. This very conservative threshold value ensures that unsaturated signals are not misclassified as saturated signals, which would introduce errors in the derived ice fraction.

For saturated polarization signals, the ice fraction is derived by minimizing the root mean square error (RMSE) between modeled multi-angle signals of Q and measurements of Q for the respective scattering angle range:

$$\mathrm{RMSE_Q}[f_{\mathrm{ice}}] = \sqrt{\frac{1}{n}\sum_{i=1}^{n}(R_{\mathrm{Q,meas}}(\theta_i) - R_{\mathrm{Q,model}}[f_{\mathrm{ice}}](\theta_i))^2}, \tag{3.27}$$

where θ is the scattering angle and I and Q are converted to reflectivity as in Weber et al. (2025c) and Eq. 3.24 in Sect. 3.3.

If the polarization signal is not saturated, total optical thickness and ice fraction are optimized simultaneously using I and Q by minimizing the combined RMSE of I and Q:

$$\mathrm{RMSE}[f_{\mathrm{ice}}, \tau] = (\mathrm{RMSE_I}[f_{\mathrm{ice}}, \tau] + \epsilon) \cdot (\mathrm{RMSE_Q}[f_{\mathrm{ice}}, \tau] + \epsilon), \tag{3.28}$$

where $\epsilon = 1 \times 10^{-4}$ is a small number. I and Q are not independent. The product form for the combined RMSE was chosen instead of a commonly used weighted sum since it showed better results.

Different non-linear optimization methods, including a global search and gradient-based minimization methods, were tested. Neural networks are, by definition, differentiable and gradients can be computed through backpropagation. Thus, gradient-based optimization methods could, in principle, be applied without having to compute numerical gradients. Nevertheless, in the case of the phase partitioning retrieval, the global search was more

computationally efficient. The global search was implemented as a coarse search followed by a fine search with final step sizes of 0.01 and 0.02 for the ice fraction in the saturated and unsaturated cases, respectively, and 0.2 for the optical thickness. The reason for the coarser resolution in the unsaturated case is the higher computation cost due to the combined retrieval of optical thickness and ice fraction and increased uncertainties of the results from the combined retrieval due to a larger influence of, e.g., 3D radiative effects.

Shadow mask

Finally, a geometric shadow mask is applied to the retrieval results since both the cloudbow retrieval as well as the phase partitioning retrieval are influenced by shadows, which affect the measured signals. The geometric shadow mask is computed with the surface meshes from the stereographic retrieval, similarly to Kölling (2020). A cloud target is inside a shadow if the vector from the target point on the cloud to the sun intersects the cloud surface mesh. Intersections within 100 m distance to the target point are not counted as intersections for a shadow. Such a geometrical shadow mask is more accurate compared to shadow masks based on a brightness threshold since the brightness of a signal is influenced by the solar geometry, different 3D radiative effects due to cloud geometry, and variations of cloud microphysics, whereas the stereographic retrieval provides accurate information about 3D cloud geometry (Volkmer et al., 2024).

3.4.2 Vertical attribution of the retrieved ice fraction

Before the retrieval is validated with synthetic data, the representative altitude of the signal respectively the retrieved ice fraction will be analyzed. Passive retrievals, such as the presented polarimetric retrieval of cloud phase partitioning, do not provide information about the vertical profile of the retrieved quantity. Thus, assumptions have to be made for the vertical profile and the retrieved quantities have to be referred to as effective quantities under the respective assumption. For the phase partitioning in low-level Arctic mixed-phase clouds, there are two possible extreme cases for the assumption of the vertical profile. One is a completely homogeneously mixed cloud, as discussed before, the other one is a cloud with a pure liquid layer on top of a pure ice layer. The forward operator used for the retrieval assumes homogeneously mixed clouds. Moreover, the ice fraction is obtained from the polarization signal, which is dominated by the first scattering order and thus representative for the cloud top. Hence, the retrieved ice fraction is defined here as the effective ice fraction of the uppermost cloud layer from cloud top up to a certain optical thickness threshold under the assumption of a homogeneously mixed cloud.

To find this effective optical thickness threshold, respectively, the cloud depth to which the retrieval is sensitive to, simulations of a plane-parallel two-layer cloud and a plane-parallel cloud with a linear ice fraction profile in the vertical direction (see Fig. 3.27) were simulated and the retrieval was applied to the simulations. The two-layer cloud consisted of a plane-parallel liquid cloud with varying optical thickness (τ_{liquid}) above an ice cloud as visualized in Fig. 3.27a. The total optical thickness (τ_{tot}) of the cloud was 5. The ice

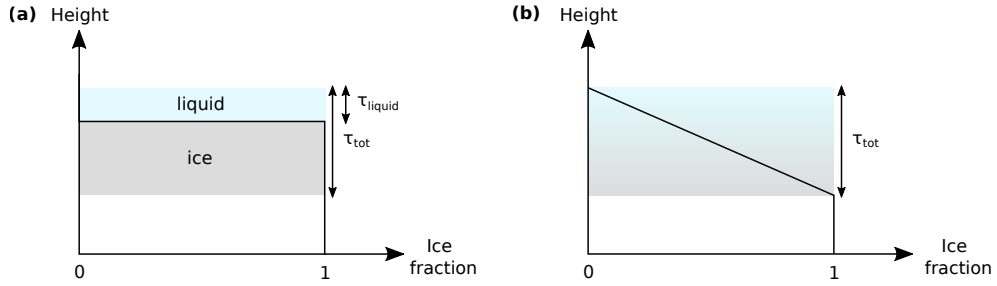

Figure 3.27: Definition of the two-layer cloud **(a)** and the linear profile cloud **(b)**.

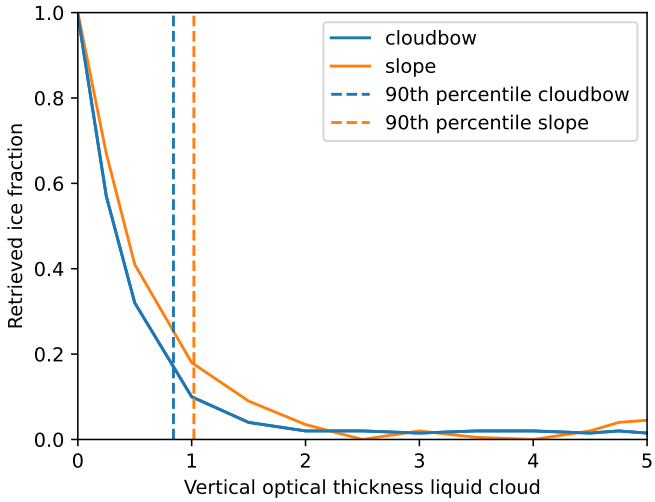

Figure 3.28: Retrieved ice fractions of the green color channel for the slope and cloudbow range for a two-layer cloud with a liquid cloud with varying optical thickness above an ice cloud, assuming a saturated polarization signal. The total optical thickness was 5, the solar zenith angle 75°. The dashed lines denote the 90th percentile of the distribution used as vertical optical thickness threshold for the cloudbow and slope range.

fraction was retrieved with the forward operator for plane-parallel clouds for the cloudbow and the slope range for every simulated liquid cloud optical thickness. Figure 3.28 shows the retrieved ice fractions for a solar zenith angle of 75° as in the synthetic data used in Sect. 3.4.3 as a function of the liquid cloud optical thickness. From the obtained ice fractions, the optical thickness of the cloud layer to which the retrieval is sensitive to could be determined. For a liquid cloud with an optical thickness larger than about 2, the ice cloud below is not detected anymore and the retrieved ice fraction is close to 0. The vertical optical thickness threshold was then defined through the 90th percentile of the distribution in Fig. 3.28. The retrieved ice fraction is interpreted as the mean ice fraction of the layer from cloud top to the optical thickness threshold. For the cloudbow range and the slope range an optical thickness threshold of about 0.8 and 1.0 was obtained for the considered case.

In addition to the two-layer cloud, a plane-parallel cloud with a linear profile of the ice

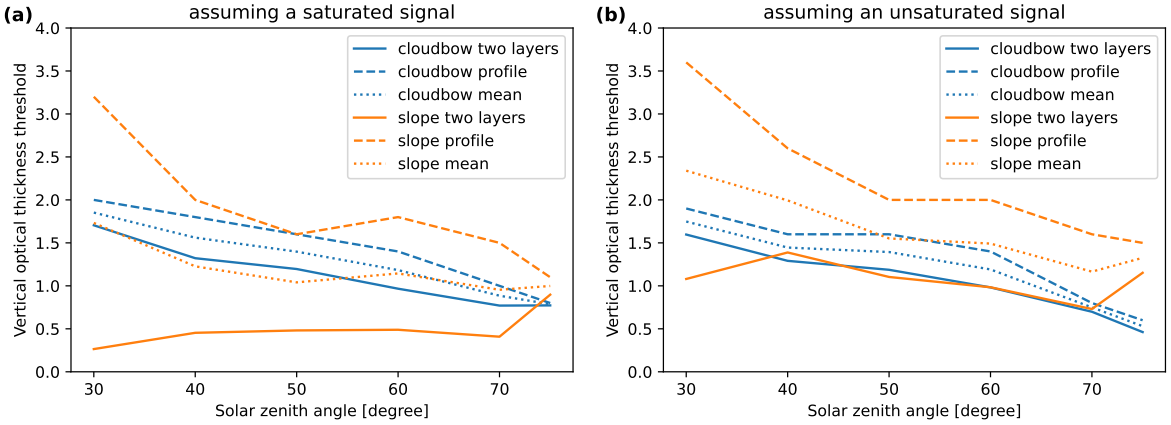

Figure 3.29: Vertical optical thickness thresholds obtained from the two-layer cloud and the profile cloud and their mean for different solar zenith angles. **(a)** Results for the assumption of a saturated polarization signal. **(b)** Results for the assumption of an unsaturated polarization signal.

fraction from 0 at cloud top to 1 at cloud base (see Fig. 3.27b) was simulated and the phase partitioning retrieval applied. From the derived ice fraction, the optical thickness threshold was computed such that the average ice fraction from cloud top to the threshold was equal to the retrieved ice fraction. The obtained threshold values are denoted by the dashed lines in Fig. 3.29. As for all retrievals based on passive remote sensing, the vertical optical thickness to which the retrieval is sensitive to depends on the solar zenith angle. To quantify this dependence for the phase retrieval, the simulations of the two-layer cloud and the profile cloud were performed for different solar zenith angles and the vertical optical thickness threshold was determined for all cases. Figure 3.29 shows the obtained optical thickness thresholds for the slope and cloudbow range obtained from the two-layer cloud and the profile cloud as discussed above, together with their mean as a function of solar zenith angle. Panel (a) shows the results under the assumption that the polarization signal is saturated and panel (b) shows the unsaturated case. For smaller solar zenith angles, the signal is sensitive to a larger optical thickness relative to the cloud top and thus to a deeper cloud layer. For the cloudbow, the vertical optical thickness threshold varies between about 2 for 30° solar zenith angle to about 1 for 75° solar zenith angle for both the saturated and unsaturated cases. In addition, there is agreement between the threshold values determined for the two-layer cloud and the profile cloud. In contrast, the differences between the two are much larger for the slope angular range. The mean varies in a similar range compared to the cloudbow range for the saturated assumption. However, the vertical optical thickness threshold for the slope range is increased if the retrieval assuming an unsaturated polarization signal is applied. This can be expected as in the unsaturated case, the ice fraction is retrieved in a combined retrieval using I and Q. Since the cloudbow is dominated by the first scattering order, the penetration depth of I and Q is almost similar. For the slope range, the influence of multiple scattering is much larger and the penetration depth for I increased. Consequently, the vertical optical thickness threshold of the slope range is higher for an unsaturated polarization signal.

To conclude, we define the retrieved ice fraction as the average ice fraction from cloud top to an optical thickness threshold between about 1 and 2, depending on the solar zenith angle. For 75° solar zenith angle, the optical thickness threshold is about 0.8 for the cloudbow, 1.0 for the slope with a saturated polarization signal and 1.5 for the slope in the unsaturated case. These values will be used for the validation of the retrieval with synthetic data in Sect. 3.4.3.

3.4.3 Retrieval validation using synthetic data

To validate the presented retrieval and characterize its uncertainties, the retrieval was applied to synthetic data. The synthetic data was computed for clouds with varying complexity, for simple plane-parallel homogeneously mixed clouds, homogeneously mixed 3D clouds, and realistic 3D clouds. This allows to isolate the different contributions to the overall uncertainty, such as e.g. the effect of 3D cloud geometry.

Homogeneously mixed plane-parallel clouds

To begin with, the case of a homogeneously mixed plane-parallel cloud is analyzed. Such a cloud has a constant ice fraction throughout the cloud. Polarized radiative transfer simulations were done with MYSTIC for different ice fractions and the retrieval using the forward operator for plane-parallel clouds was applied to the data for both the cloudbow and the slope range. Table 3.6 summarizes the results for a cloud extending from 2 to 3 km height with a total optical thickness of 5, and a solar zenith angle of 70° assuming a saturated polarization signal for three different ice fractions. In addition, the results for the combined optimization of I and Q assuming an unsaturated signal are given in Table 3.7 for plane-parallel clouds with an optical thickness of 1, 2, and 5.

Generally, there is good agreement between the true simulated ice fractions and the retrieved values, with maximum deviations of the retrieved ice fractions of 0.03. In addition, the optical thickness is retrieved correctly. This validates the retrieval method itself. The small differences between the retrieval results assuming a saturated or unsaturated polarization signal are due to the different optimization methods in both cases. The difference between the different retrieved and true values also includes uncertainties of the forward operator, which are obviously small for plane-parallel clouds.

True ice fraction	0.1	0.5	0.9
Retrieved ice fraction cloudbow	0.11	0.51	0.90
Retrieved ice fraction slope	0.13	0.51	0.92

Table 3.6: True and retrieved ice fraction for a plane-parallel homogeneously mixed cloud assuming a saturated polarization signal (using only Q for the optimization) for the green color channel of the polarization-resolving cameras. The cloud was located between 2 and 3 km height, had a total optical thickness of 5 and the solar zenith angle was 70°. Liquid and ice effective radius were 10 μm and 50 μm, respectively.

True ice fraction	0.1	0.5	0.9	0.1	0.5	0.9	0.1	0.5	0.9
Retrieved ice fraction cloudbow	0.10	0.50	0.90	0.10	0.50	0.90	0.10	0.52	0.90
Retrieved ice fraction slope	0.08	0.50	0.90	0.08	0.48	0.90	0.10	0.50	0.90
True optical thickness	1.0	1.0	1.0	2.0	2.0	2.0	5.0	5.0	5.0
Retrieved optical thickness cloudbow	1.0	1.0	1.0	2.0	2.0	2.0	5.0	5.0	5.0
Retrieved optical thickness slope	1.0	1.0	1.0	2.0	2.0	2.0	5.0	5.0	5.0

Table 3.7: True and retrieved ice fraction and optical thickness for a plane-parallel homogeneously mixed cloud assuming an unsaturated polarization signal (using I and Q combined for the optimization) for the green color channel of the polarization-resolving cameras. The cloud was located between 2 and 3 km height, had a total optical thickness of 1, 2, and 5, respectively, and the solar zenith angle was 70°. Liquid and ice effective radius were 10 μm and 50 μm.

Homogeneously mixed 3D clouds

Realistic clouds generally have a 3D cloud geometry that differs from the plane-parallel cloud assumption. Thus, the retrieval errors introduced by 3D cloud geometry are analyzed next. Here, the clouds are still assumed to be homogeneously mixed with a spatially uniform ice fraction to focus on the geometry only.

A realistic cloud field was simulated with the WRF model (Skamarock et al., 2019) as described in Weber et al. (2025c) and Sect. 3.3.1. The WRF simulations were forced with ERA5 data for 2022-04-01 and performed with 100 m horizontal resolution. More details to the WRF simulations can be found in Weber et al. (2025c) and Sect. 3.3.1. The obtained cloud field was then used as input for polarized 3D radiative transfer simulations to compute synthetic observations of the specMACS polarization-resolving cameras. The radiative transfer simulations were performed with MYSTIC. The synthetic measurement data were computed as described in Volkmer et al. (2024). The simulated viewing geometries correspond to measurements during the HALO–$(\mathcal{AC})^3$ campaign on 2022-04-01 between 10:17:15 and 10:18:45 UTC with 1 Hz temporal resolution. In this time range, the solar zenith angle was 75.6°. A detailed description of the settings needed for the radiative transfer simulations to simulate realistic specMACS measurements is given in Volkmer et al. (2024). Figure 3.30 shows the RGB image and retrieved cloud top heights for the synthetic measurement data. The viewing geometry corresponds to the measurements at 10:18 UTC shown also in Fig. 3.35. On 2022-04-01 a cold air outbreak was observed in the Fram Strait. During cold air outbreaks, cold and dry polar air masses are advected off the sea ice edge across comparably warm open ocean (Fletcher et al., 2016a; Papritz and Spengler, 2017). The clouds formed in the initial phase of the cold air outbreak typically organize into cloud streets, which are also visible in Fig. 3.30. The average cloud top height is about 675 m. A comparison of Fig. 3.30 and 3.35 indicates that the obtained synthetic observations and thus the cloud field simulated with the WRF model are realistic. However, the modeled clouds are smoother compared to the observed ones, which is caused by the lower spatial resolution of the WRF simulations due to the high computational cost. In addition, Arteaga et al. (2024) compared WRF simulations of Arctic mixed-phase clouds to in situ and radar measurements and found discrepancies between model and observations

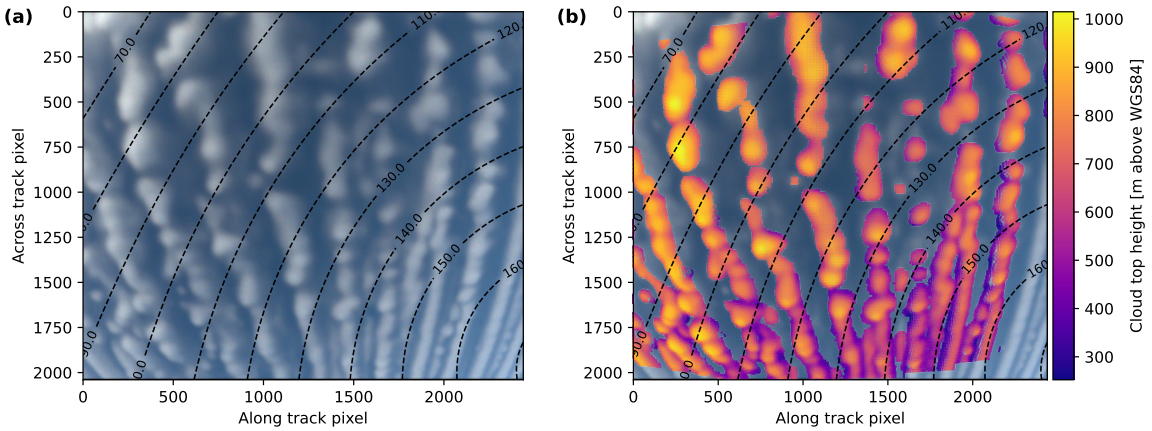

Figure 3.30: Simulation of the polLR camera of specMACS with the same viewing geometry as the measurements on 2022-04-01 at 10:18 UTC. **(a)** RGB image. **(b)** Cloud top height for all cloud targets. The dashed lines indicate the scattering angles.

such as an underestimation of ice crystal number concentrations by the model, but the WRF simulations were in general able to reproduce the overall structure of the clouds and the measured radar signals showed good agreement to the simulated signals. Thus, the synthetic measurements are suitable for a validation of the phase partitioning retrieval.

The cloud field obtained from the WRF simulations has a spatially non-uniform distribution of liquid water and ice. To study the isolated effect of the 3D cloud geometry on the retrieval results, the cloud field was converted to a field of homogeneously mixed clouds with a constant ice fraction of 0.5, keeping the total optical thickness and thus the 3D cloud geometry conserved. Then, synthetic measurements were computed through 3D radiative transfer simulations with MYSTIC as described above. Afterward, L1C data were computed from the synthetic data and the cloudbow and phase retrievals were applied as described in Sect. 3.4.1.

Figures 3.31 and 3.32 show retrieval results for the forward operators using the plane-parallel independent column approximation in the upper row and the IDEFAX in the lower row. The retrieved values in the lower right of the images correspond to the cloudbow range and the values in the upper left part to the slope range. Retrieval results are only available for parts of the images since only a 90 s period was simulated. Panels (a) and (d) display the retrieved ice fractions and optical thickness values, panels (b) and (e) the difference between retrieved and true values, and panels (c) and (f) histograms of the differences, including mean and standard deviation for the cloudbow and the slope range, respectively. The true ice fraction was 0.5 throughout the cloud field. For the optical thickness, the vertical optical thickness at the location of every cloud target point was computed from the modeled cloud field and used as ground truth since the total optical thickness is derived from the absolute intensity and represents the entire cloud column. The optical thickness is only retrieved at the cloud edges, where the clouds are optically thinner and the polarization signal is not saturated, and increases towards the centers of the clouds. In the future, the forward

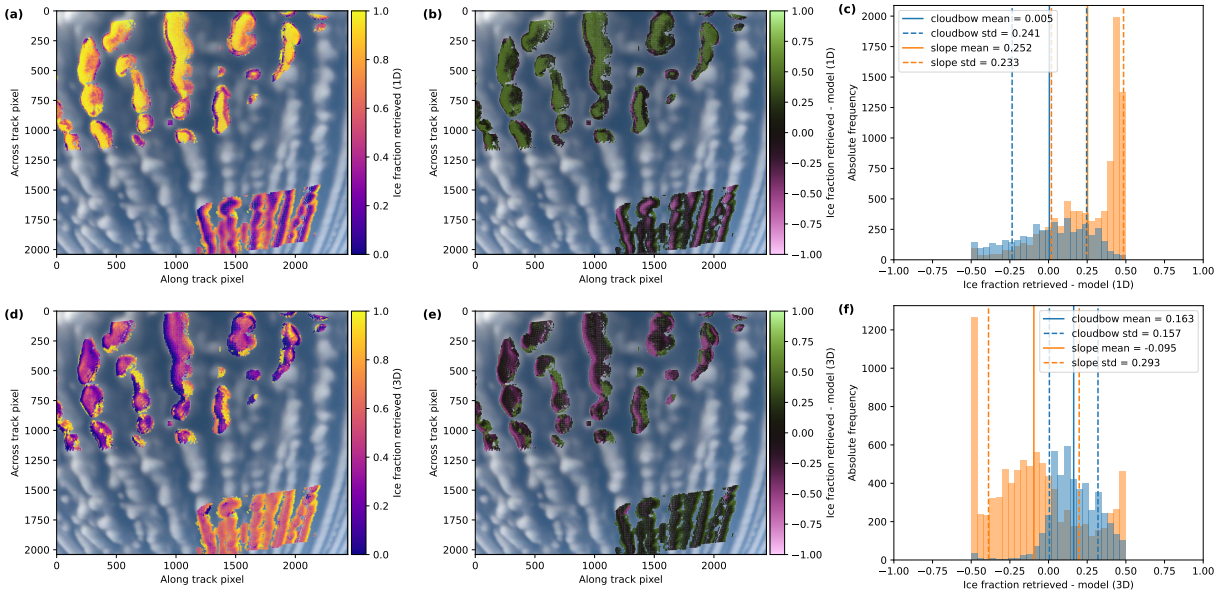

Figure 3.31: Retrieval results for the green color channel of the synthetic data for homogeneously mixed 3D clouds for the polLR camera of specMACS. **(a, d)** Retrieved ice fraction. **(b, e)** Difference between the retrieved ice fraction and the model ice fraction. **(c, f)** Histogram of the differences between retrieved and model ice fractions with mean and standard deviation for the cloudbow (blue) and the slope range (orange). The upper row **(a, b, c)** shows the results under the assumption of 1D clouds, the lower row **(d, e, f)** shows the results using the IDEFAX. The retrieved values in the upper left part of the images correspond to the slope range and the ones in the lower right part to the cloudbow range.

operator could be extended to larger optical thicknesses to derive the optical thickness for the entire clouds after the ice fraction is known. Due to the focus on phase partitioning and the significant increase in computation time for radiative transfer simulations of optically thicker clouds, the optical thickness range was restricted to smaller values in this work.

For both plane-parallel clouds and the IDEFAX, the performance of the ice fraction retrieval is different for the cloudbow range (lower right part of the images) and the slope range (upper left part of the images) in Fig. 3.31. The cloudbow range shows a small bias even for the plane-parallel assumption, with a mean difference between the retrieved and true ice fraction of 0.005±0.241. The application of the IDEFAX leads to a small overestimation of the ice fraction but significantly reduces the standard deviation with a difference of 0.163±0.157. In the slope range, the ice fraction is strongly overestimated under the plane-parallel assumption with an average difference between the retrieved and true values of 0.252±0.233. With the IDEFAX, the bias of the retrieved ice fraction is significantly reduced and the ice fraction is slightly underestimated with a difference of -0.095±0.293. Concerning the optical thickness shown in Fig. 3.32, the performance of the cloudbow and the slope range is more similar, with slightly smaller biases for the cloudbow range than for the slope range. For the cloudbow range, the IDEFAX shows a slightly larger bias but smaller standard deviation of the differences between the retrieved and true optical

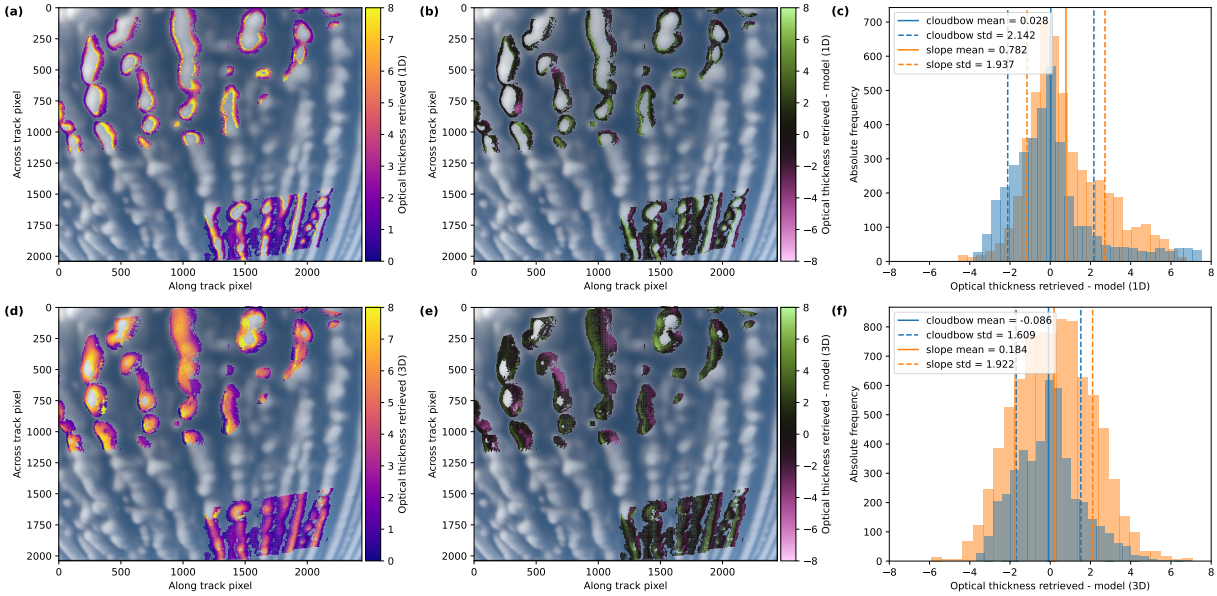

Figure 3.32: Retrieval results for the green color channel of the synthetic data for homogeneously mixed 3D clouds for the polLR camera of specMACS. **(a, d)** Retrieved optical thickness. **(b, e)** Difference between the retrieved optical thickness and the model optical thickness. **(c, f)** Histogram of the differences between retrieved and model optical thickness with mean and standard deviation for the cloudbow (blue) and the slope range (orange). The upper row **(a, b, c)** shows the results under the assumption of 1D clouds, the lower row **(d, e, f)** shows the results using the IDEFAX. The retrieved values in the upper left part of the images correspond to the slope range and the ones in the lower right part to the cloudbow range.

thickness with -0.086±1.609 compared to 0.028±2.142 for plane-parallel clouds. In the slope range, the IDEFAX reduces both the mean difference and the standard deviation from 0.782±1.937 for plane-parallel clouds to 0.184±1.922. The explanation for the deviations of the retrieved values from the true ice fraction and optical thickness is the deviation of the simulated polarization signals in the plane-parallel approximation and the IDEFAX from full polarized 3D radiative transfer simulations (see also Fig. 3.20 and 3.22). In addition, the larger area being classified as unsaturated (and thus the larger area with retrieved optical thickness values) for the IDEFAX is due to the differences between the simulated total reflectances, which were used for the classification as described in Sect. 3.4.1. For the plane-parallel approximation, the differences between retrieved and true ice fraction are especially large in the centers of the clouds, whereas the cloud sides dominate the error for the IDEFAX. The improvement of the results for the IDEFAX compared to the plane-parallel assumption is larger for the slope range than for the cloudbow range. This can be expected since the cloudbow is more strongly dominated by the first scattering order than the slope range and thus less affected by 3D radiative effects. As shown by Weber et al. (2025c) and in Sect. 3.3, 3D radiative effects can efficiently be approximated by the IDEFAX with half-spherical clouds for this type of clouds. However, the remaining 3D radiative effects still introduce retrieval errors as the standard deviations for the ice fraction

and optical thickness are still large and the biases are not negligible even for the IDEFAX. In addition, the uncertainty of the forward operator using the IDEFAX is slightly larger than the uncertainty of the plane-parallel forward operator (Weber et al., 2025c).

In principle, the retrieval errors due to 3D cloud geometry could be accounted for in the future, as 3D cloud geometry is known from the stereographic retrieval. Currently, full 3D radiative transfer simulations are too expensive to be applied in the retrieval, but a fast (potentially machine-learning-based) method for full 3D radiative transfer simulations might become available in the future. Then, full 3D radiative transfer simulations could be performed during the optimization and the retrieval could be adapted and extended accordingly.

Realistic 3D clouds

The analysis in the previous section considered clouds with a realistic cloud geometry but with a spatially uniform ice fraction and thus homogeneously mixed clouds. In reality, cloud thermodynamic phase partitioning is not constant throughout a cloud. In low-level Arctic mixed-phase clouds, a geometrically thin liquid layer is usually located at the cloud top and ice can be found below. As discussed in Sect. 3.4.2, a vertical profile of the ice fraction has to be assumed in the retrieval. The retrieved ice fraction was defined as the effective ice fraction of the uppermost cloud layer to a certain optical thickness threshold under the assumption of a homogeneously mixed cloud. In the following, the agreement of the retrieval results with this assumption is tested for realistic clouds and the uncertainty introduced by the necessary assumption of a vertical ice fraction profile is studied by applying the phase retrieval to synthetic measurement data simulated with the original, realistic cloud field obtained from the WRF simulations with spatially non-uniform phase partitioning. The retrieval errors then include both errors due to 3D cloud geometry and due to the vertical ice fraction profile. Figures 3.33 and 3.34 show the retrieval results assuming plane-parallel clouds in the upper row and using the IDEFAX in the lower row. Panels (a) and (d) display the retrieved ice fractions and optical thickness values, respectively, (b) and (e) the difference of the retrieved values to the ground truth from the model, and (c) and (f) histograms of the differences, including mean and standard deviation. To determine the ground truth for the ice fraction, optical thickness thresholds of 0.8 for the cloudbow range, 1.0 for the slope range with a saturated polarization signal, and 1.5 for the slope range in the unsaturated case, as described in Sect. 3.4.2, were used. For the optical thickness, the column vertical optical thickness at the location of every cloud target was used as ground truth, as in Sect. 3.4.3. The shadow mask was applied to the results.

As before, the behavior of the cloudbow range and the slope range is different. The IDEFAX again shows a larger bias but smaller standard deviation in the cloudbow range with an average difference between retrieved and true ice fraction of 0.223 ± 0.242 compared to 0.096 ± 0.262 for the plane-parallel approximation (see Fig. 3.33). For the slope range, the IDEFAX reduces the mean and slightly increases the standard deviation of the differences from 0.139 ± 0.247 for plane-parallel clouds to 0.049 ± 0.256. Overall, the differences of the ice fractions are still larger towards the cloud sides compared to the cloud centers. Moreover,

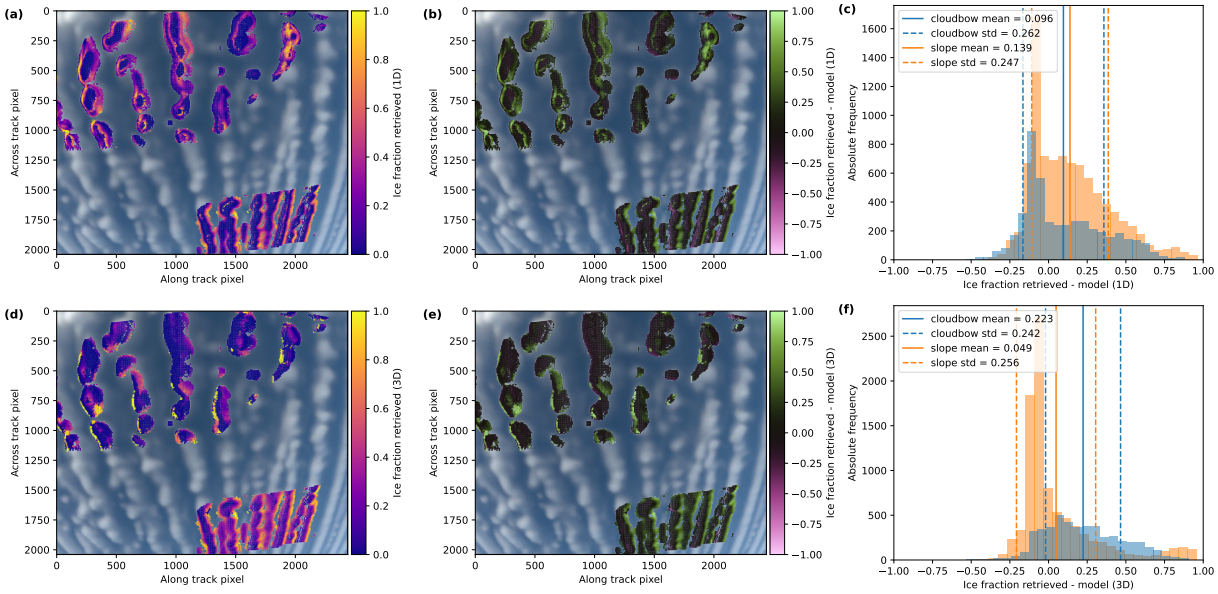

Figure 3.33: Retrieval results for the green color channel of the synthetic data for realistic 3D clouds for the polLR camera of specMACS. **(a, d)** Retrieved ice fraction. **(b, e)** Difference between the retrieved ice fraction and the model ice fraction. **(c, f)** Histogram of the differences between retrieved and model ice fractions with mean and standard deviation for the cloudbow (blue) and the slope range (orange). The upper row **(a, b, c)** shows the results under the assumption of plane-parallel clouds by the retrieval, the lower row **(d, e, f)** the results using the IDEFAX. The retrieved values in the upper left part of the images correspond to the slope range and the ones in the lower right part to the cloudbow range.

a step from small to large ice fractions is visible between the retrieved ice fractions for saturated and unsaturated regions in the slope range for the plane-parallel approximation in Fig. 3.33a. The step is due to the different penetration depths of I and Q and hence different signal locations for the saturated and unsaturated retrievals in this angular range as discussed in Sect. 3.4.2 (see also Fig. 3.29). Generally, the retrieval errors are largest for the slope angular range and the unsaturated retrieval, as the different penetration depths of I and Q in the combined retrieval introduce additional uncertainties. For optically thin parts of the clouds, where the optical thickness does not exceed the penetration depth of the polarization signal, the error is small again. It is, however, increased for the intermediate range between optically thin clouds with unsaturated polarization signal and clouds with saturated polarization signal. In comparison to the homogeneously mixed 3D clouds analyzed in Sect. 3.4.3, the mean differences and standard deviations are increased in the cloudbow range for the realistic 3D clouds. These increased errors for the realistic clouds are due to the assumption of a homogeneously mixed cloud in the forward operator and the variable vertical profile of the ice fraction in the simulated cloud field. In the slope range, there seems to be a compensating effect between the influence of 3D cloud geometry and the assumption of the vertical ice fraction profile, which leads to smaller mean and standard deviation values of the differences between the retrieved and true ice fraction. In

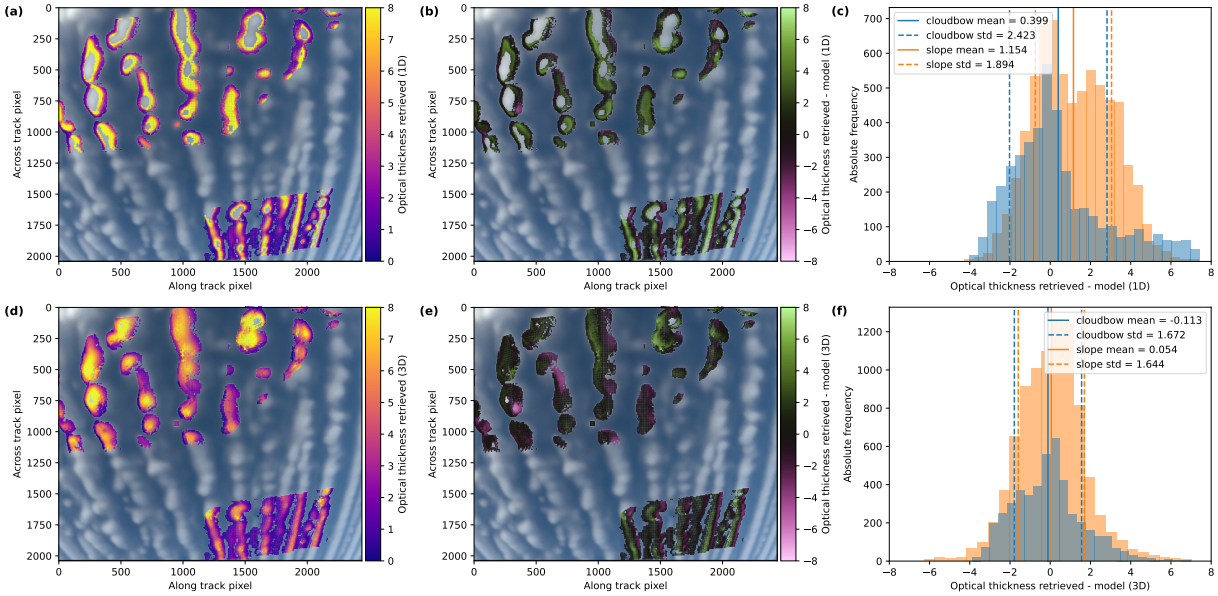

Figure 3.34: Retrieval results for the green color channel of the synthetic data for realistic 3D clouds for the polLR camera of specMACS. **(a, d)** Retrieved optical thickness. **(b, e)** Difference between the retrieved optical thickness and the model optical thickness. **(c, f)** Histogram of the differences between retrieved and model optical thicknesses with mean and standard deviation for the cloudbow (blue) and the slope range (orange). The upper row **(a, b, c)** shows the results under the assumption of plane-parallel clouds by the retrieval, the lower row **(d, e, f)** the results using the IDEFAX. The retrieved values in the upper left part of the images correspond to the slope range and the ones in the lower right part to the cloudbow range.

all cases, however, there is a significant contribution of the 3D cloud geometry to the total retrieval error. The influence of the assumption of the vertical ice fraction profile can also not be neglected.

Concerning the optical thickness displayed in Fig. 3.34, the mean differences and standard deviations are smaller for the IDEFAX than for plane-parallel clouds and smaller for the cloudbow range than the slope range, similar to the homogeneously mixed 3D clouds discussed in Sect. 3.4.3. In all cases, the mean differences and standard deviations are only slightly increased compared to the homogeneously mixed clouds. This indicates that the error due to 3D cloud geometry dominates over the error due to the assumption of a vertical ice fraction profile for the optical thickness.

The differences between retrieval and model in Fig. 3.33 and 3.34 include the errors due to the assumption of a homogeneously mixed cloud, respectively a vertical ice fraction profile, as well as errors due to 3D cloud geometry. Since no information about the vertical ice fraction profile is available from passive remote sensing information, the corresponding error cannot be reduced. The error due to 3D cloud geometry, however, could be further reduced in the future if fast full 3D radiative transfer models become available. In addition, the definition of the ground truth used for the validation is not trivial. Here, the vertical mean between cloud top and the optical thickness threshold values at the location of the

cloud target is used as discussed above and in Sect. 3.4.2. However, the observed deviation between the retrieved values and the so-defined model values could also be partly explained by a deviation of the real ground truth from the chosen model ground truth. The obtained errors thus have to be interpreted as retrieval uncertainties under these assumptions.

The errors of the retrieved ice fractions are not negligible. However, accurate measurements of cloud thermodynamic phase partitioning in mixed-phase clouds are challenging even for in situ measurements (Korolev et al., 2017). Cloud thermodynamic phase partitioning can quantitatively be computed from in situ measurements of liquid water content and total water content. Following the uncertainties of cloud water content measurements in liquid clouds given in Faber et al. (2018) and ice clouds specified by Heymsfield et al. (2010) and Hogan et al. (2012), Moser et al. (2023) concluded that in situ measurements of cloud water content in mixed-phase clouds have uncertainties in the range of 20 % to 50 %. The uncertainty of the new polarimetric retrieval of cloud phase partitioning is in the same range, but it provides two-dimensional fields of the retrieved quantities with high spatial resolution. In addition, it is very sensitive to liquid water at cloud top and can detect even small amounts of liquid water, which is difficult to detect with other passive remote sensing methods.

3.4.4 Application to measurement data

As an example case study, the retrieval of cloud thermodynamic phase partitioning is finally applied to measurements of the specMACS instrument during the HALO–$(\mathcal{AC})^3$ measurement campaign (Wendisch et al., 2024; Ehrlich et al., 2025), introduced in Sect. 3.2. Figure 3.35 shows measurements of the polLR camera of specMACS on 2022-04-01 at 10:18 UTC. These measurements correspond to the simulated data shown in the previous section. The left panel shows the RGB image and the right panel the cloud top heights for all cloud targets. Observed cloud top heights are between 400 m and 800 m with a mean cloud top height of about 570 m and cloudbow and slope range are both covered by the measurements.

Here, only the retrieval results for the neural network forward operator using the IDEFAX are presented since the IDEFAX was shown to accurately approximate the 3D cloud geometry for the considered type of low-level Arctic mixed-phase clouds (Weber et al., 2024, see Sect. 3.3) and the retrieval using the IDEFAX demonstrated a better performance as discussed in Sect. 3.4.3. Figure 3.36 shows the results of the phase retrieval, before applying the shadow mask. Panels (a) and (b) display the retrieved ice fraction and optical thickness and panels (c) and (d) the root mean square errors of the fits for I and Q. In contrast to the synthetic data, where only a short time period was simulated, the entire observation range in the along-track direction can be analyzed for the measurements. Moreover, the measurements have measurement uncertainties whose influence is included in the RMSEs in Fig. 3.36c and 3.36d. Evaluation of the angular range between the slope range and the cloudbow range is not possible since the cloudbow requires the complete angular range from 135.9° to 160° to determine the cloud droplet size distribution needed for the phase retrieval. In addition, the retrieval for the slope range is only possible for minimum scattering angles

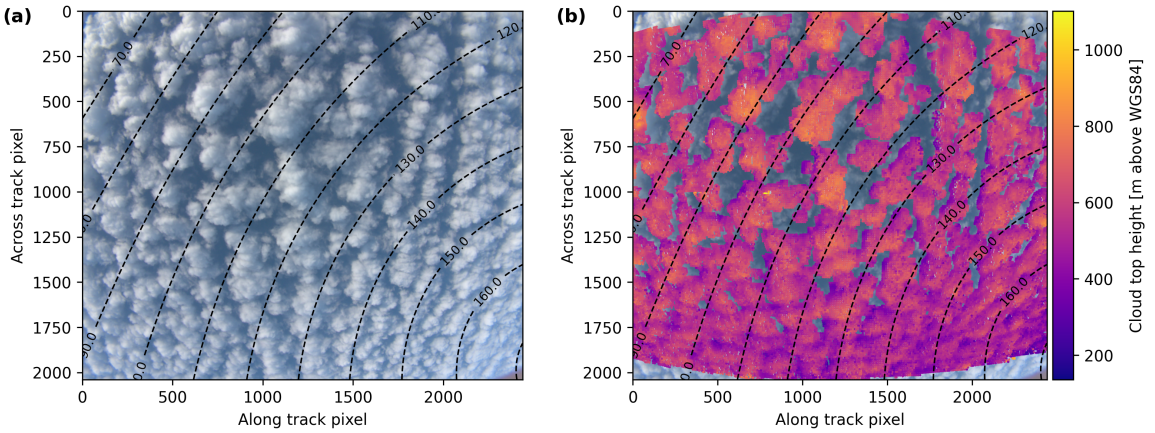

Figure 3.35: Measurement of the polLR camera of specMACS on 2022-04-01 at 10:18 UTC. **(a)** RGB image. **(b)** Cloud top height for all cloud targets. The dashed lines indicate the scattering angles.

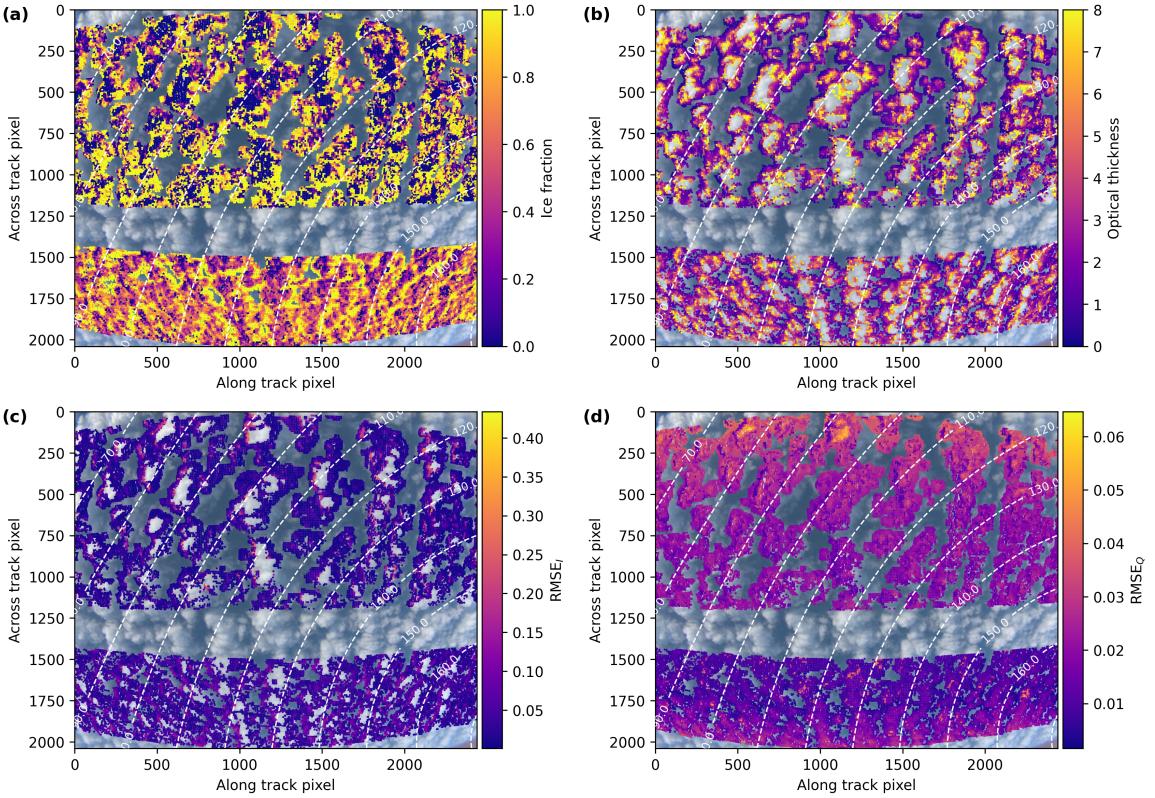

Figure 3.36: Results of the phase partitioning retrieval with the neural network forward operator for half-spherical clouds with the IDEFAX for the green color channel of the polLR camera of specMACS on 2022-04-01 at 10:18 UTC. Panels **(a)** and **(b)** display the derived ice fraction and optical thickness, respectively, and panels **(c)** and **(d)** the RMSE for I and Q. The dashed lines indicate scattering angles.

of 80° and smaller since the sensitivity of the slope angular range to cloud thermodynamic

phase decreases with increasing minimum scattering angle, as can be seen in Fig. 3.24, and the retrieved ice fractions become very uncertain for a further reduced scattering angle range.

The results show smaller ice fractions in the (higher) centers of the clouds and larger ice fractions towards the lower cloud sides. This can be expected as Arctic mixed-phase clouds usually have a liquid layer at cloud top from which ice crystals form and sediment downwards (e.g. Morrison et al., 2012). The mean derived ice fraction is about 0.62 for the cloudbow range and 0.51 for the slope range. The cloudbow range shows more continuous transitions between liquid and ice since it is more sensitive to cloud thermodynamic phase partitioning than the slope range, as can also be seen in Fig. 3.24. In addition, the slope range is more strongly affected by 3D radiative effects as discussed in Sect. 3.4.3. Thus, whenever both the cloudbow and the slope range are covered by the measurements for the same scene, the retrieval results of the cloudbow range should be preferred for further scientific analysis, keeping, however, the biases discussed in Sect. 3.4.3 in mind. The patterns of the RMSE of I and Q and panels (c) and (d) of Fig. 3.36 are related to the 3D cloud geometry as can be seen by comparing the panels to Fig. 3.35. Larger RMSEs for I are, for example, found at the cloud sides, which are oriented towards the sun, which is coming from the upper left. Moreover, the measurement uncertainties, especially for the polarization signal, are larger towards the corners of the sensor, where calibration artifacts can occur (Weber et al., 2024). As a consequence, the $\mathrm{RMSE_Q}$ increases towards the top and the bottom of the figure.

3.4.5 Further uncertainty assessment

In addition to the validation of the polarimetric phase retrieval with synthetic data, a detailed uncertainty assessment was carried out. In particular, the influence of the assumption of an ice crystal habit and ice effective radius, the spatial resolution of the cloud surface mesh for the computation of the orientation angles for the IDEFAX, and the spherical geometry of the Earth are assessed in the following sections. Moreover, the accuracy of the cloudbow retrieval, which was developed by Pörtge et al. (2023) for pure liquid water clouds in the Tropics, is investigated for Arctic mixed-phase clouds, which are the focus of this work.

Assumption of ice habit and ice effective radius

The neural-network forward operators assume the aggregate consisting of eight columns by Yang et al. (2013) as ice crystal habit and a constant ice effective radius of 50 µm, which are both typical choices. However, a real ice or mixed-phase cloud can consist of ice crystals with different radii or crystal shapes. To study the influence of these assumptions on the results of the polarized retrieval of cloud thermodynamic phase partitioning, simulations of plane-parallel clouds were performed for different habits and crystal sizes. Then, the retrieval using the forward operator for plane-parallel clouds was applied to the obtained data. The simulated clouds had a total optical thickness of 5, such that the polarization

Habit	Cloudbow range	Slope range
solid_column	0.47	0.57
plate	0.30	1.0
column_8elements	0.51	0.51
droxtal	0.46	0.59
solid_bullet_rosette	0.44	0.67
ghm	0.50	0.67

Table 3.8: Retrieved ice fractions for different habits as defined by Yang et al. (2013) and Baum et al. (2014) assuming a saturated cloud and thus using only Q for the optimization. The habit assumed by the retrieval is the *column_8elements*, the true ice fraction was 0.5, and the ice effective radius 50 µm.

Ice effective radius [µm]	Cloudbow range	Slope range
20	0.51	0.52
30	0.51	0.51
50	0.51	0.51
80	0.51	0.51

Table 3.9: Retrieved ice fractions for simulated clouds with different ice effective radii. The effective radius assumed by the retrieval is 50 µm and the true ice fraction was 0.5.

signal was saturated. Further, the simulated clouds were homogeneously mixed with an ice fraction of 0.5. The solar zenith angle was 70°, and the green color channel was simulated.

Table 3.8 summarizes the retrieved ice fractions for the slope and cloudbow angular range for simulations with different ice crystal habits. As expected, there is good agreement between the retrieved ice fractions for the simulation with the habit *column_8elements* for both angular ranges, since this is the habit assumed by the retrieval. The slight deviation of 0.51 from the true ice fraction of 0.50 can be explained by the uncertainties of the forward operator and the optimization, as well as some minor effects of noise in the Monte Carlo simulations. Other habits show varying deviations of the retrieved ice fractions from 0.50. Generally, the deviations are larger for the slope range than for the cloudbow range. This is because the (polarized) phase functions of the different habits are more similar to each other in the cloudbow range than in the slope range (see e.g. Fig. 2.8). However, except for the case that the clouds actually consist of plates instead of the assumed column aggregates, only small errors are introduced by the habit assumption compared to the total retrieval uncertainties discussed in Sect. 3.4.3, especially for the cloudbow range. Moreover, the results of the retrieval applied to simulated clouds with different ice effective radii are given in Table 3.9. In general, the visible wavelength range is primarily sensitive to the cloud optical thickness and only little influenced by the ice effective radius, which is the basic principle behind bispectral retrievals. This can also be seen in Table 3.9 as the deviations of the retrieved ice fractions from the true ice fraction of 0.50 are very small. Thus, the additional error introduced by the assumption of the constant ice crystal radius is negligible.

Cloudbow retrieval for Arctic mixed-phase clouds

The retrieval of cloud thermodynamic phase partitioning in the cloudbow range uses the effective radius and variance of the cloud droplet size distribution derived with the cloudbow retrieval by Pörtge et al. (2023) as input. The cloudbow retrieval was validated for tropical liquid water clouds by Volkmer et al. (2024). Here, it is applied to Arctic mixed-phase clouds. Thus, the performance of the cloudbow retrieval was studied for these conditions.

First, the influence of the mixed-phase and ice phase on the retrieval results was investigated. For this, a homogeneously mixed cloud with varying ice fraction was simulated and the cloudbow retrieval was applied. As before, the solar zenith angle was 70° and the total optical thickness was 5. The effective radius and variance of the liquid water droplets in the simulated clouds were 10 µm and 0.10, respectively. Figure 3.37 shows the effective radii and variances of the cloud droplet size distribution retrieved by the cloudbow retrieval for the different color channels of the polarization-resolving cameras of specMACS as a function of the ice fraction. The cloudbow retrieval works accurately up to an ice fraction of about 0.8. For larger ice fractions, the amplitude of the cloudbow gets very small, making the fit challenging. The effective radius is increasingly underestimated and the variance overestimated with increasing ice fractions.

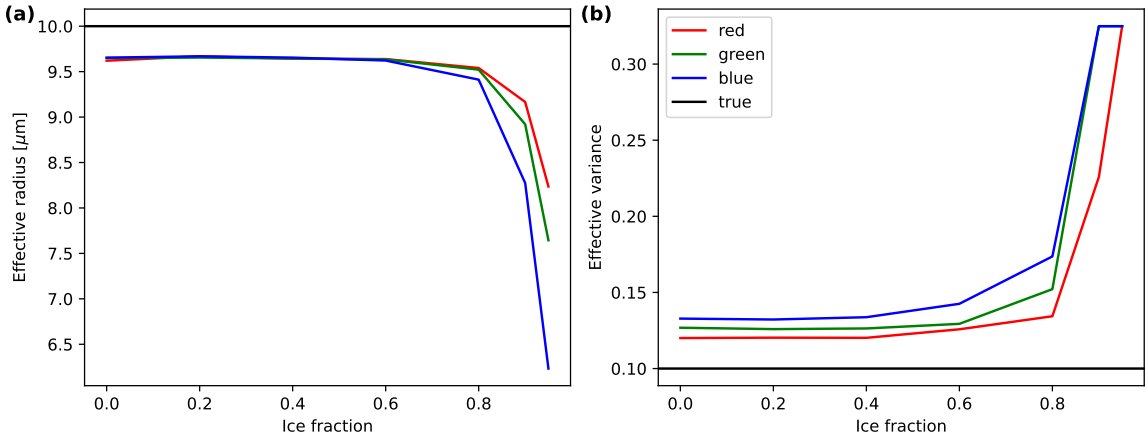

Figure 3.37: Retrieved effective radii and variances of the cloud droplet size distribution for a cloud with different ice fractions. The black line indicates the true values, the colored lines the retrieval results for the different color channels of the polarization-resolving cameras.

Moreover, for all ice fractions, the effective radius is generally slightly underestimated and the variance is slightly overestimated. The reason for this is the large solar zenith angle, as will be discussed in the following. During the HALO–$(\mathcal{AC})^3$ campaign in the Arctic, typical solar zenith angles were around 70° as used for the simulations of Fig. 3.37, while the cloudbow retrieval was developed for tropical clouds observed under small solar zenith angles. The fit of tabulated phase functions performed in the cloudbow retrieval includes a simple Rayleigh correction, which was introduced by Alexandrov et al. (2012). This correction is, however, less suited for very large solar zenith angles, as in the Arctic, where the path through the atmosphere is significantly longer. Hence, this leads also to

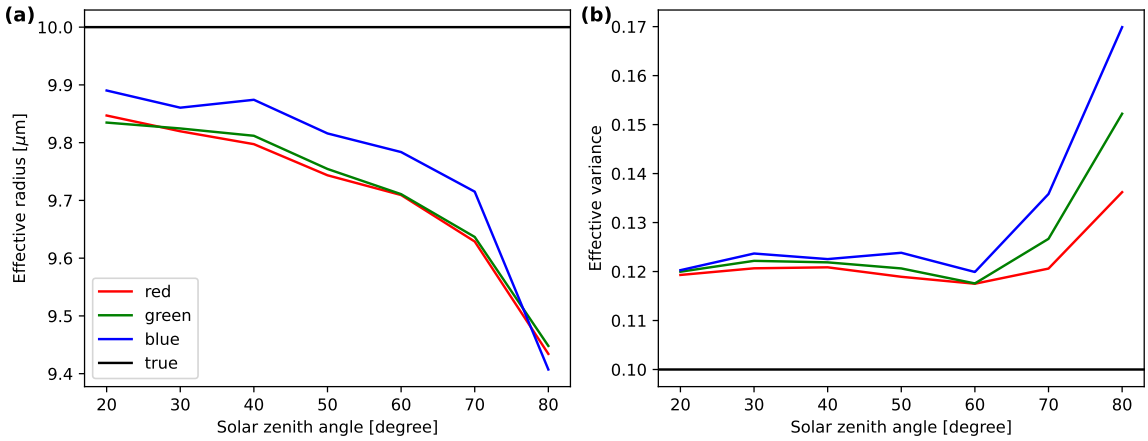

Figure 3.38: Retrieved effective radii and variances for a liquid water cloud at different solar zenith angles. The black line indicates the true values, while the colored lines show the retrieval results for the different color channels of the polarization-resolving cameras.

higher-order Rayleigh scattering contributions. To test this hypothesis, a pure liquid water cloud with an optical thickness of 5 was simulated for various solar zenith angles and the cloudbow retrieval was applied to the simulations. Figure 3.38 shows the retrieved effective radii and variances of the cloud droplet size distribution as a function of solar zenith angle and indicates an increasing underestimation of the effective radius with increasing solar zenith angles, as expected. The variations are largest for the blue wavelength range, which is strongest affected by Rayleigh scattering. It shows the best results for solar zenith angles up to 70°, indicating that the Rayleigh correction is generally performing well. For the largest solar zenith angles, the effective radius is most strongly underestimated in the blue channel.

Lastly, larger solar zenith angles also lead to smaller signal levels and thus a relatively larger influence of noise on the measurement data. To investigate the impact of noise on the cloudbow retrieval, a liquid water cloud with an optical thickness of 5 was simulated for a solar zenith angle of 30°. Then, different levels of random Gaussian noise were added to the simulations and the retrieval was applied to the results. This procedure was repeated 20 times per noise level with different random numbers to quantify the introduced uncertainty. Figure 3.39 shows the mean retrieved effective radii and variances of the cloud droplet size distribution and their standard deviations as a function of the noise level. Increased noise leads to a larger uncertainty of the retrieval results, but does not significantly change the bias.

Spatial resolution of the cloud surface mesh

For the retrieval with the forward operator using the IDEFAX, information about the cloud surface orientation is necessary. For this, the triangular meshes derived from the results of the stereographic retrieval by Kölling et al. (2019) as described in Kölling (2020) are used to define the 3D cloud geometry. The meshes are constructed from the point cloud, which is

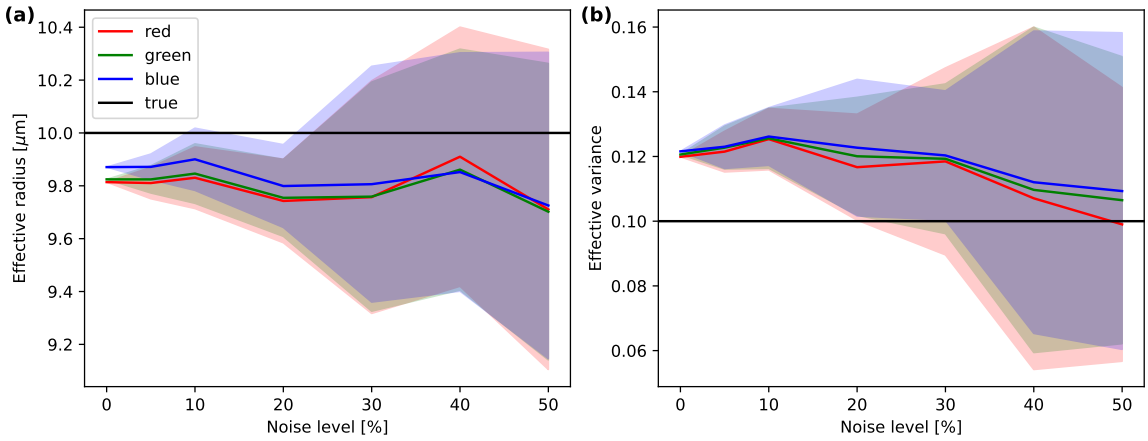

Figure 3.39: Retrieved effective radii and variances for a liquid water cloud with different noise levels. The black line indicates the true values, the colored lines the retrieval results for the different color channels of the polarization-resolving cameras. The shaded areas denote the standard deviation of retrieved effective radii and variances for the 20 retrieval runs for each color and noise level.

obtained from the stereographic reconstruction method, using Poisson surface reconstruction with a so-called octree. The depth parameter of this octree can be varied manually and affects the spatial resolution of the surface mesh. To study the influence of the spatial resolution of the surface meshes and thus the calculated cloud surface orientation angles on the phase retrieval results, surface meshes were computed for an example measurement scene with different depth parameters, representing different spatial resolutions. Then, the phase retrieval was applied to the measurements using the meshes with the different spatial resolutions. The retrieved ice fraction and optical thickness fields for three different spatial resolutions of the surface orientation angles are shown in Fig. 3.40 and histograms of the retrieved quantities are displayed in Fig. 3.41. The middle column is the default resolution, the column to the left has a lower, and the column to the right has a higher spatial resolution. In general, the mesh resolution has a comparably small influence on the retrieved ice fraction and optical thickness. More small-scale structure is visible for higher mesh resolutions and deviations are observed in the histograms especially for very small and very large ice fractions. These differences could be relevant if the small-scale structure of the ice fraction is analyzed. But, the means of the histograms of the retrieved quantities are very similar and their difference is small compared to the retrieval uncertainties. Thus, the choice of the spatial resolution of the surface mesh used to compute the cloud surface orientation angles introduces only minor uncertainties in statistical analyses of the ice fraction. The differences are larger for the slope range than the cloudbow range, since the cloudbow is less sensitive to 3D cloud geometry and the associated 3D radiative effects. The overall small influence of the spatial resolution of the cloud surface mesh on the retrieval results can be expected, since the phase retrieval is based on polarization, which is generally less affected by 3D radiative effects. Nevertheless, the influence of the spatial resolution of the cloud surface geometry for the IDEFAX on the representation of 3D radiative effects

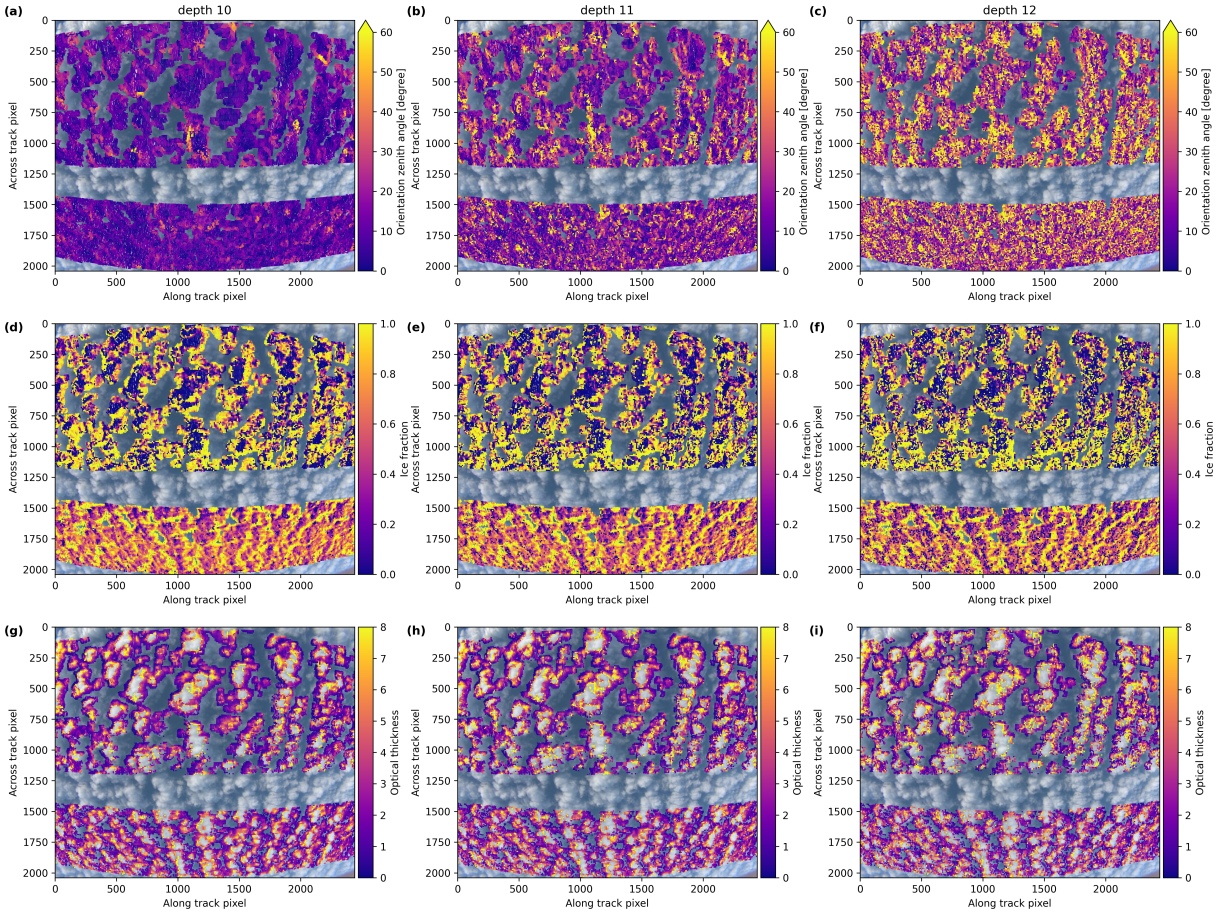

Figure 3.40: Phase retrieval results for different surface mesh resolutions in the different columns for the measurements of the green color channel of the polLR camera taken on 2022-04-01 at 10:18 UTC. **(a, b, c)** show the surface orientation zenith angles, **(d, e, f)** the retrieved ice fractions, and **(g, h, i)** the retrieved optical thickness. Depth 11 is the default for the shown example, depth 10 and 12 are lower and higher resolved surface meshes.

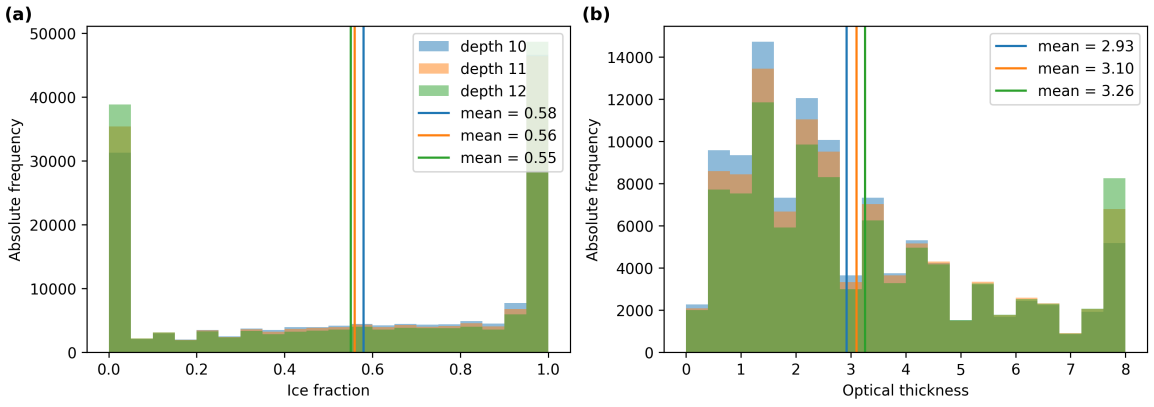

Figure 3.41: Histograms and means of the retrieved ice fraction **(a)** and optical thickness **(b)** for different spatial resolutions of the cloud surface mesh in Fig. 3.40.

and consequently the phase retrieval results could be further investigated in the future.

Spherical geometry of the Earth

Finally, the forward operators for the phase partitioning retrieval assume a plane-parallel atmosphere. In reality, however, the Earth has a spherical geometry. Thus, for large solar zenith angles, the real path through the atmosphere is shorter than in a plane-parallel atmosphere, which influences the amount of Rayleigh scattering and could introduce retrieval uncertainties. However, the spherical geometry of the Earth is relevant only for solar zenith angles larger than 80° as can be seen in Fig. 3.42. Figure 3.42 displays simulations of I and Q as a function of scattering angle for different solar zenith angles for a plane-parallel atmosphere in solid lines and considering the spherical geometry of the Earth in dashed lines. For solar zenith angles smaller than 80°, there is hardly any difference between the simulations with a spherical and plane-parallel geometry, and thus no additional uncertainties. The application of the phase partitioning retrieval to measurements at solar zenith angles larger than 80° is, however, not meaningful due to the very small signal levels, the increased influence of 3D radiative effects, and shadows, which all introduce additional uncertainties.

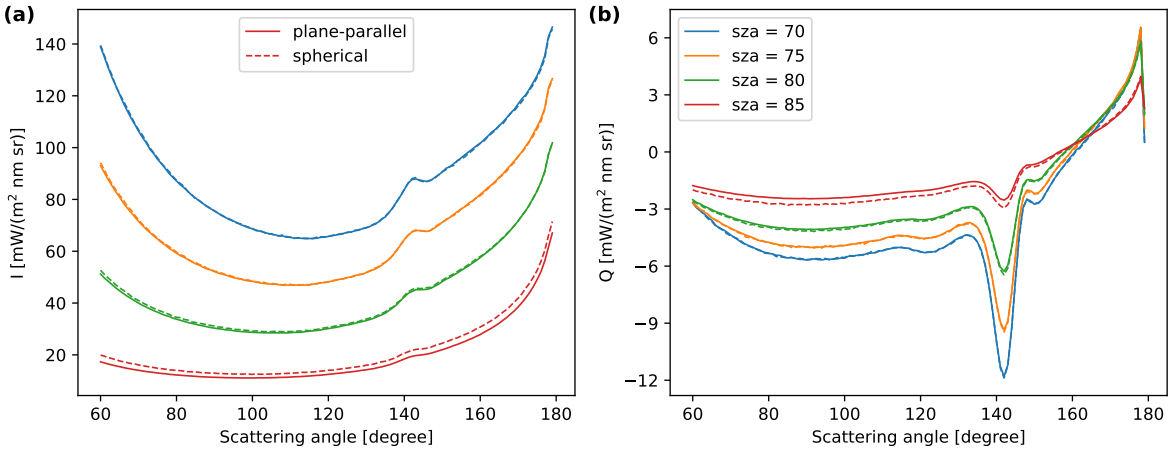

Figure 3.42: Simulations accounting for the spherical geometry of the Earth in dashed lines and simulations assuming a plane-parallel atmosphere in solid lines for different solar zenith angles and a wavelength of 550 nm. **(a)** Stokes vector component I. **(b)** Stokes vector component Q. The simulated clouds have a total optical thickness of 5 and an ice fraction of 0.5.

3.4.6 Discussion

A new retrieval of cloud thermodynamic phase partitioning from multi-angle polarimetric imaging was presented in the previous sections and applied to measurements of the polarization-resolving cameras of the specMACS instrument. The basic idea of the retrieval is to fit measured multi-angle signals of Q along the scattering plane to simulated

multi-angle signals to obtain an ice fraction, which is defined as the ratio of the ice optical thickness to the total optical thickness. In contrast to existing retrievals based on spectral measurements, the presented polarimetric retrieval provides quantitative information about cloud thermodynamic phase partitioning. The obtained ice fractions are representative for the cloud top as polarization is dominated by single scattering. For the same reason, polarization is less influenced by 3D radiative effects and the localization of the measured signal is more confined compared to the total reflectivity. 3D radiative effects are accounted for by using the IDEFAX introduced by Weber et al. (2025c) and in Sect. 3.3, where 3D cloud geometry is approximated through a field of half-spherical clouds. Information about 3D cloud geometry needed for the IDEFAX can be derived from the specMACS observations by applying a stereographic retrieval (Kölling et al., 2019). Depending on the observed cloud structure, the assumption of either plane-parallel or half-spherical clouds in the IDEFAX will be more suited and the retrieval can be performed using the respective forward operator for both assumptions.

Next, the retrieval was validated using synthetic data. Idealized cloud cases as well as a realistic cloud field of Arctic mixed-phase clouds simulated with the WRF model were used as input for 3D radiative transfer simulations. Then, the retrieval was applied to the synthetic data and the retrieved quantities were compared to the true quantities from the model. The good agreement between retrieved and true values for plane-parallel homogeneously mixed clouds validated the retrieval method itself. For realistic 3D Arctic mixed-phase clouds, mean differences between retrieved and true ice fractions of 0.096 ± 0.262 and 0.139 ± 0.247 were obtained for the cloudbow and the slope range, respectively, for the plane-parallel approximation. For the IDEFAX, the analysis showed mean differences of 0.223 ± 0.242 respectively 0.049 ± 0.256. These errors include errors due to 3D cloud geometry as well as errors due to the necessary assumption of a vertical ice fraction profile. To quantify the contributions of 3D cloud geometry and the assumption of a vertical ice fraction profile to the total error, additional synthetic data were computed for the realistic cloud field obtained from the WRF model, but with a spatially uniform ice fraction. Both the error due to 3D cloud geometry and due to the assumption of a vertical ice fraction profile have a significant contribution to the total error of the retrieved ice fraction. The additional error introduced by the assumption of an ice crystal habit and effective radius is small compared to the total error. Moreover, the cloudbow retrieval of the cloud droplet size distribution provides accurate results for ice fractions up to 0.8. With increasing solar zenith angles, the effective radius of liquid cloud droplets is increasingly underestimated and the uncertainty increases due to the increasing influence of noise. The resolution of the triangular surface mesh describing the 3D cloud geometry influences the small-scale structure of the retrieved ice fractions, but the average ice fraction is not significantly affected.

The retrieval errors are not negligible. However, quantitative measurements of cloud thermodynamic phase partitioning in mixed-phase clouds are challenging even for in situ measurements, which also have large uncertainties in this case and only provide one-dimensional information along the flight track. Even though the retrieved ice fractions have large uncertainties, the new polarized retrieval can detect very small amounts of liquid cloud

droplets in an ice cloud layer, which cannot be achieved with other passive remote sensing methods. Furthermore, the retrieval results obtained from the specMACS instrument have a high spatial resolution of about 100 m, which allows for studying small-scale processes and the horizontal distribution of cloud thermodynamic phase. Typical scales of inhomogeneities in Arctic clouds were analyzed by Schäfer et al. (2017) and Schäfer et al. (2018) and are on the order of a few hundred meters, which is resolved by the spatial resolution of the specMACS measurements.

There are some possible future improvements and extensions of the retrieval as well as potential future applications. The introduced polarimetric retrieval method could be further improved by combining it with a spectral retrieval, which is sensitive to small amounts of ice in a liquid water cloud, similarly to Riedi et al. (2010). This combination allows for a very accurate phase classification. Furthermore, the retrieval could be extended to derive the total optical thickness as an additional variable for all observations.

In addition, retrieval results with a large RMSE of the fit can, for example, be filtered out for further analysis to increase the accuracy, since a large RMSE indicates a larger uncertainty of the retrieved ice fraction. The computational efficiency of the retrieval could be further optimized by applying an improved optimization method. In the current implementation with Python, a global search was more efficient than gradient-based optimization methods. If the retrieval was translated to a different high-performance programming language, a speed-up and potentially improved optimization could be achieved. For the slope angular range, the RMSEs of the fits are much higher than for the cloudbow range, and there is less agreement between the measurements and and the best fit model for both plane-parallel clouds and the IDEFAX, especially for unsaturated polarization signals. Parts of these increased deviations can be explained by different penetration depths of I and Q in the combined retrieval for unsaturated polarization signals. However, there is also a larger influence of 3D radiative effects that are not yet captured by the plane-parallel approximation and the IDEFAX in this angular range. These remaining 3D radiative effects should be further investigated in the future. In addition, improved neural network training could also improve the fits. Since the slope angular range is less sensitive to cloud thermodynamic phase partitioning, the relative impact of small errors of the neural network forward operators is larger.

Here, the retrieval was applied to observations of low-level Arctic mixed-phase clouds during the HALO–$(\mathcal{AC})^3$ campaign and showed a liquid layer at cloud top as expected. However, the retrieval is, of course, also applicable to data measured outside the Arctic to study, for example, glaciation in deep convective clouds in the tropics. Due to the lower solar zenith angles and consequently reduced influence of 3D radiative effects, the retrieval is expected to perform better in this situation. In addition, the more sensitive cloudbow region will then be observed closer to the center of the field of view of the instrument where the measurement uncertainties are smaller. If the retrieval is applied to measurements outside the Arctic with large variations of the solar zenith angle, the threshold value of the optical thickness defining a polarization signal as saturated or not could be adapted. At the moment, it is set to a very conservative constant value. Adjusting the threshold value depending on the solar zenith angle could reduce the computation time of the retrieval.

3.5 Spectral retrieval of cloud thermodynamic phase

Besides the new polarization-based retrieval, information about cloud thermodynamic phase can also be derived from spectral measurements. The spectral retrieval methods are based on spectral absorption differences between liquid water and ice in the near infrared wavelength range and are well established. Figure 3.43 shows simulated spectra for a liquid water cloud, a mixed-phase cloud, and an ice cloud for the wavelength range between 1000 nm and 2400 nm, which can be measured by the SWIR spectrometer of the specMACS instrument. In the gray shaded wavelength range between 1550 nm and 1700 nm, the slope of the curves changes depending on the cloud thermodynamic phase. Ice clouds have a positive slope, while liquid water clouds show a negative slope, and mixed-phase clouds are in between. Based on this, Ehrlich et al. (2008) and Jäkel et al. (2013) defined so-called ice indices which use the spectral slope in this wavelength range. The spectral slope phase index or ice index can be computed with (Ruiz-Donoso et al., 2020)

$$\mathcal{I}_\mathrm{s} = 100 \cdot \frac{\lambda_\mathrm{b} - \lambda_\mathrm{a}}{R_{1640\mathrm{nm}}} \frac{dR_\lambda}{d\lambda}_{[\lambda_\mathrm{a},\lambda_\mathrm{b}]}, \tag{3.29}$$

where the wavelengths $\lambda_\mathrm{a} = 1550\,\mathrm{nm}$ and $\lambda_\mathrm{b} = 1700\,\mathrm{nm}$, and R denotes the reflectivity. With the help of radiative transfer simulations, threshold values for the ice index can be determined below or above which a cloud is classified as either liquid water, mixed-phase, or ice. Values of the ice index $\mathcal{I}_\mathrm{s} < 20$ correspond to liquid water clouds, whereas mixed-phase or ice clouds have ice indices $\mathcal{I}_\mathrm{s} > 20$ (Ehrlich et al., 2009).

The ice index can be directly computed from the measurements of the SWIR camera by converting the measured radiances to reflectivities and using Eq. 3.29. Figure 3.44 shows

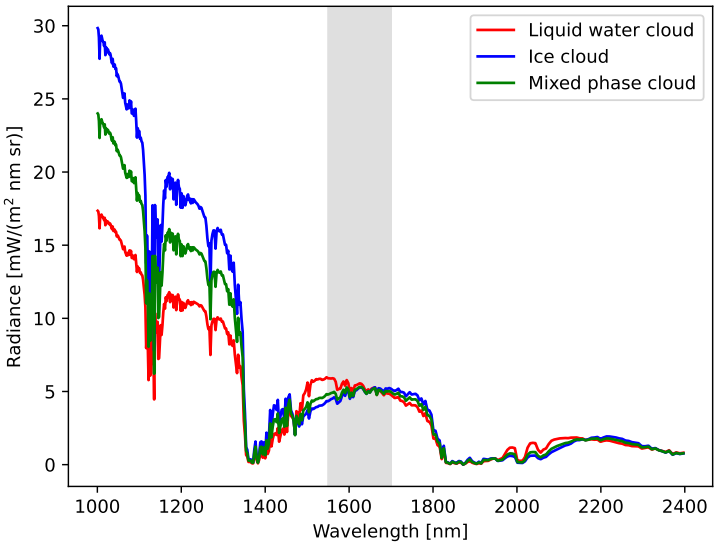

Figure 3.43: Simulated spectra for a liquid water cloud, a mixed-phase cloud, and an ice cloud with a total optical thickness of 5 and a solar zenith angle of 70°. The effective radius of liquid water droplets was 10 µm, the ice effective radius 30 µm, and the mixed-phase cloud was homogeneously mixed with 50 % liquid water and 50 % ice.

the measured reflectivity at 1640 nm for an example observation in the upper panel and the corresponding calculated ice index in the lower panel. A cloud mask was applied to the ice indices in Fig. 3.44b and for further analysis. The cloud mask is based on the brightness of the SWIR measurements at 1640 nm and uses a simple threshold value which was manually tuned. The measurements were converted to reflectivity to account for varying solar zenith angles. Measurements with reflectivities larger than 0.22 were classified as cloud. For the HALO–$(\mathcal{AC})^3$ measurements, the presence of sea ice was a challenge to not being misclassified as a cloud. At the wavelength of 1640 nm, sea ice is comparably dark, giving a sufficient contrast to the bright liquid water clouds, which are typically formed in the marginal sea ice zone during MCAOs. Thus, this wavelength was chosen for the cloud mask. The sunglint, which is also often problematic for cloud detection, was not in the field of view of the cameras during the HALO–$(\mathcal{AC})^3$ campaign due to the large solar zenith angles in the Arctic, making a simple threshold cloud mask possible.

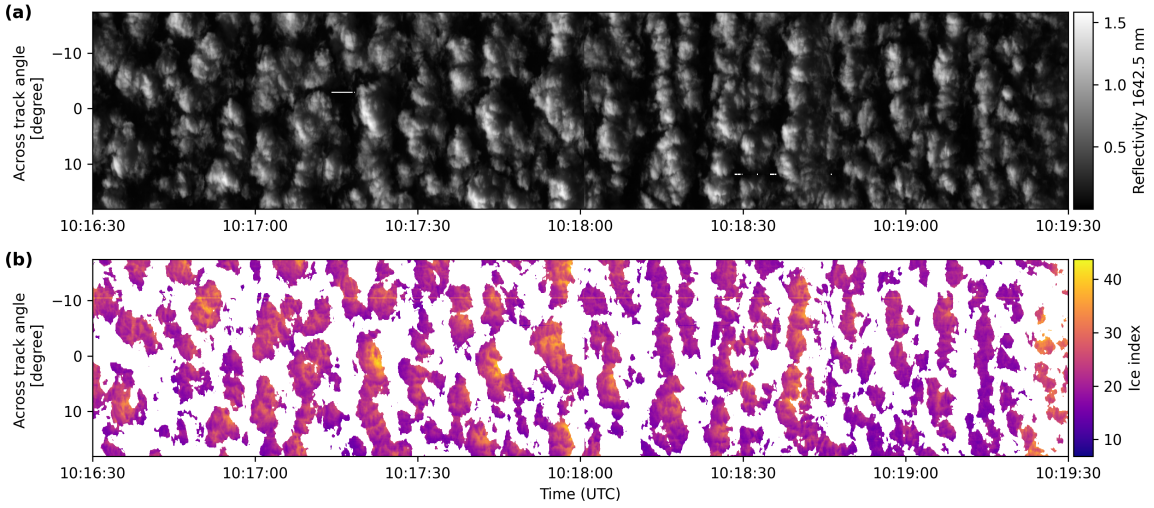

Figure 3.44: Reflectivity at 1640 nm **(a)** and ice index with the cloud mask applied **(b)** measured by the SWIR camera on 2022-04-01 from 10:16:30 to 10:19:30 UTC.

3.6 Retrieval of horizontal cloud extent

Another property of clouds which can be derived from the measurements of the specMACS instrument is their (horizontal) geometrical extent. For this, the data measured by the polarization-resolving cameras can be used. First, clouds have to be detected using the existing cloud mask. Then, the detected cloudy pixels can be clustered into individual clouds, and the geometrical horizontal size of the clouds can be computed from the clusters. In general, different cluster algorithms exist. Pörtge (2024) used the DBSCAN algorithm to cluster measurements of the polarization-resolving cameras from the EUREC^{4}A field campaign to separate them into cloud edge and cloud center. This algorithm worked reasonably well for the considered shallow cumulus clouds in the tropics. However, it has

difficulties if the clouds are less statistical but evolve with time and space with varying cloud size and cloud fraction, as during MCAOs, which are the focus of this work.

Thus, a watershedding algorithm was applied instead. The basic principle behind watershedding algorithms for image segmentation comes from geology, where topographic data is subdivided into catchments (Meyer, 1994). The Python package TOBAC (Heikenfeld et al., 2019; Sokolowsky et al., 2024) is specifically constructed for cloud identification and tracking in meteorological applications. It includes an implementation of a watershedding algorithm, which was used here. For this, the target points of the L1C data, which describe the 3D cloud geometry (similar to topographic data) and already include the cloud mask, had to be interpolated onto a regular grid. The resulting field of the cloud top heights for a typical segment is displayed in Fig. 3.45a. Then, the clustering algorithm implemented in TOBAC was applied. First, features were detected as extreme values above several subsequent threshold heights between the minimum and maximum cloud top height of a flight segment. The identified features are highlighted as crosses in Figure 3.45. Next, the segmentation was performed. The difficulty here was to determine the threshold heights for the watershedding since the cloud height varied significantly during a research flight during HALO–$(\mathcal{AC})^3$ as the clouds and boundary layer evolved with time and distance to the ice edge. This is also visible in the example segment in Fig. 3.45a, where the cloud top height differs between the beginning (upper left) with lower heights closer to the ice edge and the end (lower right, larger heights) of the segment. Thus, an adaptive threshold depending on the average cloud top height of a small time interval was defined. A threshold height of 200 m below the average cloud top height, with a minimum of 100 m and a maximum of 500 m, was chosen after trying different settings. Figure 3.45b shows the resulting segmentation with the different clusters color-coded. The segmentation results look reasonable. Finally, TOBAC provides the geometric area of the clusters from which cloud radii were computed assuming a circular shape. Only the centers of the images with viewing zenith angles smaller than 35° were included in the following analysis to avoid uncertainties due to slant viewing angles.

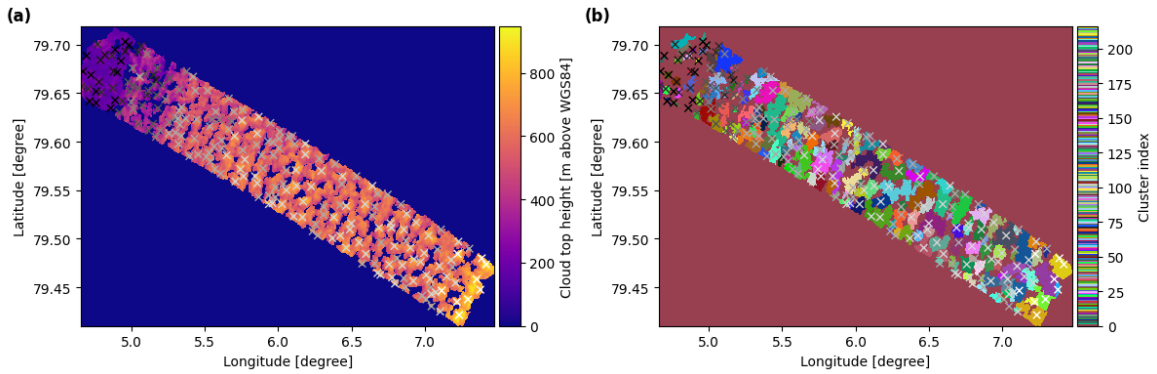

Figure 3.45: **(a)** Cloud top height of the cloud targets for a flight segment measured on 2022-04-01 by the polLR camera. **(b)** Identified features and segmented cloud clusters. The crosses indicate the detected features, and the colors display the results of the segmentation.

Chapter 4

Results

4.1 Comparison of different cloud thermodynamic phase retrieval methods

In the following, different measurements and retrieval methods of cloud thermodynamic phase, including the spectral and polarized retrievals using passive remote sensing, active remote sensing with radar and lidar measurements, and in situ measurements of cloud thermodynamic phase partitioning, will be compared and their advantages and challenges will be discussed.

4.1.1 Comparison of the spectral and polarized retrieval methods

The spectral retrieval of cloud thermodynamic phase is based on spectral absorption differences between liquid water and ice in the near infrared, as discussed in Sect. 3.5. Based on this, Ehrlich et al. (2008) defined the so-called ice index. It is a qualitative measure of the thermodynamic phase and can be used to classify clouds into liquid, mixed-phase, or ice clouds. The spectral retrieval method was applied to measurements of the SWIR camera of specMACS during HALO–$(\mathcal{AC})^3$. This yields 2D fields of cloud thermodynamic phase with a high spatial resolution of about 10 m. The spectral retrieval is very sensitive to small amounts of ice in liquid clouds. However, it is affected by 3D radiative effects, especially for the large solar zenith angles in the Arctic. In addition, the surface properties as well as the observation geometry influence the computed ice index (Jäkel et al., 2013).

In contrast, the polarization-based retrieval of cloud thermodynamic phase partitioning introduced in Sect. 3.4 exploits differences in the (polarized) scattering phase functions of liquid water and ice due to the different shapes of liquid cloud droplets and ice crystals. By fitting simulations obtained from a forward operator to multi-angle measurements of the polarization-resolving cameras of specMACS, a quantitative optical ice fraction is determined. Consequently, two-dimensional fields of the ice fraction with a spatial resolution of about 100 m are obtained. Since this retrieval uses polarization information, it is less affected by 3D radiative effects than the spectral retrieval. In addition, the polarized

retrieval provides quantitative information about cloud thermodynamic phase partitioning, although with a comparably high uncertainty. The high uncertainty can be explained by a combination of both, the remaining 3D radiative effects present in the polarization signal and the necessary assumption of a vertical ice fraction profile in the retrieval. The polarized retrieval is very sensitive to liquid cloud droplets and can detect very small amounts of liquid in ice clouds with high accuracy. Besides the different sensitivities to cloud liquid water and cloud ice discussed above, the polarized and unpolarized signals have different penetration depths. In addition, the penetration depth generally depends on the wavelength.

The specMACS instrument provides simultaneous measurements of spectral radiances as well as multi-angle polarimetric measurements and allows the application of both retrieval methods. By combining the spectral and polarized retrieval results, a very accurate phase classification into liquid, mixed-phase, and ice is possible since both retrievals have different sensitivities. The advantage of the combination of spectral and polarization information for phase classification was already shown by Riedi et al. (2010). In addition, the spectral and polarized retrievals of cloud thermodynamic phase using specMACS data have a very high spatial resolution, allowing for studying small-scale variations of the horizontal distribution of cloud phase. Schäfer et al. (2017) and Schäfer et al. (2018) found typical spatial scales of the variability of Arctic clouds of several 100 m, which is well resolved by the measurements of specMACS.

In order to start the comparison of the methods, first, the variation of the penetration depth between the different wavelengths is quantified. Vertical weighting functions of the unpolarized reflectivity (respectively absolute intensity I) were calculated for the 1640 nm channel of the SWIR camera and the center wavelengths of the three color channels of the polarization-resolving cameras, similarly to Platnick (2000). For this, a homogeneously mixed, plane-parallel cloud extending from 1 km to 2 km height with a total optical thickness of 5, an ice fraction of 0.5, and a solar zenith angle of 70° was simulated with MYSTIC and the scatter locations of the individual photons were saved. According to Platnick (2000), the vertical weighting function can be computed from the maximum penetration depth of each photon or the total number of scatterings per altitude bin. Figure 4.1 shows the vertical weighting functions for the center wavelengths of the red, green, and blue color channels of the polarization-resolving cameras and the 1640 nm channel of the SWIR obtained with the two mentioned methods in panels (a) and (b), respectively. The weighting functions for these wavelengths, calculated with both methods, are very similar.

Next, the difference between the vertical weighting functions of unpolarized and polarized signals was investigated. For this, a method to compute polarized vertical weighting functions had to be developed. The polarization signal is dominated by the first scattering orders. The contribution of each scattering order to the Q component of the Stokes vector was quantified by computing simulations of the same plane-parallel cloud as above for different scattering angles with different maximum numbers of scatterings allowed. The contribution of e.g. the first scattering order is the fraction of the simulated signal with a maximum number of scatterings of 1 to the full simulation, and so on. The contributions of each scattering order were determined separately for the slope angular range with scattering angles between 60° to 110° and the cloudbow angular range between 135° and 165° scattering

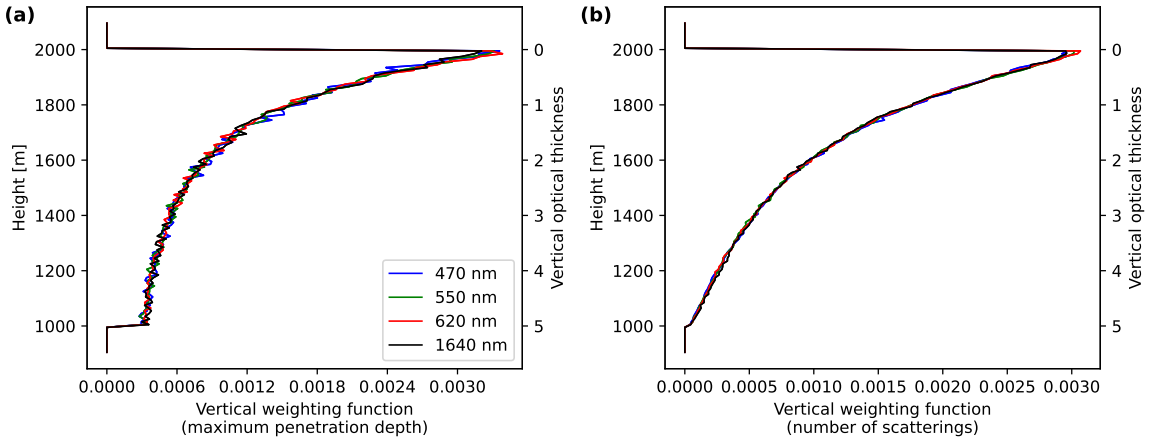

Figure 4.1: Vertical weighting functions for the absolute intensity I for a plane-parallel homogeneously mixed cloud with a total optical thickness of 5 and an ice fraction of 0.5 between 1 and 2 km height at a solar zenith angle of 70° for different wavelengths. **(a)** Vertical weighting functions computed from the maximum penetration depths of the photons. **(b)** Vertical weighting function calculated from the total number of scatterings per altitude layer.

angle. In addition, the vertical weighting functions for the different maximum numbers of scatterings were computed from the scatter locations similarly to above. For every scattering order, only the scatter locations up to the given maximum number of scatterings were considered. Finally, the polarized vertical weighting function was computed from the vertical weighting functions of the different scattering orders weighted by the contribution of the respective scattering order to the total signal. Figure 4.2 displays the obtained vertical weighting functions for the total reflectivity as above, the polarized reflectivity in the cloudbow and the slope range, and for single scattering at a wavelength of 550 nm, which is close to the center wavelength of the green color channel of the polarization-resolving cameras. As expected, the polarization signal originates from higher altitudes, closer to the cloud top than the unpolarized absolute intensity. However, it originates from lower altitudes than the single scattering signal.

The vertical weighting functions shown above were obtained under the assumption of a homogeneously mixed cloud. However, the vertical profile of the ice fraction could influence the vertical weighting function. Thus, different assumptions of the vertical ice fraction profile, including the homogeneously mixed cloud, a cloud with a linear ice fraction profile with height, and a cloud with a liquid water layer above an ice layer, were compared. Overall, the assumed ice fraction profile had only a very small influence on the vertical weighting function. However, the vertical weighting function depends on the solar zenith angle.

Due to the different penetration depths of the polarized and unpolarized signals, the polarized and spectral retrievals provide information about the cloud thermodynamic phase at two different altitudes. Thus, the combination of the spectral and polarized phase retrieval results allows for obtaining information about the vertical distribution of the cloud thermodynamic phase. This is not possible using only a single passive retrieval method

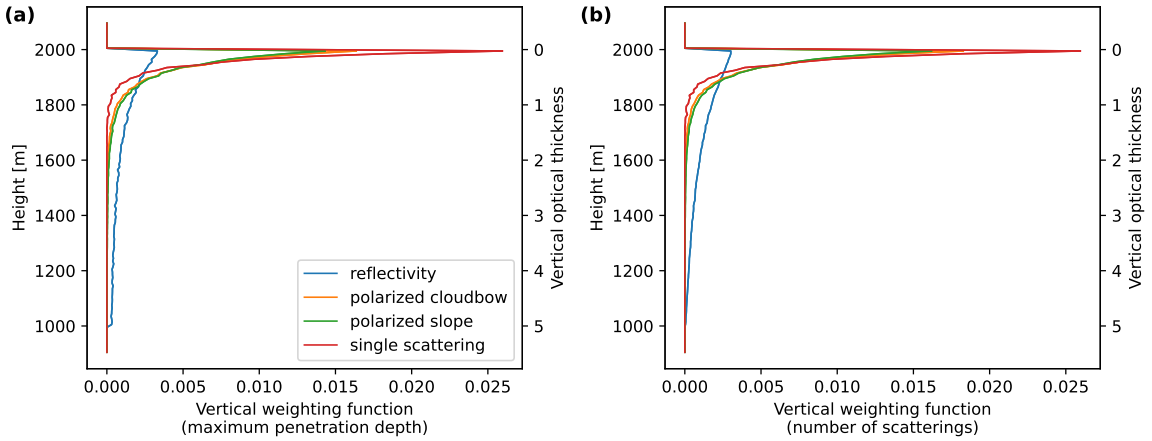

Figure 4.2: Vertical weighting functions for single scattering, polarization in the cloudbow or slope range, and the absolute intensity for a plane-parallel homogeneously mixed cloud with a total optical thickness of 5 and an ice fraction of 0.5 between 1 and 2 km height at a solar zenith angle of 70° for 550 nm wavelength. **(a)** Vertical weighting functions computed from the maximum penetration depths of the photons. **(b)** Vertical weighting function calculated from the total number of scatterings per altitude layer.

and underlines the great potential of simultaneous spectral and polarization measurements with the specMACS instrument.

Figure 4.3 shows example measurements of the ice index and ice fraction on 2022-04-01 between 11:15:55 and 11:17:55 UTC. The upper row corresponds to the spectral retrieval, and the lower row corresponds to the polarized retrieval. Panels (a) and (d) display the radiance and RGB image measured by the SWIR and polLR cameras, panels (b) and (e) fields of the retrieved ice indices and ice fractions, and panels (c) and (f) histograms of the ice indices and ice fractions. The spectral retrieval shows an average ice index of about 23, indicating a mixed-phase cloud. This is in agreement with the retrieved ice fractions between 0.35 and 0.63 obtained from the polarized retrieval, depending on the considered scattering angle range. The differences between the slope range and the cloudbow range are due to the biases of the respective retrievals as discussed in Sect. 3.4. Keeping the biases in mind, the results of cloudbow and slope range agree with each other and with the spectral retrieval. The histograms of the ice fraction in Fig. 4.3, especially for the slope angular range, have a bimodal structure with higher frequencies towards ice fractions of 0 and 1. In general, the frequency of occurrence of the ice fraction based on in situ measurements also shows a U-shape at a similar spatial resolution with higher frequencies towards pure liquid water and pure ice clouds (Korolev et al., 2017). The mixed-phase regime is not a stable state and thus less frequent than the pure liquid water and ice phases.

4.1.2 Comparison to radar and lidar data

Besides passive remote sensing, information about cloud thermodynamic phase can also be obtained from active remote sensing with radar and lidar instruments. While passive

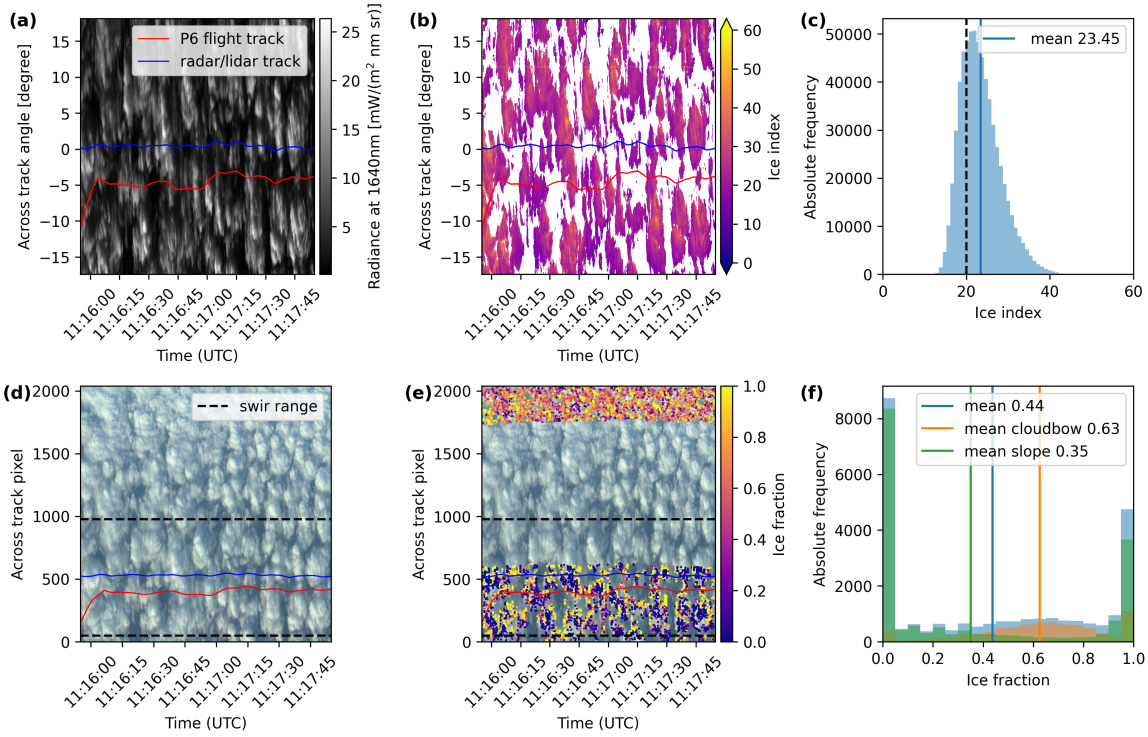

Figure 4.3: Observations of the SWIR and polLR cameras on 2022-04-01 between 11:15:55 and 11:17:55 UTC. **(a)** Radiance at 1640 nm measured by the SWIR. **(b)** Retrieved ice indices. **(c)** Histogram of the ice indices with their mean. **(d)** RGB image of the measurements by the polLR. **(e)** Retrieved ice fractions using the IDEFAX forward operator for the cloudbow range in the upper part and the slope range in the lower part for the green color channel. **(f)** Histograms of the ice fractions for the cloudbow range, slope range, and all measurements. The blue lines in panels **(a)** and **(d)** indicate the nadir direction, and the red lines represent the flight track of the P6 aircraft. The field of view of the SWIR relative to the polLR is denoted by the black dashed lines in panels **(d)** and **(e)**. The vertical dashed line in panel **(c)** represents the threshold value of the ice index (mixed-phase above, liquid below) between liquid and mixed-phase clouds.

imaging provides high-spatial resolution information in the horizontal, active remote sensing contributes vertical information about clouds and aerosols along the flight track. Lidars are typically operated in the visible and near-infrared parts of the spectrum, often at 355, 532, or 1064 nm. The backscattered laser signal is described using Mie theory. Lidar measurements of mixed-phase clouds are often dominated by small liquid water droplets, which create strong backscatter signals and lead to attenuation (e.g. Korolev et al., 2017). In addition, depolarization lidar measurements help to distinguish cloud thermodynamic phase. Spherical cloud droplets produce only very small or no depolarization, whereas ice crystals with complex shapes can create strong depolarization. In contrast to lidars, cloud radars have much longer wavelengths respectively smaller frequencies, such as e.g. 35 GHz in the Ka-band. The radar signal is, in general, also described using Mie theory. However, for the observations of comparably small hydrometeors, such as supercooled liquid cloud droplets or ice crystals in low-level Arctic mixed-phase clouds, the Rayleigh approximation

can be applied. In the Rayleigh scattering regime, the extinction cross section and radar reflectivity are proportional to the particle diameter D^6 (Petty, 2006). Consequently, the radar signal is dominated by the larger ice crystals and the contribution of the liquid cloud droplets is negligibly small. Additional information about the thermodynamic phase can be obtained from measurements of the Doppler velocity, since liquid cloud droplets and ice crystals have different fall speeds. The fall speeds of small liquid cloud droplets are very small, whereas ice crystals reach larger velocities depending on their shape.

The remote sensing setup of HALO during HALO–$(\mathcal{AC})^3$ included also radar and lidar instruments (Ehrlich et al., 2025). The HALO Microwave Package (HAMP) consists of a Ka-band cloud radar operating at a frequency of 35 GHz and passive microwave radiometers at various frequencies (Mech et al., 2014). The HAMP radar provides radar reflectivity and radar linear depolarization ratio measurements with a temporal resolution of 1 Hz and a vertical resolution of 30 m. In addition, the WAter vapor Lidar Experiment in Space (WALES) lidar has a high spectral resolution channel at 532 nm measuring the backscatter coefficient and particle linear depolarization, a water vapor differential absorption lidar system at 935 nm, and an additional aerosol channel at 1064 nm (Wirth et al., 2009). The measurements have a temporal resolution of 1 Hz and 15 m vertical resolution. The data measured by HAMP and WALES during HALO–$(\mathcal{AC})^3$ is available from Dorff et al. (2024) and Wirth and Groß (2024).

Figure 4.4 shows example measurements of the WALES lidar and the HAMP radar corresponding to the specMACS observations in Fig. 4.3. The lidar and radar track are indicated by the blue line in Fig. 4.3. The high radar reflectivity in panel (b) indicates the presence of ice crystals already close to cloud top, which are precipitating towards the surface. Moreover, there are high lidar backscatter ratios visible at cloud top in panel (a) and the lidar depolarization in panel (c) shows values close to zero at the very cloud top. This could indicate the presence of supercooled liquid water at the top of the cloud, as it is expected for low-level Arctic mixed-phase clouds.

The different sensitivities of lidar and radar measurements can be exploited more quantitatively in synergistic radar-lidar retrievals of cloud microphysical properties (Ewald et al., 2021; Delanoë and Hogan, 2008). The synergistic retrieval method by Ewald et al. (2021) is based on the variational optimal estimation retrieval of ice cloud properties VarCloud by Delanoë and Hogan (2008), which has recently been extended to also derive liquid water cloud properties (Aubry et al., 2024). Starting from an initial guess, cloud properties are optimized until lidar and radar backscatter signals obtained from forward operators with the current best choice of cloud properties agree with the measurements. The retrieval results also include a phase classification. However, a large number of assumptions have to be made in the synergistic retrievals. Figure 4.5 shows the results of this phase classification for the same example scene as before in Fig. 4.3 and 4.4. The VarCloud retrieval results were provided by Florian Ewald (Ewald, 2025). The classification detected mostly "ice" with only small areas of "supercooled water" or "supercooled + ice" close to cloud top. Thus, VarCloud detects more pure ice clouds compared to the passive observations. However, the observed kind of low-level Arctic mixed-phase clouds is also very challenging for synergistic radar-lidar retrievals, which are typically tuned for more stratiform clouds.

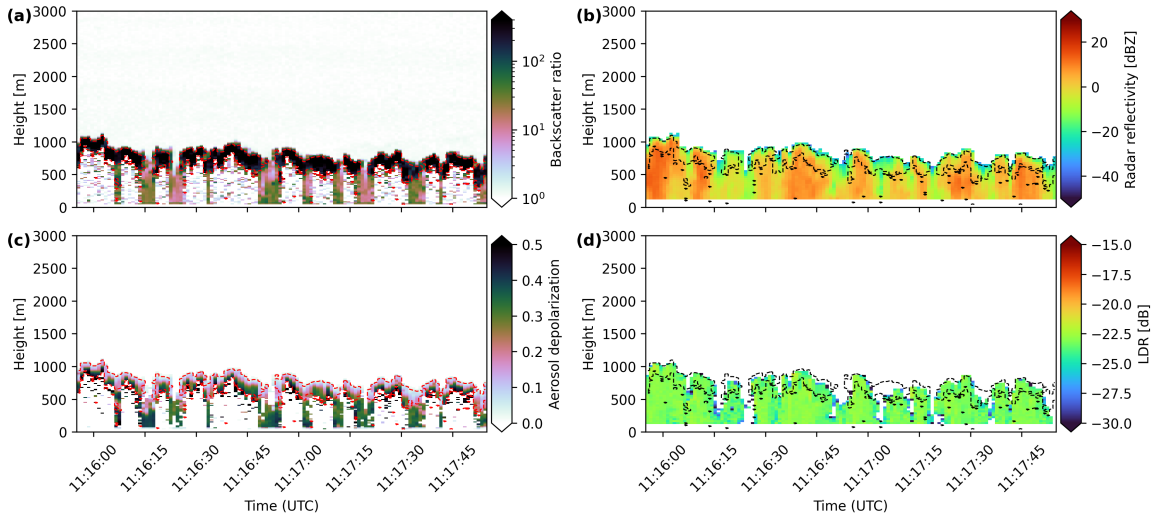

Figure 4.4: Lidar (left column) and radar (right column) measurements taken on 2022-04-01 between 11:15:55 and 11:17:55 UTC. **(a)** Lidar backscatter ratio. **(b)** Radar reflectivity. **(c)** Lidar aerosol depolarization. **(d)** Radar linear depolarization ratio. The red and black dashed lines indicate the areas with lidar backscatter ratios larger than 100. Lidar depolarization data with backscatter ratios smaller than 10 were filtered out to focus on cloud data only.

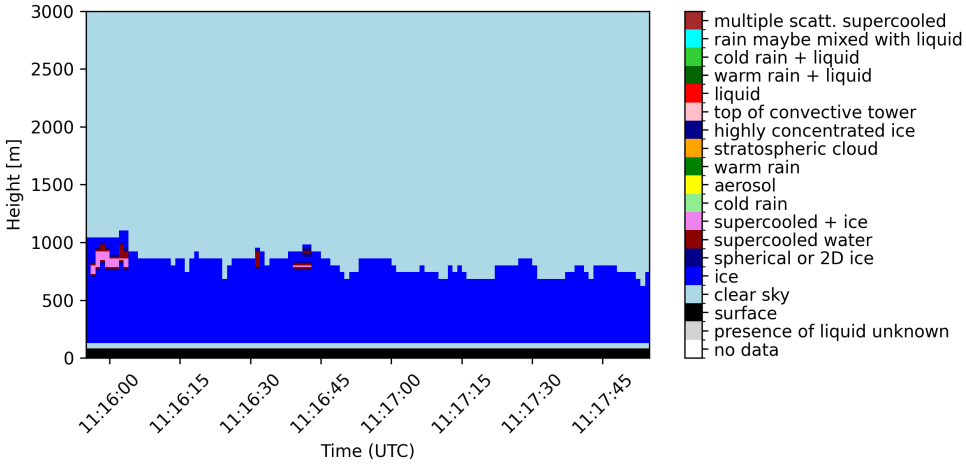

Figure 4.5: Phase classification from the synergistic radar-lidar retrieval VarCloud on 2022-04-01 between 11:15:55 and 11:17:55 UTC.

4.1.3 Comparison to in situ data

Finally, in situ measurements can provide quantitative measurements of cloud thermodynamic phase along the one-dimensional flight track. There is a large number of different measurement techniques and in situ probes, including, for example, scattering probes, imaging probes, or hot-wire probes. However, phase discrimination in mixed-phase clouds is also challenging for in situ instruments, such that a combination of different measure-

ment techniques is generally recommended (Korolev et al., 2017). In addition, in situ measurements often suffer from comparably low sampling statistics.

During HALO–$(\mathcal{AC})^3$, the P6 aircraft (Wesche et al., 2016) was equipped with in situ instrumentation, and some coordinated flights between HALO and P6 were performed (Ehrlich et al., 2025). The instrumentation on P6 included different scattering and optical array probes that measure the particle number size distribution and derived quantities in different size ranges. The cloud droplet probe (CDP) is sensitive to particles between 2.8 µm to 50 µm size and was used to compute the LWC, assuming that particles smaller than 50 µm are liquid cloud droplets and larger particles are ice crystals (Moser et al., 2023). This assumption is, in general, reasonable for low-level Arctic mixed-phase clouds, but it introduces uncertainties (McFarquhar et al., 2017; Korolev et al., 2017). The cloud imaging probe (CIP) and precipitation imaging probe (PIP) provide measurements of the particle number size distribution for the larger size range between 30 µm and 6.4 mm (Moser et al., 2023). The IWC was derived from their measurements using the mass-diameter relationships by Field et al. (2006) and Brown and Francis (1995). The uncertainty of the measured cloud water content in mixed-phase clouds was estimated to be between 20 % to 50 % (Moser et al., 2023). Finally, an ice mass fraction quantifying the thermodynamic phase can be obtained from the fraction of the IWC to the total cloud water content.

Additional information about the thermodynamic phase is provided by the polar nephelometer (PN), which measures the non-normalized scattering phase function (Gayet et al., 1997). From the phase functions, asymmetry parameters and extinction coefficients can be derived. These allow for the distinction between spherical and non-spherical particles and, hence, liquid cloud droplets and ice crystals.

The data of the above mentioned in situ probes is available with 1 Hz resolution from Moser et al. (2023) and Dupuy et al. (2024). Figure 4.6 shows measurements of the extinction coefficient, asymmetry parameter, and ice mass fraction in the first, second, and third columns, respectively, for the same scene as shown in Fig. 4.3 above. The upper row displays the time series, the lower row histograms of the measured quantities. During this time period, there was an overflight of HALO over P6 at 11:16:55 UTC. The flight track of the P6 aircraft is indicated by the red line in Fig. 4.3. The cloud top height during the segment was around 800 m, and the flight altitude of P6 was about 550 m. Towards the end of the segment from about 11:19:40 UTC, the P6 aircraft started to descend. Extinction coefficients smaller than 1 km^{-1} and asymmetry parameters smaller than 0.8 are generally an indication of the ice phase, whereas higher values are related to mixed-phase and liquid water clouds (Moser et al., 2023). A comparison of all measured variables from the in situ probes indicates that the observed clouds are in a mixed-phase regime. At the end, during the descent of the aircraft, more ice is observed at lower altitudes.

The in situ measurements are in agreement with the remote sensing observations discussed in the previous sections. The observed spectral ice indices with an average value of 23.45 were above the threshold value for mixed-phase clouds, and the average ice fraction of 0.44 and the histograms of the polarized phase retrieval also correspond to a mixed-phase cloud. In addition, radar and lidar measurements indicated a layer containing supercooled liquid water droplets and ice crystals at cloud top.

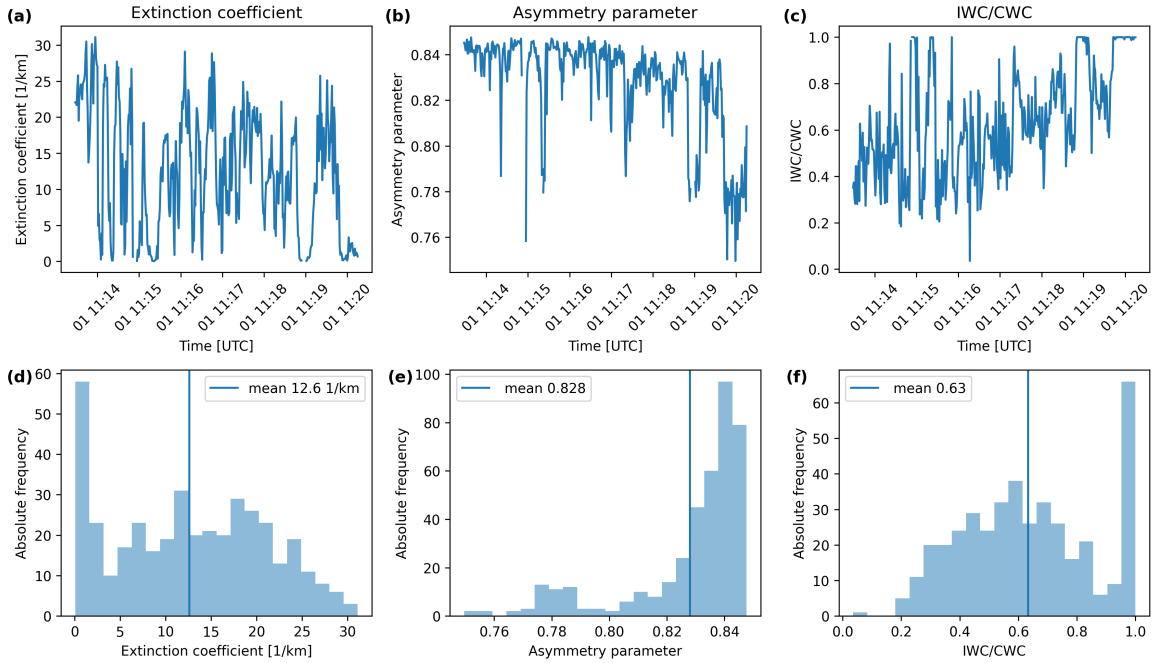

Figure 4.6: In-situ measurements taken by the instruments on the P6 aircraft on 2022-04-01 during the HALO overflight at 11:16:55 UTC. Time series of the extinction coefficient, asymmetry parameter, and the ice mass fraction, the ratio of the IWC to the total cloud water content, are shown in panels **(a)**, **(b)**, and **(c)**, respectively, and the corresponding histograms with mean values are displayed in panels **(d)**, **(e)**, and **(f)**.

4.2 Case study: Evolution of clouds during a strong cold air outbreak

The content of this section was already published in Weber et al. (2025b) and Weber et al. (2025a). Parts of the introduction of Sect. 4.2 and the results of Sect. 4.2.1 are included in Weber et al. (2025b). Further parts of the introduction of Sect. 4.2 and Sect. 4.2.2 to 4.2.5 can be found in Weber et al. (2025a). The content has been slightly restructured and additional discussions have been added.

As a case study, the data collected on the research flight conducted by HALO on 2022-04-01 during the HALO–$(\mathcal{AC})^3$ campaign are analyzed in detail. The flight targeted the Fram Strait region, where a MCAO was observed on that day. Figure 4.7 shows the MCAO index defined in Eq. 2.6 computed from ERA5 data (Hersbach et al., 2023a,b) in panel (a) and the MODIS satellite image in panel (b). The flight track is superimposed in red, and contours of the mean sea level pressure and the geopotential height at 500 hPa from ERA5 data are displayed in panel (a). According to Papritz and Spengler (2017) and Dahlke et al. (2022), the event observed on this day with average MCAO indices of around 8 K in the Fram Strait region can be classified as a moderate to strong MCAO. It appears to be a

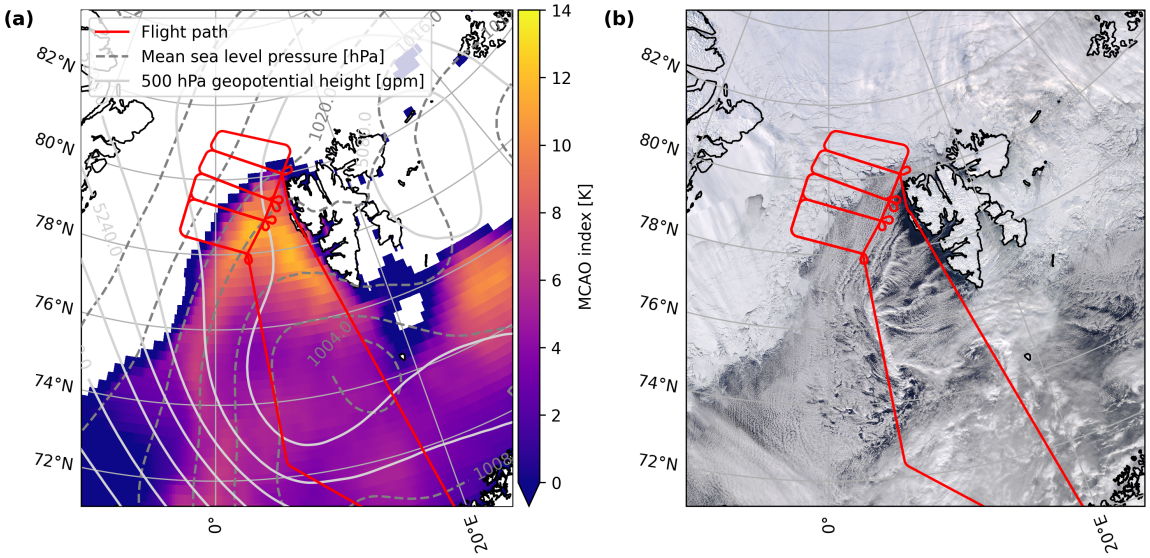

Figure 4.7: MCAO index from ERA5 data (Hersbach et al., 2023a,b) **(a)** and MODIS satellite image downloaded from NASA Worldview (https://worldview.earthdata.nasa.gov/) **(b)** for 2022-04-01. The red lines indicate the flight track. In addition, the mean sea level pressure and geopotential height at 500 hPa from ERA5 are shown as gray dashed and light gray solid lines, respectively, in panel **(a)**.

typical event for this region during that time of the year (Kirbus et al., 2024). The synoptic situation was characterized by a high-pressure system over Greenland and the Central Arctic and a low-pressure system above Scandinavia, the Barents Sea, and Russia. This led, together with a local low-pressure system south of Svalbard, to a northerly flow in the Fram Strait. The satellite image in Fig. 4.7b shows cloud streets extending southwards from the ice edge. In addition, there are local effects due to the topography of Svalbard visible with several convergence lines and cloud-free regions southwest of the island. The flight pattern targeted the initial phase of the MCAO following the quasi-Lagrangian sampling approach with flight legs oriented perpendicular to and along the wind direction (Wendisch et al., 2024). This quasi-Lagrangian observation strategy allows for studying the temporal evolution of thermodynamic and cloud properties observed during the MCAO.

For this purpose, measurements and retrieval results were combined with backward trajectories, which allow for assigning every measurement the time or distance the air mass has traveled southwards since passing the ice edge. The backward trajectories were computed from ERA5 wind fields (Kirbus, 2025) using Lagranto (Sprenger and Wernli, 2015). Every 1 minute along each HALO flight track, a trajectory was initialized horizontally at the location of HALO, and vertically at 920 hPa pressure altitude, which roughly corresponds to cloud top. The trajectories were calculated backwards for 24 hours also tracing the sea ice concentration (SIC) from the combined AMSR2-MODIS dataset (Ludwig et al., 2020). The obtained backward trajectories have an improved reliability as the dropsondes released from the HALO aircraft have been assimilated in ERA5. Furthermore, the trajectories cover comparably short timescales and therefore the influence of errors remains small (Kirbus

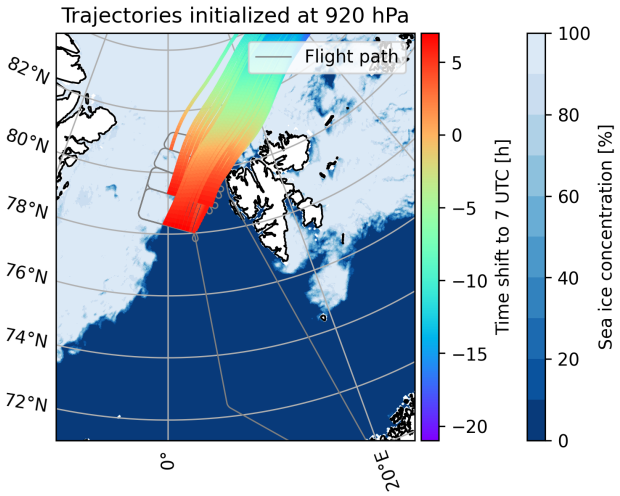

Figure 4.8: Backward trajectories along the flight track together with AMSR2-MODIS sea ice concentration (Ludwig et al., 2020) for 2022-04-01. For better visibility, only every 20th backward trajectory is shown. The color coding displays the time along the trajectories.

et al., 2024).

Figure 4.8 displays the backward trajectories obtained for the flight on 2022-04-01, together with the AMSR2-MODIS sea ice concentration. They indicate a southward flow from the Arctic towards the North Atlantic. The time and distance above open ocean were computed for every trajectory by integrating the fraction of open water (1 - SIC) over time and distance, respectively, similar to Spensberger and Spengler (2021). For better comparability, the evolution of the cloud properties is analyzed both as a function of time and distance above open ocean, as some studies use time while others use distance. In addition, the wind speed is not constant along the trajectories.

For the analyses presented in the following Sect. 4.2.1 to 4.3, only measurements above open ocean were considered. Over sea ice, the measurements and retrievals based on passive remote sensing have additional uncertainties due to the influence of the surface, especially for thin clouds. In addition, it is difficult to detect clouds above sea ice correctly. Thus, a sea ice mask was computed from the combined AMSR2-MODIS dataset. All observations and measurements with sea ice concentrations larger than 80 %, which is a typical choice for the definition of the ice edge, were excluded from further analysis. At this threshold value, sea ice still partially affects the measurements, but cloud formation begins as soon as small fractions of open ocean are present, and this initial phase should not be excluded from the analyses.

In the following Sect. 4.2.1, the temporal and spatial evolution of macroscopical and microphysical cloud properties are analyzed, focusing on cloud thermodynamic phase partitioning. In addition, the temperature dependence and vertical distribution of cloud thermodynamic phase are investigated in Sect. 4.2.2 and 4.2.3. Finally, the influence of ice processes on cloud liquid water in the observed low-level Arctic mixed-phase clouds is studied by applying a simple adiabatic cloud model in Sect. 4.2.4.

4.2.1 Temporal evolution of cloud properties

Macroscopic cloud properties

Information about the macroscopic properties of the observed clouds, such as their horizontal extent and top height, was obtained from specMACS observations using different retrieval methods. Cloud top height was computed with the stereographic retrieval method by Kölling et al. (2019). The cloud fraction was derived by applying the cloud mask by Pörtge et al. (2023) every minute to the measurements of the polarization-resolving cameras. The cloud fraction and cloud top height respectively cloud top temperature are important quantities since they directly impact the cloud radiative effect. Horizontal cloud extent was derived from the specMACS measurements with a watershedding algorithm as described in Sect. 3.6. The applied watershedding algorithm provides the horizontal cross-sectional area of a cloud from which the cloud radius was computed by assuming a circular shape. The obtained cloud properties were combined with backward trajectories to study their evolution with time and space during the MCAO observed on 2022-04-01.

Figure 4.9 shows the cloud top height (left column), cloud fraction (middle column), and cloud radius (right column) as a function of time (upper row) and distance (lower row) traveled above open ocean. The histograms for every time or distance bin are normalized by the total number of observations of the respective bin. In addition, Figure 4.10 displays RGB images taken by the polarization-resolving cameras at four points in time (30 min, 60 min, 90 min, and 150 min above open ocean) to illustrate the observed cloud morphology. Parts of Fig. 4.9 and 4.10 have also been shown in Wendisch et al. (2024).

The cloud top height in Fig. 4.9a and 4.9d increases stepwise and almost linearly with time and distance from about 250 m close to the ice edge to about 1.5 km after 300 min. This increase of cloud top height with time is typical for the evolution of clouds during MCAOs as the atmospheric boundary layer deepens with time (Murray-Watson et al., 2023; Kirbus et al., 2024). The cloud fraction (see Fig. 4.9b and 4.9e) remained comparably constant during the first hours of the observed MCAO as can also be seen in the RGB images in Fig. 4.10. Cloud fractions close to 1 are observed at very small distances and times above open ocean. These high cloud fractions are due to the misidentification of bright sea ice in the marginal ice zone as clouds by the cloud mask, which is based on the brightness. In contrast, Murray-Watson et al. (2023) found increasing cloud fractions during the first hours of MCAOs followed by a slight decrease and generally slightly higher cloud fraction values. However, they used satellite observations which had a much coarser spatial resolution of 25 km compared to the high spatial resolution of 10 m to 100 m of the airborne specMACS observations, and the cloud fraction strongly depends on the threshold values applied in the cloud mask.

Finally, the cloud radius increases from radii of approximately 0.5 km to 1 km, with high variability. These results agree with the increasing roll circulation wavelength from initially 1 km to 2 km derived from data measured by the radar installed on the P5 aircraft on the same day and in the same region (Schirmacher et al., 2024). The cloud radius distribution consists of a mixture of smaller and larger clouds (see Fig. 4.10).

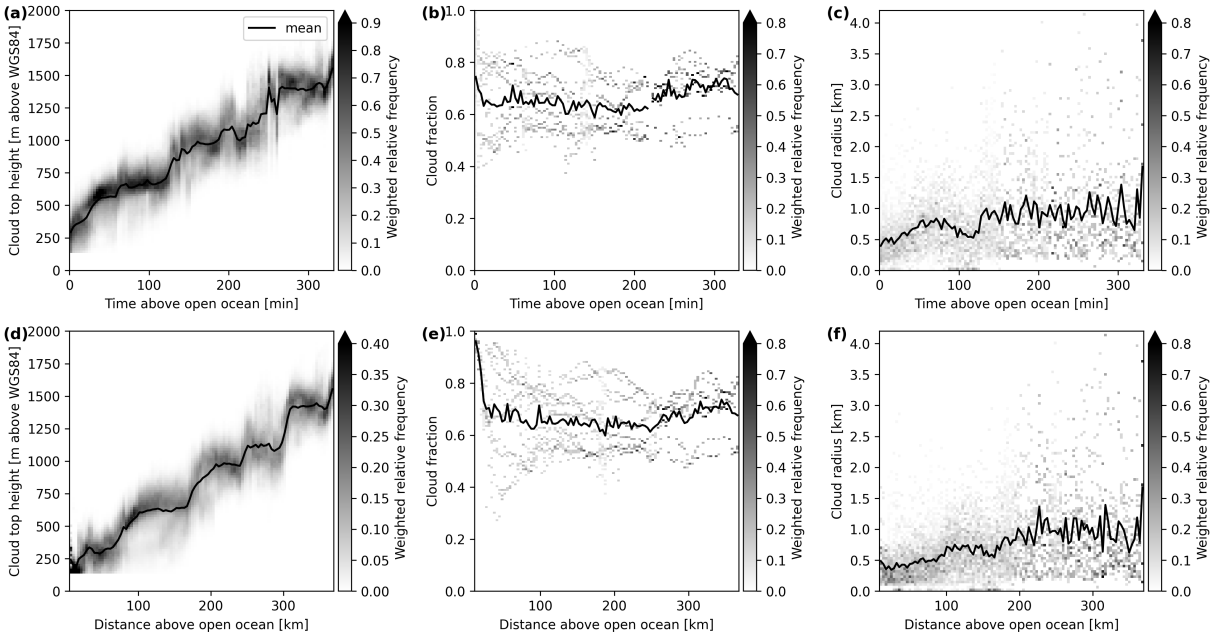

Figure 4.9: Histograms of cloud top height **(a, d)**, cloud fraction **(b, e)**, and cloud radius **(c, f)** as a function of time (upper row) and distance (lower row) above open ocean. The black line indicates the mean.

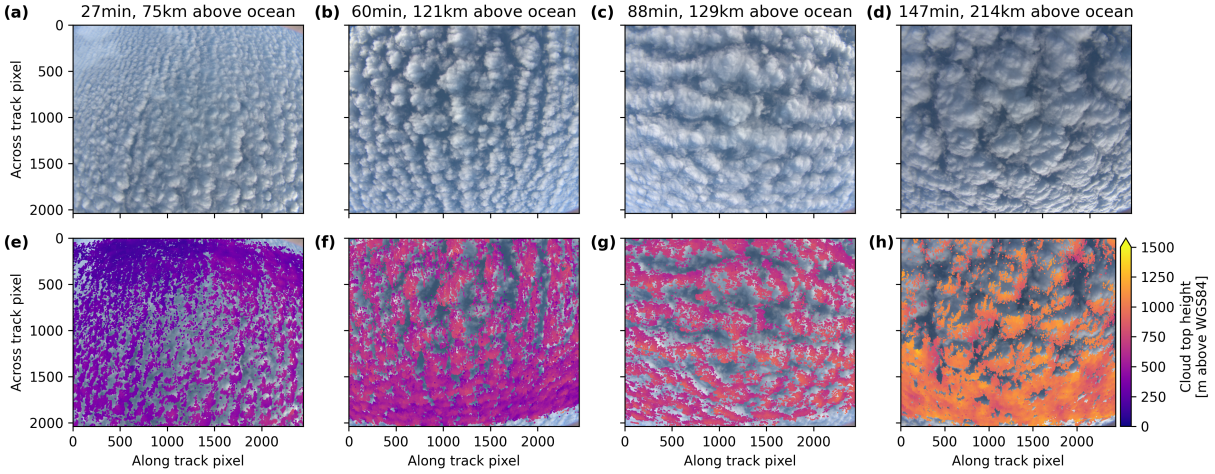

Figure 4.10: Example RGB images (upper row) and cloud top heights (lower row) at four different points in time, about 30 min, 60 min, 90 min, and 150 min above open ocean.

The different shapes of the curves describing, e.g., the evolution of the cloud top height during the first kilometers above open ocean compared to the first minutes above open ocean in Fig. 4.9 can be explained by changing wind speeds due to the off-ice acceleration at the sea ice edge. Moreover, the RGB images in Fig. 4.10 show cloud streets in panels (a) to (c), which are often observed in the initial phase of a MCAO (Brümmer, 1999). After about 150 min, more cellular structures evolve that are visible in panel (d), indicating a

transition of cloud morphology from the cloud streets towards a cellular cloud regime.

Cloud microphysical properties

The same analysis as for the macrophysical quantities was also performed for microphysical cloud characteristics such as the effective radius of liquid water droplets and the cloud thermodynamic phase partitioning. The cloud droplet effective radius was derived with the cloudbow retrieval by Pörtge et al. (2023). The cloud thermodynamic phase partitioning is characterized using the ice fraction from the polarimetric retrieval and the spectral ice index as described in Sect. 3.4 and 3.5. If not mentioned otherwise, the results of the polarized phase retrieval for the cloudbow angular range using the IDEFAX forward operator are shown and only observations with saturated polarization signals are considered because they provide the smallest uncertainties. Nevertheless, the results still have a high uncertainty, especially when the solar zenith angle is very large. All shown measurements of the effective radius and ice fraction correspond to the green color channel of the polarization-resolving cameras. Figure 4.11 displays the evolution of the effective radius of the liquid water droplets (a, d), the ice index (b, e), and the ice fraction (c, f) as a function of time and distance above open ocean. For later times (after approx. 210 min), no measurements of the effective radius and the ice fraction are available because the solar zenith angle during this part of the flight was too large for the cloudbow to be inside the field of view of the cameras.

The effective radius of liquid cloud droplets shows a rapid increase from about 5 µm to 7.5 µm in the first approximately 30 min. It remains then constant until about 150 min above open ocean, even though the cloud top height increases with time throughout the observed time period, which is usually accompanied by an increase in droplet size. At the same time, the ice index indicates the presence of ice crystals. Hence, the constant effective radius during this time could be explained by ice crystals competing with the cloud droplets for the available water vapor, limiting the growth of cloud droplets on the one hand, or freezing of larger cloud droplets on the other hand. Afterward, the effective radius becomes more variable and increases slightly, which coincides with the transition from cloud streets to cellular structures. In the more convective cellular regime, liquid water is formed in the convective updrafts at the centers of the cells, which could lead to further increasing effective radii at the higher cloud tops (Schirmacher et al., 2024; Maherndl et al., 2024b). However, the number of measurements is also smaller in this time range due to larger solar zenith angles, and the results are therefore more uncertain. The spike in the evolution of the effective radius at very small distances in panel (d) is due to the influence of sea ice, which was not completely filtered out and should be treated as an outlier.

The evolution of the effective radius of liquid cloud droplets during MCAOs was also studied by Murray-Watson et al. (2023), who found increasing effective radii with time and larger sizes between about 12 µm and 18 µm. The effective radii were, however, derived from MODIS satellite data with a bispectral retrieval, which has large uncertainties for Arctic mixed-phase clouds and a much coarser spatial resolution. In addition, they focused on liquid water clouds only. In situ measurements of the effective radius conducted by

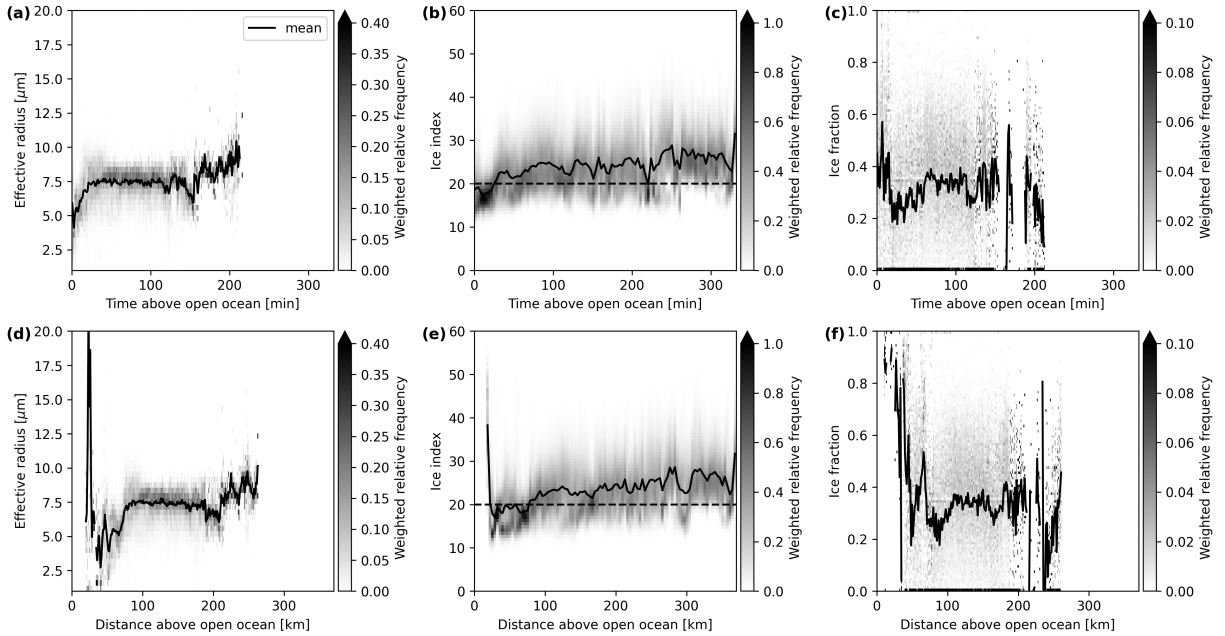

Figure 4.11: Histograms of the effective radius of the liquid water droplets **(a, d)**, the ice index **(b, e)**, and the ice fraction **(c, f)** as a function of time (upper row) and distance (lower row) above open ocean. The black solid line indicates the mean, the black dashed line in panels **(b)** and **(e)** is the threshold value between the liquid water and the mixed phase.

the P6 aircraft during the same day and in the same region show average effective radii of about 4 µm during the first 100 min above open ocean and slightly increasing radii for larger times. While the effective radii derived from cloudbow observations of specMACS are representative for cloud top, the P6 aircraft was flying lower inside the cloud. This could explain the slightly smaller observed values of the in situ measurements compared to the cloudbow retrieval results.

The evolution of cloud thermodynamic phase is studied using the spectral ice index and the ice fractions from the polarized phase retrieval in the middle and right columns of Fig. 4.11, respectively. As discussed in Sect. 4.1.1, the results of the multi-angle polarimetric retrieval of the ice fraction and the spectral approach applied to derive the ice index have different penetration depths. Both are representative for the cloud top, but the spectral signal originates from slightly deeper altitudes within the cloud than the polarized signal. The ice index is smaller than 20 during the first 30 min, indicating a pure liquid water cloud. Afterward, it transforms into a mixed-phase cloud with slightly increasing ice indices over time. The transition from pure liquid water to the mixed phase occurs during the same time range as the rapid increase of the effective radius at the beginning. Larger effective radii increase the probability for freezing of liquid water droplets and heterogeneous ice formation. In addition, during the same time range, the cloud top height increased and the cloud top temperature decreased. Thus, a threshold temperature and size of the cloud liquid water droplets could be reached that initiate the formation of ice crystals.

The evolution of the ice fraction shows a similar structure. The higher ice fractions close to the ice edge are caused by a misclassification of sea ice as cloud. The cloud mask using the spectral data is more accurate here, as a wavelength of 1640 nm, where sea ice is comparably dark, was chosen. The cloud mask for the polarized retrieval is much more affected by sea ice. A combination of both masks is not possible because the observation ranges of the spectral and polarized retrievals are different. Considering the initially high ice fraction as outliers and taking the high bias of the ice fraction for the cloudbow range into account, the ice fraction at the beginning was in the range of 0.2. It then increases until about 90 min above open ocean and stays almost constant, but the cloud top is still dominated by liquid water. The initially faster decrease of the ice fraction appears slightly later than the increase of the spectral ice index, which is more sensitive to ice and representative for slightly lower altitudes, deeper within the cloud. From around 150 min above open ocean, when the transition from cloud streets to cells was observed, the ice fraction becomes variable but also uncertain.

4.2.2 Dependence of cloud thermodynamic phase on temperature

To investigate the temperature dependence of the thermodynamic phase partitioning, retrieval results of the ice index and ice fraction using data from the specMACS instrument were combined with measurements of the cloud top temperature from the Video airbornE Longwave Observations within siX channels (VELOX) instrument, which was also operated on board HALO. VELOX is a thermal imager that measures brightness temperatures at six different wavelength channels between 7.7 µm and 12 µm (Schäfer et al., 2022). It has a spatial resolution similar to specMACS of about 10 m at typical flight altitudes and a field of view of $35.5° \times 28.7°$. The data from VELOX are available from Schäfer et al. (2023). Here, the brightness temperatures measured by the first broadband channel (covering the wavelength range between 7.7 µm and 12 µm) were used, which are representative for the cloud top for measurements in the Arctic with low atmospheric water vapor contents. The measurements from VELOX and specMACS were matched to obtain corresponding cloud top temperature measurements for every ice index, respectively, ice fraction measurement. Since the field of view of VELOX in across-track direction is smaller than that of the polarization-resolving cameras of specMACS, and due to the large solar zenith angles, measurements of the ice fraction in the cloudbow range could not be matched with cloud top temperature measurements. Thus, the following analysis is restricted to data of the ice index and the ice fraction derived from the more uncertain slope angular range.

Figure 4.12 shows the ice index (blue) and ice fraction (orange) as a function of cloud top temperature, similar to the pseudo-vertical profiles introduced by Rosenfeld and Lensky (1998). The individual panels correspond to different time ranges above open ocean. This depiction was chosen since the thermodynamic structure of the boundary layer during MCAOs changes with time above open ocean. Vertical profiles of the air temperature and potential temperature measured by dropsondes during the research flight on 2022-04-01 are shown in Fig. 4.13. The dropsonde data are available from George et al. (2024). They were combined with trajectory data to assign every measurement a time above open ocean.

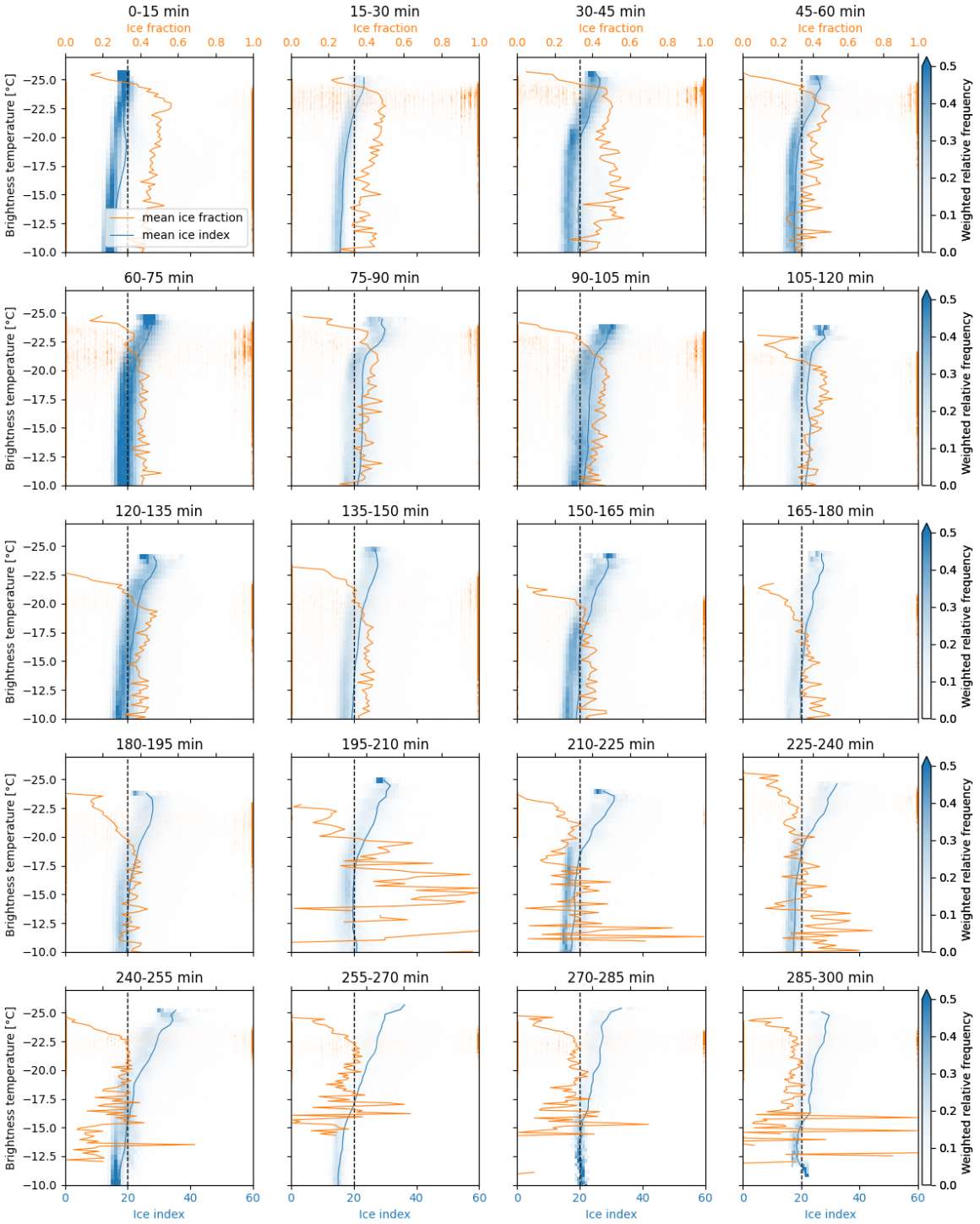

Figure 4.12: Histograms of ice index (blue) and ice fraction (orange) as a function of the brightness temperature between 7.7 µm and 12 µm (representative for cloud top) for different time ranges above open ocean. The blue and orange solid lines denote the respective mean. The black dashed line indicates the threshold value of the ice index between the liquid water and the mixed phase. The ice fraction was derived with the IDEFAX for the slope angular range.

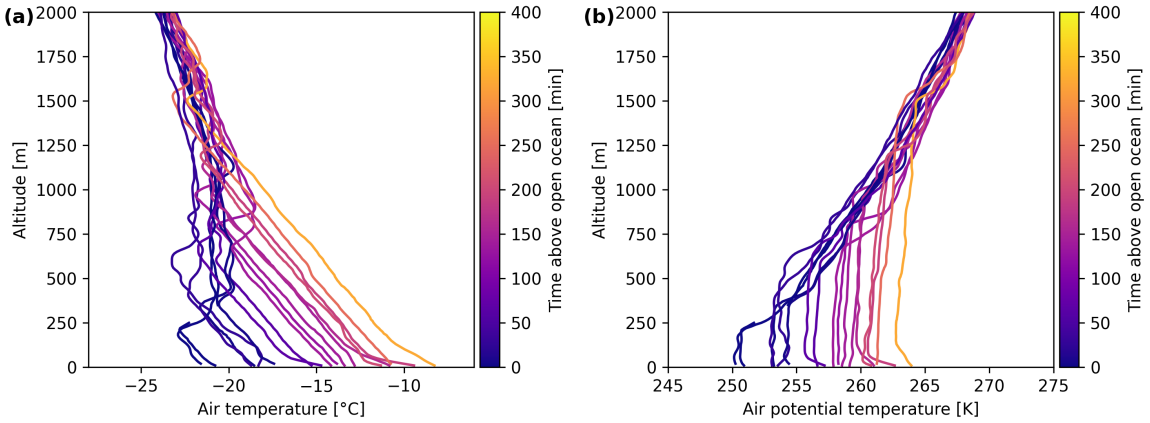

Figure 4.13: Air temperature **(a)** and potential temperature **(b)** measured by the dropsondes on 2022-04-01. The colors indicate the time above open ocean at the location of the individual dropsondes.

In general, the temperature decreases with height, and an inversion marks the top of the boundary layer. The altitude of the inversion layer increases with time above open ocean as the boundary layer deepens. In addition, the temperature increases with time. A detailed study of the thermodynamic evolution of the MCAO on 2022-04-01 during HALO–$(\mathcal{AC})^3$ can be found in Kirbus et al. (2024) and Wendisch et al. (2025). During the first hour above open ocean, high diabatic heating rates exceeding $6\,\mathrm{K\,h^{-1}}$ and moistening rates larger than $0.3\,\mathrm{g\,kg^{-1}\,h^{-1}}$ were observed at the surface. The heat and moisture are increasingly mixed upward as the time above open ocean increases and the boundary layer develops.

During the first 15 min after passing the ice edge, the ice index in Fig. 4.12 is below the threshold value of 20 for all temperatures, which indicates a liquid water cloud. At later times, the ice index is still almost constant with temperature except for the coldest part, where it increases with decreasing temperature and crosses the threshold value from the liquid water into the mixed-phase regime. This indicates that ice formation happens preferentially at the coldest temperatures. This is reasonable as several studies based on in situ measurements have shown that the relative fraction of ice increases with decreasing temperature (Korolev et al., 2017). With time, the transition from the liquid water to the mixed phase shifts to higher temperatures, and the ice indices at the coldest temperatures further increase. This could be explained by ice, which is continuously formed at the coldest temperatures at the cloud top and sediments downwards. Consequently, the relative fraction of ice increases and liquid water might additionally be depleted through riming or the WBF mechanism.

The ice fraction derived with the polarimetric retrieval for the slope angular range is mostly constant or slightly increasing with decreasing temperature. However, a strong decrease of the ice fraction with decreasing temperature can be observed at the lowest temperatures. This indicates that there is a very thin, more liquid-dominated layer at the cloud top, which is not detected by the spectral retrieval. As discussed in Sect. 4.1.1, the spectral retrieval is sensitive to lower altitudes within the cloud than the polarized retrieval, and the polarized retrieval is more sensitive to liquid water. At longer times above open

ocean in the last two rows of Fig. 4.12, the retrieved ice fraction becomes variable and uncertain due to increasing solar zenith angles and a decreasing number of data points.

4.2.3 Vertical distribution of cloud thermodynamic phase

Moreover, the vertical distribution of cloud thermodynamic phase was studied. The retrieved ice fractions and ice indices can be combined with the cloud top height measurements obtained from the stereographic retrieval. In this way, pseudo-vertical profiles of the ice index and ice fraction are derived, similar to the method by Rosenfeld and Lensky (1998) for the effective radius. In addition, the results of the spectral and polarized retrievals of cloud thermodynamic phase provide vertical information at different altitudes, as the signals of both methods originate from different penetration depths within the cloud.

Fig. 4.14 displays several examples of pseudo-vertical profiles for the ice index (blue) and ice fraction (orange) for different time ranges above open ocean. Here again, the ice fraction derived for the more certain cloudbow range using the IDEFAX is analyzed, and only measurements with a saturated polarization signal were considered. Similar to the results presented in the previous section, the ice index in the first 15 min above open ocean is mostly below 20, indicating a pure liquid water cloud. The ice fraction is affected by sea ice in this first time range and hence overestimated. Afterward, the ice index and ice fraction both increase with time and height, and the clouds are in a mixed-phase regime throughout the vertical profiles. This agrees with the temperature dependence of the cloud thermodynamic phase discussed in the previous section, as the temperature typically decreases with altitude (see Fig. 4.13). At the very top, the ice fraction shows a strong and sharp decrease for most time ranges. This decrease is also partly captured in the vertical profiles of the ice index, but it is less pronounced for the ice index. This confirms the existence of a geometrically thin, more liquid-dominated mixed-phase layer at cloud top compared to the altitudes directly below. This layer has a geometrical thickness of approximately 100 m to 200 m. For times above open ocean larger than 210 min, the cloudbow range was outside the field of view of the specMACS instrument due to large solar zenith angles and no ice fractions could be derived.

Additional vertical information is obtained from active remote sensing measurements. During HALO–$(\mathcal{AC})^3$, the WALES lidar and HAMP radar were employed on board HALO. The lidar and radar measurements were combined with backward trajectories to create composites as a function of time and distance above open ocean. To this end, the data were sorted into one minute bins and all measurements of a certain time bin were averaged. Figure 4.15 shows the corresponding results for the lidar backscatter ratio (first row), aerosol depolarization (second row), and radar reflectivity (third row). The cloud top height in both lidar and radar data shows a linear increase with time and distance, similar to the measurements of specMACS discussed in Sect. 4.2.1. At the cloud top, the lidar backscatter ratio is high and the depolarization is close to zero, indicating spherical particles. As the lidar is particularly sensitive to small liquid cloud droplets with a high number concentration, this hints at the presence of supercooled liquid water in this layer. The radar reflectivity increases with time and from cloud top towards the surface, as the radar signal

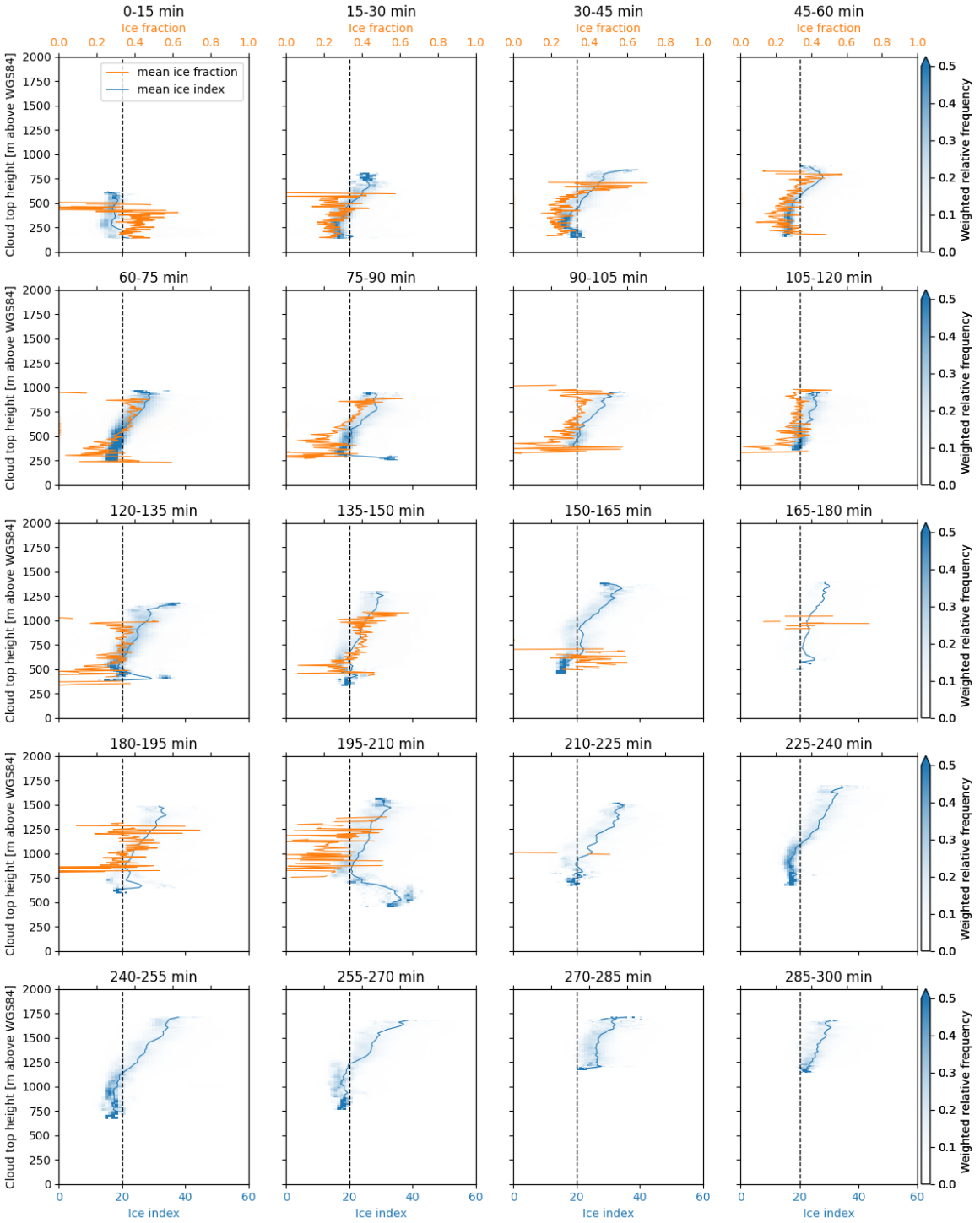

Figure 4.14: Histograms of ice index (blue) and ice fraction (orange) as a function of cloud top height for different time ranges above open ocean. The solid lines denote the respective means. The ice fraction was derived with the IDEFAX for the cloudbow range and only saturated observations were included in the analysis.

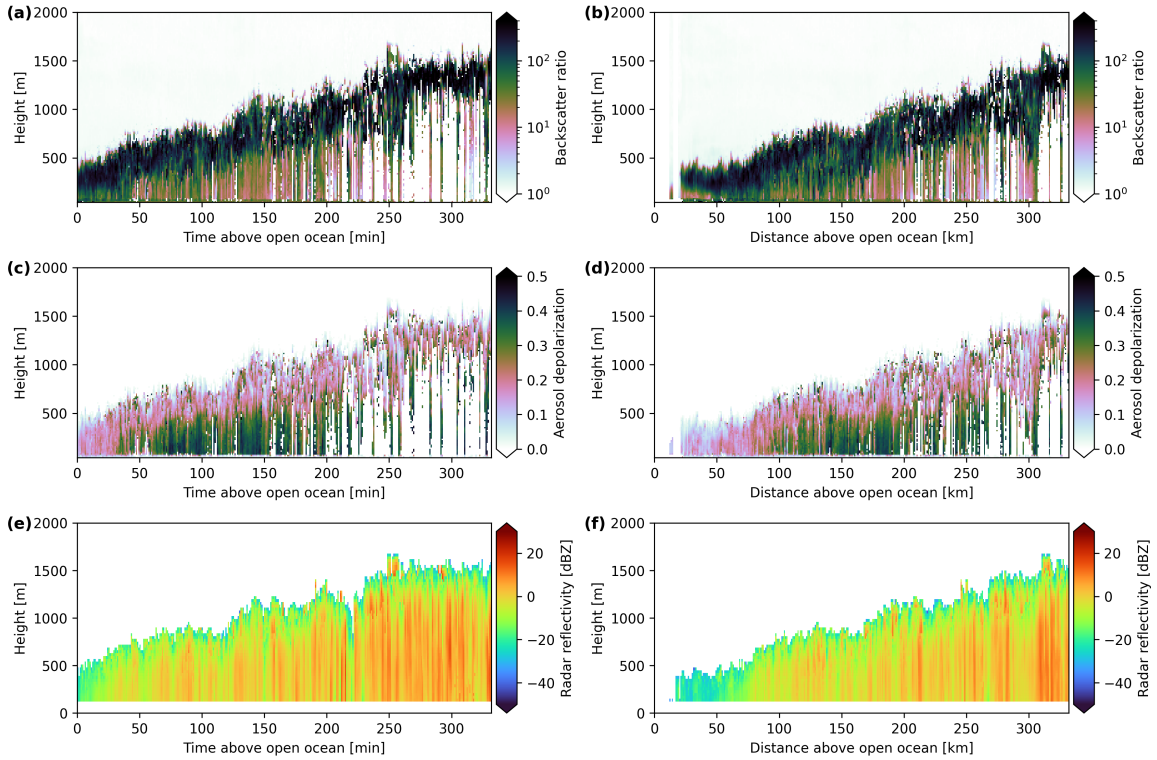

Figure 4.15: Lidar and radar measurements as a function of time (left column) and distance (right column) above open ocean on 2022-04-01. **(a, b)** Lidar backscatter ratio. **(c, d)** Aerosol depolarization. **(e, f)** Radar reflectivity. The depolarization data was filtered for cloud data only, with backscatter ratios larger than 10.

is dominated by the larger ice crystals. These sediment downwards and grow further during their descent. After about 30 min to 45 min above open ocean, the radar reflectivity exceeds the threshold value for precipitation of −5 dBZ (Schirmacher et al., 2024). Moreover, the high radar reflectivities at high altitudes indicate the presence of ice close to the cloud top. However, the cloud top, which is well characterized through passive remote sensing, is difficult to measure for radars and lidars due to non-uniform beam filling. In addition, the lidar and radar measurements do not provide quantitative information about the phase partitioning.

A geometrical thin supercooled layer at cloud top from which ice crystals form and sediment downwards is the expected typical structure of low-level Arctic mixed-phase clouds (e.g. Morrison et al., 2012; Tan et al., 2023; Moser et al., 2025). Both passive and active remote sensing measurements qualitatively show this distinct structure, but some differences between them are discussed in the following. The passive remote sensing measurements originate from the cloud top and the cloud sides, and were combined to pseudo-vertical profiles. Thus, it was assumed that the vertical structure of cloud thermodynamic phase partitioning in the cloud centers is similar to the structure at the cloud sides. In contrast, the lidar and radar measurements provide data of actual vertical profiles through the clouds.

In the updraft regions of the convective cells, liquid cloud droplets and ice crystals grow through depositional growth, and enhanced ice production and precipitation compared to the cloud boundaries and riming are observed (Maherndl et al., 2024b; Schirmacher et al., 2024). These updraft regions are observed by the radar and lidar but not necessarily represented by the ice index and ice fraction measurements, except for the highest altitudes, which are typically found in the centers of the convective cells (Schirmacher et al., 2024). In addition, the cloud sides are more strongly affected by entrainment than the cloud centers. Entrainment could lead to reduced fractions of cloud liquid water, in addition to increasing ice formation due to decreasing temperatures and increasing cloud droplet sizes with height. This together could explain the observed vertical profiles of the ice fraction. A similar structure of low-level Arctic mixed-phase clouds above open ocean, with increasing fractions of ice clouds at higher altitudes due to decreasing temperatures, was also reported by Wendisch et al. (2024), based on in situ measurements.

An increasing radar reflectivity with decreasing height is not a contradiction to the observed increasing ice fraction with increasing height. The radar reflectivity is very sensitive to the size of the ice crystals, which increases with decreasing height as the larger ice crystals sediment and further grow during their descent, and to a lesser degree, is influenced by the number concentration. In contrast, the ice fraction is a quantitative optical measure that reflects the optical thickness of both phases and depends on the sizes and number concentrations of cloud liquid water and cloud ice.

4.2.4 Application of the adiabatic cloud model

The analyses in the previous sections showed that the liquid water clouds, which form at the very beginning of a MCAO close to the ice edge, rapidly transform into a mixed-phase regime. However, it was not investigated how ice processes influence the cloud liquid water with time and throughout the vertical cloud extent. The WBF mechanism and riming, for example, could impact the cloud droplet size and number concentration. To further study these effects, measured vertical profiles of the effective radius of the liquid cloud droplets are compared to vertical profiles calculated with an adiabatic cloud model for different time ranges above open ocean. The applied adiabatic cloud model predicts vertical profiles of the liquid water content of an adiabatically rising air parcel, and hence does not include ice processes or collision-coalescence. The differences between the measured and calculated profiles provide insights into microphysical processes in the observed mixed-phase clouds and their temporal evolution.

According to the adiabatic cloud model introduced in Sect. 2.4, the effective radius can be computed with (Grosvenor et al., 2018; Brenguier et al., 2000, see also Eq. 2.30)

$$r_{\mathrm{eff}} = \left(\frac{3}{4\pi\rho_{\mathrm{w}}}\right)^{1/3} (f_{\mathrm{ad}} C_{\mathrm{w}})^{1/3} (k N_{\mathrm{d}})^{-1/3} h^{1/3}. \tag{4.1}$$

Here, ρ_{w} is the density of liquid water and $h = z - z_{\mathrm{base}}$ is the height above the cloud base height. k is the factor converting volume mean radii to effective radii. It was assumed to

be $k = 0.8$, which is a typical value for maritime clouds (Martin et al., 1994; Pawlowska and Brenguier, 2000). The condensation rate C_{w} depends on temperature and pressure (Grosvenor et al., 2018) and is computed from the dropsonde measurements using Eq. 2.27. The adiabaticity f_{ad} accounts for the reduction of the condensation rate through entrainment and is, as a first approximation, assumed to be constant with height. A detailed discussion of uncertainties and assumptions of the adiabatic cloud model can be found in Grosvenor et al. (2018). Here, the adiabaticity was computed with an entrainment model to further account for variations of the entrainment with height (de Rooy et al., 2013):

$$f_{\mathrm{ad}} = \exp(-\epsilon h), \tag{4.2}$$

with $\epsilon = 1\,\mathrm{km}^{-1}$, which is a typical value. The cloud base height of the liquid water cloud z_{base} was derived from dropsonde data and the cloud heights from the stereographic respectively cloudbow retrieval of specMACS as described below, and increases with time above open ocean as the boundary layer develops. Concerning the dropsonde data, the cloud base height was defined as the height where the relative humidity with respect to liquid water first exceeded 99 %. For the specMACS measurements, the minimum height of the measurements, where an effective radius was determined with the cloudbow retrieval, was used. A relation for the cloud base height as a function of time above open ocean was obtained by fitting a linear curve through the cloud base heights obtained from the dropsondes and specMACS. This relation is used to compute the cloud base height and consequently the adiabatic effective radius for different times above open ocean.

Finally, the cloud droplet number concentration N_{d} was derived from in situ measurements of the P6 aircraft, which performed collocated measurements with HALO on 2022-04-01. The combined particle number size distributions measured by the CDP, CIP, and PIP were integrated over size for particles smaller than 50 µm diameter, assuming these particles to be liquid (Moser et al., 2023; Moser et al., 2023). The obtained cloud droplet number concentrations were combined with backward trajectories (Kirbus and Wendisch, 2024; Herber et al., 2022) to investigate their temporal evolution. Figure 4.16 displays the cloud droplet number concentration as a function of time and distance above open ocean in panels (a) and (b), respectively. The color-coding denotes the height of the respective measurements. During the first 40 min above open ocean, the cloud droplet number concentration increases with time. In this time range, the clouds are still decoupled from the surface, as indicated by the variation of the potential temperature with height in Fig. 4.13b (Sotiropoulou et al., 2014; Gierens et al., 2020). Afterward, the cloud droplet number concentration decreases with time. Decreasing number concentrations during the initial phase of MCAOs were also observed by, e.g., Murray-Watson et al. (2023) and can be explained with entrainment and aerosol scavenging through precipitation (Abel et al., 2017; Sanchez et al., 2022; Murray-Watson et al., 2023). The initial increase of the cloud droplet number concentration is not captured in Murray-Watson et al. (2023), potentially due to the much coarser resolution and higher uncertainties of the satellite-derived measurements in the study compared to the in situ measurements used here. However, this initial increase was also observed by, e.g., Abel et al. (2017).

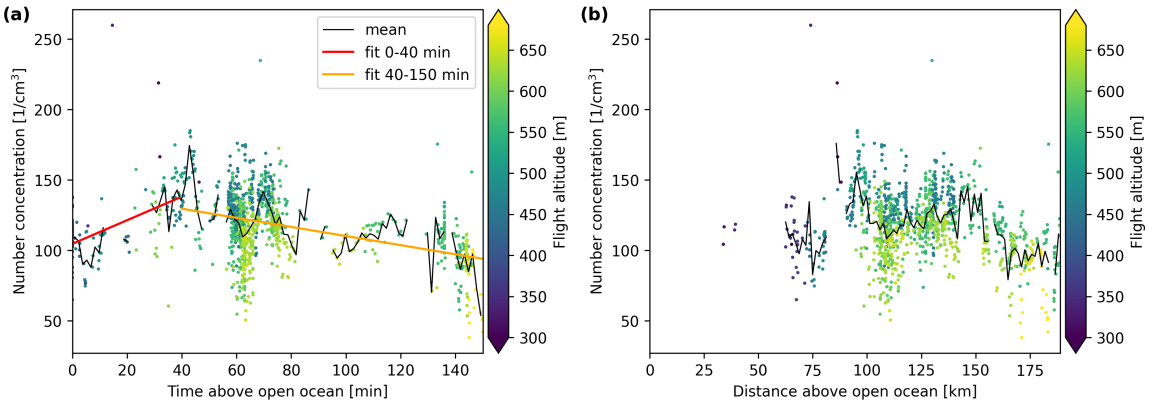

Figure 4.16: Cloud droplet number concentration as a function of time **(a)** and distance **(b)** above open ocean from in situ measurements. The color coding denotes the height of the measurements. The red and orange solid lines are linear fits to the data for times smaller and larger than 40 min, respectively. Only measurements with a LWC$> 0.1\,\mathrm{g\,m^{-3}}$ and with a sea ice concentration smaller than 80 % were used.

In addition, the number concentration in Fig. 4.16 shows only small variations with height. Lower number concentrations are measured at higher altitudes, which can, for example, be explained by the influence of entrainment or by freezing of supercooled liquid cloud droplets. However, the vertical variation of the number concentration is small compared to the measurement uncertainties, such that the cloud droplet number concentration can be assumed to be approximately constant with height. A vertically constant number concentration is a required assumption for the adiabatic cloud model, and this was also observed in other studies, such as Brenguier et al. (2000) and Painemal and Zuidema (2011) for stratocumulus clouds and by Gerber et al. (2008) for small cumulus clouds.

For the adiabatic cloud model, linear fits were applied separately to times smaller and larger than 40 min to obtain a relation for the number concentration as a function of time above open ocean. The orange and red lines in Fig. 4.16a show the resulting fits. Due to the limited range of the P6 aircraft, measurements of the number concentration are only available for the first 150 min above open ocean. They were extrapolated to larger times using the obtained linear fit. With this, the adiabatic vertical profiles of the effective radius of liquid cloud droplets were calculated for any time above open ocean.

Pseudo-vertical profiles of the measured effective radius of liquid cloud droplets from the cloudbow retrieval were computed following the method by Rosenfeld and Lensky (1998), Lensky and Rosenfeld (2006), and Zhang et al. (2011), which has also been applied to deep convective clouds, including cloud ice (e.g. Freud et al., 2008). To this end, the individual measurements of the effective radius of liquid cloud droplets are combined with the corresponding cloud top heights, yielding a combined pseudo-vertical profile.

Figure 4.17 shows the measured and calculated adiabatic vertical profiles of the effective radius for different time ranges above open ocean. Large deviations of the two profiles are observed in the first row of Fig. 4.17, especially at the lower altitudes. At these times, close to the ice edge, the clouds are decoupled from the surface, as discussed above, and the par-

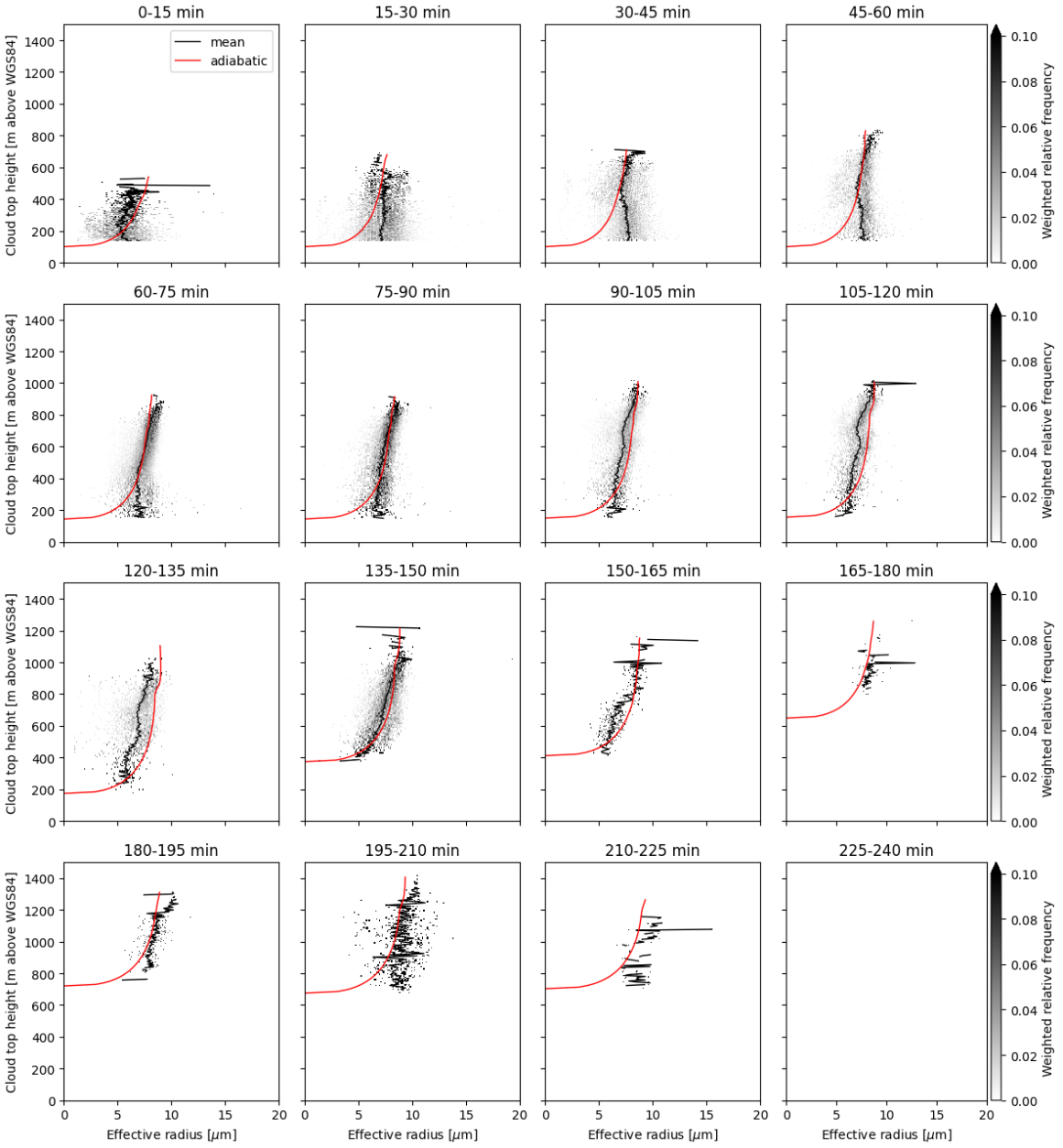

Figure 4.17: Vertical profiles of the effective radius of liquid cloud droplets for different time ranges above open ocean. The black solid line indicates the mean measured effective radius. The red solid lines are vertical profiles calculated using the adiabatic cloud model.

cel model is not applicable. In addition, the measured and calculated profiles mostly differ at the cloud base. A reason for this could be that the lowermost part of the clouds with very small effective radii of the liquid cloud droplets is too optically thin to be captured by the measurements, or is geometrically not visible for large viewing angles in combination with high cloud fractions. In addition, the initial growth of small liquid cloud droplets at the cloud base is fast and the cloud base height is difficult to determine, such that small

uncertainties have a larger influence. Besides that, there is in general a good agreement of the profiles, which indicates that the cloud ice does not significantly impact the cloud liquid water during the observed initial phase of the cold air outbreak and that the adiabatic cloud model is applicable here. The profiles calculated with the adiabatic cloud model were not fitted to the measured pseudo-vertical profiles. Instead, the input variables for the model were computed from the measurements as described above. Deviations between the adiabatic model and the direct measurements are explained either by uncertainties of the input variables and the measurements, by droplet collision and coalescence, or by ice processes, which are not accounted for in the adiabatic cloud model.

First, the uncertainties of the input variables to the model are discussed. The measurement uncertainties of the cloud droplet number concentration from in situ observations are about 10 % to 30 % (Moser et al., 2023), which corresponds to an uncertainty of the calculated adiabatic effective radius of about 10 %. In addition, the vertical variation of the number concentration in Fig. 4.16 is about 50 %, which could explain deviations between the effective radii of up to 25 %. The cloud base height also has uncertainties, as it is derived from measurement data, but these uncertainties only shift the computed effective radius profile in the vertical direction. Other uncertainties arise from the interpolation between the condensation rates computed from the individual dropsondes. However, the condensation rate varies only slightly with temperature and pressure in the observed temperature range.

Furthermore, an entrainment model (Eq. 4.2) was applied to compute the adiabaticity. The effective radius is, in general, only slightly influenced by entrainment (Freud et al., 2008). Variations of the adiabaticity by 10 % in Eq. 4.1 change the calculated effective radius by less than 4 % for the observed cloud droplet sizes. Nevertheless, the agreement between the measured and calculated vertical profiles of the effective radius varied depending on the chosen value of the adiabaticity. The good agreement for the applied entrainment model indicates that this model realistically describes entrainment in the observed clouds. However, the adiabaticity could, in principle, also be reduced by other processes than entrainment. In mixed-phase clouds, simultaneously growing liquid cloud droplets and ice crystals compete for the available water vapor. This can lead to a reduced growth of liquid cloud droplets, similar to the influence of entrainment. At least a part of the reduction of the adiabaticity could potentially be attributed to this effect. From the measurements, it is not possible to directly distinguish between the impact of entrainment and ice crystals competing with the liquid cloud droplets for the available water vapor. However, the observed clouds are still dominated by liquid water, and the ice fraction and ice index are comparably small (see Fig. 4.14). In addition, the applied entrainment model is a realistic assumption. Thus, entrainment is likely the dominating factor here, but the influence of the ice crystals on the droplet growth introduces an additional uncertainty.

Moreover, the uncertainty of the measured effective radii from the cloudbow retrieval based on an evaluation with synthetic data is $-0.2 \pm 1.6\,\mu\text{m}$ (Volkmer et al., 2024; Pörtge, 2024). In summary, the uncertainties of the input variables used to calculate the adiabatic effective radius and the uncertainties of the measured effective radii can explain the observed differences between the measured profiles and the adiabatic cloud model.

Besides measurement uncertainties, droplet collision and coalescence processes can lead

to deviations of the observed profiles of the effective radius from the adiabatic cloud model. Collision and coalescence is relevant if the effective radius of liquid cloud droplets exceeds 14 µm (Freud and Rosenfeld, 2012). The observed liquid cloud droplets have maximum effective radii of about 10 µm, which is much smaller than this threshold. Therefore, collision and coalescence can be neglected in the observed clouds.

Another possible explanation for deviations between the adiabatic model and the observed effective radii is ice processes, such as ice formation through freezing, ice crystal growth through the WBF mechanism, and riming.

Ice formation in mixed-phase clouds predominantly happens through heterogeneous freezing of supercooled liquid cloud droplets (de Boer et al., 2011; Cui et al., 2006; Ansmann et al., 2005). Hence, the formation of ice crystals decreases the cloud droplet number concentration. The probability for a supercooled liquid water droplet to freeze increases with increasing droplet size and decreasing temperature, but it also strongly depends on the efficiency of the IN. The ice crystal number concentration, computed from in situ measurements of the particle number size distributions from particles larger than 50 µm, amounts to about $20\,\mathrm{L}^{-1}$, which is four orders of magnitude smaller than the observed cloud droplet number concentration. Hence, the influence of the conversion of liquid water droplets into ice crystals through freezing on the effective radius can be neglected.

A second ice process that can influence the liquid cloud droplets is the WBF mechanism. The effect of the WBF mechanism depends on whether the thermodynamic phases are homogeneously or inhomogeneously mixed within the cloud and on the spatial scales of this mixing. The spatial scales of single phases and the mixed-phase were studied by Korolev and Milbrandt (2022) and vary between 100 km and 100 m, which is the maximum resolution of the in situ measurements applied. If the liquid water and ice phases are inhomogeneously mixed and thus spatially separated, the interaction between both phases is limited and the WBF mechanism is less effective. The influence of the WBF mechanism on the effective radius of liquid cloud droplets also depends on the mixing scenario. Similar to the effect of entrainment, the effective radius can either be reduced and the number concentration remains constant. Or, the number concentration decreases while the effective radius remains constant. Hence, deviations of the adiabatic effective radius from the measured radii indicate a homogeneous mixing scenario, if the deviations are observed in a region where the WBF mechanism is active. The WBF mechanism is active only in a distinct regime with supersaturation with respect to ice and subsaturation with respect to liquid water (Korolev, 2007).

Information about the supersaturation during the research flight on 2022-04-01 is available from the dropsondes of HALO and the in situ measurements of the P6 aircraft. Figure 4.18 displays vertical profiles of the relative humidity above liquid water in panel (a) and above ice in panel (b) measured by the dropsondes. A layer with supersaturation above both liquid water and ice is observed in the upper part for most times, which coincides with regions of high lidar backscatter ratio, indicating the presence of liquid cloud droplets. In this height range, liquid water droplets and ice crystals grow simultaneously. Close to the cloud top, there is usually a thin layer with supersaturation above ice only, which could be explained by entrainment. At lower altitudes, only supersaturation above ice is reached. This is

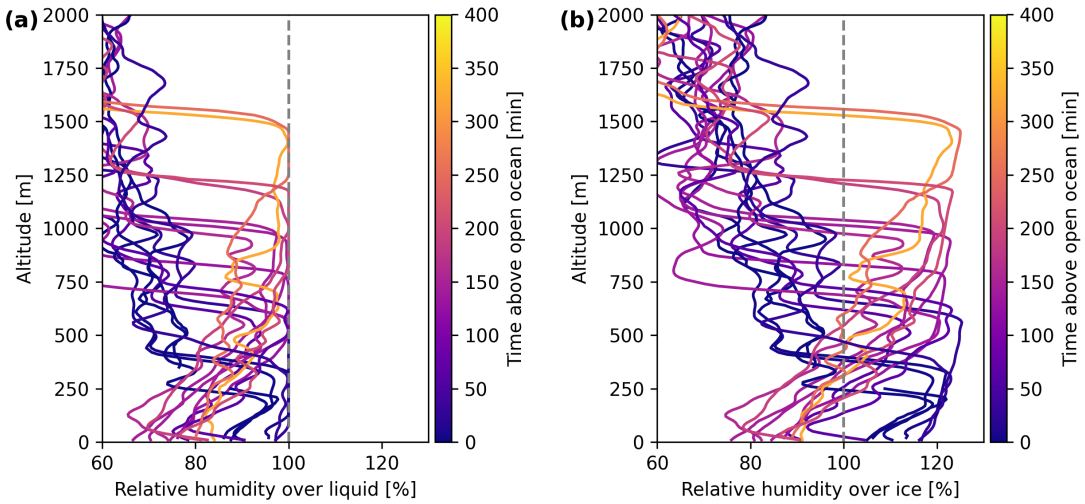

Figure 4.18: Vertical profiles of the relative humidity with respect to liquid water **(a)** and ice **(b)** measured by the dropsondes on 2022-04-01. The colors indicate the time above open ocean of the respective dropsonde. The gray dashed line corresponds to 100 % relative humidity.

the region where the WBF mechanism is active and larger radar reflectivities indicate the presence of ice.

The measured profiles of the effective radius for the time ranges between 90 min and 135 min show some variations of the slope with height and larger deviations from the adiabatic cloud model in regions where the WBF mechanism could be active. However, there are only a few dropsonde measurements, which cover only parts of the time ranges, and the in situ data provide only limited vertical information. This makes it difficult to directly relate these deviations to the WBF mechanism, and the deviations are in general small compared to the measurement uncertainties. Moreover, the small ice crystal number concentration measured by the in situ probes indicates that no significant ice multiplication has taken place. Thus, even if the WBF mechanism is active, the measurements suggest that its influence on the effective radius is small. This can be due to inhomogeneous mixing of the liquid water and ice phase, the small ice crystal number concentration, or a combination of both, which makes the WBF mechanism less effective and limits its impact on the effective radius of the liquid cloud droplets. If highly resolved measurements of the vertical profiles of the cloud droplet number concentration were available, both effects could be distinguished.

Another ice process that can explain deviations between the adiabatic cloud model and the measured effective radius profiles, especially in regions where the WBF mechanism is not active, is riming. However, laboratory measurements indicate that the influence of riming on the cloud droplet size distribution is small (Ávila et al., 2009). The collision efficiencies for riming depend on the particle size, and their dependence on the cloud droplet size exhibits an approximately rectangular shape, where liquid cloud droplets must reach a critical size for collisions with ice crystals, depending on the crystal shape (Wang and Ji, 2000). According to the theoretically computed collision efficiencies by Wang and Ji

(2000), the effective radius of liquid water droplets could be slightly reduced by riming. The retrieved effective radii smaller than 7.5 µm are close to the critical radius for riming, and actually riming was observed during the research flight on 2022-04-01 (Schirmacher et al., 2024; Maherndl et al., 2024a). However, the collision probability is small due to the low ice crystal number concentrations. Furthermore, the normalized rime masses computed from in situ and radar measurements by Maherndl et al. (2024a) show only light riming with mean values of about 0.03 on this day, which is small.

In summary, there is agreement between the measured vertical profiles of the effective radius of liquid cloud droplets and the applied adiabatic cloud model within the range given by the measurement uncertainties. Collision and coalescence processes can be neglected in the observed clouds. Ice processes, such as heterogeneous freezing of supercooled liquid cloud droplets, riming, and the WBF mechanism, did not significantly impact the cloud liquid water in the initial phase of this MCAO. Therefore, the adiabatic cloud model can also be applied to the observed low-level Arctic mixed-phase clouds, except for cases where the clouds are decoupled from the surface.

4.2.5 Discussion

In the previous part of Sect. 4.2, the evolution of cloud properties during the MCAO measured on 2022-04-01 during HALO–$(\mathcal{AC})^3$ was analyzed with a focus on cloud thermodynamic phase partitioning. Cloud top height and horizontal extent increased with time and distance above open ocean, while the cloud fraction stayed almost constant during the observed first five hours of the MCAO. Moreover, the effective radius of liquid water droplets increased from about 5 µm to 7.5 µm during the first approximately 30 min and remained constant afterward. This initial increase of the effective radius coincided with an increase of the ice index and ice fraction and a transition from a pure liquid water to a mixed-phase cloud regime. Furthermore, the temperature dependence and vertical distribution of the cloud thermodynamic phase and their temporal evolution were analyzed. The ice index and ice fraction generally increased with decreasing temperature, indicating that ice formation happened preferentially at the coldest temperatures. In agreement with this, the ice index and ice fraction increased with increasing height, except for a geometrically thin layer at cloud top, where increasing fractions of supercooled liquid water were observed. Additionally, the influence of ice processes on cloud liquid water was studied by applying an adiabatic cloud model. Agreement within the uncertainties of the measured and calculated vertical profiles of the effective radius of liquid water droplets was observed, except for short times above open ocean close to the ice edge, when the clouds were still decoupled from the surface. This indicated that ice processes such as ice formation through heterogeneous freezing of supercooled liquid water droplets, riming, and the WBF mechanism did not significantly impact the cloud liquid water during the initial phase of the observed MCAO. Collision and coalescence were not relevant in the observed clouds due to the small droplet sizes. It is concluded that the adiabatic cloud model with the applied entrainment model realistically represents liquid water in the observed low-level Arctic mixed-phase clouds.

Phase partitioning and phase transitions during MCAOs have not been studied in a quasi-

Lagrangian way in detail so far in the literature, as these are difficult to observe. Combining remote sensing measurements with a high spatial and temporal resolution following a quasi-Lagrangian sampling strategy on a long-range aircraft with some collocated in situ measurements allows to fill this gap.

Nevertheless, some limitations of the presented results will be discussed in the following. The cloud mask for the polarization-resolving cameras of specMACS struggles in the presence of sea ice, where ice can falsely be identified as clouds. This is a known issue for brightness-based cloud masks from passive imaging methods. In contrast to the results of the cloudbow retrieval, it is difficult to filter these measurements out for the phase partitioning retrieval, as measurements of sea ice and ice clouds both show a high ice fraction and cannot easily be distinguished. Thus, an improved cloud mask combining, for example, measurements of the spectral cameras, the polarization-resolving cameras, and the thermal imager on board of HALO should be developed in the future to improve the results. In addition, the large solar zenith angles in the Arctic lead to increased uncertainties of the retrievals of the specMACS instrument. On the one hand, three-dimensional radiative effects have a stronger influence on the phase retrievals for large solar zenith angles. On the other hand, the cloudbow is then observed at the edge of the field of view of the polarization-resolving cameras, where the measurement uncertainties are larger (Weber et al., 2024). The results of the cloudbow retrieval and the polarized phase partitioning retrieval were filtered, excluding retrieval results with a large RMSE between the fitted model and the measurement, to eliminate the most uncertain results.

Moreover, spatially uniform vertical profiles of the phase partitioning were assumed to construct the pseudo-vertical profiles in Sect. 4.2.3. A study similar to Lensky and Rosenfeld (2006), based on model data, could be repeated for cloud thermodynamic phase partitioning to investigate the validity of this assumption.

For the adiabatic cloud model, the assumption of a vertically constant cloud droplet number concentration is not completely correct, and there are large uncertainties in all the input parameters to the calculated adiabatic effective radius profiles from the model. In the future, it would be helpful to have vertical profiles measured by the in situ probes. During the research flight analyzed here, measurements were only taken at a limited number of constant flight levels. Accurate and simultaneous measurements of the effective radius of liquid cloud droplets, pressure, temperature, supersaturation, and cloud droplet number concentration in regions with ice supersaturation and liquid water subsaturation where the WBF mechanism is active would allow for further studying the effect of the WBF mechanism and even quantify it. Moreover, the observed low-level Arctic mixed-phase clouds were precipitating. In principle, the adiabatic cloud model is only applicable to non-precipitating clouds. However, here it was applied only to the liquid part of the clouds, whereas the precipitation was in the ice phase.

Furthermore, it should be mentioned that the definition of the ice fraction varies strongly between different studies, depending on the type of measurements and the application (Korolev et al., 2017). In addition, different threshold values are used to define the liquid water, mixed, and ice phases. This must be kept in mind when comparing the results of different studies on phase partitioning. In this work, the ice fraction is an optical ice

fraction defined by the optical thickness, and the ice index is a qualitative measure of cloud thermodynamic phase.

4.3 Statistics of the cloud evolution

This section was already published in Weber et al. (2025b). The content has been slightly restructured to improve the readability.

During HALO–$(\mathcal{AC})^3$, a variety of different MCAO conditions were sampled (Walbröl et al., 2024), which allows for studying the variability and dependence of cloud properties on the MCAO strength. Between 2022-03-21 and the end of the campaign on 2022-04-12, an unusually long cold phase with several MCAOs occurred. Especially strong MCAO events, exceeding the 90th and 75th percentiles of the climatology, were observed on 2022-03-25 and 2022-04-02, respectively (Walbröl et al., 2024). HALO conducted six flights during the cold phase of the campaign, which targeted MCAOs. An overview of these flights is given in Fig. 4.19, where MODIS satellite images and the flight tracks are shown for the research flights on 2022-03-21, 2022-03-28, 2022-03-29, 2022-03-30, 2022-04-01, and 2022-04-04. The research flights covered mostly the Fram Strait region, but for example on 2022-03-29 the area south-east of Svalbard was sampled. Some parts of the flights are affected by the topography of the island of Svalbard, causing, e.g., convergence lines downstream. The long cold period led to increasing sea ice extent north and south-east of Svalbard.

The strength of the observed MCAO varied between the different research flights. Mean and maximum values of the MCAO index along the flight tracks computed from ERA5 data (Hersbach et al., 2023a,b) are summarized in Table 4.1. The strongest observed MCAO events were on 2022-04-01, which was studied in detail in the previous section, and on 2022-03-29. Weaker MCAO conditions were, for example, measured on 2022-03-30. In addition, the flights sampled different parts of the MCAO. For example, the research flight on 2022-04-01 focused on the very initial phase of the MCAO, whereas the other research flights also covered regions further downstream. Thus, different parts of the temporal and spatial evolution were sampled.

The quasi-Lagrangian flight strategy applied to all flights of the HALO–$(\mathcal{AC})^3$ campaign (Wendisch et al., 2024) allows for studying the temporal and spatial evolution of cloud properties similar to the analysis in the previous section. Specifically, the evolution of macroscopic cloud properties, such as the cloud top height, cloud fraction, and horizontal cloud extent, as well as the evolution of cloud microphysical properties, such as the effective radius of liquid water droplets and cloud thermodynamic phase partitioning, will be analyzed in the following. This approach is similar to the one applied in Sect. 4.2, but now it is extended to all six MCAO cases observed during HALO–$(\mathcal{AC})^3$.

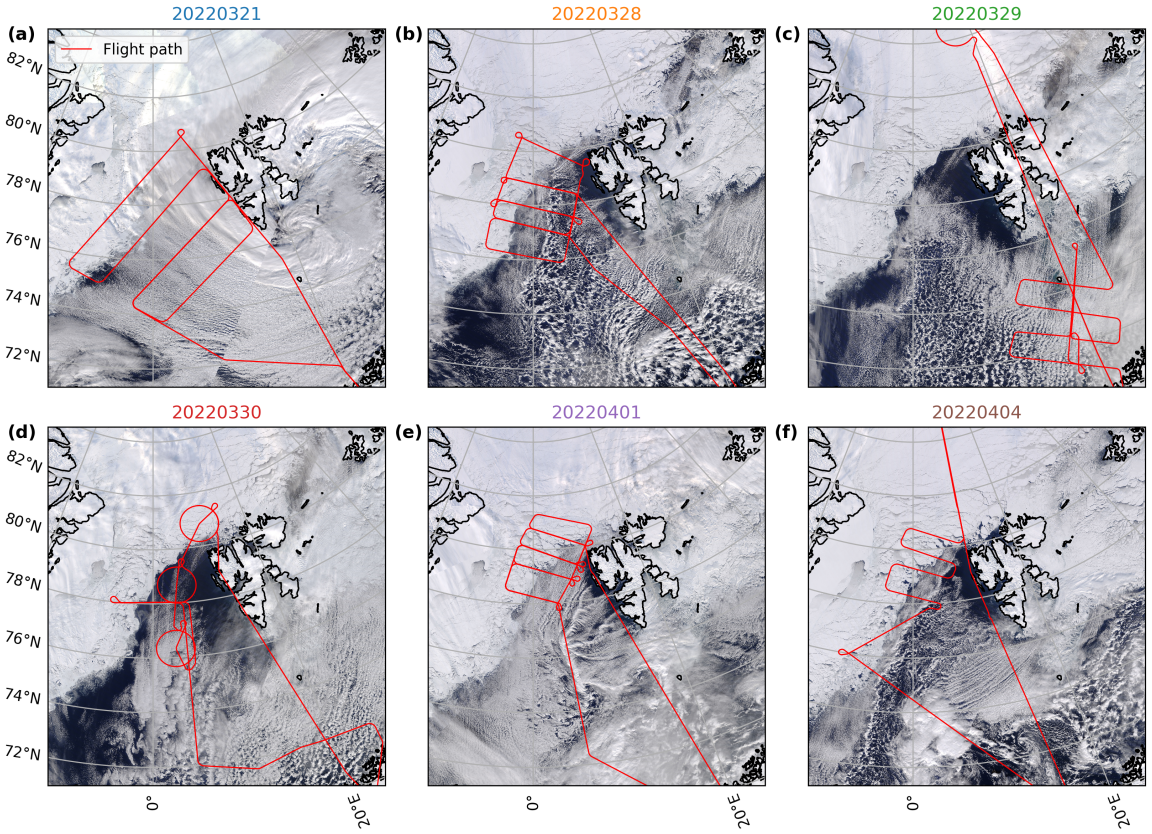

Figure 4.19: MODIS satellite images downloaded from NASA Worldview for all MCAO flights of HALO–$(\mathcal{AC})^3$. The red lines indicate the flight tracks.

Research flight	Mean MCAO index [K]	Maximum MCAO index [K]
20220321	1.91	7.62
20220328	3.28	7.35
20220329	5.32	9.23
20220330	0.44	3.25
20220401	6.59	11.85
20220404	1.89	7.51

Table 4.1: Mean and maximum MCAO indices along flight track computed from ERA5 data (Hersbach et al., 2023a,b) for all MCAO flights of HALO–$(\mathcal{AC})^3$. The colors correspond to the colors of the research flights in Fig. 4.20 and 4.21.

4.3.1 Macroscopic cloud properties

Cloud top height, cloud fraction, and horizontal cloud extent were derived from specMACS measurements and combined with backward trajectories as discussed in Sect. 4.2. Figure 4.20 displays histograms of these quantities as a function of time (upper row) and distance (lower

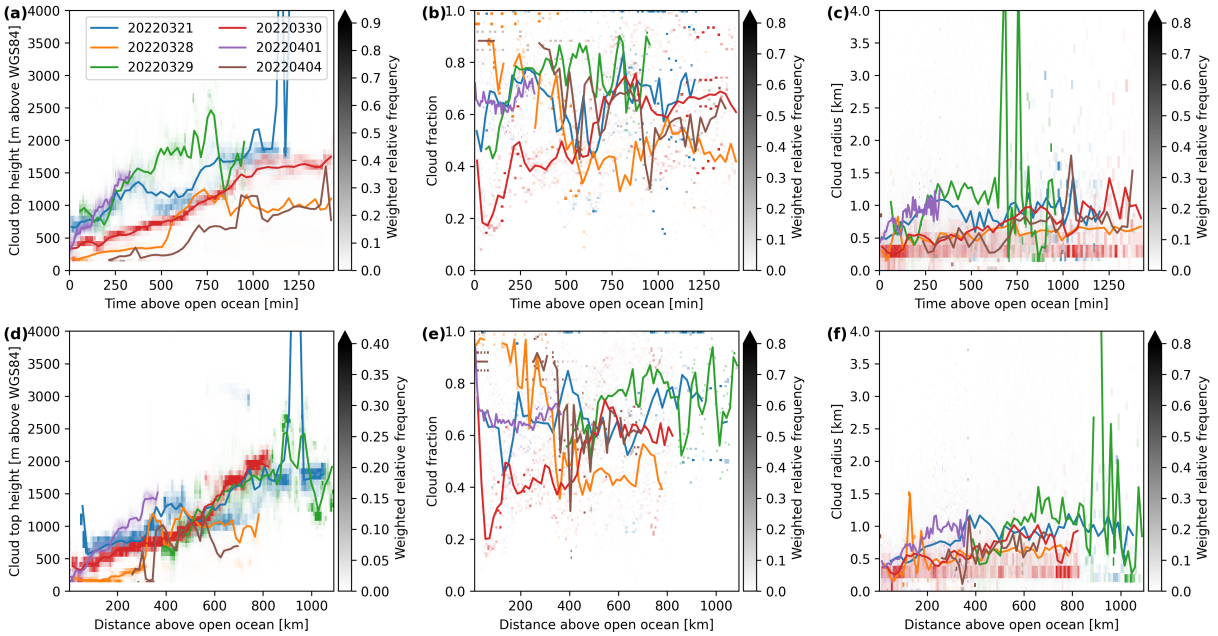

Figure 4.20: Histograms of cloud top height **(a, d)**, cloud fraction **(b, e)**, and cloud radius **(c, f)** as a function of time (upper row) and distance (lower row) above open ocean with their respective mean for all MCAO flights during HALO–$(\mathcal{AC})^3$.

row) above open ocean together with their mean for all flights in different colors. The first, second, and third columns correspond to the cloud top height, cloud fraction, and cloud radius, respectively. In general, there is a large variability between the different research flights, which were performed under varying MCAO conditions and partly in different regions.

The cloud top height in panels (a) and (d) increases with time and distance from the ice edge for all research flights from a few hundred meters to a maximum of about 2.5 km. The largest cloud top heights are observed during the flights on 2022-04-01 (purple line) and 2022-03-29 (green line), which were the strongest observed MCAOs, and lower cloud top heights are reached during the weaker MCAOs. In addition, the increase is faster for these strong events compared to the weaker ones. Larger cloud top heights for stronger MCAOs were also observed by Murray-Watson et al. (2023) and Schirmacher et al. (2024). The very large cloud top heights on 2022-03-21 at large times and distances are due to high-level cirrus clouds south-west of Svalbard, as can also be seen in Fig. 4.19a.

A similar picture is found for the horizontal cloud extent in Fig. 4.20c and 4.20f. The cloud radius generally increases with time and distance above open ocean from a few hundred meters to about 1.5 km. Larger cloud radii are associated with the stronger events on 2022-04-01 and 2022-03-29, and smaller radii are observed during the weaker events on 2022-04-04, 2022-03-30, and 2022-03-28. Similar to the cloud top height, the increase of the cloud radius is faster for stronger events than for weaker MCAOs.

In contrast, the cloud fraction shows a more complicated behavior and a large variability.

At small times and distances close to the ice edge, there is an impact of misclassified sea ice. In addition, there are some island effects affecting cloud cover (see Fig. 4.19). In general, the cloud fraction remains either relatively constant or increases with time, with typical values between 0.4 and 0.8. The stronger events tend to have larger cloud fractions compared to the weaker ones. This agrees with the observations of larger cloud fractions during the first hours of MCAOs for stronger events by Murray-Watson et al. (2023). The flight on 2022-03-28 is an exception and strongly affected by the local topography of Svalbard.

4.3.2 Cloud microphysical properties

specMACS provides measurements of cloud microphysical properties, including the effective radius of liquid water droplets, the ice index, and the ice fraction. These measurements were also combined with backward trajectories similar to Sect. 4.2 to investigate their temporal and spatial evolution during all research flights targeting MCAOs. Figure 4.21 shows the results of this analysis. The first, second, and third columns display the effective radius, ice index, and ice fraction, respectively, as a function of time (upper row) and distance (lower row) above open ocean.

The effective radius of liquid cloud droplets increases with time and distance above open ocean, and sizes between about 3 µm and 17 µm were observed. Larger effective radii are reached during the stronger events on 2022-04-01 and 2022-03-29, for which the growth of the cloud droplets is also faster. This can be expected as the effective radius in general increases with height within a cloud, and larger cloud top heights were observed for stronger MCAOs in Fig. 4.20. In contrast, Murray-Watson et al. (2023) found smaller effective radii for stronger MCAOs compared to weaker events. However, they focused on liquid-dominated clouds only and the retrieved effective radii from satellite observations are much more uncertain and have a much coarser spatial resolution than the effective radii derived with the polarimetric cloudbow retrieval.

Concerning the cloud thermodynamic phase, the ice indices and ice fractions generally increase with time above open ocean. The patterns of both ice index and ice fraction are very similar. Initial values of the ice index are below or around 20, which is the threshold value between liquid water and mixed-phase clouds, and increase to about 30 to 50, depending on the research flight. In addition, the ice fraction increases with time and distance from very small values around 0.2 to approximately 0.5 to 0.8. As already discussed, the ice fraction is overestimated at small times and distances close to the ice edge due to the misclassification of sea ice as clouds. The large variability of both the ice index and ice fraction also reflects the larger uncertainty in the thermodynamic phase retrievals compared to the stereographic or the cloudbow retrieval. The described increase in the ice index and ice fraction indicates a transition from a liquid-dominated to a mixed-phase regime with increasing amounts of ice. This phase transition is faster for the stronger observed MCAOs on 2022-04-01, 2022-03-29, and 2022-03-21. In addition, stronger events reach higher ice indices and ice fractions. The faster phase transition and higher ice fractions for stronger events agree with the higher observed cloud top heights and larger effective radii for these events, since typically colder temperatures at higher altitudes and larger cloud droplets

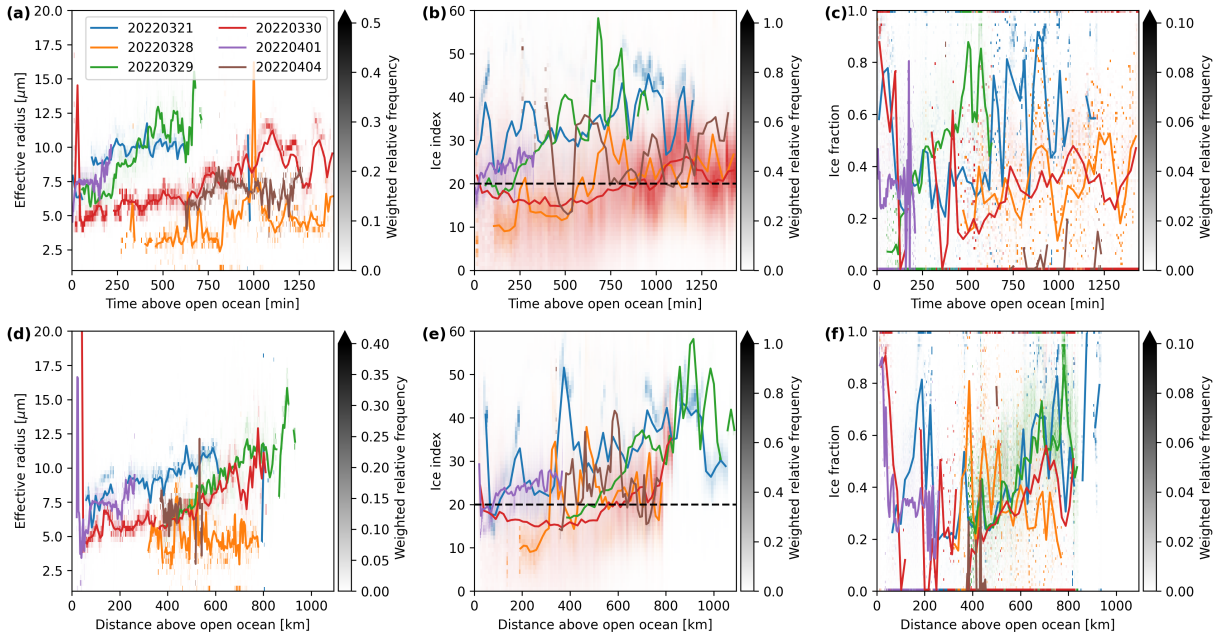

Figure 4.21: Histograms of effective radius of liquid cloud droplets **(a, d)**, ice index **(b, e)**, and ice fraction **(c, f)** as a function of time (upper row) and distance (lower row) above open ocean for all MCAO flights of HALO–$(\mathcal{AC})^3$. The solid lines indicate the mean of the respective flight, the black dashed line in panels **(b)** and **(e)** is the threshold value between the liquid water and the mixed phase.

increase the probability of ice formation. For the case study of the MCAO on 2022-04-01, the observed transition from a pure liquid water to a mixed-phase cloud coincided with the increase of the effective radius from about 5 µm to 7.5 µm. This relation also holds for the other research flights. The ice index increases approximately above the threshold value of 20 when the effective radius reaches a threshold size of around 7.5 µm. However, it should be investigated in the future, whether this might also be coincidence.

4.3.3 Discussion

In the previous sections, the evolution of cloud macro- and microphysical properties during all measured MCAO flights of HALO–$(\mathcal{AC})^3$ was analyzed and compared. The cloud top heights and horizontal extents increased with time and distance traveled above open ocean during all observed MCAOs. However, the increase was stronger and faster for more intense MCAOs. Similarly, the effective radius of liquid cloud droplets increased over time and reached larger sizes for stronger MCAOs. Finally, increasing ice indices and ice fractions with time and a transition from an initially liquid water to a mixed-phase regime were observed during all MCAOs. This transition happened earlier for stronger MCAOs, and larger ice indices and ice fractions were reached for the stronger events. In all observed cases, the transition from the liquid water to the mixed phase coincided with an increase of the effective radius of the liquid cloud droplets and the cloud top height. As the boundary layer and clouds evolve and the cloud top height increases, the liquid cloud droplets grow

to larger sizes and the cloud top temperature typically decreases, leading to an increasing probability of ice formation through heterogeneous freezing.

In general, a large variability was observed between the different MCAO cases measured during HALO–$(\mathcal{AC})^3$. The measurements were performed in partly different regions, with different MCAO strengths, different parts of the evolution were sampled, and some island effects also affected the measurements. Only a small number of six MCAOs could be studied, which, however, covered a large range of MCAO conditions (Walbröl et al., 2024). The quasi-Lagrangian airborne measurements complement satellite-based studies as they have a much higher spatial resolution and additional cloud properties, such as cloud thermodynamic phase partitioning, can be studied. In general, the same limitations as for the case study in Sect. 4.2 apply, including, for example, the issue of the cloud mask in the presence of sea ice and increased measurement uncertainties due to large solar zenith angles in the Arctic.

In the analysis presented in the previous sections, the MCAOs were distinguished based on their strength, quantified by the MCAO index. Besides the MCAO strength, the aerosol concentration also affects the evolution of cloud properties (Murray-Watson et al., 2023) and was not considered so far. The effect of aerosols on the cloud properties could be further studied in the future, using in situ measurements and WALES lidar observations to characterize the aerosol conditions.

Chapter 5

Summary and outlook

5.1 Summary

The Arctic is warming faster than the global average, making it a hotspot of global warming. The reasons for the observed Arctic amplification are related to distinct characteristics of the Arctic in contrast to lower latitudes and can be explained by local and remote processes and feedback mechanisms. Apart from the surface albedo feedback, two important factors relevant to Arctic amplification that are poorly represented by models are low-level Arctic mixed-phase clouds and air mass transformations during meridional transports into and out of the Arctic. Mixed-phase clouds are frequently observed in the Arctic and can persist for hours to days. The partitioning of the cloud thermodynamic phase and its spatial distribution are important since the thermodynamic phase affects the radiative effect of clouds, cloud cover, and cloud lifetime. However, mixed-phase clouds and their thermodynamic phase partitioning are not well represented in models. At the same time, they play an important role, accompanying meridional heat and moisture transports during warm air intrusions and cold air outbreaks that link the Arctic and mid-latitudes. Models of different scales struggle to correctly represent the intense air mass transformations during meridional transports and the microphysical evolution of the associated clouds. Hence, observations of the evolution of clouds and their microphysics during marine cold air outbreaks (MCAOs) and warm air intrusions (WAIs) are needed to improve the process understanding and provide constraints to models.

The main objective of this work was to study the macro- and microphysical properties of low-level Arctic mixed-phase clouds, in particular the thermodynamic phase partitioning, and their temporal evolution during MCAOs based on quasi-Lagrangian observations of the airborne specMACS instrument during the HALO–$(\mathcal{AC})^3$ campaign. To this end, a new quantitative retrieval of cloud thermodynamic phase partitioning using multi-angle polarimetric imaging was developed and validated with synthetic data. The retrieval was applied to the measurements together with other existing retrievals of cloud properties, and combined with backward trajectories to analyze the temporal evolution of the clouds during the observed MCAOs in a quasi-Lagrangian way. In the following, the results of the four

main parts of this work, the calibration of the polarization-resolving cameras of specMACS, the parameterization of 3D cloud geometry and the neural-network-based forward operator, the polarimetric phase retrieval, and the quasi-Lagrangian analysis of the evolution of clouds during MCAOs, will be summarized.

Sensor characterization

First, a complete characterization and calibration of the two 2D RGB polarization-resolving cameras of specMACS was performed. The results are published in Weber et al. (2024). With the calibration, raw measurements can be converted into georeferenced, absolute calibrated Stokes vectors rotated into the scattering plane. The calibration measurements were conducted at the Calibration Home Base of DLR. The geometric calibration of the polarization-resolving cameras included determining the camera model, defining the intrinsic viewing directions of the cameras, and georeferencing. The two cameras have a large combined field of view of about $91° \times 117°$ along-track and across-track, and a high spatial resolution of about 10 m for typical flight altitudes. Moreover, a radiometric calibration was performed. The dark signal of the polarization-resolving cameras is small with negligible spatial variability and dependence on exposure time and temperature. The noise characteristics are well described by the Poisson model, and the non-linearity of the sensor is smaller than 1 %. The spectral response functions of the red, green, and blue color channels were determined, and a polarization calibration was conducted. For the polarization calibration, a theoretical model was applied and validated with laboratory measurements. Finally, a vignetting correction and absolute radiometric calibration were obtained from flat-field measurements. Depending on the channel, the total radiometric uncertainty is between 3.8 % and 5.8 % for typical signal levels. The uncertainty is dominated by the uncertainty of the polarization calibration and increases towards the corners of the sensor. The calibration was validated by applying it to observations of the sunglint, which is a well-characterized target, and comparing the observations with polarized radiative transfer simulations of the same measurement scene. Observations and simulations agreed within the characterized uncertainties. With this method, using observations of the sunglint on the ocean surface and simulations, in-flight calibrations could be performed and the stability of the sensor can be monitored continuously between laboratory calibrations. Alongside this calibration activity in the laboratory, the calibration of the VNIR spectrometer of specMACS was repeated and showed no significant changes compared to the previous calibration from Ewald et al. (2016).

Forward operator for polarized 3D radiative transfer

A sensitivity analysis for the polarimetric phase retrieval showed that 3D radiative effects due to the cloud geometry cannot be neglected for low-level Arctic mixed-phase clouds. At the same time, information about the 3D cloud geometry is available from specMACS measurements by using the stereographic retrieval by Kölling et al. (2019). However, polarized 3D radiative transfer simulations are computationally expensive. Thus, a parameterization

of 3D cloud geometry was developed and applied to construct a fast forward operator for polarized radiative transfer for the phase retrieval. The results are published in Weber et al. (2025c). The new InDEpendent column local halF-sphere ApproXimation (IDEFAX) is a simplified cloud model based on the independent column approximation. Every pixel is approximated by an independent field of 3D half-spherical clouds, which is defined by the local surface orientation angles of the cloud and the cloud fraction. Hence, the IDEFAX has only three additional parameters compared to the commonly used plane-parallel approximation, making it easy to implement and allowing for tabulation of simulated radiances. Fast forward solutions providing radiative transfer simulation results for the Stokes vector components I, Q, and U were constructed for the plane-parallel approximation and the IDEFAX. Due to the large number of input parameters defining the solar and viewing geometry as well as the cloud macro- and microphysical properties, the forward operator is based on feed-forward neural networks instead of a simple look-up table. The forward operator is designed for the specMACS instrument. It could, however, be adapted for other polarimetric instruments or new retrievals by changing the parameter ranges or including new parameters. The prediction errors of the neural networks are small compared to typical measurement uncertainties. Both the IDEFAX and the neural networks were validated against full 3D radiative transfer simulations for a realistic field of low-level Arctic mixed-phase clouds simulated with the WRF model. The IDEFAX showed a significantly improved representation of 3D radiative effects compared to the plane-parallel independent column approximation. On top of that, the neural-network-based forward operator is about 5 orders of magnitude faster than the full 3D radiative transfer simulations and has only small memory requirements.

Polarized phase retrieval

Next, the new quantitative retrieval of cloud thermodynamic phase partitioning using multi-angle polarimetric imaging was developed and validated with synthetic data, addressing the first scientific objective of this work, which was the development and validation of such a retrieval. The results are published in Weber et al. (2025d). The polarization signal is sensitive to the thermodynamic phase of the cloud in two distinct angular ranges, the slope range between 60° and 110° scattering angle and the cloudbow range between 135° and 165°. The basic idea of the retrieval is to fit multi-angle polarimetric measurements of the Stokes vector component Q, describing linear polarization, in either of the angular ranges to simulated multi-angle signals to determine a quantitative ice fraction defined as the ratio of the ice optical thickness to the total cloud optical thickness. The previously introduced neural-network-based forward operator, using either the plane-parallel approximation or the IDEFAX, is applied in the retrieval to obtain simulated multi-angle signals. As the retrieval is based on polarization measurements and the polarization signal is dominated by single scattering, the results are representative for the cloud top. A detailed analysis of the vertical location of the measured signal showed that the signal originates from a vertical optical thickness of about 0.8 below the cloud top for the cloudbow range and of 1.0 to 1.5 for the slope range for a solar zenith angle of 75°. In contrast to most other phase

retrievals, the introduced polarized retrieval provides quantitative information about the thermodynamic phase partitioning with a high spatial resolution of about 100 m at typical flight altitudes, and is less affected by 3D radiative transfer effects.

The retrieval was validated with synthetic data for idealized cloud cases and a realistic field of low-level Arctic mixed-phase clouds obtained from the WRF model. The deviations between the true and retrieved ice fractions for homogeneously mixed plane-parallel clouds were smaller than 0.03, validating the retrieval method. The differences were much larger for the realistic 3D cloud field, with mean differences of 0.096 ± 0.262 and 0.139 ± 0.247 for the ice fractions derived from the cloudbow and slope angular ranges, respectively, using the IDEFAX. The contributions to the deviations due to the 3D cloud geometry and the necessary assumption of a vertical ice fraction profile in the retrieval were quantified using additional synthetic data of the 3D cloud field converted to a field with spatially uniform ice fraction. Both are significant. The retrieval errors are not negligible, but quantitative measurements of cloud thermodynamic phase partitioning are challenging, and in situ methods also have high uncertainties.

An assessment of further sources of uncertainty of the retrieval results showed that the uncertainty introduced by the assumption of an ice effective radius and ice crystal habit in the phase retrieval is small compared to the overall uncertainties. In addition, the cloudbow retrieval of the effective radius and variance of the cloud droplet size distribution provides reliable results even for mixed-phase clouds with ice fractions of up to 0.8. Larger solar zenith angles, as observed in the Arctic, lead to an increasing underestimation of the effective radius with increasing solar zenith angles and larger uncertainties due to increasing noise. The spherical geometry of the Earth can be neglected for solar zenith angles up to 80° and hence does not significantly affect the retrieval results. Finally, the spatial resolution of the surface mesh used for computing the cloud surface orientation angles in the IDEFAX affects the small-scale structure of the derived ice fractions. However, the impact on the average ice fraction is small.

Moreover, the new polarized phase retrieval and the spectral phase retrieval by Ehrlich et al. (2008) were applied to specMACS measurements for an example observation during HALO–$(\mathcal{AC})^3$ and compared to information about cloud thermodynamic phase from active remote sensing and in situ measurements for the same scene. All phase retrieval methods agreed that the observed clouds were in a mixed-phase regime. In contrast to the other retrieval methods, the spectral and polarized phase retrievals using passive remote sensing observations provide high-spatial resolution information about the cloud thermodynamic phase in the horizontal dimension, and quantitative information is obtained with the new polarized retrieval. In addition, some limited vertical information at two distinct altitudes is available due to the different penetration depths of the measured signals. The penetration depths were quantified by calculating vertical weighting functions for the respective signals. While the qualitative spectral ice index is very sensitive to ice and originates from deeper within the cloud, the polarization-based quantitative ice fraction can detect even small amounts of liquid water in an ice layer at the cloud top, which is not possible with other passive remote sensing methods. Therefore, simultaneous hyperspectral and polarization measurements with specMACS are particularly useful.

Analyses of MCAOs

In the last part of this work, the evolution of cloud properties and cloud transitions during MCAOs in the Arctic were studied in a quasi-Lagrangian way by combining retrieval results from the specMACS measurements during HALO–$(\mathcal{AC})^3$ with backward trajectories. This allows for addressing the second scientific objective of this work, the characterization of macro- and microphysical cloud properties and their evolution during MCAOs. The results are published in Weber et al. (2025b) and Weber et al. (2025a). The trajectories were used to assign every measurement a time and distance the air mass has traveled above the open ocean since passing the sea ice edge. Moreover, an additional derivation of the geometrical size of a cloud based on a watershedding algorithm was implemented.

In a case study, the temporal evolution of macro- and microphysical cloud properties during the initial phase of a strong MCAO on 2022-04-01 in the Fram Strait was investigated. Increasing cloud top heights and horizontal cloud extents, along with an almost constant cloud fraction with increasing time above open ocean were observed. The measurements of the ice index and ice fraction indicated a transition from an initially pure liquid water cloud to a mixed-phase cloud within the first approximately 30 min above open ocean. At the same time, the effective radius of the liquid cloud droplets increased from 5 µm to 7.5 µm. Later, the clouds remained in the mixed-phase regime with slightly increasing fractions of ice and an almost constant effective radius with increasing time traveled above open ocean.

In addition, the temperature dependence and vertical distribution of the cloud thermodynamic phase were analyzed. The observed ice index and ice fraction increased with decreasing temperature. This indicates that ice formation occurred preferably at the coldest temperatures. In agreement with that, the pseudo-vertical profiles of the ice index and ice fractions showed increasing values with height. However, a geometrically thin layer with increasing fractions of supercooled liquid water was observed at the cloud top.

Based on the use of the adiabatic vertical cloud model assumption, it became clear that the influence of cloud ice on liquid cloud droplets was small during the observed initial phase of the MCAO on 2022-04-01. Measured pseudo-vertical profiles of the effective radius of liquid cloud droplets were compared to predicted profiles of the cloud droplet size for a pure liquid water cloud that is subject to adiabatic lifting only. Agreement between the measurements and the predictions from this adiabatic cloud model within the uncertainties of the measurements and the input variables was found, except for observations close to the sea ice edge, where the clouds were decoupled from the surface. Hence, the adiabatic cloud model with the applied entrainment model realistically represents the liquid water in the observed clouds. Collision and coalescence and ice processes, such as ice formation through heterogeneous freezing, riming, and the Wegener-Bergeron-Findeisen mechanism (WBF mechanism), which are not included in the adiabatic cloud model, did not significantly affect the supercooled liquid water droplets in these clouds.

Similar to the case study, the quasi-Lagrangian evolution of macro- and microphysical cloud properties was studied for all six observed MCAOs during HALO–$(\mathcal{AC})^3$ to analyze their variability and dependence on the MCAO strength. During all MCAOs, the cloud top height and horizontal cloud extent increased with time and distance above open ocean,

but the increase was stronger and faster for the stronger MCAOs. Furthermore, increasing effective radii of the liquid cloud droplets with increasing time above open ocean were observed for all cases. The droplets reached the largest sizes during the most intense events. A transition from an initially pure liquid water cloud to a mixed-phase cloud, indicated by increasing ice indices and ice fractions, was detected for all MCAOs. This transition occurred earlier for stronger MCAOs and was accompanied by an increase in the droplet effective radius. Moreover, larger ice indices and ice fractions were reached during the stronger events. The variability between the observed MCAOs was large. The measurements covered partly different regions and sampled MCAOs under different conditions, different strengths, and different parts of their evolution.

Cloud thermodynamic phase partitioning and phase transitions of clouds during MCAOs are challenging to observe. They have not been studied in a quasi-Lagrangian way in the literature so far. The measurements of specMACS and other remote sensing instruments on board a long-range research aircraft collected following a quasi-Lagrangian sampling strategy and with additional collocated in situ measurements provide a unique opportunity to fill this gap. The high-spatial resolution measurements of macro- and microphysical cloud properties with specMACS and the possibility of quantifying cloud thermodynamic phase partitioning complement existing studies based on satellite observations. The collected dataset can help to further the understanding of microphysical processes relevant to Arctic mixed-phase clouds and their evolution during MCAOs. Moreover, the data can be used for model evaluation to improve the representation of these clouds in the future.

5.2 Future work

Possible technical improvements of the retrievals and methods developed in this work have already been discussed in the respective methods and results sections. Besides the technical improvements, the new polarized phase retrieval could be extended to derive additional quantities, and it can serve as a basis for new retrievals in the future. Furthermore, several possible future applications of the methods and analyses introduced in this work and ideas for future scientific studies will be briefly discussed in the following.

Pörtge (2024) used the effective radius from the cloudbow retrieval and measurements of the total intensity I of the polarization-resolving cameras of specMACS to derive the cloud optical thickness for liquid water clouds using a simple look-up table. The effective radius and optical thickness were then applied to further retrieve the cloud droplet number concentration as described by Grosvenor et al. (2018). The polarized phase retrieval allows for extending these retrievals to mixed-phase clouds. Once the ice fraction and the effective radius of the liquid cloud droplets are known, the total cloud optical thickness can be determined from measurements of I by the polarization-resolving cameras. The neural network forward operator is currently only trained for optical thickness values up to 8, but it could be extended to also derive larger optical thickness values. An extension to larger values is, however, computationally expensive for the IDEFAX. After the cloud optical thickness is known, the cloud droplet number concentration could be calculated from the

effective radius of the cloud droplets and the liquid water fraction of the total cloud optical thickness. For low-level Arctic mixed-phase clouds, the uncertainty of the derived optical thickness and number concentration would be very high if the plane-parallel approximation had to be applied. However, the uncertainties are much smaller for observations at smaller solar zenith angles or for more stratiform clouds.

In addition, the ice fraction derived with the polarized phase retrieval could be used to extend bispectral retrievals of cloud properties. Bispectral retrievals use radiance measurements at two different wavelengths to derive the effective radius and optical thickness of a cloud (Nakajima and King, 1990). They were first developed for pure liquid water clouds and later extended to pure ice clouds. Mixed-phase clouds are typically either excluded or a bispectral retrieval assuming liquid water clouds is applied. This leads to large uncertainties of the retrieved quantities for mixed-phase clouds (Lee et al., 2006). If the effective radius of the liquid cloud droplets and the ice fraction are known, the total cloud optical thickness and ice crystal effective radius could be derived from radiance measurements at two wavelengths similar to existing bispectral retrievals. This way, the radiative properties of mixed-phase clouds could be completely characterized. The specMACS instrument allows for such a retrieval as simultaneous polarization and hyperspectral measurements are available. Measurements from the polarization-resolving cameras can be used to derive the effective radius of liquid cloud droplets and the ice fraction with the cloudbow retrieval and the polarized phase retrieval, respectively. Afterward, the measurements of the spectrometers can be applied in a bispectral retrieval to derive the total cloud optical thickness and the ice crystal effective radius. In her Bachelor's thesis, Brand (2025) showed the potential of this method and applied it to an example observation.

A critical point in remote sensing retrievals of clouds that contain ice crystals is the assumption of an ice crystal habit. This assumption introduces large uncertainties in bispectral retrievals for ice clouds (Zinner et al., 2016; Loeb et al., 2018) and also contributes to the uncertainty of the polarized phase retrieval. Multi-angle polarization signals contain information about the shape of the ice crystals. They can be used to derive ice crystal asymmetry parameters and to constrain the crystal habit in bispectral retrievals (van Diedenhoven et al., 2012, 2013; Wang et al., 2021; Erdtmann, 2023). It could be investigated whether the information content of multi-angle polarimetric measurements is large enough to constrain the ice crystal habit and, at the same time, derive the ice fraction. For this, a multi-angle polarimetric variational retrieval method could be imagined. Moreover, synergistic radar-lidar retrievals also rely on a priori assumptions about the observed clouds. Ewald et al. (2021) demonstrated that additional passive remote sensing observations of solar radiance can help to select a realistic ice crystal habit. Recently, the synergistic radar-lidar retrieval VarCloud was extended to derive properties of supercooled liquid water (Aubry et al., 2024). It could be investigated if the information content of spectral and multi-angle polarimetric measurements (ice crystal habit and thermodynamic phase) can improve synergistic radar-lidar retrievals.

In the statistical analysis of the evolution of clouds during MCAOs, the different MCAOs were distinguished in terms of their strength. However, the aerosol conditions also affect the microphysical evolution of clouds and their impact could be studied in the future.

In addition, the quasi-Lagrangian observations of the cloud transitions during MCAOs presented in this work could be used for model evaluation. Mixed-phase clouds and the evolution of clouds during meridional air mass transformations, such as MCAOs, are not well represented in models. To this end, modeled cloud properties, for example, from the high-resolution ICON-LEM model, could be combined with backward trajectories, similar to the measurements. The evolution of the cloud properties in the model and the observations could then be compared in an Eulerian and a quasi-Lagrangian way for the six observed MCAOs. Model tuning could help to identify reasons for potential differences and to improve the model. The thermodynamic evolution of MCAOs in dropsonde observations and in the ICON weather prediction model was compared from an Eulerian and a quasi-Lagrangian perspective by Wendisch et al. (2025). Similarly, the representation of clouds and their transitions in ICON and other models could be studied using the observations of this work. Furthermore, comparing the observed cloud properties and simulations of low-level Arctic mixed-phase clouds with Lagrangian cloud models could provide further insights into the microphysical processes determining the properties and the evolution of these clouds.

Future studies could also investigate the small-scale structure of the microphysical cloud properties in low-level Arctic mixed-phase clouds to further the process understanding. Typical spatial scales of the inhomogeneity of the cloud optical thickness in Arctic clouds are on the order of 100 m (Schäfer et al., 2017, 2018). These scales are resolved by the high-spatial resolution measurements of specMACS. The spatial variability of cloud properties in low-level Arctic mixed-phase clouds was studied by Schirmacher et al. (2024) and Maherndl et al. (2024b) using radar and in situ measurements. specMACS observations provide 2D information in the horizontal and could be used to analyze small-scale variations of cloud microphysical properties in detail.

Finally, the developed polarized phase retrieval can be applied to data collected in many other regions of the world, some of them with even better-suited observation geometries for systematic application of the methods developed in this work. The PERCUSION campaign took place in August and September 2024 from Cape Verde and Barbados and focused on the intertropical convergence zone and deep convective clouds in the Tropics. With the polarized phase retrieval, freezing processes in these clouds can be investigated. An example observation from the PERCUSION campaign on 2024-09-26 at 17:28:30 UTC with the retrieved cloud top height, effective radius of liquid cloud droplets, and ice fraction is shown in Fig. 5.1. Ice fractions close to 1 are observed at the highest cloud top heights, where ice is expected and no effective radii can be derived with the cloudbow retrieval. Due to the much smaller solar zenith angles, the influence of 3D radiative effects on the ice fraction retrieval is much smaller and the cloudbow range is inside the field of view of the polarization-resolving cameras and the spectrometers. This allows for combining all existing retrievals and measurements, applying a bispectral retrieval extended to mixed-phase clouds, and computing a cloud droplet number concentration as explained above. In addition, the plane-parallel assumption needed to derive some of the cloud properties introduces much smaller uncertainties compared to measurements during HALO–$(\mathcal{AC})^3$, and there are no issues due to misidentified sea ice.

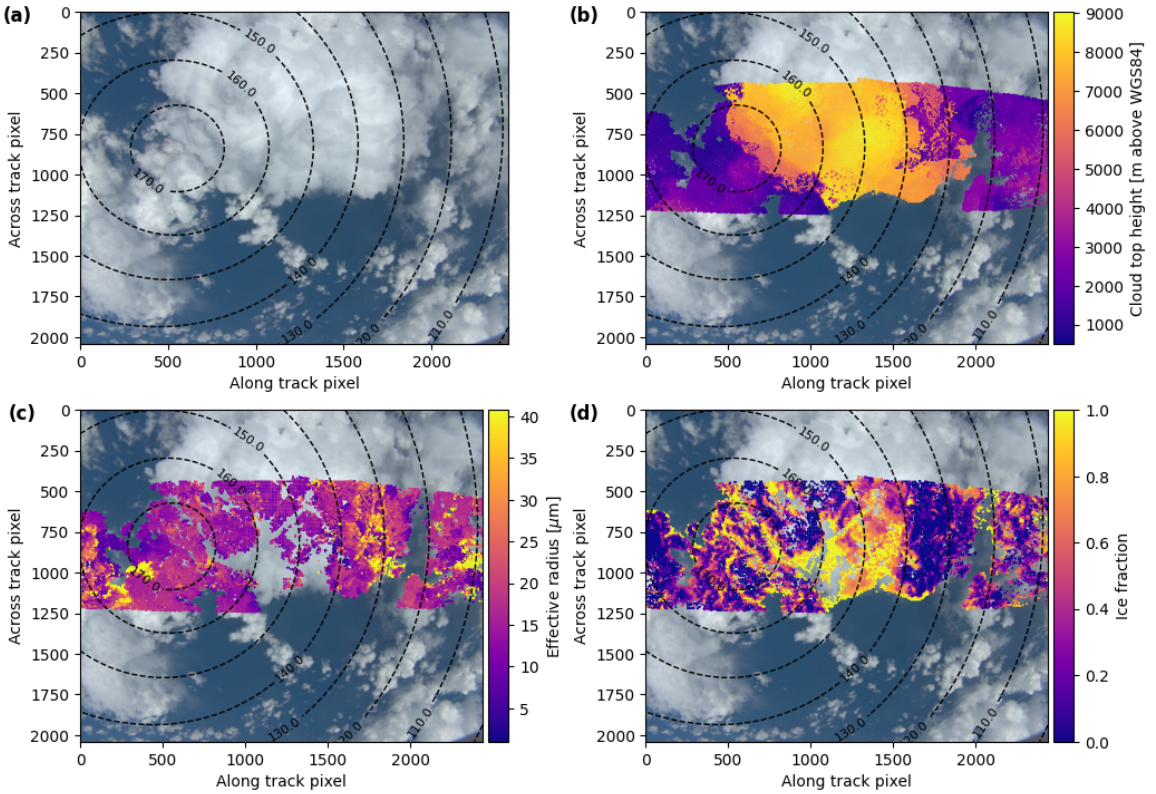

Figure 5.1: Example observation of the polLR camera of specMACS during the PERCUSION campaign on 2024-09-06 at 17:28:30 UTC. **(a)** RGB image. **(b)** Cloud top height from the stereographic retrieval. **(c)** Effective radius of liquid cloud droplets from the cloudbow retrieval. **(d)** Ice fraction from the polarized phase retrieval. The ice fraction was derived assuming plane-parallel clouds and the results have not been filtered with the shadow mask or for small RMSEs. The retrieval results of the cloudbow and phase retrievals for the green color channel are shown.

Appendix A

Derivation of the adiabatic effective radius

In the following, the derivation of Eq. 2.30 is shown. The effective radius is related to the volume mean radius through (Martin et al., 1994)

$$r_{\mathrm{eff}}^3 = \frac{1}{k} r_{\mathrm{v}}^3, \tag{A.1}$$

as already introduced in Eq. 2.29 and the volume mean radius is defined as (Grosvenor et al., 2018)

$$r_{\mathrm{v}}^3 = \frac{\int_0^\infty r^3 n(r) dr}{\int_0^\infty n(r) dr} = \frac{1}{N_{\mathrm{d}}} \int_0^\infty r^3 n(r) dr. \tag{A.2}$$

In addition, the LWC is calculated with

$$\mathrm{LWC} = \frac{4\pi\rho_{\mathrm{w}}}{3} \int_0^\infty r^3 n(r) dr. \tag{A.3}$$

Inserting Eq. A.2 into Eq. A.1 and applying the definition of the LWC in Eq. A.3 yields

$$r_{\mathrm{eff}}^3 = \frac{1}{k} \frac{1}{N_{\mathrm{d}}} \mathrm{LWC} \frac{3}{4\pi\rho_{\mathrm{w}}}. \tag{A.4}$$

According to the adiabatic cloud model, the LWC is defined as (Brenguier et al., 2000)

$$\mathrm{LWC} = f_{\mathrm{ad}} C_{\mathrm{w}} h. \tag{A.5}$$

Inserting this into Eq. A.4 and taking the cubic root gives the formula for the effective radius in the adiabatic cloud model:

$$r_{\mathrm{eff}} = \left(\frac{3}{4\pi\rho_{\mathrm{w}}} \right)^{1/3} (f_{\mathrm{ad}} C_{\mathrm{w}})^{1/3} (k N_{\mathrm{d}})^{-1/3} h^{1/3}. \tag{A.6}$$

Appendix B

Derivation of cloud geometrical thickness from the adiabatic cloud model

Following the adiabatic cloud model and Grosvenor et al. (2018), the liquid water content can be defined as

$$\mathrm{LWC}(z) = f_{\mathrm{ad}}\mathrm{LWC}_{\mathrm{ad}}(z) = f_{\mathrm{ad}}C_{\mathrm{w}}(z - z_{\mathrm{base}}), \tag{B.1}$$

with the adiabaticity f_{ad}, the condensation rate C_{w}, and z and z_{base} being the height and the cloud base height. Integrating this equation with respect to height gives the LWP

$$\mathrm{LWP} = \frac{1}{2} f_{\mathrm{ad}} C_{\mathrm{w}} d^2, \tag{B.2}$$

where $d = z_{\mathrm{top}} - z_{\mathrm{base}}$ is the geometrical thickness of the cloud. On the other hand, the liquid water path is related to the optical thickness, assuming an extinction efficiency of 2 for geometrical optics, through

$$\tau = \frac{3}{2} \frac{\mathrm{LWP}}{\rho_{\mathrm{w}} r_{\mathrm{eff}}}. \tag{B.3}$$

Combining Eq. B.2 and B.3 and solving for d finally give the formula for the geometrical thickness of a cloud as a function of the optical thickness using the adiabatic cloud model:

$$d = \sqrt{\frac{4}{3} \frac{\rho_{\mathrm{w}} r_{\mathrm{eff}}}{f_{\mathrm{ad}} C_{\mathrm{w}}} \tau}. \tag{B.4}$$

Glossary

BAHAMAS Basic HALO Measurement And Sensor system.

BRDF bidirectional reflectance distribution function.

CCN cloud condensation nucleus.

CDP cloud droplet probe.

CHB Calibration Home Base.

CIP cloud imaging probe.

DN digital number.

DOLP degree of linear polarization.

EUREC^{4}A ElUcidating the RolE of Cloud-Circulation Coupling in ClimAte measurement campaign.

FWHM full width at half maximum.

HALO High Altitude and LOng range research aircraft.

HALO–$(\mathcal{AC})^3$ HALO–$(\mathcal{AC})^3$ measurement campaign.

HAMP HALO Microwave Package.

ICA independent column approximation.

IDEFAX InDEpendent column local halF-sphere ApproXimation.

IN ice nucleus.

IWC ice water content.

LIS large integrating sphere.

LWC liquid water content.

LWP liquid water path.

MAE mean absolute error.

MCAO marine cold air outbreak.

MYSTIC Monte Carlo code for the physically correct tracing of photons in cloudy atmospheres.

P5 Polar 5 aircraft.

P6 Polar 6 aircraft.

PERCUSION Persistent EarthCare underflight studies of the ITCZ and organized convection measurement campaign.

PIP precipitation imaging probe.

PN polar nephelometer.

polLL specMACS polarization camera looking to the lower left.

polLR specMACS polarization camera looking to the lower right.

RMSE root mean square error.

RTE radiative transfer equation.

SIC sea ice concentration.

specMACS spectrometer of the Munich Aerosol Cloud Scanner.

SST sea surface temperature.

SWIR spectrometer of specMACS sensitive to the shortwave infrared wavelength range.

VELOX Video airbornE Longwave Observations within siX channels.

VNIR spectrometer of specMACS sensitive to the visible and near-infrared wavelength range.

WAI warm air intrusion.

WALES WAter vapor Lidar Experiment in Space.

WBF mechanism Wegener-Bergeron-Findeisen mechanism.

WRF Weather Research and Forecasting (WRF) model.

Bibliography

Abel, S. J., Boutle, I. A., Waite, K., Fox, S., Brown, P. R. A., Cotton, R., Lloyd, G., Choularton, T. W., and Bower, K. N.: The Role of Precipitation in Controlling the Transition from Stratocumulus to Cumulus Clouds in a Northern Hemisphere Cold-Air Outbreak, Journal of the Atmospheric Sciences, 74, 2293 – 2314, doi:10.1175/JAS-D-16-0362.1, 2017.

Ahn, E., Huang, Y., Siems, S. T., and Manton, M. J.: A Comparison of Cloud Microphysical Properties Derived From MODIS and CALIPSO With In Situ Measurements Over the Wintertime Southern Ocean, Journal of Geophysical Research: Atmospheres, 123, 11,120–11,140, doi:10.1029/2018JD028535, 2018.

Alexandrov, M. D., Cairns, B., Emde, C., Ackerman, A. S., and van Diedenhoven, B.: Accuracy assessments of cloud droplet size retrievals from polarized reflectance measurements by the research scanning polarimeter, Remote Sensing of Environment, 125, 92–111, doi:10.1016/j.rse.2012.07.012, 2012.

Alexandrov, M. D., Cairns, B., Emde, C., and Van Diedenhoven, B.: Correction of cloud optical thickness retrievals from nadir reflectances in the presence of 3D radiative effects. Part I: concept and tests on 3D RT simulations, Frontiers in Remote Sensing, 5, doi:10.3389/frsen.2024.1397631, 2024.

Ansmann, A., Mattis, I., Müller, D., Wandinger, U., Radlach, M., Althausen, D., and Damoah, R.: Ice formation in Saharan dust over central Europe observed with temperature/humidity/aerosol Raman lidar, J. Geophys. Res., 110, doi:10.1029/2004JD005000, 2005.

Arteaga, D., Planche, C., Tridon, F., Dupuy, R., Baudoux, A., Banson, S., Baray, J.-L., Mioche, G., Ehrlich, A., Mech, M., Mertes, S., Wendisch, M., Wobrock, W., and Jourdan, O.: Arctic mixed-phase clouds simulated by the WRF model: Comparisons with ACLOUD radar and in situ airborne observations and sensitivity of microphysics properties, Atmospheric Research, 307, 107 471, doi:10.1016/j.atmosres.2024.107471, 2024.

Aubry, C., Delanoë, J., Groß, S., Ewald, F., Tridon, F., Jourdan, O., and Mioche, G.: Lidar–radar synergistic method to retrieve ice, supercooled water and mixed-phase cloud properties, Atmospheric Measurement Techniques, 17, 3863–3881, doi:10.5194/amt-17-3863-2024, 2024.

Ávila, E. E., Castellano, N. E., Saunders, C. P. R., Bürgesser, R. E., and Aguirre Varela,

G. G.: Initial stages of the riming process on ice crystals, Geophysical Research Letters, 36, doi:10.1029/2009GL037723, 2009.

Bailey, M. P. and Hallett, J.: A Comprehensive Habit Diagram for Atmospheric Ice Crystals: Confirmation from the Laboratory, AIRS II, and Other Field Studies, Journal of the Atmospheric Sciences, 66, 2888 – 2899, doi:10.1175/2009JAS2883.1, 2009.

Bass, M., Stryland, E. W. V., Williams, D. R., and Wolfe, W. L.: Handbook of Optics Volume II Devices, Measurements, and Properties, McGraw-Hill, Inc., 2nd edn., 1995.

Bass, M., DeCusatis, C. M., Enoch, J. M., Lakshminarayanan, V., Li, G., MacDonald, C., Mahajan, V. N., and Stryland, E. V.: Handbook of Optics Volume I Geometrical and Physical Optics, Polarized Light, Components and Instruments, McGraw-Hill, Inc., 3rd edn., 2010.

Baum, B. A., Yang, P., Heymsfield, A. J., Bansemer, A., Cole, B. H., Merrelli, A., Schmitt, C., and Wang, C.: Ice cloud single-scattering property models with the full phase matrix at wavelengths from 0.2 to 100µm, Journal of Quantitative Spectroscopy and Radiative Transfer, 146, 123–139, doi:10.1016/j.jqsrt.2014.02.029, electromagnetic and Light Scattering by Nonspherical Particles XIV, 2014.

Baumgartner, A.: Characterization of Integrating Sphere Homogeneity with an Uncalibrated Imaging Spectrometer, in: Proc. WHISPERS 2013, pp. 1–4, URL `https://elib.dlr.de/83300/`, 2013.

Baumgartner, A.: Grating monochromator wavelength calibration using an echelle grating wavelength meter, Opt. Express, 27, 13 596–13 610, doi:10.1364/OE.27.013596, 2019.

Baumgartner, A.: Traceable Imaging Spectrometer Calibration and Transformation of Geometric and Spectral Pixel Properties, Ph.D. thesis, Universität Osnabrück, doi:10.48693/38, 2022.

Baur, F., Scheck, L., Stumpf, C., Köpken-Watts, C., and Potthast, R.: A neural-network-based method for generating synthetic 1.6 μm near-infrared satellite images, Atmospheric Measurement Techniques, 16, 5305–5326, doi:10.5194/amt-16-5305-2023, 2023.

Beer, C., Zimov, N., Olofsson, J., Porada, P., and Zimov, S.: Protection of Permafrost Soils from Thawing by Increasing Herbivore Density, Scientific Reports, 10, doi:10.1038/s41598-020-60938-y, 2020.

Bergeron, T.: On the physics of cloud and precipitation, in: Proceedings of the Fifth Assembly of International Union of Geodesy and Geophysics, p. 156–178, Lisbon, Portugal, 1935.

Block, K., Schneider, F. A., Mülmenstädt, J., Salzmann, M., and Quaas, J.: Climate models disagree on the sign of total radiative feedback in the Arctic, Tellus A: Dynamic Meteorology and Oceanography, 2020.

Boettcher, M., Schäfler, A., Sprenger, M., Sodemann, H., Kaufmann, S., Voigt, C., Schlager, H., Summa, D., Di Girolamo, P., Nerini, D., Germann, U., and Wernli, H.: Lagrangian matches between observations from aircraft, lidar and radar in a warm conveyor belt crossing orography, Atmospheric Chemistry and Physics, 21, 5477–5498, doi:10.5194/acp-

21-5477-2021, 2021.

Bohren, C. and Huffman, D.: Absorption and Scattering of Light by Small Particles, Wiley, 2004.

Bradski, G.: The OpenCV Library, Dr. Dobb's Journal of Software Tools, 2000.

Brand, R.: Bispectral Retrievals in Mixed-Phase Clouds, Bachelor's thesis, Ludwig-Maximilians-Universität München, 2025.

Brenguier, J.-L., Pawlowska, H., Schüller, L., Preusker, R., Fischer, J., and Fouquart, Y.: Radiative Properties of Boundary Layer Clouds: Droplet Effective Radius versus Number Concentration, Journal of the Atmospheric Sciences, 57, 803 – 821, doi:10.1175/1520-0469(2000)057<0803:RPOBLC>2.0.CO;2, 2000.

Brown, P. R. A. and Francis, P. N.: Improved Measurements of the Ice Water Content in Cirrus Using a Total-Water Probe, Journal of Atmospheric and Oceanic Technology, 12, 410 – 414, doi:10.1175/1520-0426(1995)012<0410:IMOTIW>2.0.CO;2, 1995.

Brümmer, B.: Boundary-layer modification in wintertime cold-air outbreaks from the Arctic sea ice, Boundary-Layer Meteorology, 80, 109–125, doi:10.1007/BF00119014, 1996.

Brümmer, B.: Roll and Cell Convection in Wintertime Arctic Cold-Air Outbreaks, Journal of the Atmospheric Sciences, 56, 2613 – 2636, doi:10.1175/1520-0469(1999)056<2613:RACCIW>2.0.CO;2, 1999.

Buras, R. and Mayer, B.: Efficient unbiased variance reduction techniques for Monte Carlo simulations of radiative transfer in cloudy atmospheres: The solution, Journal of Quantitative Spectroscopy and Radiative Transfer, 112, 434–447, doi:10.1016/j.jqsrt.2010.10.005, 2011.

Cairns, B., Russell, E. E., and Travis, L. D.: Research Scanning Polarimeter: calibration and ground-based measurements, in: Polarization: Measurement, Analysis, and Remote Sensing II, edited by Goldstein, D. H. and Chenault, D. B., vol. 3754, pp. 186 – 196, International Society for Optics and Photonics, SPIE, doi:10.1117/12.366329, 1999.

Cesana, G., Waliser, D. E., Jiang, X., and Li, J.-L. F.: Multimodel evaluation of cloud phase transition using satellite and reanalysis data, Journal of Geophysical Research: Atmospheres, 120, 7871–7892, doi:10.1002/2014JD022932, 2015.

Cesana, G. V., Khadir, T., Chepfer, H., and Chiriaco, M.: Southern Ocean Solar Reflection Biases in CMIP6 Models Linked to Cloud Phase and Vertical Structure Representations, Geophysical Research Letters, 49, e2022GL099 777, doi:10.1029/2022GL099777, e2022GL099777 2022GL099777, 2022.

Chandrasekhar, S.: Radiative Transfer, Dover Books on Intermediate and Advanced Mathematics, Dover Publications, 1960.

Chen, Z., Wang, X., and Liang, R.: Calibration method of microgrid polarimeters with image interpolation, Appl. Opt., 54, 995–1001, doi:10.1364/AO.54.000995, 2015.

Chipman, R., Lam, W. S. T., and Young, G.: Polarized Light and Optical Systems, CRC Press, 1st edn., doi:10.1201/9781351129121, 2018.

Choi, Y.-S., Ho, C.-H., Park, C.-E., Storelvmo, T., and Tan, I.: Influence of cloud phase composition on climate feedbacks, Journal of Geophysical Research: Atmospheres, 119, 3687–3700, doi:10.1002/2013JD020582, 2014.

Cohen, J., Screen, J. A., Furtado, Jason C.and Barlow, M., Whittleston, D., Coumou, D., Francis, J., Dethloff, K., Entekhabi, D., Overland, J., and Jones, J.: Recent Arctic amplification and extreme mid-latitude weather, Nature Geoscience, 7, 627–637, doi:10.1038/ngeo2234, 2014.

Cohen, J., Zhang, X., Francis, J., Jung, T., Kwok, R., Overland, J., Ballinger, T. J., Bhatt, U. S., Chen, H. W., Coumou, D., Feldstein, S., Gu, H., Handorf, D., Henderson, G., Ionita, M., Kretschmer, M., Laliberte, F., Lee, S., Linderholm, H. W., Maslowski, W., Peings, Y., Pfeiffer, K., Rigor, I., Semmler, T., Stroeve, J., Taylor, P. C., Vavrus, S., Vihma, T., Wang, S., Wendisch, M., Wu, Y., and Yoon, J.: Divergent consensuses on Arctic amplification influence on midlatitude severe winter weather, Nature Climate Change, 10, 20–29, doi:10.1038/s41558-019-0662-y, 2020.

Cohen, J., Agel, L., Barlow, M., Garfinkel, C. I., and White, I.: Linking Arctic variability and change with extreme winter weather in the United States, Science, 373, 1116–1121, doi:10.1126/science.abi9167, 2021.

Cornet, C., C-Labonnote, L., and Szczap, F.: Three-dimensional polarized Monte Carlo atmospheric radiative transfer model (3DMCPOL): 3D effects on polarized visible reflectances of a cirrus cloud, Journal of Quantitative Spectroscopy and Radiative Transfer, 111, 174–186, doi:10.1016/j.jqsrt.2009.06.013, 2010.

Cox, C. and Munk, W.: Measurement of the Roughness of the Sea Surface from Photographs of the Sun's Glitter, J. Opt. Soc. Am., 44, 838–850, doi:10.1364/JOSA.44.000838, 1954a.

Cox, C. and Munk, W.: Statistics of the sea surface derived from sun glitter, Journal of Marine Research, 13, 198–227, 1954b.

Cui, Z., Carslaw, K. S., Yin, Y., and Davies, S.: A numerical study of aerosol effects on the dynamics and microphysics of a deep convective cloud in a continental environment, Journal of Geophysical Research: Atmospheres, 111, doi:10.1029/2005JD005981, 2006.

Curry, J. A. and Webster, P. J.: Thermodynamics of atmospheres and oceans, Academic Press, 1999.

Dahlke, S., Solbès, A., and Maturilli, M.: Cold Air Outbreaks in Fram Strait: Climatology, Trends, and Observations During an Extreme Season in 2020, Journal of Geophysical Research: Atmospheres, 127, 1–18, doi:10.1029/2021JD035741, 2022.

Davis, A. B.: Cloud remote sensing with sideways looks: theory and first results using Multispectral Thermal Imager data, in: Algorithms and Technologies for Multispectral, Hyperspectral, and Ultraspectral Imagery VIII, edited by Shen, S. S. and Lewis, P. E., vol. 4725, pp. 397 – 405, International Society for Optics and Photonics, SPIE, doi:10.1117/12.478772, 2002.

de Boer, G., Morrison, H., Shupe, M. D., and Hildner, R.: Evidence of liquid dependent ice nucleation in high-latitude stratiform clouds from surface remote sensors, Geophysical

Research Letters, 38, doi:10.1029/2010GL046016, 2011.

de Rooy, W. C., Bechtold, P., Fröhlich, K., Hohenegger, C., Jonker, H., Mironov, D., Pier Siebesma, A., Teixeira, J., and Yano, J.-I.: Entrainment and detrainment in cumulus convection: an overview, Quarterly Journal of the Royal Meteorological Society, 139, 1–19, doi:10.1002/qj.1959, 2013.

Delanoë, J. and Hogan, R. J.: A variational scheme for retrieving ice cloud properties from combined radar, lidar, and infrared radiometer, Journal of Geophysical Research: Atmospheres, 113, doi:10.1029/2007JD009000, 2008.

Deschamps, P.-Y., Breon, F.-M., Leroy, M., Podaire, A., Bricaud, A., Buriez, J.-C., and Seze, G.: The POLDER mission: instrument characteristics and scientific objectives, IEEE Transactions on Geoscience and Remote Sensing, 32, 598–615, doi:10.1109/36.297978, 1994.

Di Girolamo, L., Liang, L., and Platnick, S.: A global view of one-dimensional solar radiative transfer through oceanic water clouds, Geophysical Research Letters, 37, doi:https://doi.org/10.1029/2010GL044094, 2010.

Diner, D. J., Xu, F., Garay, M. J., Martonchik, J. V., Rheingans, B. E., Geier, S., Davis, A., Hancock, B. R., Jovanovic, V. M., Bull, M. A., Capraro, K., Chipman, R. A., and McClain, S. C.: The Airborne Multiangle SpectroPolarimetric Imager (AirMSPI): a new tool for aerosol and cloud remote sensing, Atmospheric Measurement Techniques, 6, 2007–2025, doi:10.5194/amt-6-2007-2013, 2013.

DLR Remote Sensing Technology Institute: The Calibration Home Base for Imaging Spectrometers, Journal of large-scale research facilities, 2, A82, doi:10.17815/jlsrf-2-137, 2016.

Dorff, H., Aubry, C., Ewald, F., Hirsch, L., Jansen, F., Konow, H., Mech, M., Ori, D., Ringel, M., Walbröl, A., Crewell, S., Ehrlich, A., Wendisch, M., and Ament, F.: Unified Airborne Active and Passive Microwave Measurements over Arctic Sea Ice and Ocean during the HALO-$(AC)^3$ Campaign in Spring 2022 (v2.7), doi:10.1594/PANGAEA.974108, 2024.

Dupuy, R., Mioche, G., Gourbeyre, C., and Jourdan, O.: French Airborne Measurement Platform (PMA) cloud particle size distribution and volumic cloud particle scattering properties dataset near Svalbard for the HALO-AC3 measurement campaign in 2022, doi:10.1594/PANGAEA.965734, 2024.

Ehrlich, A., Bierwirth, E., Wendisch, M., Gayet, J.-F., Mioche, G., Lampert, A., and Heintzenberg, J.: Cloud phase identification of Arctic boundary-layer clouds from airborne spectral reflection measurements: test of three approaches, Atmospheric Chemistry and Physics, 8, 7493–7505, doi:10.5194/acp-8-7493-2008, 2008.

Ehrlich, A., Wendisch, M., Bierwirth, E., Gayet, J.-F., Mioche, G., Lampert, A., and Mayer, B.: Evidence of ice crystals at cloud top of Arctic boundary-layer mixed-phase clouds derived from airborne remote sensing, Atmospheric Chemistry and Physics, 9, 9401–9416, doi:10.5194/acp-9-9401-2009, 2009.

Ehrlich, A., Wolf, K., Luebke, A., Zoeger, M., and Giez, A.: Broadband solar and terrestrial,

upward and downward irradiance measured by BACARDI on HALO during the EUREC4A Field Campaign, Aeris, URL https://doi.org/10.25326/160, 2021.

Ehrlich, A., Crewell, S., Herber, A., Klingebiel, M., Lüpkes, C., Mech, M., Becker, S., Borrmann, S., Bozem, H., Buschmann, M., Clemen, H.-C., De La Torre Castro, E., Dorff, H., Dupuy, R., Eppers, O., Ewald, F., George, G., Giez, A., Grawe, S., Gourbeyre, C., Hartmann, J., Jäkel, E., Joppe, P., Jourdan, O., Jurányi, Z., Kirbus, B., Lucke, J., Luebke, A. E., Maahn, M., Maherndl, N., Mallaun, C., Mayer, J., Mertes, S., Mioche, G., Moser, M., Müller, H., Pörtge, V., Risse, N., Roberts, G., Rosenburg, S., Röttenbacher, J., Schäfer, M., Schaefer, J., Schäfler, A., Schirmacher, I., Schneider, J., Schnitt, S., Stratmann, F., Tatzelt, C., Voigt, C., Walbröl, A., Weber, A., Wetzel, B., Wirth, M., and Wendisch, M.: A comprehensive in situ and remote sensing data set collected during the HALO–$(\mathcal{AC})^3$ aircraft campaign, Earth System Science Data, 17, 1295–1328, doi:10.5194/essd-17-1295-2025, 2025.

Emde, C., Buras, R., Mayer, B., and Blumthaler, M.: The impact of aerosols on polarized sky radiance: model development, validation, and applications, Atmospheric Chemistry and Physics, 10, 383–396, doi:10.5194/acp-10-383-2010, 2010.

Emde, C., Barlakas, V., Cornet, C., Evans, F., Korkin, S., Ota, Y., Labonnote, L. C., Lyapustin, A., Macke, A., Mayer, B., and Wendisch, M.: IPRT polarized radiative transfer model intercomparison project – Phase A, Journal of Quantitative Spectroscopy and Radiative Transfer, 164, 8–36, doi:10.1016/j.jqsrt.2015.05.007, 2015.

Emde, C., Buras-Schnell, R., Kylling, A., Mayer, B., Gasteiger, J., Hamann, U., Kylling, J., Richter, B., Pause, C., Dowling, T., and Bugliaro, L.: The libRadtran software package for radiative transfer calculations (version 2.0.1), Geoscientific Model Development, 9, 1647–1672, doi:10.5194/gmd-9-1647-2016, 2016.

Erdtmann, D.: Remote sensing of arctic cirrus microphysics using hyperspectral reflectivity measurements and polarized imaging, Master's thesis, Ludwig-Maximilians-Universität München, 2023.

Eshelman, L. M. and Shaw, J. A.: Visualization of all-sky polarization images referenced in the instrument, scattering, and solar principal planes, Optical Engineering, 58, 082 418, doi:10.1117/1.OE.58.8.082418, 2019.

European Centre for Medium-Range Weather Forecasts: ERA5 Reanalysis (0.25 Degree Latitude-Longitude Grid), URL https://gdex.ucar.edu/datasets/d633000/, last access: 30 October 2023, 2019.

Ewald, F.: Personal communication, 2025.

Ewald, F., Kölling, T., Baumgartner, A., Zinner, T., and Mayer, B.: Design and characterization of specMACS, a multipurpose hyperspectral cloud and sky imager, Atmospheric Measurement Techniques, 9, 2015–2042, doi:10.5194/amt-9-2015-2016, 2016.

Ewald, F., Groß, S., Wirth, M., Delanoë, J., Fox, S., and Mayer, B.: Why we need radar, lidar, and solar radiance observations to constrain ice cloud microphysics, Atmospheric Measurement Techniques, 14, 5029–5047, doi:10.5194/amt-14-5029-2021, 2021.

Faber, S., French, J. R., and Jackson, R.: Laboratory and in-flight evaluation of measurement uncertainties from a commercial Cloud Droplet Probe (CDP), Atmospheric Measurement Techniques, 11, 3645–3659, doi:10.5194/amt-11-3645-2018, 2018.

Field, P. R., Heymsfield, A. J., and Bansemer, A.: Shattering and Particle Interarrival Times Measured by Optical Array Probes in Ice Clouds, Journal of Atmospheric and Oceanic Technology, 23, 1357 – 1371, doi:10.1175/JTECH1922.1, 2006.

Field, P. R., Cotton, R. J., McBeath, K., Lock, A. P., Webster, S., and Allan, R. P.: Improving a convection-permitting model simulation of a cold air outbreak, Quarterly Journal of the Royal Meteorological Society, 140, 124–138, doi:10.1002/qj.2116, 2014.

Field, P. R., Brozkova, R., Chen, M., Dudhia, J., Lac, C., Hara, T., Honnert, R., Olson, J., Siebesma, P., de Roode, S., Tomassini, L., Hill, A., and McTaggart-Cowan, R.: Exploring the convective grey zone with regional simulations of a cold air outbreak, Quarterly Journal of the Royal Meteorological Society, 143, 2537–2555, doi:10.1002/qj.3105, 2017.

Fielding, M. D., Schäfer, S. A. K., Hogan, R. J., and Forbes, R. M.: Parametrizing cloud geometry and its application in a subgrid cloud-edge erosion scheme, Quarterly Journal of the Royal Meteorological Society, 146, 1651–1667, doi:10.1002/qj.3758, 2020.

Findeisen, W.: Die kolloidmeteorologischen Vorgänge bei der Niederschlagsbildung, Meteorologische Zeitschrift, 55, 121–133, 1938.

Fletcher, J., Mason, S., and Jakob, C.: The Climatology, Meteorology, and Boundary Layer Structure of Marine Cold Air Outbreaks in Both Hemispheres, Journal of Climate, 29, 1999 – 2014, doi:10.1175/JCLI-D-15-0268.1, 2016a.

Fletcher, J. K., Mason, S., and Jakob, C.: A Climatology of Clouds in Marine Cold Air Outbreaks in Both Hemispheres, Journal of Climate, 29, 6677 – 6692, doi:10.1175/JCLI-D-15-0783.1, 2016b.

Forsberg, R., Hvidegaard, S. M., Skourup, H., and Simonsen, S.: Three decades of polar airborne campaigns in the Arctic and Antarctica, in: AGU Fall Meeting Abstracts, vol. 2023 of *AGU Fall Meeting Abstracts*, pp. C31C–1365, 2023.

Forster, L., Seefeldner, M., Baumgartner, A., Kölling, T., and Mayer, B.: Ice crystal characterization in cirrus clouds II: radiometric characterization of HaloCam for the quantitative analysis of halo displays, Atmospheric Measurement Techniques, 13, 3977–3991, doi:10.5194/amt-13-3977-2020, 2020.

Forster, L., Weber, A., and Mayer, B.: CrystalTrace: a Monte Carlo raytracing algorithm for radiative transfer in cirrus clouds with oriented ice crystals, Atmospheric Measurement Techniques, 18, 7853–7863, doi:10.5194/amt-18-7853-2025, 2025.

Francis, J. A. and Vavrus, S. J.: Evidence for a wavier jet stream in response to rapid Arctic warming, Environmental Research Letters, 10, 014 005, doi:10.1088/1748-9326/10/1/014005, 2015.

Freud, E. and Rosenfeld, D.: Linear relation between convective cloud drop number concentration and depth for rain initiation, Journal of Geophysical Research: Atmospheres, 117, doi:10.1029/2011JD016457, 2012.

Freud, E., Rosenfeld, D., Andreae, M. O., Costa, A. A., and Artaxo, P.: Robust relations between CCN and the vertical evolution of cloud drop size distribution in deep convective clouds, Atmospheric Chemistry and Physics, 8, 1661–1675, doi:10.5194/acp-8-1661-2008, 2008.

Gabriel, P. M. and Evans, K. F.: Simple Radiative Transfer Methods for Calculating Domain-Averaged Solar Fluxes in Inhomogeneous Clouds, Journal of Atmospheric Sciences, 53, 858 – 877, doi:10.1175/1520-0469(1996)053<0858:SRTMFC>2.0.CO;2, 1996.

Gao, S. and Gruev, V.: Bilinear and bicubic interpolation methods for division of focal plane polarimeters, Opt. Express, 19, 26 161–26 173, doi:10.1364/OE.19.026161, 2011.

Gayet, J. F., Crépel, O., Fournol, J. F., and Oshchepkov, S.: A new airborne polar Nephelometer for the measurements of optical and microphysical cloud properties. Part I: Theoretical design, Annales Geophysicae, 15, 451–459, doi:10.1007/s00585-997-0451-1, 1997.

Geerts, B., Giangrande, S. E., McFarquhar, G. M., Xue, L., Abel, S. J., Comstock, J. M., Crewell, S., DeMott, P. J., Ebell, K., Field, P., Hill, T. C. J., Hunzinger, A., Jensen, M. P., Johnson, K. L., Juliano, T. W., Kollias, P., Kosovic, B., Lackner, C., Luke, E., Lüpkes, C., Matthews, A. A., Neggers, R., Ovchinnikov, M., Powers, H., Shupe, M. D., Spengler, T., Swanson, B. E., Tjernström, M., Theisen, A. K., Wales, N. A., Wang, Y., Wendisch, M., and Wu, P.: The COMBLE Campaign: A Study of Marine Boundary Layer Clouds in Arctic Cold-Air Outbreaks, Bulletin of the American Meteorological Society, 103, E1371 – E1389, doi:10.1175/BAMS-D-21-0044.1, 2022.

Gege, P., Fries, J., Haschberger, P., Schötz, P., Schwarzer, H., Strobl, P., Suhr, B., Ulbrich, G., and Jan Vreeling, W.: Calibration facility for airborne imaging spectrometers, ISPRS Journal of Photogrammetry and Remote Sensing, 64, 387–397, doi:10.1016/j.isprsjprs.2009.01.006, 2009.

George, G., Luebke, A. E., Klingebiel, M., Mech, M., and Ehrlich, A.: Dropsonde measurements from HALO and POLAR 5 during HALO-(AC)^3 in 2022 (Level-3), PANGAEA, doi:10.1594/PANGAEA.968900, in: George, G et al. (2024): Dropsonde measurements from HALO and POLAR 5 during HALO-(AC)^3 in 2022 [dataset bundled publication]. PANGAEA, https://doi.org/10.1594/PANGAEA.968891, 2024.

Gerber, H., Frick, G., Jensen, J., and Hudson, J.: Entrainment, Mixing, and Microphysics in Trade-Wind Cumulus, Journal of the Meteorological Society of Japan, 86, 87–106, 2008.

Gierens, R., Kneifel, S., Shupe, M. D., Ebell, K., Maturilli, M., and Löhnert, U.: Low-level mixed-phase clouds in a complex Arctic environment, Atmospheric Chemistry and Physics, 20, 3459–3481, doi:10.5194/acp-20-3459-2020, 2020.

Giez, A., Mallaun, C., Nenakhov, V., and Zöger, M.: Calibration of a Nose Boom Mounted Airflow Sensor on an Atmospheric Research Aircraft by Inflight Maneuvers, Tech. rep., URL `https://elib.dlr.de/145969/`, 2021.

Giménez, Y., Lapray, P.-J., Foulonneau, A., and Bigué, L.: Calibration for polarization

filter array cameras: recent advances, in: Fourteenth International Conference on Quality Control by Artificial Vision, edited by Cudel, C., Bazeille, S., and Verrier, N., vol. 11172, p. 1117216, International Society for Optics and Photonics, SPIE, doi:10.1117/12.2521752, 2019.

Giménez, Y., Lapray, P.-J., Foulonneau, A., and Bigué, L.: Calibration algorithms for polarization filter array camera: survey and evaluation, Journal of Electronic Imaging, 29, 041 011, doi:10.1117/1.JEI.29.4.041011, 2020.

Goloub, P., Herman, M., Chepfer, H., Riedi, J., Brogniez, G., Couvert, P., and Séze, G.: Cloud thermodynamical phase classification from the POLDER spaceborne instrument, Journal of Geophysical Research: Atmospheres, 105, 14 747–14 759, doi:10.1029/1999JD901183, 2000.

Griffiths, D.: Introduction to electrodynamics, Pearson, fourth edition edn., 2013.

Gross, H.: Handbook of Optical Systems Volume 1 Fundamentals of Technical Optics, Wiley-VCH, 1. ed., 2. repr. edn., 2011.

Grosvenor, D. P., Sourdeval, O., Zuidema, P., Ackerman, A., Alexandrov, M. D., Bennartz, R., Boers, R., Cairns, B., Chiu, J. C., Christensen, M., Deneke, H., Diamond, M., Feingold, G., Fridlind, A., Hünerbein, A., Knist, C., Kollias, P., Marshak, A., McCoy, D., Merk, D., Painemal, D., Rausch, J., Rosenfeld, D., Russchenberg, H., Seifert, P., Sinclair, K., Stier, P., van Diedenhoven, B., Wendisch, M., Werner, F., Wood, R., Zhang, Z., and Quaas, J.: Remote Sensing of Droplet Number Concentration in Warm Clouds: A Review of the Current State of Knowledge and Perspectives, Reviews of Geophysics, 56, 409–453, doi:10.1029/2017RG000593, 2018.

Gryschka, M., Fricke, J., and Raasch, S.: On the impact of forced roll convection on vertical turbulent transport in cold air outbreaks, Journal of Geophysical Research: Atmospheres, 119, 12,513–12,532, doi:10.1002/2014JD022160, 2014.

Gutleben, M.: Long-range-transported Saharan air layers and their radiative effects determined by airborne lidar measurements, Ph.D. thesis, Ludwig-Maximilians-Universität München, URL `http://nbn-resolving.de/urn:nbn:de:bvb:19-277095`, 2020.

Hansen, J. E.: Multiple scattering of polarized light in planetary atmospheres part II. Sunlight reflected by terrestrial water clouds, J. Atmos. Sci., 28, 1400–1426, 1971.

Hansen, J. E. and Travis, L. D.: Light scattering in planetary atmospheres, Space Sci. Rev., 16, 527–610, doi:10.1007/BF00168069, 1974.

Hascoet, L. and Pascual, V.: The Tapenade automatic differentiation tool: Principles, model, and specification, ACM Trans. Math. Softw., 39, 1–43, doi:10.1145/2450153.2450158, 2013.

Hecht, E.: Optik, Walter de Gruyter, Berlin/Boston, 7th edn., 2018.

Heikenfeld, M., Marinescu, P. J., Christensen, M., Watson-Parris, D., Senf, F., van den Heever, S. C., and Stier, P.: tobac 1.2: towards a flexible framework for tracking and analysis of clouds in diverse datasets, Geoscientific Model Development, 12, 4551–4570, doi:10.5194/gmd-12-4551-2019, 2019.

Heikkila, J. and Silven, O.: A four-step camera calibration procedure with implicit image correction, in: Proceedings of IEEE Computer Society Conference on Computer Vision and Pattern Recognition, pp. 1106–1112, doi:10.1109/CVPR.1997.609468, 1997.

Herber, A., Schneider, J., Borrmann, S., Voigt, C., and Moser, M.: Master tracks in different resolutions during POLAR 6 campaign P6_231_HALO_2022, doi:10.1594/PANGAEA.947701, 2022.

Hersbach, H., Bell, B., Berrisford, P., Biavati, G., Horányi, A., Muñoz Sabater, J., Nicolas, J., Peubey, C., Radu, R., Rozum, I., Schepers, D., Simmons, A., Soci, C., Dee, D., and Thépaut, J.-N.: ERA5 hourly data on pressure levels from 1940 to present, doi:10.24381/cds.bd0915c6, accessed on 2025-04-03, 2023a.

Hersbach, H., Bell, B., Berrisford, P., Biavati, G., Horányi, A., Muñoz Sabater, J., Nicolas, J., Peubey, C., Radu, R., Rozum, I., Schepers, D., Simmons, A., Soci, C., Dee, D., and Thépaut, J.-N.: ERA5 hourly data on single levels from 1940 to present, doi:10.24381/cds.adbb2d47, accessed on 2025-04-03, 2023b.

Hess, M., Koepke, P., and Schult, I.: Optical properties of aerosols and clouds: the software package OPAC, Bulletin of the American Meteorological Society, 79, 831–844, 1998.

Heymsfield, A. J., Schmitt, C., Bansemer, A., and Twohy, C. H.: Improved Representation of Ice Particle Masses Based on Observations in Natural Clouds, Journal of the Atmospheric Sciences, 67, 3303 – 3318, doi:10.1175/2010JAS3507.1, 2010.

Heymsfield, A. J., Schmitt, C., and Bansemer, A.: Ice Cloud Particle Size Distributions and Pressure-Dependent Terminal Velocities from In Situ Observations at Temperatures from 0° to -86°C, Journal of the Atmospheric Sciences, 70, 4123 – 4154, doi:10.1175/JAS-D-12-0124.1, 2013.

Hofer, S., Hahn, L. C., Shaw, J. K., McGraw, Z. S., Bruno, O., Hellmuth, F., Pietschnig, M., Mostue, I. A., David, R. O., Carlsen, T., and Storelvmo, T.: Realistic representation of mixed-phase clouds increases projected climate warming, Communications Earth & Environment, 5, 390, doi:10.1038/s43247-024-01524-2, 2024.

Hogan, R. J., Tian, L., Brown, P. R. A., Westbrook, C. D., Heymsfield, A. J., and Eastment, J. D.: Radar Scattering from Ice Aggregates Using the Horizontally Aligned Oblate Spheroid Approximation, Journal of Applied Meteorology and Climatology, 51, 655 – 671, doi:10.1175/JAMC-D-11-074.1, 2012.

Hovenier, J. and Van Der Mee, C. V. M.: Fundamental relationships relevant to the transfer of polarized light in a scattering atmosphere, Astronomy and Astrophysics, 128, 1–16, 1983.

Iacono, M. J., Delamere, J. S., Mlawer, E. J., Shephard, M. W., Clough, S. A., and Collins, W. D.: Radiative forcing by long-lived greenhouse gases: Calculations with the AER radiative transfer models, Journal of Geophysical Research, 113, doi:10.1029/2008jd009944, 2008.

Inoue, J., Sato, K., Rinke, A., Cassano, J. J., Fettweis, X., Heinemann, G., Matthes, H., Orr, A., Phillips, T., Seefeldt, M., Solomon, A., and Webster, S.: Clouds and

Radiation Processes in Regional Climate Models Evaluated Using Observations Over the Ice-free Arctic Ocean, Journal of Geophysical Research: Atmospheres, 126, 1–25, doi:10.1029/2020JD033904, 2021.

Intrieri, J. M., Fairall, C. W., Shupe, M. D., Persson, P. O. G., Andreas, E. L., Guest, P. S., and Moritz, R. E.: An annual cycle of Arctic surface cloud forcing at SHEBA, Journal of Geophysical Research: Oceans, 107, SHE 13–1–SHE 13–14, doi:10.1029/2000JC000439, 2002.

IPCC: Climate Change 2021: The Physical Science Basis. Contribution of Working Group I to the Sixth Assessment Report of the Intergovernmental Panel on Climate Change, In Press, doi:10.1017/9781009157896, 2021.

Ishizaka, Y., Kurahashi, Y., and Tsuruta, H.: Microphysical Properties of Winter Stratiform Clouds over the Southwest Islands Area in Japan, Journal of the Meteorological Society of Japan. Ser. II, 73, 1137–1151, doi:10.2151/jmsj1965.73.6_1137, 1995.

Jäkel, E., Walter, J., and Wendisch, M.: Thermodynamic phase retrieval of convective clouds: impact of sensor viewing geometry and vertical distribution of cloud properties, Atmospheric Measurement Techniques, 6, 539–547, doi:10.5194/amt-6-539-2013, 2013.

Janesick, J. R.: Photon Transfer, Society of Photo-Optical Instrumentation Engineers, 2007.

Jeffries, M. O., Overland, J. E., and Perovich, D. K.: The Arctic shifts to a new normal, Physics Today, 66, 35–40, doi:10.1063/PT.3.2147, 2013.

Jourdan, O., Mioche, G., Garrett, T. J., Schwarzenböck, A., Vidot, J., Xie, Y., Shcherbakov, V., Yang, P., and Gayet, J.-F.: Coupling of the microphysical and optical properties of an Arctic nimbostratus cloud during the ASTAR 2004 experiment: Implications for light-scattering modeling, Journal of Geophysical Research: Atmospheres, 115, doi:10.1029/2010JD014016, 2010.

Jurkat-Witschas, T., Voigt, C., Groß, S., Kaufmann, S., Sauer, D., la Torre Castro, E. D., Krämer, M., Schäfler, A., Afchine, A., Attinger, R., Garcia, I. B., Beer, C. G., Bugliaro, L., Clemen, H.-C., Dekoutsidis, G., Ehrlich, A., Grawe, S., Hahn, V., Hendricks, J., Järvinen, E., Klimach, T., Krüger, K., Krüger, O., Lucke, J., Luebke, A. E., Marsing, A., Mayer, B., Mayer, J., Mertes, S., Milenko, R.-Z., Moser, M., Müller, H., Nenakhov, V., Pöhlker, M., Pöschl, U., Pörtge, V., Rautenhaus, M., Righi, M., Röttenbacher, J., Schaefer, J., Schnaiter, M., Schneider, J., Schumann, U., Spelten, N., Stratmann, F., Tomsche, L., Wagner, S., Wang, Z., Weber, A., Wendisch, M., Wernli, H., Wetzel, B., Wirth, M., Zahn, A., Ziereis, H., and Zöger, M.: CIRRUS-HL: Picturing High- and Midlatitude Summer Cirrus and Contrail Cirrus above Europe with Airborne Measurements aboard the Research Aircraft HALO, Bulletin of the American Meteorological Society, 106, E2300 – E2327, doi:10.1175/BAMS-D-23-0270.1, 2025.

Khain, A. P. and Pinsky, M.: Microphysical Processes in Ice and Mixed-Phase Clouds, p. 344–496, Cambridge University Press, doi:10.1017/9781139049481.007, 2018.

Kirbus, B.: Personal communication, 2025.

Kirbus, B. and Wendisch, M.: Five-day backwards trajectories at one minute resolution along the flight tracks of the Polar 6 research aircraft during HALO-(AC)3, doi:10.1594/PANGAEA.971921, 2024.

Kirbus, B., Schirmacher, I., Klingebiel, M., Schäfer, M., Ehrlich, A., Slättberg, N., Lucke, J., Moser, M., Müller, H., and Wendisch, M.: Thermodynamic and cloud evolution in a cold-air outbreak during HALO-(AC)^3: quasi-Lagrangian observations compared to the ERA5 and CARRA reanalyses, Atmospheric Chemistry and Physics, 24, 3883–3904, doi:10.5194/acp-24-3883-2024, 2024.

Knobelspiesse, K., Tan, Q., Bruegge, C., Cairns, B., Chowdhary, J., van Diedenhoven, B., Diner, D., Ferrare, R., van Harten, G., Jovanovic, V., Ottaviani, M., Redemann, J., Seidel, F., and Sinclair, K.: Intercomparison of airborne multi-angle polarimeter observations from the Polarimeter Definition Experiment, Appl. Opt., 58, 650–669, doi:10.1364/AO.58.000650, 2019.

Kölling, T.: Cloud geometry for passive remote sensing, Ph.D. thesis, Ludwig-Maximilians-Universität München, URL `http://nbn-resolving.de/urn:nbn:de:bvb:19-261616`, 2020.

Kölling, T., Zinner, T., and Mayer, B.: Aircraft-based stereographic reconstruction of 3-D cloud geometry, Atmospheric Measurement Techniques, 12, 1155–1166, doi:10.5194/amt-12-1155-2019, 2019.

Kolstad, E. and Bracegirdle, T.: Marine cold-air outbreaks in the future: an assessment of IPCC AR4 model results for the Northern Hemisphere, Climate Dynamics, 30, 871–885, doi:10.1007/s00382-007-0331-0, 2008.

Kolstad, E. W., Bracegirdle, T. J., and Seierstad, I. A.: Marine cold-air outbreaks in the North Atlantic: temporal distribution and associations with large-scale atmospheric circulation, Climate Dynamics, 33, 187–197, doi:10.1007/s00382-008-0431-5, 2009.

Komurcu, M., Storelvmo, T., Tan, I., Lohmann, U., Yun, Y., Penner, J. E., Wang, Y., Liu, X., and Takemura, T.: Intercomparison of the cloud water phase among global climate models, Journal of Geophysical Research: Atmospheres, 119, 3372–3400, doi:10.1002/2013JD021119, 2014.

Kordecki, A., Palus, H., and Bal, A.: Practical vignetting correction method for digital camera with measurement of surface luminance distribution, SIViP, 10, 1417–1424, doi:10.1007/s11760-016-0941-2, 2016.

Korolev, A.: Limitations of the Wegener–Bergeron–Findeisen Mechanism in the Evolution of Mixed-Phase Clouds, Journal of the Atmospheric Sciences, 64, 3372 – 3375, doi:10.1175/JAS4035.1, 2007.

Korolev, A. and Leisner, T.: Review of experimental studies of secondary ice production, Atmospheric Chemistry and Physics, 20, 11 767–11 797, doi:10.5194/acp-20-11767-2020, 2020.

Korolev, A. and Milbrandt, J.: How Are Mixed-Phase Clouds Mixed?, Geophysical Research Letters, 49, e2022GL099 578, doi:10.1029/2022GL099578, e2022GL099578 2022GL099578,

2022.

Korolev, A., McFarquhar, G., Field, P. R., Franklin, C., Lawson, P., Wang, Z., Williams, E., Abel, S. J., Axisa, D., Borrmann, S., Crosier, J., Fugal, J., Krämer, M., Lohmann, U., Schlenczek, O., Schnaiter, M., and Wendisch, M.: Mixed-Phase Clouds: Progress and Challenges, Meteorological Monographs, 58, 5.1 – 5.50, doi:10.1175/AMSMONOGRAPHS-D-17-0001.1, 2017.

Krautstrunk, M. and Giez, A.: The Transition From FALCON to HALO Era Airborne Atmospheric Research, pp. 609–624, Springer Berlin Heidelberg, Berlin, Heidelberg, doi:10.1007/978-3-642-30183-4_37, 2012.

Kretzschmar, J., Salzmann, M., Mülmenstädt, J., and Quaas, J.: Arctic clouds in ECHAM6 and their sensitivity to cloud microphysics and surface fluxes, Atmospheric Chemistry and Physics, 19, 10 571–10 589, doi:10.5194/acp-19-10571-2019, 2019.

Kretzschmar, J., Stapf, J., Klocke, D., Wendisch, M., and Quaas, J.: Employing airborne radiation and cloud microphysics observations to improve cloud representation in ICON at kilometer-scale resolution in the Arctic, Atmospheric Chemistry and Physics, 20, 13 145–13 165, doi:10.5194/acp-20-13145-2020, 2020.

Lackner, C. P., Geerts, B., Juliano, T. W., Xue, L., and Kosovic, B.: Vertical Structure of Clouds and Precipitation During Arctic Cold-Air Outbreaks and Warm-Air Intrusions: Observations From COMBLE, Journal of Geophysical Research: Atmospheres, 128, 1–23, doi:10.1029/2022JD038403, 2023.

Lamb, D. and Verlinde, J.: Physics and Chemistry of Clouds, Cambridge University Press, 2011.

Landgren, O., Seierstad, I., and Iversen, T.: Projected future changes in Marine Cold-Air Outbreaks associated with Polar Lows in the Northern North-Atlantic Ocean, Climate Dynamics, 53, 2573–2585, doi:10.1007/s00382-019-04642-2, 2019.

Lane, C., Rode, D., and Rösgen, T.: Calibration of a polarization image sensor and investigation of influencing factors, Appl. Opt., 61, C37–C45, doi:10.1364/AO.437391, 2022.

Lee, J., Yang, P., Dessler, A., Baum, B., and Platnick, S.: The influence of thermodynamic phase on the retrieval of mixed-phase cloud microphysical and optical properties in the visible and near-infrared region, IEEE Geoscience and Remote Sensing Letters, 3, 287–291, doi:10.1109/LGRS.2006.864374, 2006.

Lensky, I. M. and Rosenfeld, D.: The time-space exchangeability of satellite retrieved relations between cloud top temperature and particle effective radius, Atmospheric Chemistry and Physics, 6, 2887–2894, doi:10.5194/acp-6-2887-2006, 2006.

Libbrecht, K. G.: Physical Dynamics of Ice Crystal Growth, Annual Review of Materials Research, 47, 271–295, doi:10.1146/annurev-matsci-070616-124135, 2017.

Liou, K.-N. and Yang, P.: Light Scattering by Ice Crystals, Cambridge University Press, 2016.

Lloyd, G., Choularton, T. W., Bower, K. N., Gallagher, M. W., Crosier, J., O'Shea, S., Abel, S. J., Fox, S., Cotton, R., and Boutle, I. A.: In situ measurements of cloud microphysical and aerosol properties during the break-up of stratocumulus cloud layers in cold air outbreaks over the North Atlantic, Atmospheric Chemistry and Physics, 18, 17 191–17 206, doi:10.5194/acp-18-17191-2018, 2018.

Loeb, N. G., Yang, P., Rose, F. G., Hong, G., Sun-Mack, S., Minnis, P., Kato, S., Ham, S.-H., Smith, W. L., Hioki, S., and Tang, G.: Impact of Ice Cloud Microphysics on Satellite Cloud Retrievals and Broadband Flux Radiative Transfer Model Calculations, Journal of Climate, 31, 1851 – 1864, doi:10.1175/JCLI-D-17-0426.1, 2018.

Lohmann, U., Lüönd, F., and Mahrt, F.: An Introduction to Clouds: From the Microscale to Climate, Cambridge University Press, doi:10.1017/CBO9781139087513, 2016.

LUCID Vision Labs Inc.: Phoenix 5.0 MP Polarization Model (IMX250MZR/MYR), URL `https://thinklucid.com/product/phoenix-5-0-mp-polarized-model/`, last accessed: 2023-07-17, 2023.

Ludwig, V., Spreen, G., and Pedersen, L. T.: Evaluation of a New Merged Sea-Ice Concentration Dataset at 1 km Resolution from Thermal Infrared and Passive Microwave Satellite Data in the Arctic, Remote Sensing, 12, doi:10.3390/rs12193183, 2020.

Maahn, M., Goren, T., Shupe, M. D., and de Boer, G.: Liquid Containing Clouds at the North Slope of Alaska Demonstrate Sensitivity to Local Industrial Aerosol Emissions, Geophysical Research Letters, 48, e2021GL094 307, doi:10.1029/2021GL094307, e2021GL094307 2021GL094307, 2021.

Mages, Z., Kollias, P., Zhu, Z., and Luke, E. P.: Surface-based observations of cold-air outbreak clouds during the COMBLE field campaign, Atmospheric Chemistry and Physics, 23, 3561–3574, doi:10.5194/acp-23-3561-2023, 2023.

Maherndl, N., Moser, M., Lucke, J., Mech, M., Risse, N., Schirmacher, I., and Maahn, M.: Quantifying riming from airborne data during the HALO-$(AC)^3$ campaign, Atmospheric Measurement Techniques, 17, 1475–1495, doi:10.5194/amt-17-1475-2024, 2024a.

Maherndl, N., Moser, M., Schirmacher, I., Bansemer, A., Lucke, J., Voigt, C., and Maahn, M.: How does riming influence the observed spatial variability of ice water in mixed-phase clouds?, Atmospheric Chemistry and Physics, 24, 13 935–13 960, doi:10.5194/acp-24-13935-2024, 2024b.

Marchant, B., Platnick, S., Meyer, K., and Wind, G.: Evaluation of the MODIS Collection 6 multilayer cloud detection algorithm through comparisons with CloudSat Cloud Profiling Radar and CALIPSO CALIOP products, Atmospheric Measurement Techniques, 13, 3263–3275, doi:10.5194/amt-13-3263-2020, 2020.

Marchuk, G. I., Mikhailov, G. A., Nazaraliev, M. A., Darbinjan, R. A., Kargin, B. A., and Elepov, B. S.: The Monte Carlo Methods in Atmospheric Optics, Springer, Berlin, Heidelberg, doi:10.1007/978-3-540-35237-2, 1980.

Marshak, A. and Davis, A.: 3D Radiative Transfer in Cloudy Atmospheres, Springer, iSBN-13 978-3-540-23958-1, 2005.

Marshak, A., Davis, A., Wiscombe, W., and Cahalan, R.: Radiative smoothing in fractal clouds, Journal of Geophysical Research: Atmospheres, 100, 26 247–26 261, doi:10.1029/95JD02895, 1995.

Martin, G. M., Johnson, D. W., and Spice, A.: The Measurement and Parameterization of Effective Radius of Droplets in Warm Stratocumulus Clouds, Journal of Atmospheric Sciences, 51, 1823 – 1842, doi:10.1175/1520-0469(1994)051<1823:TMAPOE>2.0.CO;2, 1994.

Martins, J. V., Fernandez-Borda, R., McBride, B., Remer, L., and Barbosa, H. M. J.: The Harp Hype Ran Gular Imaging Polarimeter and the Need for Small Satellite Payloads with High Science Payoff for Earth Science Remote Sensing, in: IGARSS 2018 - 2018 IEEE International Geoscience and Remote Sensing Symposium, pp. 6304–6307, doi:10.1109/IGARSS.2018.8518823, 2018.

Mateling, M. E., Pettersen, C., Kulie, M. S., and L'Ecuyer, T. S.: Marine Cold-Air Outbreak Snowfall in the North Atlantic: A CloudSat Perspective, Journal of Geophysical Research: Atmospheres, 128, 1–20, doi:10.1029/2022JD038053, 2023.

Matus, A. V. and L'Ecuyer, T. S.: The role of cloud phase in Earth's radiation budget, Journal of Geophysical Research: Atmospheres, 122, 2559–2578, doi:10.1002/2016JD025951, 2017.

Mayer, B.: Radiative transfer in the cloudy atmosphere, EPJ Web of Conferences, 1, 75–99, doi:10.1140/epjconf/e2009-00912-1, 2009.

Mayer, B. and Kylling, A.: Technical note: The libRadtran software package for radiative transfer calculations - description and examples of use, Atmospheric Chemistry and Physics, 5, 1855–1877, doi:10.5194/acp-5-1855-2005, 2005.

Mayer, J., Bugliaro, L., Mayer, B., Piontek, D., and Voigt, C.: Bayesian cloud-top phase determination for Meteosat Second Generation, Atmospheric Measurement Techniques, 17, 4015–4039, doi:10.5194/amt-17-4015-2024, 2024.

McCoy, D. T., Hartmann, D. L., Zelinka, M. D., Ceppi, P., and Grosvenor, D. P.: Mixed-phase cloud physics and Southern Ocean cloud feedback in climate models, Journal of Geophysical Research: Atmospheres, 120, 9539–9554, doi:10.1002/2015JD023603, 2015.

McCoy, I. L., Wood, R., and Fletcher, J. K.: Identifying Meteorological Controls on Open and Closed Mesoscale Cellular Convection Associated with Marine Cold Air Outbreaks, Journal of Geophysical Research: Atmospheres, 122, 11,678–11,702, doi:10.1002/2017JD027031, 2017.

McFarquhar, G. M. and Heymsfield, A. J.: The Definition and Significance of an Effective Radius for Ice Clouds, Journal of the Atmospheric Sciences, 55, 2039 – 2052, doi:10.1175/1520-0469(1998)055<2039:TDASOA>2.0.CO;2, 1998.

McFarquhar, G. M., Zhang, G., Poellot, M. R., Kok, G. L., McCoy, R., Tooman, T., Fridlind, A., and Heymsfield, A. J.: Ice properties of single-layer stratocumulus during the Mixed-Phase Arctic Cloud Experiment: 1. Observations, Journal of Geophysical Research: Atmospheres, 112, doi:10.1029/2007JD008633, 2007.

McFarquhar, G. M., Baumgardner, D., Bansemer, A., Abel, S. J., Crosier, J., French, J., Rosenberg, P., Korolev, A., Schwarzoenboeck, A., Leroy, D., Um, J., Wu, W., Heymsfield, A. J., Twohy, C., Detwiler, A., Field, P., Neumann, A., Cotton, R., Axisa, D., and Dong, J.: Processing of Ice Cloud In Situ Data Collected by Bulk Water, Scattering, and Imaging Probes: Fundamentals, Uncertainties, and Efforts toward Consistency, Meteorological Monographs, 58, 11.1 – 11.33, doi:10.1175/AMSMONOGRAPHS-D-16-0007.1, 2017.

Mech, M., Orlandi, E., Crewell, S., Ament, F., Hirsch, L., Hagen, M., Peters, G., and Stevens, B.: HAMP – the microwave package on the High Altitude and LOng range research aircraft (HALO), Atmospheric Measurement Techniques, 7, 4539–4553, doi:10.5194/amt-7-4539-2014, 2014.

Merk, D., Deneke, H., Pospichal, B., and Seifert, P.: Investigation of the adiabatic assumption for estimating cloud micro- and macrophysical properties from satellite and ground observations, Atmospheric Chemistry and Physics, 16, 933–952, doi:10.5194/acp-16-933-2016, 2016.

Meyer, D., Hogan, R. J., Dueben, P. D., and Mason, S. L.: Machine Learning Emulation of 3D Cloud Radiative Effects, Journal of Advances in Modeling Earth Systems, 14, 1–13, doi:https://doi.org/10.1029/2021MS002550, 2022.

Meyer, F.: Topographic distance and watershed lines, Signal Processing, 38, 113–125, doi:10.1016/0165-1684(94)90060-4, mathematical Morphology and its Applications to Signal Processing, 1994.

Michaelis, J., Schmitt, A. U., Lüpkes, C., Hartmann, J., Birnbaum, G., and Vihma, T.: Observations of marine cold-air outbreaks: a comprehensive data set of airborne and dropsonde measurements from the Springtime Atmospheric Boundary Layer Experiment (STABLE), Earth System Science Data, 14, 1621–1637, doi:10.5194/essd-14-1621-2022, 2022.

Mie, G.: Beiträge zur Optik trüber Medien, speziell kolloidaler Metallösungen, Annalen der Physik, 330, 377–445, doi:10.1002/andp.19083300302, 1908.

Mihoubi, S., Lapray, P.-J., and Bigué, L.: Survey of Demosaicking Methods for Polarization Filter Array Images, Sensors, 18, doi:10.3390/s18113688, 2018.

Min, Q., Joseph, E., Lin, Y., Min, L., Yin, B., Daum, P. H., Kleinman, L. I., Wang, J., and Lee, Y.-N.: Comparison of MODIS cloud microphysical properties with in-situ measurements over the Southeast Pacific, Atmospheric Chemistry and Physics, 12, 11 261–11 273, doi:10.5194/acp-12-11261-2012, 2012.

Mioche, G., Jourdan, O., Ceccaldi, M., and Delanoë, J.: Variability of mixed-phase clouds in the Arctic with a focus on the Svalbard region: a study based on spaceborne active remote sensing, Atmospheric Chemistry and Physics, 15, 2445–2461, doi:10.5194/acp-15-2445-2015, 2015.

Mioche, G., Jourdan, O., Delanoë, J., Gourbeyre, C., Febvre, G., Dupuy, R., Monier, M., Szczap, F., Schwarzenboeck, A., and Gayet, J.-F.: Vertical distribution of microphysical properties of Arctic springtime low-level mixed-phase clouds over the Greenland and

Norwegian seas, Atmospheric Chemistry and Physics, 17, 12 845–12 869, doi:10.5194/acp-17-12845-2017, 2017.

Mishchenko, M., Travis, L., and Lacis, A.: Scattering, Absorption, and Emission of Light by Small Particles, Cambridge University Press, third electronic release edn., 2002.

Mitchell, D. L.: Evolution of Snow-Size Spectra in Cyclonic Storms. Part I: Snow Growth by Vapor Deposition and Aggregation, Journal of Atmospheric Sciences, 45, 3431 – 3451, doi:10.1175/1520-0469(1988)045<3431:EOSSSI>2.0.CO;2, 1988.

Morimatsu, M., Monno, Y., Tanaka, M., and Okutomi, M.: Monochrome And Color Polarization Demosaicking Using Edge-Aware Residual Interpolation, in: 2020 IEEE International Conference on Image Processing (ICIP), pp. 2571–2575, doi:10.1109/ICIP40778.2020.9191085, 2020.

Morrison, H., Thompson, G., and Tatarskii, V.: Impact of Cloud Microphysics on the Development of Trailing Stratiform Precipitation in a Simulated Squall Line: Comparison of One- and Two-Moment Schemes, Monthly Weather Review, 137, 991–1007, doi:10.1175/2008mwr2556.1, 2009.

Morrison, H., De Boer, G., Feingold, G., Harrington, J., Shupe, M., and Sulia, K.: Resilience of persistent Arctic mixed-phase clouds, Nature Geoscience, 5, 11–17, doi:10.1038/ngeo1332, 2012.

Moser, M., Lucke, J., De La Torre Castro, E., Mayer, J., and Voigt, C.: DLR in situ cloud measurements during HALO-(AC)^3 Arctic airborne campaign, doi:10.1594/PANGAEA.963247, 2023.

Moser, M., Voigt, C., Jurkat-Witschas, T., Hahn, V., Mioche, G., Jourdan, O., Dupuy, R., Gourbeyre, C., Schwarzenboeck, A., Lucke, J., Boose, Y., Mech, M., Borrmann, S., Ehrlich, A., Herber, A., Lüpkes, C., and Wendisch, M.: Microphysical and thermodynamic phase analyses of Arctic low-level clouds measured above the sea ice and the open ocean in spring and summer, Atmospheric Chemistry and Physics, 23, 7257–7280, doi:10.5194/acp-23-7257-2023, 2023.

Moser, M., Voigt, C., Eppers, O., Lucke, J., De La Torre Castro, E., Mayer, J., Dupuy, R., Mioche, G., Jourdan, O., Clemen, H.-C., Schneider, J., Joppe, P., Mertes, S., Wetzel, B., Borrmann, S., Klingebiel, M., Mech, M., Lüpkes, C., Crewell, S., Ehrlich, A., Herber, A., and Wendisch, M.: The Arctic Low-Level Mixed-Phase Haze Regime and its Microphysical Differences to Mixed-Phase Clouds, EGUsphere, 2025, 1–33, doi:10.5194/egusphere-2025-3876, 2025.

Murphy, D. M. and Koop, T.: Review of the vapour pressures of ice and supercooled water for atmospheric applications, Quarterly Journal of the Royal Meteorological Society, 131, 1539–1565, doi:10.1256/qj.04.94, 2005.

Murray-Watson, R. J., Gryspeerdt, E., and Goren, T.: Investigating the development of clouds within marine cold-air outbreaks, Atmospheric Chemistry and Physics, 23, 9365–9383, doi:10.5194/acp-23-9365-2023, 2023.

Nakajima, T. and King, M. D.: Determination of the Optical Thickness and Effec-

tive Particle Radius of Clouds from Reflected Solar Radiation Measurements. Part I: Theory, Journal of Atmospheric Sciences, 47, 1878 – 1893, doi:10.1175/1520-0469(1990)047<1878:DOTOTA>2.0.CO;2, 1990.

Nakanishi, M. and Niino, H.: An Improved Mellor–Yamada Level-3 Model: Its Numerical Stability and Application to a Regional Prediction of Advection Fog, Boundary-Layer Meteorology, 119, 397–407, doi:10.1007/s10546-005-9030-8, 2006.

Nakanishi, M. and Niino, H.: Development of an Improved Turbulence Closure Model for the Atmospheric Boundary Layer, Journal of the Meteorological Society of Japan. Ser. II, 87, 895–912, doi:10.2151/jmsj.87.895, 2009.

Nash, D., Waliser, D., Guan, B., Ye, H., and Ralph, F. M.: The Role of Atmospheric Rivers in Extratropical and Polar Hydroclimate, Journal of Geophysical Research: Atmospheres, 123, 6804–6821, doi:10.1029/2017JD028130, 2018.

Olson, J. B., Kenyon, J. S., Angevine, W. A., Brown, J. M., Pagowski, M., and Sušelj, K.: A Description of the MYNN-EDMF Scheme and the Coupling to Other Components in WRF–ARW, doi:10.25923/N9WM-BE49, 2019.

Overland, J., Dunlea, E., Box, J. E., Corell, R., Forsius, M., Kattsov, V., Olsen, M. S., Pawlak, J., Reiersen, L.-O., and Wang, M.: The urgency of Arctic change, Polar Science, 21, 6–13, doi:10.1016/j.polar.2018.11.008, iSAR-5/ Fifth International Symposium on Arctic Research, 2019.

Painemal, D. and Zuidema, P.: Assessment of MODIS cloud effective radius and optical thickness retrievals over the Southeast Pacific with VOCALS-REx in situ measurements, Journal of Geophysical Research: Atmospheres, 116, doi:10.1029/2011JD016155, 2011.

Papritz, L. and Spengler, T.: A Lagrangian Climatology of Wintertime Cold Air Outbreaks in the Irminger and Nordic Seas and Their Role in Shaping Air–Sea Heat Fluxes, Journal of Climate, 30, 2717 – 2737, doi:10.1175/JCLI-D-16-0605.1, 2017.

Pawlowska, H. and Brenguier, J.-L.: Microphysical properties of stratocumulus clouds during ACE-2, Tellus B, 52, 868–887, doi:10.1034/j.1600-0889.2000.00076.x, 2000.

Petty, G. W.: A First Course in Atmospheric Radiation, Sundog Publishing, second edition edn., 2006.

Pithan, F. and Mauritsen, T.: Arctic amplification dominated by temperature feedbacks in contemporary climate models, Nature Geoscience, 7, 181–184, doi:10.1038/ngeo2071, 2014.

Pithan, F., Medeiros, B., and Mauritsen, T.: Mixed-phase clouds cause climate model biases in Arctic wintertime temperature inversions, Climate Dynamics, doi:10.1007/s00382-013-1964-9, 2014.

Pithan, F., Ackerman, A., Angevine, W. M., Hartung, K., Ickes, L., Kelley, M., Medeiros, B., Sandu, I., Steeneveld, G.-J., Sterk, H. A. M., Svensson, G., Vaillancourt, P. A., and Zadra, A.: Select strengths and biases of models in representing the Arctic winter boundary layer over sea ice: the Larcform 1 single column model intercomparison, Journal of Advances in Modeling Earth Systems, 8, 1345–1357, doi:10.1002/2016MS000630, 2016.

Pithan, F., Svensson, G., Caballero, R., Chechin, D., Cronin, T. W., Ekman, A. M. L., Neggers, R., Shupe, M. D., Solomon, A., Tjernström, M., and Wendisch, M.: Role of air-mass transformations in exchange between the Arctic and mid-latitudes, Nature Geoscience, 11, 805–812, doi:10.1038/s41561-018-0234-1, 2018.

Platnick, S.: Vertical photon transport in cloud remote sensing problems, Journal of Geophysical Research: Atmospheres, 105, 22 919–22 935, doi:10.1029/2000JD900333, 2000.

Pörtge, V., Kölling, T., Weber, A., Volkmer, L., Emde, C., Zinner, T., Forster, L., and Mayer, B.: High-spatial-resolution retrieval of cloud droplet size distribution from polarized observations of the cloudbow, Atmospheric Measurement Techniques, 16, 645–667, doi:10.5194/amt-16-645-2023, 2023.

Pörtge, V. T.: Understanding cloud droplet size distributions from multi-angle polarimetric observations, URL `http://nbn-resolving.de/urn:nbn:de:bvb:19-340021`, 2024.

Powell, S. B. and Gruev, V.: Calibration methods for division-of-focal-plane polarimeters, Opt. Express, 21, 21 039–21 055, doi:10.1364/OE.21.021039, 2013.

Previdi, M., Smith, K. L., and Polvani, L. M.: Arctic amplification of climate change: a review of underlying mechanisms, Environmental Research Letters, 16, 093 003, doi:10.1088/1748-9326/ac1c29, 2021.

Pruppacher, H. R. and Klett, J. D.: Microphysics of Clouds and Precipitation, Kluwer Academic Publishers, Dordrecht, 2nd rev. and enl. edn., 1997.

Rammeloo, C. and Baumgartner, A.: Spectroradiometer Calibration for Radiance Transfer Measurements, Sensors, 23, doi:10.3390/s23042339, 2023.

Rantanen, M., Karpechko, A. Y., Lipponen, A., Nordling, K., Hyvärinen, O., Ruosteenoja, K., Vihma, T., and Laaksonen, A.: The Arctic has warmed nearly four times faster than the globe since 1979, Communications Earth & Environment, 3, doi:10.1038/s43247-022-00498-3, 2022.

Ratliff, B. M., LaCasse, C. F., and Tyo, J. S.: Interpolation strategies for reducing IFOV artifacts in microgrid polarimeter imagery, Opt. Express, 17, 9112–9125, doi:10.1364/OE.17.009112, 2009.

Riedi, J., Marchant, B., Platnick, S., Baum, B. A., Thieuleux, F., Oudard, C., Parol, F., Nicolas, J.-M., and Dubuisson, P.: Cloud thermodynamic phase inferred from merged POLDER and MODIS data, Atmospheric Chemistry and Physics, 10, 11 851–11 865, doi:10.5194/acp-10-11851-2010, 2010.

Rodriguez, J., Lew-Yan-Voon, L., Martins, R., and Morel, O.: A Practical Calibration Method for RGB Micro-Grid Polarimetric Cameras, IEEE Robotics and Automation Letters, 7, 9921–9928, doi:10.1109/LRA.2022.3192655, 2022.

Rogers, R. R. and Yau, M. K.: A Short Course in Cloud Physics, Butterworth-Heinemann, third edition edn., 1989.

Rosenfeld, D. and Lensky, I. M.: Satellite-Based Insights into Precipitation Formation Pro-

cesses in Continental and Maritime Convective Clouds, Bulletin of the American Meteorological Society, 79, 2457 – 2476, doi:10.1175/1520-0477(1998)079<2457:SBIIPF>2.0.CO;2, 1998.

Ruiz-Donoso, E., Ehrlich, A., Schäfer, M., Jäkel, E., Schemann, V., Crewell, S., Mech, M., Kulla, B. S., Kliesch, L.-L., Neuber, R., and Wendisch, M.: Small-scale structure of thermodynamic phase in Arctic mixed-phase clouds observed by airborne remote sensing during a cold air outbreak and a warm air advection event, Atmospheric Chemistry and Physics, 20, 5487–5511, doi:10.5194/acp-20-5487-2020, 2020.

Sanchez, K. J., Zhang, B., Liu, H., Brown, M. D., Crosbie, E. C., Gallo, F., Hair, J. W., Hostetler, C. A., Jordan, C. E., Robinson, C. E., Scarino, A. J., Shingler, T. J., Shook, M. A., Thornhill, K. L., Wiggins, E. B., Winstead, E. L., Ziemba, L. D., Saliba, G., Lewis, S. L., Russell, L. M., Quinn, P. K., Bates, T. S., Porter, J., Bell, T. G., Gaube, P., Saltzman, E. S., Behrenfeld, M. J., and Moore, R. H.: North Atlantic Ocean SST-gradient-driven variations in aerosol and cloud evolution along Lagrangian cold-air outbreak trajectories, Atmospheric Chemistry and Physics, 22, 2795–2815, doi:10.5194/acp-22-2795-2022, 2022.

Sandu, I. and Stevens, B.: On the Factors Modulating the Stratocumulus to Cumulus Transitions, Journal of the Atmospheric Sciences, 68, 1865 – 1881, doi:10.1175/2011JAS3614.1, 2011.

Sato, Y., Miura, H., Yashiro, H., Goto, D., Takemura, T., Tomita, H., and Nakajima, T.: Unrealistically pristine air in the Arctic produced by current global scale models, Scientific Reports, 6, doi:10.1038/srep26561, 2016.

Schäfer, M., Bierwirth, E., Ehrlich, A., Jäkel, E., Werner, F., and Wendisch, M.: Directional, horizontal inhomogeneities of cloud optical thickness fields retrieved from ground-based and airbornespectral imaging, Atmospheric Chemistry and Physics, 17, 2359–2372, doi:10.5194/acp-17-2359-2017, 2017.

Schäfer, M., Loewe, K., Ehrlich, A., Hoose, C., and Wendisch, M.: Simulated and observed horizontal inhomogeneities of optical thickness of Arctic stratus, Atmospheric Chemistry and Physics, 18, 13 115–13 133, doi:10.5194/acp-18-13115-2018, 2018.

Schäfer, M., Wolf, K., Ehrlich, A., Hallbauer, C., Jäkel, E., Jansen, F., Luebke, A. E., Müller, J., Thoböll, J., Röschenthaler, T., Stevens, B., and Wendisch, M.: VELOX – a new thermal infrared imager for airborne remote sensing of cloud and surface properties, Atmospheric Measurement Techniques, 15, 1491–1509, doi:10.5194/amt-15-1491-2022, 2022.

Schäfer, M., Rosenburg, S., Ehrlich, A., Röttenbacher, J., and Wendisch, M.: Two-dimensional cloud-top and surface brightness temperature with 1 Hz temporal resolution derived at flight altitude from VELOX during the HALO-$(AC)^3$ field campaign, doi:10.1594/PANGAEA.963401, 2023.

Scheck, L.: A neural network based forward operator for visible satellite images and its adjoint, Journal of Quantitative Spectroscopy and Radiative Transfer, 274, 107 841,

doi:10.1016/j.jqsrt.2021.107841, 2021.

Scheck, L., Weissmann, M., and Mayer, B.: Efficient Methods to Account for Cloud-Top Inclination and Cloud Overlap in Synthetic Visible Satellite Images, Journal of Atmospheric and Oceanic Technology, 35, 665 – 685, doi:10.1175/JTECH-D-17-0057.1, 2018.

Schirmacher, I., Schnitt, S., Klingebiel, M., Maherndl, N., Kirbus, B., Ehrlich, A., Mech, M., and Crewell, S.: Clouds and precipitation in the initial phase of marine cold-air outbreaks as observed by airborne remote sensing, Atmospheric Chemistry and Physics, 24, 12 823–12 842, doi:10.5194/acp-24-12823-2024, 2024.

Schmale, J., Arnold, S. R., Law, K. S., Thorp, T., Anenberg, S., Simpson, W. R., Mao, J., and Pratt, K. A.: Local Arctic Air Pollution: A Neglected but Serious Problem, Earth's Future, 6, 1385–1412, doi:10.1029/2018EF000952, 2018.

Schäfer, S. A. K., Hogan, R. J., Klinger, C., Chiu, J. C., and Mayer, B.: Representing 3-D cloud radiation effects in two-stream schemes: 1. Longwave considerations and effective cloud edge length, Journal of Geophysical Research: Atmospheres, 121, 8567–8582, doi:10.1002/2016JD024876, 2016.

Screen, J. A.: An ice-free Arctic: what could it mean for European weather?, Weather, 76, 327–328, doi:10.1002/wea.4069, 2021.

Seppala, H., Zhang, Z., and Zheng, X.: Developing a Lagrangian Frame Transformation on Satellite Data to Study Cloud Microphysical Transitions in Arctic Marine Cold Air Outbreaks, Geophysical Research Letters, 52, 1–10, doi:10.1029/2025GL115637, 2025.

Serreze, M. and Francis, J.: The Arctic Amplification Debate, Climate Change, 76, 241–264, doi:10.1007/s10584-005-9017-y, 2006.

Serreze, M. C. and Barry, R. G.: Processes and impacts of Arctic amplification: A research synthesis, Global and Planetary Change, 77, 85–96, doi:10.1016/j.gloplacha.2011.03.004, 2011.

Shang, H., Chen, L., Bréon, F. M., Letu, H., Li, S., Wang, Z., and Su, L.: Impact of cloud horizontal inhomogeneity and directional sampling on the retrieval of cloud droplet size by the POLDER instrument, Atmospheric Measurement Techniques, 8, 4931–4945, doi:10.5194/amt-8-4931-2015, 2015.

Shupe, M. D.: Clouds at Arctic Atmospheric Observatories. Part II: Thermodynamic Phase Characteristics, Journal of Applied Meteorology and Climatology, 50, 645 – 661, doi:10.1175/2010JAMC2468.1, 2011.

Shupe, M. D., Matrosov, S. Y., and Uttal, T.: Arctic Mixed-Phase Cloud Properties Derived from Surface-Based Sensors at SHEBA, Journal of the Atmospheric Sciences, 63, 697 – 711, doi:10.1175/JAS3659.1, 2006.

Shupe, M. D., Rex, M., Blomquist, B., Persson, P. O. G., Schmale, J., Uttal, T., Althausen, D., Angot, H., Archer, S., Bariteau, L., Beck, I., Bilberry, J., Bucci, S., Buck, C., Boyer, M., Brasseur, Z., Brooks, I. M., Calmer, R., Cassano, J., Castro, V., Chu, D., Costa, D., Cox, C. J., Creamean, J., Crewell, S., Dahlke, S., Damm, E., de Boer, G., Deckelmann,

H., Dethloff, K., Dütsch, M., Ebell, K., Ehrlich, A., Ellis, J., Engelmann, R., Fong, A. A., Frey, M. M., Gallagher, M. R., Ganzeveld, L., Gradinger, R., Graeser, J., Greenamyer, V., Griesche, H., Griffiths, S., Hamilton, J., Heinemann, G., Helmig, D., Herber, A., Heuzé, C., Hofer, J., Houchens, T., Howard, D., Inoue, J., Jacobi, H.-W., Jaiser, R., Jokinen, T., Jourdan, O., Jozef, G., King, W., Kirchgaessner, A., Klingebiel, M., Krassovski, M., Krumpen, T., Lampert, A., Landing, W., Laurila, T., Lawrence, D., Lonardi, M., Loose, B., Lüpkes, C., Maahn, M., Macke, A., Maslowski, W., Marsay, C., Maturilli, M., Mech, M., Morris, S., Moser, M., Nicolaus, M., Ortega, P., Osborn, J., Pätzold, F., Perovich, D. K., Petäjä, T., Pilz, C., Pirazzini, R., Posman, K., Powers, H., Pratt, K. A., Preußer, A., Quéléver, L., Radenz, M., Rabe, B., Rinke, A., Sachs, T., Schulz, A., Siebert, H., Silva, T., Solomon, A., Sommerfeld, A., Spreen, G., Stephens, M., Stohl, A., Svensson, G., Uin, J., Viegas, J., Voigt, C., von der Gathen, P., Wehner, B., Welker, J. M., Wendisch, M., Werner, M., Xie, Z., and Yue, F.: Overview of the MOSAiC expedition: Atmosphere, Elementa: Science of the Anthropocene, 10, 00 060, doi:10.1525/elementa.2021.00060, 2022.

Skamarock, W. C., Klemp, J. B., Dudhia, J., Gill, D. O., Liu, Z., Berner, J., Wang, W., Powers, J. G., Duda, M. G., Barker, D. M., and Huang, X.-Y.: A Description of the Advanced Research WRF Model Version 4, Tech. rep., doi:10.5065/1DFH-6P97, 2019.

Smit, J. M., Rietjens, J. H. H., van Harten, G., Noia, A. D., Laauwen, W., Rheingans, B. E., Diner, D. J., Cairns, B., Wasilewski, A., Knobelspiesse, K. D., Ferrare, R., and Hasekamp, O. P.: SPEX airborne spectropolarimeter calibration and performance, Appl. Opt., 58, 5695–5719, doi:10.1364/AO.58.005695, 2019.

Smith, D. M., Screen, J. A., Deser, C., Cohen, J., Fyfe, J. C., García-Serrano, J., Jung, T., Kattsov, V., Matei, D., Msadek, R., Peings, Y., Sigmond, M., Ukita, J., Yoon, J.-H., and Zhang, X.: The Polar Amplification Model Intercomparison Project (PAMIP) contribution to CMIP6: investigating the causes and consequences of polar amplification, Geoscientific Model Development, 12, 1139–1164, doi:10.5194/gmd-12-1139-2019, 2019.

Smith, E. and Sheridan, S.: Projections of cold air outbreaks in CMIP6 earth system models, Climatic Change, 169, doi:10.1007/s10584-021-03259-x, 2021.

Sokolowsky, G. A., Freeman, S. W., Jones, W. K., Kukulies, J., Senf, F., Marinescu, P. J., Heikenfeld, M., Brunner, K. N., Bruning, E. C., Collis, S. M., Jackson, R. C., Leung, G. R., Pfeifer, N., Raut, B. A., Saleeby, S. M., Stier, P., and van den Heever, S. C.: *tobac* v1.5: introducing fast 3D tracking, splits and mergers, and other enhancements for identifying and analysing meteorological phenomena, Geoscientific Model Development, 17, 5309–5330, doi:10.5194/gmd-17-5309-2024, 2024.

Solomon, A., Shupe, M. D., Svensson, G., Barton, N. P., Batrak, Y., Bazile, E., Day, J. J., Doyle, J. D., Frank, H. P., Keeley, S., Remes, T., and Tolstykh, M.: The winter central Arctic surface energy budget: A model evaluation using observations from the MOSAiC campaign, Elementa: Science of the Anthropocene, 11, 00 104, doi:10.1525/elementa.2022.00104, 2023.

Sony Semiconductor Solutions Corporation: Polarization Image Sensor, URL `https:`

//www.sony-semicon.com/en/products/is/industry/polarization.html, last accessed: 2023-07-17, 2023.

Sotiropoulou, G., Sedlar, J., Tjernström, M., Shupe, M. D., Brooks, I. M., and Persson, P. O. G.: The thermodynamic structure of summer Arctic stratocumulus and the dynamic coupling to the surface, Atmospheric Chemistry and Physics, 14, 12 573–12 592, doi:10.5194/acp-14-12573-2014, 2014.

Spensberger, C. and Spengler, T.: Sensitivity of Air-Sea Heat Exchange in Cold-Air Outbreaks to Model Resolution and Sea-Ice Distribution, Journal of Geophysical Research: Atmospheres, 126, 1–13, doi:10.1029/2020JD033610, 2021.

Sprenger, M. and Wernli, H.: The LAGRANTO Lagrangian analysis tool – version 2.0, Geoscientific Model Development, 8, 2569–2586, doi:10.5194/gmd-8-2569-2015, 2015.

Stevens, B., Cotton, W. R., Feingold, G., and Moeng, C.-H.: Large-Eddy Simulations of Strongly Precipitating, Shallow, Stratocumulus-Topped Boundary Layers, Journal of the Atmospheric Sciences, 55, 3616 – 3638, doi:10.1175/1520-0469(1998)055<3616:LESOSP>2.0.CO;2, 1998.

Stevens, B., Ament, F., Bony, S., Crewell, S., Ewald, F., Gross, S., Hansen, A., Hirsch, L., Jacob, M., Kölling, T., Konow, H., Mayer, B., Wendisch, M., Wirth, M., Wolf, K., Bakan, S., Bauer-Pfundstein, M., Brueck, M., Delanoë, J., Ehrlich, A., Farrell, D., Forde, M., Gödde, F., Grob, H., Hagen, M., Jäkel, E., Jansen, F., Klepp, C., Klingebiel, M., Mech, M., Peters, G., Rapp, M., Wing, A. A., and Zinner, T.: A High-Altitude Long-Range Aircraft Configured as a Cloud Observatory: The NARVAL Expeditions, Bulletin of the American Meteorological Society, 100, 1061 – 1077, doi:10.1175/BAMS-D-18-0198.1, 2019.

Stevens, B., Bony, S., Farrell, D., Ament, F., Blyth, A., Fairall, C., Karstensen, J., Quinn, P. K., Speich, S., Acquistapace, C., Aemisegger, F., Albright, A. L., Bellenger, H., Bodenschatz, E., Caesar, K.-A., Chewitt-Lucas, R., de Boer, G., Delanoë, J., Denby, L., Ewald, F., Fildier, B., Forde, M., George, G., Gross, S., Hagen, M., Hausold, A., Heywood, K. J., Hirsch, L., Jacob, M., Jansen, F., Kinne, S., Klocke, D., Kölling, T., Konow, H., Lothon, M., Mohr, W., Naumann, A. K., Nuijens, L., Olivier, L., Pincus, R., Pöhlker, M., Reverdin, G., Roberts, G., Schnitt, S., Schulz, H., Siebesma, A. P., Stephan, C. C., Sullivan, P., Touzé-Peiffer, L., Vial, J., Vogel, R., Zuidema, P., Alexander, N., Alves, L., Arixi, S., Asmath, H., Bagheri, G., Baier, K., Bailey, A., Baranowski, D., Baron, A., Barrau, S., Barrett, P. A., Batier, F., Behrendt, A., Bendinger, A., Beucher, F., Bigorre, S., Blades, E., Blossey, P., Bock, O., Böing, S., Bosser, P., Bourras, D., Bouruet-Aubertot, P., Bower, K., Branellec, P., Branger, H., Brennek, M., Brewer, A., Brilouet, P.-E., Brügmann, B., Buehler, S. A., Burke, E., Burton, R., Calmer, R., Canonici, J.-C., Carton, X., Cato Jr., G., Charles, J. A., Chazette, P., Chen, Y., Chilinski, M. T., Choularton, T., Chuang, P., Clarke, S., Coe, H., Cornet, C., Coutris, P., Couvreux, F., Crewell, S., Cronin, T., Cui, Z., Cuypers, Y., Daley, A., Damerell, G. M., Dauhut, T., Deneke, H., Desbios, J.-P., Dörner, S., Donner, S., Douet, V., Drushka, K., Dütsch, M., Ehrlich, A., Emanuel, K., Emmanouilidis, A., Etienne, J.-C., Etienne-Leblanc, S., Faure, G., Feingold,

G., Ferrero, L., Fix, A., Flamant, C., Flatau, P. J., Foltz, G. R., Forster, L., Furtuna, I., Gadian, A., Galewsky, J., Gallagher, M., Gallimore, P., Gaston, C., Gentemann, C., Geyskens, N., Giez, A., Gollop, J., Gouirand, I., Gourbeyre, C., de Graaf, D., de Groot, G. E., Grosz, R., Güttler, J., Gutleben, M., Hall, K., Harris, G., Helfer, K. C., Henze, D., Herbert, C., Holanda, B., Ibanez-Landeta, A., Intrieri, J., Iyer, S., Julien, F., Kalesse, H., Kazil, J., Kellman, A., Kidane, A. T., Kirchner, U., Klingebiel, M., Körner, M., Kremper, L. A., Kretzschmar, J., Krüger, O., Kumala, W., Kurz, A., L'Hégaret, P., Labaste, M., Lachlan-Cope, T., Laing, A., Landschützer, P., Lang, T., Lange, D., Lange, I., Laplace, C., Lavik, G., Laxenaire, R., Le Bihan, C., Leandro, M., Lefevre, N., Lena, M., Lenschow, D., Li, Q., Lloyd, G., Los, S., Losi, N., Lovell, O., Luneau, C., Makuch, P., Malinowski, S., Manta, G., Marinou, E., Marsden, N., Masson, S., Maury, N., Mayer, B., Mayers-Als, M., Mazel, C., McGeary, W., McWilliams, J. C., Mech, M., Mehlmann, M., Meroni, A. N., Mieslinger, T., Minikin, A., Minnett, P., Möller, G., Morfa Avalos, Y., Muller, C., Musat, I., Napoli, A., Neuberger, A., Noisel, C., Noone, D., Nordsiek, F., Nowak, J. L., Oswald, L., Parker, D. J., Peck, C., Person, R., Philippi, M., Plueddemann, A., Pöhlker, C., Pörtge, V., Pöschl, U., Pologne, L., Posyniak, M., Prange, M., Quiñones Meléndez, E., Radtke, J., Ramage, K., Reimann, J., Renault, L., Reus, K., Reyes, A., Ribbe, J., Ringel, M., Ritschel, M., Rocha, C. B., Rochetin, N., Röttenbacher, J., Rollo, C., Royer, H., Sadoulet, P., Saffin, L., Sandiford, S., Sandu, I., Schäfer, M., Schemann, V., Schirmacher, I., Schlenczek, O., Schmidt, J., Schröder, M., Schwarzenboeck, A., Sealy, A., Senff, C. J., Serikov, I., Shohan, S., Siddle, E., Smirnov, A., Späth, F., Spooner, B., Stolla, M. K., Szkółka, W., de Szoeke, S. P., Tarot, S., Tetoni, E., Thompson, E., Thomson, J., Tomassini, L., Totems, J., Ubele, A. A., Villiger, L., von Arx, J., Wagner, T., Walther, A., Webber, B., Wendisch, M., Whitehall, S., Wiltshire, A., Wing, A. A., Wirth, M., Wiskandt, J., Wolf, K., Worbes, L., Wright, E., Wulfmeyer, V., Young, S., Zhang, C., Zhang, D., Ziemen, F., Zinner, T., and Zöger, M.: EUREC^{4}A, Earth System Science Data, 13, 4067–4119, doi:10.5194/essd-13-4067-2021, 2021.

Stokes, G. G.: On the Composition and Resolution of Streams of Polarized Light from different Sources, Transactions of the Cambridge Philosophical Society, 9, 399, 1851.

Stroeve, J., Serreze, M., Holland, M., Kay, J., Malanik, J., and Barrett, A.: The Arctic's rapidly shrinking sea ice cover: a research synthesis, Climatic Change, 110, 1005–1027, doi:10.1007/s10584-011-0101-1, 2012.

Takahashi, T.: Influence of Liquid Water Content and Temperature on the Form and Growth of Branched Planar Snow Crystals in a Cloud, Journal of the Atmospheric Sciences, 71, 4127 – 4142, doi:10.1175/JAS-D-14-0043.1, 2014.

Tan, I. and Storelvmo, T.: Evidence of Strong Contributions From Mixed-Phase Clouds to Arctic Climate Change, Geophysical Research Letters, 46, 2894–2902, doi:10.1029/2018GL081871, 2019.

Tan, I., Storelvmo, T., and Zelinka, M. D.: Observational constraints on mixed-phase clouds imply higher climate sensitivity, Science, 352, 224–227, doi:10.1126/science.aad5300, 2016.

Tan, I., Sotiropoulou, G., Taylor, P. C., Zamora, L., and Wendisch, M.: A Review of

the Factors Influencing Arctic Mixed-Phase Clouds: Progress and Outlook, chap. 5, pp. 103–132, American Geophysical Union (AGU), doi:10.1002/9781119700357.ch5, 2023.

Tancik, M., Srinivasan, P. P., Mildenhall, B., Fridovich-Keil, S., Raghavan, N., Singhal, U., Ramamoorthi, R., Barron, J. T., and Ng, R.: Fourier features let networks learn high frequency functions in low dimensional domains, in: Proceedings of the 34th International Conference on Neural Information Processing Systems, NIPS '20, Curran Associates Inc., Red Hook, NY, USA, 2020.

Tewari, M., Chen, F., Wang, W., Dudhia, J., LeMone, M. A., Mitchell, K., Ek, M., Gayno, G., Wegiel, J., and Cuenca, R. H.: Implementation and verification of the unified NOAH land surface model in the WRF model, in: 20th Conference on Weather Analysis and Forecasting/16th Conference on Numerical Weather Prediction, URL `https://ams.confex.com/ams/84Annual/techprogram/paper_69061.htm`, 2004.

Thompson, D. R., McCubbin, I., Gao, B. C., Green, R. O., Matthews, A. A., Mei, F., Meyer, K. G., Platnick, S., Schmid, B., Tomlinson, J., and Wilcox, E.: Measuring cloud thermodynamic phase with shortwave infrared imaging spectroscopy, Journal of Geophysical Research: Atmospheres, 121, 9174–9190, doi:10.1002/2016JD024999, 2016.

Tomassini, L., Field, P. R., Honnert, R., Malardel, S., McTaggart-Cowan, R., Saitou, K., Noda, A. T., and Seifert, A.: The "Grey Zone" cold air outbreak global model intercomparison: A cross evaluation using large-eddy simulations, Journal of Advances in Modeling Earth Systems, 9, 39–64, doi:10.1002/2016MS000822, 2017.

Tornow, F., Ackerman, A. S., and Fridlind, A. M.: Preconditioning of overcast-to-broken cloud transitions by riming in marine cold air outbreaks, Atmospheric Chemistry and Physics, 21, 12 049–12 067, doi:10.5194/acp-21-12049-2021, 2021.

Tornow, F., Ackerman, A. S., Fridlind, A. M., Cairns, B., Crosbie, E. C., Kirschler, S., Moore, R. H., Painemal, D., Robinson, C. E., Seethala, C., Shook, M. A., Voigt, C., Winstead, E. L., Ziemba, L. D., Zuidema, P., and Sorooshian, A.: Dilution of Boundary Layer Cloud Condensation Nucleus Concentrations by Free Tropospheric Entrainment During Marine Cold Air Outbreaks, Geophysical Research Letters, 49, 1–10, doi:10.1029/2022GL098444, 2022.

Tornow, F., Ackerman, A. S., Fridlind, A. M., Tselioudis, G., Cairns, B., Painemal, D., and Elsaesser, G.: On the Impact of a Dry Intrusion Driving Cloud-Regime Transitions in a Midlatitude Cold-Air Outbreak, Journal of the Atmospheric Sciences, 80, 2881 – 2896, doi:10.1175/JAS-D-23-0040.1, 2023.

Toubbe, B., Bailleul, T., Deuze, J., Goloub, P., Hagolle, O., and Herman, M.: In-flight calibration of the POLDER polarized channels using the Sun's glitter, IEEE Transactions on Geoscience and Remote Sensing, 37, 513–524, doi:10.1109/36.739104, 1999.

Tyo, J. S., LaCasse, C. F., and Ratliff, B. M.: Total elimination of sampling errors in polarization imagery obtained with integrated microgrid polarimeters, Opt. Lett., 34, 3187–3189, doi:10.1364/OL.34.003187, 2009.

Uttal, T., Curry, J. A., McPhee, M. G., Perovich, D. K., Moritz, R. E., Maslanik, J. A.,

Guest, P. S., Stern, H. L., Moore, J. A., Turenne, R., Heiberg, A., Serreze, M. C., Wylie, D. P., Persson, O. G., Paulson, C. A., Halle, C., Morison, J. H., Wheeler, P. A., Makshtas, A., Welch, H., Shupe, M. D., Intrieri, J. M., Stamnes, K., Lindsey, R. W., Pinkel, R., Pegau, W. S., Stanton, T. P., and Grenfeld, T. C.: Surface Heat Budget of the Arctic Ocean, Bulletin of the American Meteorological Society, 83, 255 – 276, doi:10.1175/1520-0477(2002)083<0255:SHBOTA>2.3.CO;2, 2002.

van de Hulst, H.: Light Scattering by Small Particles, Dover Books on Physics, Dover Publications, 1981.

van Diedenhoven, B., Cairns, B., Geogdzhayev, I. V., Fridlind, A. M., Ackerman, A. S., Yang, P., and Baum, B. A.: Remote sensing of ice crystal asymmetry parameter using multi-directional polarization measurements - Part 1: Methodology and evaluation with simulated measurements, Atmospheric Measurement Techniques, 5, 2361–2374, doi:10.5194/amt-5-2361-2012, 2012.

van Diedenhoven, B., Cairns, B., Fridlind, A. M., Ackerman, A. S., and Garrett, T. J.: Remote sensing of ice crystal asymmetry parameter using multi-directional polarization measurements - Part 2: Application to the Research Scanning Polarimeter, Atmospheric Chemistry and Physics, 13, 3185–3203, doi:10.5194/acp-13-3185-2013, 2013.

Vant-Hull, B., Marshak, A., Remer, L. A., and Li, Z.: The Effects of Scattering Angle and Cumulus Cloud Geometry on Satellite Retrievals of Cloud Droplet Effective Radius, IEEE Transactions on Geoscience and Remote Sensing, 45, 1039–1045, doi:10.1109/TGRS.2006.890416, 2007.

Volkmer, L., Pörtge, V., Jakub, F., and Mayer, B.: Model-based evaluation of cloud geometry and droplet size retrievals from two-dimensional polarized measurements of specMACS, Atmospheric Measurement Techniques, 17, 1703–1719, doi:10.5194/amt-17-1703-2024, 2024.

Várnai, T. and Marshak, A.: Observations of Three-Dimensional Radiative Effects that Influence MODIS Cloud Optical Thickness Retrievals, Journal of the Atmospheric Sciences, 59, 1607 – 1618, doi:10.1175/1520-0469(2002)059<1607:OOTDRE>2.0.CO;2, 2002.

Várnai, T. and Marshak, A.: A method for analyzing how various parts of clouds influence each other's brightness, Journal of Geophysical Research: Atmospheres, 108, doi:10.1029/2003JD003561, 2003.

Walbröl, A., Michaelis, J., Becker, S., Dorff, H., Ebell, K., Gorodetskaya, I., Heinold, B., Kirbus, B., Lauer, M., Maherndl, N., Maturilli, M., Mayer, J., Müller, H., Neggers, R. A. J., Paulus, F. M., Röttenbacher, J., Rückert, J. E., Schirmacher, I., Slättberg, N., Ehrlich, A., Wendisch, M., and Crewell, S.: Contrasting extremely warm and long-lasting cold air anomalies in the North Atlantic sector of the Arctic during the HALO-$(\mathcal{AC})^3$ campaign, Atmospheric Chemistry and Physics, 24, 8007–8029, doi:10.5194/acp-24-8007-2024, 2024.

Wallace, J. and Hobbs, P.: Atmospheric Science: An Introductory Survey, Elsevier Inc.,

2nd edn., 2006.

Walsh, J. E.: Intensified warming of the Arctic: Causes and impacts on middle latitudes, Global and Planetary Change, 117, 52–63, doi:10.1016/j.gloplacha.2014.03.003, 2014.

Wang, C., Platnick, S., Meyer, K., Zhang, Z., and Zhou, Y.: A machine-learning-based cloud detection and thermodynamic-phase classification algorithm using passive spectral observations, Atmospheric Measurement Techniques, 13, 2257–2277, doi:10.5194/amt-13-2257-2020, 2020.

Wang, P. K. and Ji, W.: Collision Efficiencies of Ice Crystals at Low–Intermediate Reynolds Numbers Colliding with Supercooled Cloud Droplets: A Numerical Study, Journal of the Atmospheric Sciences, 57, 1001 – 1009, doi:10.1175/1520-0469(2000)057<1001:CEOICA>2.0.CO;2, 2000.

Wang, Y., Yang, P., King, M. D., and Baum, B. A.: Optical Property Model for Cirrus Clouds Based on Airborne Multi-Angle Polarization Observations, Remote Sensing, 13, doi:10.3390/rs13142754, 2021.

Weber, A., Kölling, T., Pörtge, V., Baumgartner, A., Rammeloo, C., Zinner, T., and Mayer, B.: Polarization upgrade of specMACS: calibration and characterization of the 2D RGB polarization-resolving cameras, Atmospheric Measurement Techniques, 17, 1419–1439, doi:10.5194/amt-17-1419-2024, 2024.

Weber, A., Hoffmann, F., and Mayer, B.: Quasi-Lagrangian observations of cloud transitions during the initial phase of marine cold air outbreaks in the Arctic – Part 2: Vertical cloud structure, EGUsphere, 2025, 1–26, doi:10.5194/egusphere-2025-5832, 2025a.

Weber, A., Kirbus, B., Wendisch, M., and Mayer, B.: Quasi-Lagrangian observations of cloud transitions during the initial phase of marine cold air outbreaks in the Arctic – Part 1: Temporal and spatial evolution, EGUsphere, 2025, 1–25, doi:10.5194/egusphere-2025-5831, 2025b.

Weber, A., Köcher, G., and Mayer, B.: Parameterization of 3D cloud geometry and a neural-network-based fast forward operator for polarized radiative transfer, Atmospheric Measurement Techniques, 18, 5805–5821, doi:10.5194/amt-18-5805-2025, 2025c.

Weber, A., Pörtge, V., Emde, C., and Mayer, B.: Retrieval of cloud thermodynamic phase partitioning from multi-angle polarimetric imaging of Arctic mixed-phase clouds, Atmospheric Measurement Techniques, 18, 7581–7601, doi:10.5194/amt-18-7581-2025, 2025d.

Wegener, A.: Thermodynamik der Atmosphäre, J. A. Barth, Leipzig, 1911.

Wendisch, M., Brückner, M., Burrows, J. P., Crewell, S., Dethloff, K., Ebell, K., Lüpkes, C., Macke, A., Notholt, J., Quaas, J., Rinke, A., and Tegen, I.: Understanding causes and effects of rapid warming in the Arctic, Eos, 98, doi:10.1029/2017EO064803, 2017.

Wendisch, M., Macke, A., Ehrlich, A., Lüpkes, C., Mech, M., Chechin, D., Dethloff, K., Velasco, C. B., Bozem, H., Brückner, M., Clemen, H.-C., Crewell, S., Donth, T., Dupuy, R., Ebell, K., Egerer, U., Engelmann, R., Engler, C., Eppers, O., Gehrmann, M., Gong, X., Gottschalk, M., Gourbeyre, C., Griesche, H., Hartmann, J., Hartmann, M., Heinold, B.,

Herber, A., Herrmann, H., Heygster, G., Hoor, P., Jafariserajehlou, S., Jäkel, E., Järvinen, E., Jourdan, O., Kästner, U., Kecorius, S., Knudsen, E. M., Köllner, F., Kretzschmar, J., Lelli, L., Leroy, D., Maturilli, M., Mei, L., Mertes, S., Mioche, G., Neuber, R., Nicolaus, M., Nomokonova, T., Notholt, J., Palm, M., van Pinxteren, M., Quaas, J., Richter, P., Ruiz-Donoso, E., Schäfer, M., Schmieder, K., Schnaiter, M., Schneider, J., Schwarzenböck, A., Seifert, P., Shupe, M. D., Siebert, H., Spreen, G., Stapf, J., Stratmann, F., Vogl, T., Welti, A., Wex, H., Wiedensohler, A., Zanatta, M., and Zeppenfeld, S.: The Arctic Cloud Puzzle: Using ACLOUD/PASCAL Multiplatform Observations to Unravel the Role of Clouds and Aerosol Particles in Arctic Amplification, Bulletin of the American Meteorological Society, 100, 841 – 871, doi:10.1175/BAMS-D-18-0072.1, 2019.

Wendisch, M., Handorf, D., Tegen, I., Neggers, R. A. J., and Spreen, G.: Glimpsing the Ins and Outs of the Arctic Atmospheric Cauldron, Eos, 102, doi:10.1029/2021EO155959, 2021.

Wendisch, M., Brückner, M., Crewell, S., Ehrlich, A., Notholt, J., Lüpkes, C., Macke, A., Burrows, J. P., Rinke, A., Quaas, J., Maturilli, M., Schemann, V., Shupe, M. D., Akansu, E. F., Barrientos-Velasco, C., Bärfuss, K., Blechschmidt, A.-M., Block, K., Bougoudis, I., Bozem, H., Böckmann, C., Bracher, A., Bresson, H., Bretschneider, L., Buschmann, M., Chechin, D. G., Chylik, J., Dahlke, S., Deneke, H., Dethloff, K., Donth, T., Dorn, W., Dupuy, R., Ebell, K., Egerer, U., Engelmann, R., Eppers, O., Gerdes, R., Gierens, R., Gorodetskaya, I. V., Gottschalk, M., Griesche, H., Gryanik, V. M., Handorf, D., Harm-Altstädter, B., Hartmann, J., Hartmann, M., Heinold, B., Herber, A., Herrmann, H., Heygster, G., Höschel, I., Hofmann, Z., Hölemann, J., Hünerbein, A., Jafariserajehlou, S., Jäkel, E., Jacobi, C., Janout, M., Jansen, F., Jourdan, O., Jurányi, Z., Kalesse-Los, H., Kanzow, T., Käthner, R., Kliesch, L. L., Klingebiel, M., Knudsen, E. M., Kovács, T., Körtke, W., Krampe, D., Kretzschmar, J., Kreyling, D., Kulla, B., Kunkel, D., Lampert, A., Lauer, M., Lelli, L., von Lerber, A., Linke, O., Löhnert, U., Lonardi, M., Losa, S. N., Losch, M., Maahn, M., Mech, M., Mei, L., Mertes, S., Metzner, E., Mewes, D., Michaelis, J., Mioche, G., Moser, M., Nakoudi, K., Neggers, R., Neuber, R., Nomokonova, T., Oelker, J., Papakonstantinou-Presvelou, I., Pätzold, F., Pefanis, V., Pohl, C., van Pinxteren, M., Radovan, A., Rhein, M., Rex, M., Richter, A., Risse, N., Ritter, C., Rostosky, P., Rozanov, V. V., Donoso, E. R., Garfias, P. S., Salzmann, M., Schacht, J., Schäfer, M., Schneider, J., Schnierstein, N., Seifert, P., Seo, S., Siebert, H., Soppa, M. A., Spreen, G., Stachlewska, I. S., Stapf, J., Stratmann, F., Tegen, I., Viceto, C., Voigt, C., Vountas, M., Walbröl, A., Walter, M., Wehner, B., Wex, H., Willmes, S., Zanatta, M., and Zeppenfeld, S.: Atmospheric and Surface Processes, and Feedback Mechanisms Determining Arctic Amplification: A Review of First Results and Prospects of the (AC)3 Project, Bulletin of the American Meteorological Society, 104, E208 – E242, doi:10.1175/BAMS-D-21-0218.1, 2023.

Wendisch, M., Crewell, S., Ehrlich, A., Herber, A., Kirbus, B., Lüpkes, C., Mech, M., Abel, S. J., Akansu, E. F., Ament, F., Aubry, C., Becker, S., Borrmann, S., Bozem, H., Brückner, M., Clemen, H.-C., Dahlke, S., Dekoutsidis, G., Delanoë, J., De La Torre Castro, E., Dorff, H., Dupuy, R., Eppers, O., Ewald, F., George, G., Gorodetskaya,

I. V., Grawe, S., Groß, S., Hartmann, J., Henning, S., Hirsch, L., Jäkel, E., Joppe, P., Jourdan, O., Jurányi, Z., Karalis, M., Kellermann, M., Klingebiel, M., Lonardi, M., Lucke, J., Luebke, A. E., Maahn, M., Maherndl, N., Maturilli, M., Mayer, B., Mayer, J., Mertes, S., Michaelis, J., Michalkov, M., Mioche, G., Moser, M., Müller, H., Neggers, R., Ori, D., Paul, D., Paulus, F. M., Pilz, C., Pithan, F., Pöhlker, M., Pörtge, V., Ringel, M., Risse, N., Roberts, G. C., Rosenburg, S., Röttenbacher, J., Rückert, J., Schäfer, M., Schaefer, J., Schemann, V., Schirmacher, I., Schmidt, J., Schmidt, S., Schneider, J., Schnitt, S., Schwarz, A., Siebert, H., Sodemann, H., Sperzel, T., Spreen, G., Stevens, B., Stratmann, F., Svensson, G., Tatzelt, C., Tuch, T., Vihma, T., Voigt, C., Volkmer, L., Walbröl, A., Weber, A., Wehner, B., Wetzel, B., Wirth, M., and Zinner, T.: Overview: quasi-Lagrangian observations of Arctic air mass transformations – introduction and initial results of the HALO–$(\mathcal{AC})^3$ aircraft campaign, Atmospheric Chemistry and Physics, 24, 8865–8892, doi:10.5194/acp-24-8865-2024, 2024.

Wendisch, M., Kirbus, B., Ori, D., Shupe, M. D., Crewell, S., Sodemann, H., and Schemann, V.: Observed and modeled Arctic airmass transformations during warm air intrusions and cold air outbreaks, Atmospheric Chemistry and Physics, 25, 15 047–15 076, doi:10.5194/acp-25-15047-2025, 2025.

Wesche, C., Steinhage, D., and Nixdorf, U.: Polar aircraft Polar5 and Polar6 operated by the Alfred Wegener Institute, Journal of large-scale research facilities, 2, A87, doi:10.17815/jlsrf-2-153, 2016.

Wirth, M. and Groß, S.: Aircraft measurements of backscatter ratio, particle depolarization and water vapour molecular density profiles over Arctic sea ice and ocean during the HALO-$(AC)^3$ campaign in spring 2022, doi:10.1594/PANGAEA.967086, 2024.

Wirth, M., Fix, A., Mahnke, P., Schwarzer, H., Schrandt, F., and Ehret, G.: The airborne multi-wavelength water vapor differential absorption LIDAR WALES: system design and performance, Applied Physics B: Lasers and Optics, 96, 201–213, doi:10.1007/s00340-009-3365-7, 2009.

Wissmeier, U., Buras, R., and Mayer, B.: paNTICA: A Fast 3D Radiative Transfer Scheme to Calculate Surface Solar Irradiance for NWP and LES Models, Journal of Applied Meteorology and Climatology, 52, 1698 – 1715, doi:10.1175/JAMC-D-12-0227.1, 2013.

Woollings, T., Barriopedro, D., Methven, J., Son, S.-W., Martius, O., Harvey, B., Sillmann, J., Lupo, A. R., and Seneviratne, S.: Blocking and its Response to Climate Change, Current Climate Change Reports, 4, 287–300, doi:10.1007/s40641-018-0108-z, 2018.

Wu, P. and Ovchinnikov, M.: Cloud Morphology Evolution in Arctic Cold-Air Outbreak: Two Cases During COMBLE Period, Journal of Geophysical Research: Atmospheres, 127, 1–20, doi:10.1029/2021JD035966, 2022.

Xia, Z. and McFarquhar, G. M.: Dependence of Cloud Macrophysical Properties and Phase Distributions on Environmental Conditions Over the North Atlantic and Southern Ocean: Results From COMBLE and MARCUS, Journal of Geophysical Research: Atmospheres, 129, 1–24, doi:10.1029/2023JD039869, 2024.

Yang, P., Bi, L., Baum, B. A., Liou, K.-N., Kattawar, G. W., Mishchenko, M. I., and Cole, B.: Spectrally Consistent Scattering, Absorption, and Polarization Properties of Atmospheric Ice Crystals at Wavelengths from 0.2 to 100 μm, Journal of the Atmospheric Sciences, 70, 330 – 347, doi:10.1175/JAS-D-12-039.1, 2013.

Young, G., Jones, H. M., Choularton, T. W., Crosier, J., Bower, K. N., Gallagher, M. W., Davies, R. S., Renfrew, I. A., Elvidge, A. D., Darbyshire, E., Marenco, F., Brown, P. R. A., Ricketts, H. M. A., Connolly, P. J., Lloyd, G., Williams, P. I., Allan, J. D., Taylor, J. W., Liu, D., and Flynn, M. J.: Observed microphysical changes in Arctic mixed-phase clouds when transitioning from sea ice to open ocean, Atmospheric Chemistry and Physics, 16, 13 945–13 967, doi:10.5194/acp-16-13945-2016, 2016.

Zdunkowski, W., Trautmann, T., and Bott, A.: Radiation in the Atmosphere: A Course in Theoretical Meteorology, Cambridge University Press, doi:10.1017/CBO9780511535796, 2007.

Zhang, J., Luo, H., Hui, B., and Chang, Z.: Non-uniformity correction for division of focal plane polarimeters with a calibration method, Appl. Opt., 55, 7236–7240, doi:10.1364/AO.55.007236, 2016.

Zhang, S., Xue, H., and Feingold, G.: Vertical profiles of droplet effective radius in shallow convective clouds, Atmospheric Chemistry and Physics, 11, 4633–4644, doi:10.5194/acp-11-4633-2011, 2011.

Zhang, Z.: A flexible new technique for camera calibration, IEEE Transactions on Pattern Analysis and Machine Intelligence, 22, 1330–1334, doi:10.1109/34.888718, 2000.

Zinner, T., Hausmann, P., Ewald, F., Bugliaro, L., Emde, C., and Mayer, B.: Ground-based imaging remote sensing of ice clouds: uncertainties caused by sensor, method and atmosphere, Atmospheric Measurement Techniques, 9, 4615–4632, doi:10.5194/amt-9-4615-2016, 2016.

Zinth, W. and Zinth, U.: Optik. Lichtstrahlen - Wellen - Photonen, Oldenbourg Verlag, München, 4th edn., 2013.

Acknowledgements

An dieser Stelle möchte ich mich noch bei einer ganzen Reihe an Menschen bedanken, ohne die es diese Arbeit so nicht geben würde.

Zunächst möchte ich mich bei meinem Betreuer Prof. Dr. Bernhard Mayer dafür bedanken, dass er mir diese Arbeit ermöglicht hat. Danke für das Vertrauen in mich, für die stets offene Tür, für wertvolle Anregungen und für die intensive Betreuung. Außerdem gilt mein Dank Prof. Dr. Markus Rapp, der nicht nur sofort bereit war, Zweitgutachter zu sein, sondern das specMACS-Team seit Jahren unterstützt und die Messungen im Kalibrierlabor finanziert hat. Ein großes Danke geht auch an Veronika Pörtge. Danke für die gute Zusammenarbeit, die schöne aber auch anstrengende gemeinsame Zeit auf Messkampagnen, im Kalibrierlabor, beim Kennenlernen und Troubleshooten von specMACS u.v.m. Danke auch an das restliche specMACS-Team, insbesondere an Tobias Zinner und Lea Volkmer, die immer mit Rat und Tat zur Seite standen.

Außerdem möchte ich mich bei Andreas Baumgartner und Clemens Rammeloo bedanken, die gemeinsam mit uns die Kalibriermessungen im Labor durchgeführt haben. Danke an Gregor Köcher für das Rechnen der WRF Simulationen, an Philipp Gregor und Leonhard Scheck für Ideen und Hilfe zu neuronalen Netzen und an Claudia Emde, ohne die Polarisation für mich wahrscheinlich immer noch ein Buch mit sieben Siegeln wäre. Des weiteren möchte ich mich bei Benjamin Kirbus für das Rechnen der Rückwärtstrajektorien bedanken. Danke auch an Florian Ewald für das zur Verfügung stellen der VarCloud-Retrievalergebnisse, an Michael Schäfer und Sophie Rosenburg für Hilfe mit den VELOX-Daten und an Manuel Moser für Informationen zu den In-situ-Messungen. Mein Dank gilt außerdem Prof. Dr. Fabian Hoffmann für Ideen und wertvolles Feedback zum adiabatischen Wolkenmodell.

Darüber hinaus möchte ich mich beim gesamten HALO–$(\mathcal{AC})^3$-Kampagnen-Team für die Unterstützung, bereichernde Diskussionen, Feedback und Ideen während der Kampagnenzeit und bei den vielen Workshops bedanken. Hier gilt mein Dank insbesondere Prof. Dr. Manfred Wendisch und den Kolleg*innen aus Leipzig. Danke auch an das Team von FX und vor allem an Tommy Leder, den besten Flugzeugmechaniker der Welt, und seine Kolleg*innen. Danke an Tobias Kölling für Hilfe bei specMACS-Notfällen zu jeder Tages- und Nachtzeit und an Dieter Schell und Rolf Maser für die vielen großen und kleinen Reparaturen am Instrument.

Zusätzlich möchte ich mich bei meinen Bürokolleg*innen Leonie von Terzi und Alexander Geiß für die gute gemeinsame Zeit bedanken. Außerdem geht ein herzliches Vergelts Gott

an Markus Garhammer und Barbara Baumann, die das ganze Institut am Laufen halten. Danke für die immerwährende Unterstützung und die netten Gespräche beim morgentlichen Tee kochen. Danke auch an die vielen anderen Mitglieder des Instituts, die noch nicht genannt wurden, für die nette Zeit und gute Gespräche. Danke an Paul Ockenfuß, Fabian Jakub, Richard Maier, Mihail Manev, Ben Ascher, Stefan Kneifel, Anja Stallmach und viele mehr.

Vielen Dank an alle, die Teile dieser Arbeit Korrektur gelesen haben.

Schließlich möchte ich mich noch bei meinen Freund*innen, meiner Familie, meinen Eltern und meiner Schwester dafür bedanken, dass sie immer hinter mir stehen und mich immer unterstützt haben. Und natürlich danke Michi, dass du immer für mich da bist!

Sollte ich an dieser Stelle noch jemanden vergessen haben, dann fühlt euch bitte trotzdem angesprochen!

Financial support. This research was supported by the German Research Foundation (DFG) within the project SPP 1294 under project number 442667104.

Transparency note. I used Grammarly to improve the grammar and the punctuation in this work.